The University Of Sheffield.

The prediction of wind turbine performance with passive flow control solutions

Paul Fadojutimi

A thesis submitted in partial fulfilment of the requirements for the degree of Doctor of Philosophy

The University of Sheffield
Faculty of Engineering
Department of Mechanical Engineering

May 2026

ACKNOWLEDGEMENTS

I would like to thank God first and foremost for this opportunity, and my parents for encouraging me to embark on this endeavour, my brothers for their words of encouragement during this process, and my project supervisor, Dr Andrew Nowakowski, for his guidance.

ABSTRACT

Wind turbines are dependent on blade technology for the conversion of wind energy into electrical power. There are several Horizontal Axis Wind Turbine (HAWT) studies that have investigated the aerodynamic performance of the turbine blade under steady conditions. These studies have been beneficial for the development of blade technology; however, they do not reflect the real operating conditions of HAWTs and therefore are of limited applicability. This thesis makes an original contribution to the wind engineering corpus by addressing a clear gap in existing numerical studies, in which HAWT aerodynamics are predominantly modelled under steady inflow assumptions. In contrast, the present work presents a consistent and robust numerical framework to model the blade efficiency of the NREL Phase VI turbine using Computational Fluid Dynamics (CFD) under unsteady inflow conditions. Furthermore, the numerical study analyses the performance of PFC devices under unsteady conditions and evaluates their effectiveness across different flow regimes.

This thesis demonstrates that passive devices are useful technological solutions for the optimization of the NREL Phase VI. The microtab, Gurney flap and riblet configurations are utilized to enhance power output across a range of TSRs. The Gurney flap was found to be most effective at $\lambda = 3.79$ and $\lambda = 2.92$ where overall power efficiency is improved by 3.5% and 2.23%. The microtab also yielded comparable improvements in the aerodynamic performance by modifying the pressure distribution near the trailing edge and increasing the effective camber of the blade. This configuration enhanced lift and improved power efficiency across the investigated power range. The slip length model is used to represent the riblet configurations which are investigated in the parametric study. The optimal configuration for the riblet geometry is shown to be Riblet Geometry III where the $h+ = 8$-15, demonstrating a significant reduction in viscous drag and cross flow fluctuations.

NOMENCLATURE

ABL – Atmospheric Boundary Layer

AOA – Angle of Attack

BEM – Blade Element Momentum

CFD – Computational Fluid Dynamics

DNS – Direct Numerical Simulation

GHG – Greenhouse Gases

HAWT - Horizontal Axis Wind Turbine

NACA – National Advisory Committee for Aeronautics

NREL – National Renewable Energy Laboratory

PAJVG – Passive Air Jet Vane Generators

PFC – Passive Flow Control

PIV – Particle Image Velocimetry

Re – Reynolds Number

TKE – Turbulence Kinetic Energy

TSR – Tip Speed Ratio

UDF – User Defined Function

VAWT – Vertical Axis Wind Turbine

VVG – Vane Vortex Generators

WALE – Wall Adapting Local Eddy- Viscosity

WT – Wind Turbine

Greek Symbols

α – Angle of attack

θ_{cp}, θ_T – tip pitch angle, local twist angle

λ – Tip Speed ratio

ϕ – Inflow Angle

Γ – circulation around aerofoil

ρ - Density of air – 1.225 (kg/m^3)

Ω – rotational speed of the rotor

μ - dynamic viscosity of air – 1.82×10^{-5} (Ns/m^2)

τ_w – wall shear

σ – solidity

ω - angular velocity

Symbols

A	Cross-sectional Area (m^2)
A	Axial induction factor
a’	Azimuthal interference factor
C	Contour
C	Chord Length (m)
C_D,C_L	Coefficient of Drag and Lift
C_f, C_p	Coefficient of skin friction and pressure
C_P,C_T	Coefficient of Power and Thrust
D	Drag (N)
dl	Infinitesimal length of contour
F	Axial force coefficient
F_{tip}	Tip loss factor
L, L′	Lift Force (N)
L_s	Slip Length
M	Mach Number
N	Number of blades
P	Power (W)
p∞	Freestream pressure (Pa)
R	Radius (m)
Re	Reynolds Number
S	Total Area of Contour (m^2)
T	Thrust (N)
t	Tangent unit vector
U1, U	Outflow velocity and average velocity (m/s)
Vo,V∞,vrel	Inflow velocity, freestream velocity and relative velocity (m/s)
X	Dimensionless distance

CONTENTS

LIST OF TABLES

LIST OF FIGURES

DECLARATION

I, the author, confirm that the Thesis is my own work. I am aware of the University's Guidance on the Use of Unfair Means. This work has not previously been presented for an award at this, or any other, university.

1 INTRODUCTION

1.1 Background: Recent developments in wind turbine technology

The wind turbine has undergone many evolutions through the ages; it began as a rudimentary windmill used for grinding grain and pumping water in Persia between 500-900AD. Europeans developed their own windmills during the Middle Ages which were also used for food production. The Dutch horizontal-axis windmill was the most popular type of wind machine for many centuries, and it became the prototype for the wind turbine (WT). James Blyth, a Scottish professor, designed the first modern WT in 1887; although small and inefficient it could power a few light bulbs and a small lathe. An American engineer called Charles F. Brush was working contemporaneous to Blyth to create a larger and more effective WT. Brush's turbine was one of the first modern WTs to produce electricity; it was 17m in diameter, consisting of 144 blades, with a 12kW generator (1).

Over the course of the next century, the use of WTs became more widespread, and the subsequent redesigns of the WT helped to improve its capacity to produce electricity. The advancement of wind technology in the late 20th century was useful in creating large commercial WTs within the United States. The U.S. government financed the research and development of the first generation of multi-megawatt turbine technologies in tandem with the National Science Foundation in the 1980s (2). Many of the novel engineering devices that were created back then are still in use today: this includes the variable-speed generator, steel tube towers, and composite blade materials. Figure 1.1 depicts a modern horizontal-axis wind turbine.

Figure 1.1: A modern horizontal-axis wind turbine

Wind turbines are now established as a mature technology for electricity generation; decades of research have enhanced the overall performance of WTs and have made them more efficient in generating energy. The rapid proliferation of WTs across the world, particularly in China and the US, is a testament to the development of wind technology. Advances in technology have facilitated the growth of the wind energy sector, making it the fastest-growing sector for energy production (3).

Modern WTs have been made more efficient through research and refinement of the rotor blades' design. The modern blade is larger now than it was at the turn of the century, the diametric length of a turbine's blade was approximately 60m back then. The blade span of the average onshore WT has doubled in length; it measures 120m from tip-to-tip (4). Figure 1.2 illustrates the growth in the diametric span of the average turbine blade. The utilisation of larger rotor blades has reduced the cost of electricity generation, especially, as modern turbines operate at elevated heights with access to faster winds. The bigger blades can sweep larger areas capturing more wind and therefore generate more power. This trend of increasing the size of WTs and the length of the rotor blades is expected to continue as it increases the capacity factor and reduces the cost of energy production.

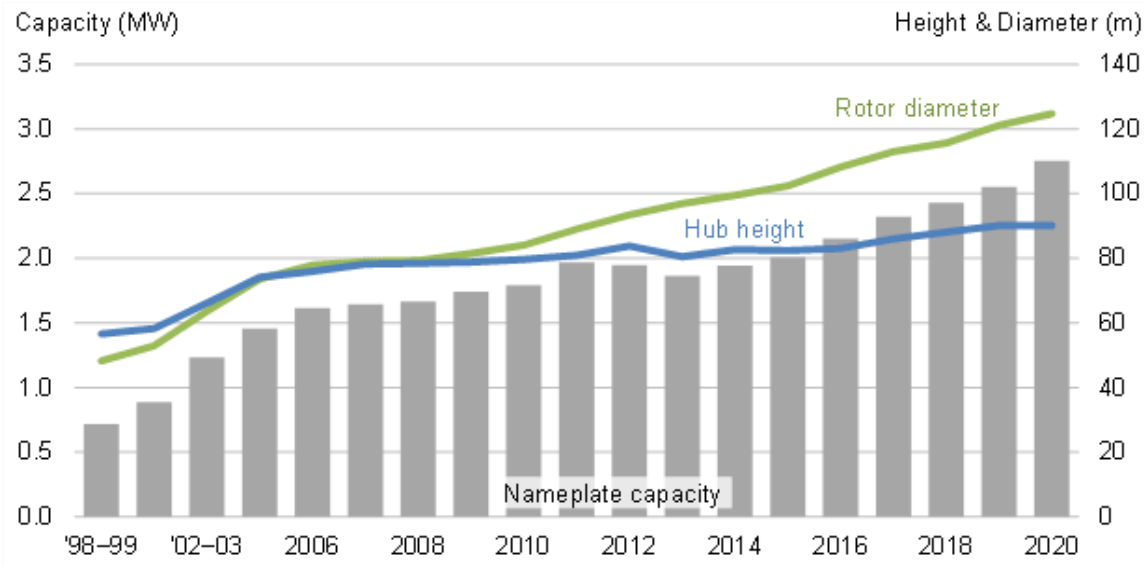

Figure 1.2: The average rotor diameter, turbine height and nameplate capacity of commercial WTs in the 21st century (4)

Recent blade innovation includes modifications to the original shape of the commercial WT. The modern blade is more sophisticated in aerodynamic design, use of materials, and configuration than ever before. Figure 1.3 shows a contrast between the modern state-of-the-art blade, and a blade made in the 1980s. Many design innovations have been applied

to the 1980s blade: which includes a curved tip shape to reduce noise pollution, and a higher tip to allow for the reduction of torque. Furthermore, the blades are made sleeker and lighter with high-lift aerofoils, which allows the blades to move faster and enhances turbine performance. The modern blades of a WT are 90% lighter than the 1980s blade this allows the WT to operate more efficiently (5). The aeroelastic tailoring offers improved energy capture and system durability, whilst the blade couplings increase energy yield.

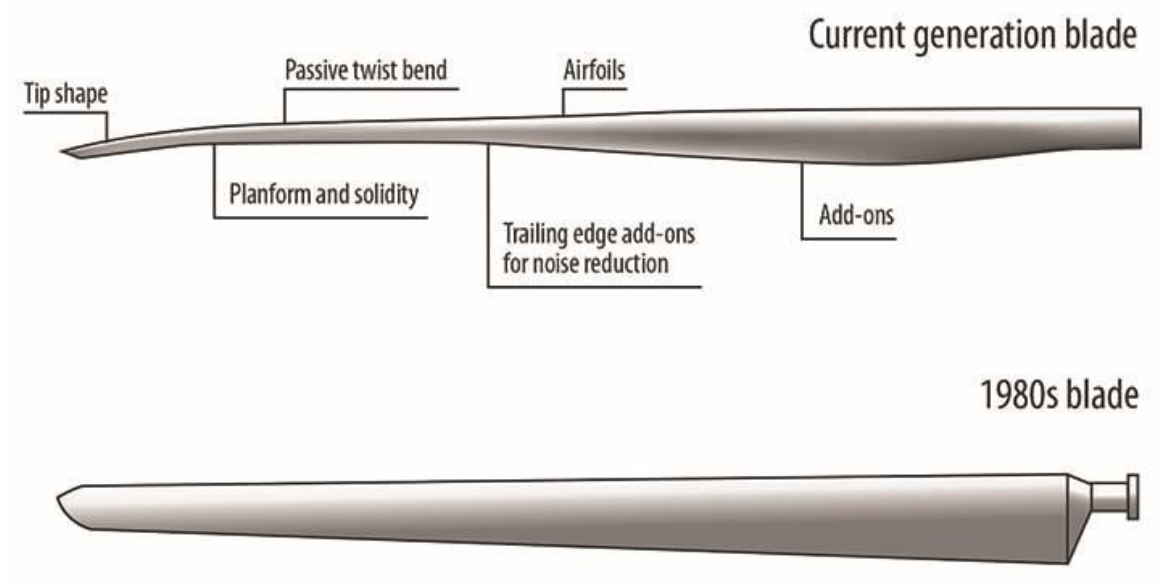

Figure 1.3: A schematic of a modern commercial WT blade in comparison to a 1980s blade (5)

An essential aspect of improving the performance of WTs is the manufacturing of materials. WT research has established some of the design constraints required to create high-quality materials. Examples of material innovation within the energy sector in recent decades are numerous; semiconductor materials, fibre-reinforced composites, rare-earth magnets, lubricants, etc. Blades are manufactured from the same materials as they were in the 1990s - low-composite fibres and durable epoxy resins. These materials give the blade the necessary properties to function: the durability to last decades, an attrition-resistant surface, and the adaptability to perform in inclement weather. Further innovation in material science would improve the functionality of blades and improve strength, stiffness, and weight properties at a low cost (5). Materials of interest include resin matrix, fibre reinforcement, and core materials which can potentially give blades the above-mentioned attributes. Other WT components would also benefit from innovations in material science.

1.2 The Importance of Wind Energy

1.2.1 The Greenhouse Gas Effect

Since the advent of the Industrial Revolution and the invention of the steam engine in the 18th century, there has been a dramatic increase in the volume of greenhouse gas (GHG) emissions. The contribution of conventional power sources to GHG emissions has been a source of consternation for environmentalists for over a century. The emission of gases such as carbon dioxide (CO_2), methane (CH_4), nitrous oxide (N_2O) and fluorinated gases is particularly damaging to the Earth's atmosphere. GHGs trap the sun's infrared radiation in the form of heat, warming the Earth's surface before reemitting the radiation into space. The combustion of fossil fuels has created an imbalance in the ecological cycle, an inordinate amount of GHG is produced, and the gases absorb more radiation than necessary which causes the temperature of the Earth to rise. The Earth's temperature has been rising by 0.08 °C every decade since the 1880s, however, since the 1980s there has been a rise of 0.18° C according to the NOAA's annual climate report (6). Furthermore, 2020 was recorded as the second-warmest year on record based on NOAA's temperature data displayed in Figure 1.4. The increase in global surface temperature illustrates the deleterious effect that anthropogenic GHG emissions are having on the environment.

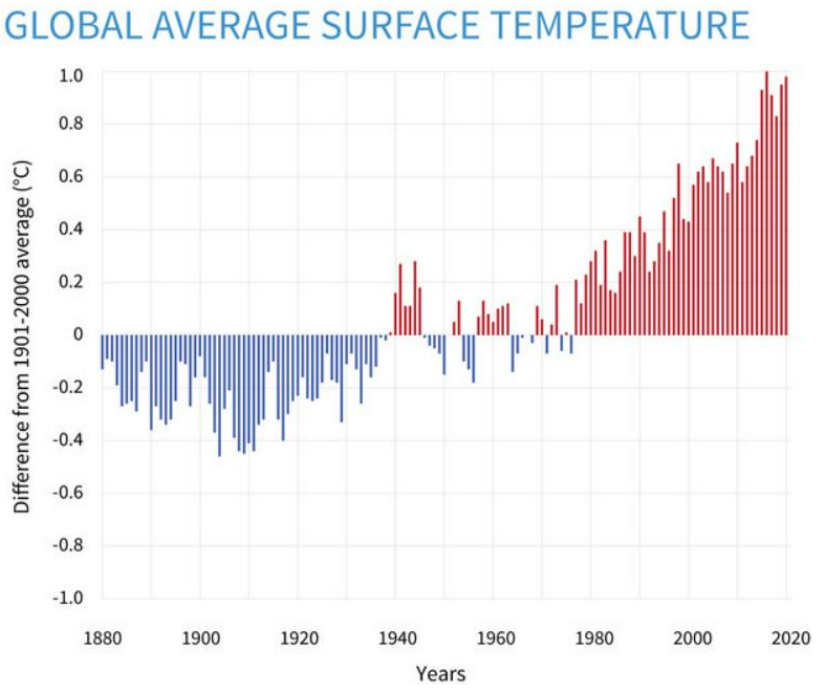

Figure 1.4: Global Average Surface Temperature (1880 -2020) (6)

Climate scientists have warned of the ecological damage that anthropogenic GHGs can incur on the Earth's environment. Human activities enhance the greenhouse effect and cause the emission of billions of tonnes of CO_2 emissions every year which causes global warming. Climate change is increasingly destroying the environment: by causing extreme weather events such as floods, droughts, heatwaves, and hurricanes. As well, as damage to nature: loss of biodiversity, destruction of ozone layers, increased forest mortality and the loss of wildlife. Furthermore, the rising sea levels, desertification and food insecurity threaten to destroy the way of life of various people groups around the world. The energy sector is the biggest contributor to GHG emissions accounting for three-fourths of global emissions (7). To decrease GHG emissions a reduction in the production and consumption of fossil fuels is a sine qua non. Accordingly, the depletion of fossil fuel reserves has given the global community a greater incentive to develop their renewable resources. The development of low-carbon technologies within the wind energy industry is an integral part of achieving climate neutrality. It is in this context, a global drive for the reduction of GHG emissions, that this research takes place.

1.2.2 Wind Energy Expansion

The wind industry is predicted to grow by leaps and bounds in the coming decades forming a third of the global market share for electricity generation by 2050 (8). The expansion of the wind industry as per the Paris Agreement requires nation-states to take a transformative approach to energy generation. As a response to international treaty stipulations, signatory countries are committing to replace their fossil fuel sources with renewable energy supplies to achieve carbon neutrality by 2050. The Paris Agreement outlines the need for increased electrification, accelerated wind power deployment, and technological development for the sustainability goals to be realized by the middle of the century. Wind power is expected to become the foremost power source in the world, with an installed power capacity of 6000 GW (8). To reach these lofty goals – to optimize and develop wind power – a thorough understanding of the current limitations of WTs is required. Furthermore, an evaluation of the technological trends within the wind energy industry would help to advance the state-of-the-art and to achieve climate goals.

Wind power is a clean source of renewable energy that does not emit any air or water pollutants, it utilises natural sources for power production and is, therefore, better for the environment. The primary benefit of using renewable energy sources for power generation is the reduction of GHGs which are detrimental to the Earth's atmosphere. The total power capacity of renewable energy amounted to 2802 GW by the end of 2020; this represents a 9.28% (260 GW) increase in energy capacity from the previous year (9). A subsequent

increase in renewable energy capacity occurred in 2021 of 290 GW. The expansion of the renewable energy sector is forecasted to continue apace and eventually rise to 4800 GW by 2026 (10). Figure 1.5 illustrates the yearly growth in renewable electricity generation from 2019 to 2021 – bioenergy, solar, hydro and wind – the increase suggests a growing demand for sustainable energy. In particular, the wind industry, saw a marked increase in its expansion, the growth (almost doubled) from 58GW in 2019 to 111 GW in 2020 (11).

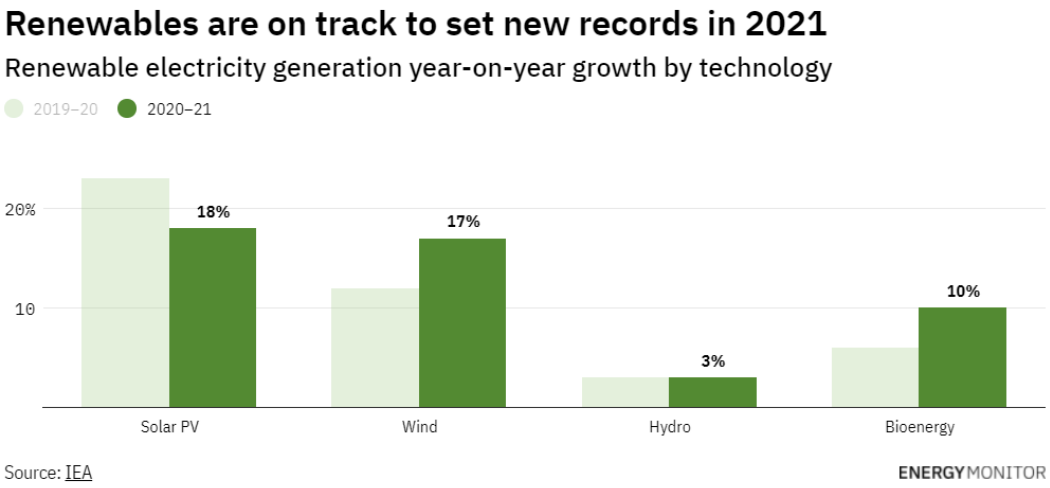

Figure 1.5: Renewable Electricity Generation (10)

1.3 The optimisation of wind energy

The intense heating of the Earth's surface causes hot air to rise in equatorial regions, and the cooler air (due to its higher pressure) moves from the northern hemisphere in a southern direction towards the Equator. The reverse process takes place in the southern hemisphere with the cooler air moving northward to the Equator. The Coriolis effect causes the winds to be deflected in a clockwise/anticlockwise motion, producing a cyclonic rotation. Wind patterns are therefore an epiphenomenon of solar energy striking the Earth's surface and the Coriolis force deflecting the wind in correspondence to the Earth's rotation.

Accordingly, wind energy is unevenly distributed varying greatly by location and terrain. Accessing stronger winds requires a geophysical understanding of the landscapes designated for WT installation. WTs extract kinetic energy from the Earth's atmosphere and convert it into electricity. The wind speeds are highest in the troposphere and therein resides the largest sources of kinetic energy. The wind speed of air increases with altitude within the lower troposphere, hence the drive to increase the hub height of the average

WT. Also, in many regions of the world, the mean surface wind speeds are up to 70% higher over open oceans than on land (12). This veritable fact has spurred the development of offshore energy services.

An optimized engineering approach to WT distribution would enable the maximum energy generation for the minimum costs. The power of the wind law explicates the relationship between wind speed and wind energy: wind power is directly proportional to the cubic wind speed. Coastal areas tend to experience stronger winds providing the optimal conditions for the placement of wind farms. To produce the maximum power possible WTs are usually positioned in coastal areas. A cut-in speed of 6-9 mph is enough to initiate the spinning of the rotor blades but to yield the maximum energy possible the wind speed must be between 31-55 mph. Figure 1.6 shows the speed at which WTs generate the most power. If the limit is exceeded, then no power is produced, and the WT may experience some damage. Meteorological factors such as the mean wind speed, distribution, and direction are taken into consideration for optimal electricity generation. Power generation potential is also limited by the geometric design of the wind farm – the orientation, spacing and positioning of individual turbines.

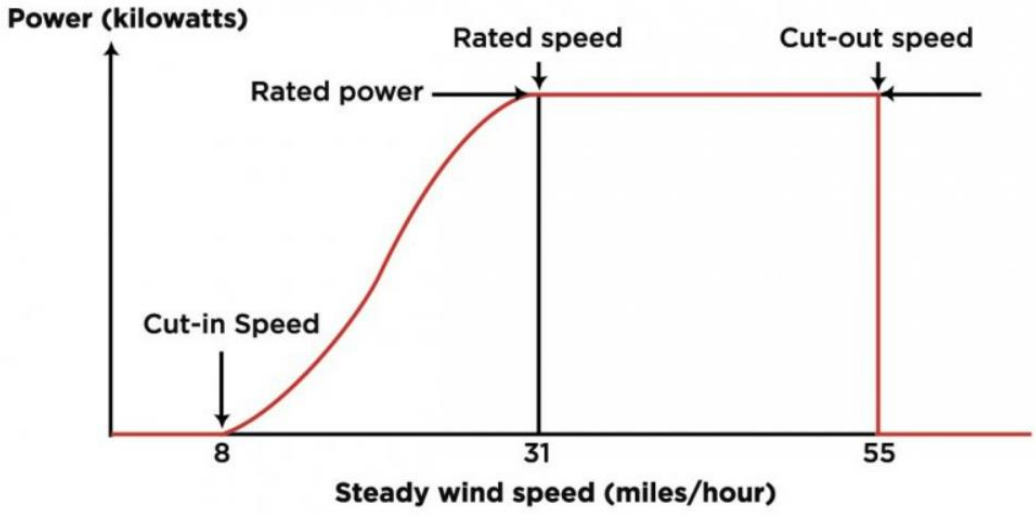

Figure 1.6: Typical wind turbine power with steady wind speed (13)

Wind energy is a competitive source of energy as it is both free and inexhaustible. Despite remaining substantial, the cost of installation has decreased significantly. The growth of wind energy deployment is correlated with this steep decline in the cost of wind energy production. Novel technologies have reduced installation and maintenance costs, making the price of energy generation as little as $0.04 per kWh (14). The modern WT is the

product of almost half of a century of research, it represents the integration of various optimised subsystems. Decreasing the operational cost of energy production further through innovation to near-zero has encouraged increased wind energy deployment and the expansion of wind resources.

Wind energy science has the potential to reduce costs of energy generation further through technological advancements. An interdisciplinary approach to contemporary research challenges would facilitate an improvement in the system performance of commercial turbines. Innovation has already reduced the economic and environmental costs of power generation creating a potential pathway for the replacement of traditional energy sources. The three primary drivers of wind cost reduction are increased hub heights, rotor diameter and power rating. The development of these design parameters and their effect on power optimisation and cost reduction are discussed in the opening section of this disquisition. The energy of the wind is calculated using Equation 1.1.

$$P = \frac{1}{2}\rho C_p A V^3$$

Equation 1.1

P represents the instantaneous power generated, C_p is the power coefficient, the air density is ρ, V is for air velocity, and A is the swept area of the rotor. A small increase in hub height allows the turbines to operate in atmospheric regions with significantly greater V which increases power generation. Also, generators and power electronics have greater power capacities and can produce more power (at a constant C_p). The power coefficient is a measure of the WTs system performance (aerodynamic, electrical, and mechanical). An improvement in the aerodynamic design of the rotor blade would directly affect the electricity produced by a wind machine. Furthermore, the increase in rotor length means that there is a greater swept A , which allows for larger energy capture. A WT with larger blades can operate at lower wind speeds and still maintain the same power output provided the swept area is large enough. The optimisation of the turbine's subsystems - power electronics and generators - has increased power production. And the creation of larger rotors and taller WTs are the primary factors in the reduction of the cost of energy production. The next generation of WT will require advancement in technology and innovative research that builds on acquired knowledge in the wind energy field.

Energy researchers examine the wind patterns to ascertain the optimal placement of wind farms, and the economic feasibility of wind projects. By collecting the ambient air characteristics (temperature, pressure, wind velocity) of a turbine at hub height

meteorologists can determine the power generating capacity. The wind speed at hub height is calculated using Equation 1.2.

$$V_{hub\ height} = \left(\frac{p \cdot T}{1.225\ R}\right)^{\frac{1}{3}} \cdot V_{local}$$

Equation 1.2

The air pressure and temperature are signified by p and T, respectively. The atmospheric gas constant, R, is given as 287.053 J K^{-1} kg^{-1}. The wind velocity in the areas surrounding the turbine is designated V_{local} , and $V_{hub\ height}$ is the wind speed at rotor height. Using Equation 1.1 and 1.2 it is possible to work out the maximum power generation potential of a turbine. The actual power yielded from the wind's kinetic energy can also be deduced once the capacity factor is known.

1.4 The commercial wind turbine

The working principle of a commercial WT is simple: the wind's kinetic energy is converted into mechanical power through the rotating of the turbine's blade. The wind flows across the rotor blades creating a pressure difference due to their airfoil shape, with lower pressure on the suction side and higher pressure on the pressure side. The corollary effect is the production of a lift force perpendicular to the relative wind, which causes the blade to move in a rotary motion. As the blades move the rotor starts to spin which causes the drive shaft to turn, the gearbox speeds up the rotation from 30 to 60 revolutions per minute to 1000 to 1800 revolutions per minute (depending on turbine design). The generator uses magnetic fields to convert the rotational energy into electrical energy, a process known as electromagnetic induction. Faraday's law describes how a changing magnetic flux through a conductor induces an electromotive force. The electricity from the generator is transmitted via cables to a transformer, and then to the windfarm's substation, it is then converted to the right voltage and distributed to an electricity grid which powers the local homes and businesses.

Most utility-scale turbines installed in wind farms have a three-bladed design . There are two main types of WTs used in these plants: the vertical-axis wind turbines (VAWT), and the horizontal-axis wind turbines (HAWT). The HAWT is the most common type of wind machine in use today. It has its axis of rotation horizontal to the ground with the airflow parallel to the blades. Most commercial HAWTs are upwind turbines they have their rotors fixed at the front of the turbine facing the oncoming wind flow. A yaw mechanism is used to orientate the rotor towards the direction of the wind to harness the kinetic energy. The

larger HAWTs use anemometers and electric controls to measure wind direction and speed, the turbine adjusts itself in the right direction through the pitch system. The downwind turbine has its rotors positioned at the backside of the turbine with the nacelle at the front facing the wind direction. Figure 1.7 shows an illustration of the components of a HAWT.

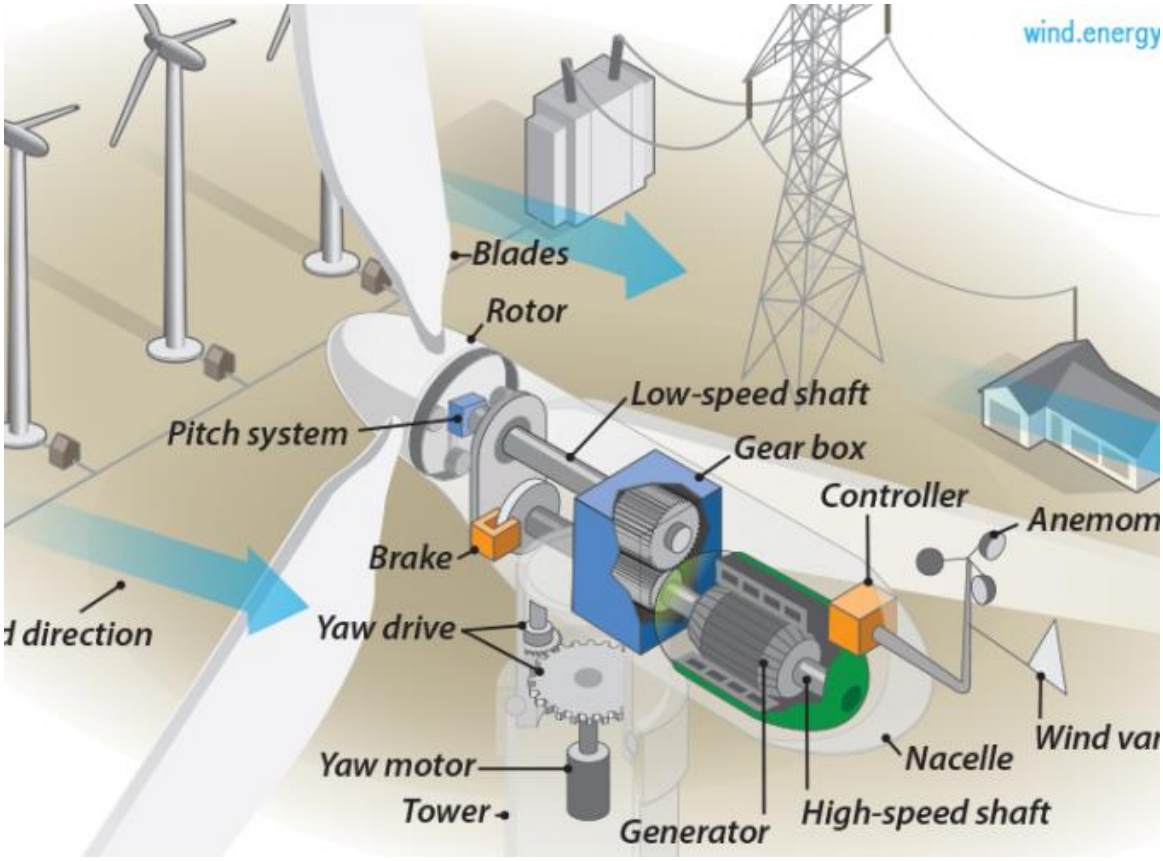

Figure 1.7: Electromechanical components of a wind turbine (15)

The construction of the HAWT is a complex enterprise; it involves the manufacture and soldering of multifarious parts. The major parts of the WT are the tower, nacelle, rotor, and generator. The tower is typically made of round tubular steel which is 3-4m in diameter (16). The average hub height of a tower is displayed in Figure 1.2 as being approximately 90m, however, there are turbines far larger. For instance, a state-of-the-art turbine developed by GE Renewable Energy called Haliade-X has a height of 260m and a rotor diameter of 220m with a power capacity of 14 MW (17). The aerodynamic design of the rotor blade produces a lift force when the wind hits the blade. A large lift-to-drag ratio causes the rotor blades to move at fast tip speeds with high efficiency. The hub is manufactured from cast iron, a robust material that allows it to hold the blades together as they rotate. The nacelle is located on top of the tower; it houses the generator and gearbox. These electromechanical components comprise the HAWT and when fitted

together they form a powerful machine with a great generational capacity. According to the US Department of Energy, the average commercial turbine (2.75MW) generates 843,000 kWh per month which is enough to power 940 homes in the US (18).

1.5 Wind Profiles

The wind's characteristics within the atmospheric boundary layer (ABL) have been a subject of interest within engineering research since their effect on large structures (buildings, towers, and bridges) was first discovered (19). The behaviour of the wind is often complex and mercurial; wind intensity tends to vary with temporal and spatial distance. The Coriolis effect best describes why this is, the insolation of the Earth's uneven surface combined with its rotation produces fluctuations in wind velocity and direction. In addition, wind turbulence can be influenced by any of the following factors: topography, thermal gradients, diurnal, and seasonal cycles (20). Each of these factors affects wind flow aerodynamics and can cause vortices or irregular wind flow. Furthermore, hills, buildings, and trees can act as obstacles to airflow and cause turbulence. Unsteady wind affects the capacity of WTs to harness the kinetic energy of the wind.

Atmospheric wind operates based on the physical laws: the conservation of mass, momentum, and energy (21). Despite this, wind turbulence is a difficult phenomenon to predict because it can occur due to the slightest change in the terrain. This makes wind turbulence a somewhat random occurrence. HAWTs experience turbulence, wind shear, and skewed flow all of which affect blade inflow conditions. The combined effects of these adverse flow conditions can lead to unsteady blade loading and a shorter fatigue life (22). Analysing the structural response of HAWTs to aerodynamic loads is key to improving turbine performance and efficiency.

The advances in wind turbine aerodynamics have led to the modern HAWT reaching a power efficiency of approximately 50%, which is close to Betz's theoretical limit of 59.3% (23). The HAWT is therefore a highly optimized machine, and its performance can be predicted if inflow conditions are well understood. Most research into HAWT performance assumes steady inflow conditions, an ideal that rarely occurs in practice. There is a lack of numerical studies validating the HAWT's performance in unsteady wind, thus, the effects of unsteady wind on aerodynamic performance remain an open-ended research question (24) (25). Predicting HAWT performance in real circumstances is an important step in optimising turbine design and has the potential to further improve aerodynamic efficiency. This thesis addresses this gap in wind literature through a comprehensive examination of HAWT studies, and the application of robust numerical methodology for aerodynamic evaluation.

1.6 Aims and Objectives

The aim of this thesis is to investigate the aerodynamic performance of the NREL Phase VI under unsteady wind conditions and to evaluate the effectiveness of passive flow control devices in enhancing aerodynamic performance.

To achieve this aim, the following objectives are addressed:

- To critically review existing numerical and experimental studies on HAWT aerodynamics, with particular emphasis on the limitations associated with steady inflow assumptions and their implications for predicting turbine performance in real operating conditions.
- To develop and validate a numerical modelling framework for the NREL Phase VI wind turbine, employing Blade Element Momentum (BEM) theory and three-dimensional Computational Fluid Dynamics (CFD) to assess aerodynamic performance under both steady and unsteady wind conditions.
- To implement and model passive flow control devices, including microtabs, Gurney flaps, and riblet geometries, using the slip-length modelling approach for riblet surfaces.
- To evaluate the impact of passive flow control devices on turbine aerodynamic performance under unsteady inflow conditions, quantifying changes in power output, torque, and flow behaviour across a range of tip-speed ratios.
- To conduct a systematic parametric and comparative assessment of passive flow control strategies, identifying the operating regimes in which each device is most effective and establishing their relative advantages and limitations for HAWT applications.

1.7 Thesis Outline

Chapter 1 gives a synopsis of the historical and modern developments within the wind industry and explains the operating mechanisms of the HAWT.

Chapter 2 explains the fundamental principles of wind turbine aerodynamics and evaluates the methods used to assess the aerodynamic performance of HAWTs. Passive flow control strategies are also discussed within the chapter.

Chapter 3 provides an exposition of the method of analyses used within this paper with regards to the meshing technique, numerical and turbulence modelling.

Chapter 4 uses Qblade software and ANSYS FLUENT to simulate the performance of the NREL Phase VI turbine and provides comparative analysis.

Chapter 5 explores the implementation of passive flow control strategies (microtabs, Gurney flaps, and riblets) and their effects on aerodynamic performance.

Chapter 6 summarises the key findings, discusses their implications for HAWT design, and provides recommendations for future research

2 LITERATURE REVIEW

2.1 Introduction

The last century has seen major historical improvements in wind turbine design such as the development of power electronics, the redesign of rotor blades, and the use of stronger/durable materials for WT construction. Many of the innovations in the wind energy industry have come about through research into WT aerodynamics. For example, the experimental studies carried out by Poul La Cour at the turn of the 20th century were instrumental in the development of the WT. La Cour's method of investigation involved wind tunnel testing and field experiments where an anemometer was mounted on a pole and used to characterize wind flow. His research demonstrated that WTs operate more efficiently with fewer rotor blades, and regulators can be used to ensure a steady supply of electricity (26) (27). La Cour also corrected the misapprehension that rotor blades were driven by the force of the wind; instead, he confirmed that the rotor blade is driven by a suction force acting on the blade (26). La Cour was one of many pioneers in rotor aerodynamics; he helped to broaden the understanding of aerodynamic principles and to optimize the design of turbine blades. His seminal work in WT aerodynamics laid the foundation for the development of the rotor blade and the creation of multi-megawatt turbines.

Poul La Cour published several popular disquisitions on physics and technology and delivered thousands of lectures at various high schools and village halls across Denmark. In 1904, La Cour taught courses at Askov folk high school in wind engineering to several of his students. Johannes Juul was one of the first students to be taught the principles of windmill theory, maintenance, and development. Like La Cour, Juul believed that wind technology should be developed to harness the abundant wind resources available in Denmark. Juul would eventually follow in the footsteps of his mentor and become a pioneer in WT development with the invention of the world's first alternating current WTs at Vester Egesborg (28). After World War II, Johannes Juul embarked on a project to develop a state-of-the-art WT to enhance Denmark's energy supply system. He developed a two-blade turbine with a power rating of 10 kW through wind tunnel testing, for which he received international acclaim. The turbine was designed with aerodynamic tip brakes and an automatic braking system to prevent the rotor from operating in strong winds. In 1962, Juul invented a more powerful WT called the "Gedser Turbine" which was a three-bladed upwind turbine with a yawing mechanism, an aerodynamic braking tip, and an asynchronous generator (29). The Gedser Turbine had a power rating of 200 kW and was

considered an innovative design at the time and the prototype for the modern commercial WT. The achievements of Poul La Cour and Johannes Juul underscore the importance of practical experimentation in the development of the WT.

2.2 1D Momentum Theory

The development of rotor aerodynamics facilitated the growth of the WT industry in the 20th century. The initial attempts to resolve steam navigation problems using screw propellers helped to establish the foundations of rotor theory. In response to technical problems, W. J. M. Rankine and R. E. Froude formulated the 1D momentum theory to predict propeller performance (26). The 1D momentum theory is a simple concept for analysing wind turbine aerodynamics. The rotor is modelled as a simple actuator disc with negligible thickness within a control volume. The flow velocity is constant and normal to the rotor's axis of rotation. Figure 2.1 illustrates the flow of the air in relation to the actuator disc. The turbine extracts kinetic energy from the air which causes the velocity of the air to decrease as it reaches the rotor plane, and causes an immediate pressure rise to occur. The cross-sectional area of the flow at the inlet is smaller and expands downstream of the propeller due to the decrease in velocity. Knowledge of the inflow conditions and induced flow velocity allows one to predict the thrust and power performance of the rotor. The Rankine-Froude theory relies on several simplifying assumptions:

1. Wind flow is steady and homogenous.
2. Wind flow is incompressible and inviscid, with irrotational and isentropic conditions.
3. Flow velocity and loading are uniform across the disc
4. The actuator disc does not obstruct or impede flow passage.
5. The pressure outside the streamline boundary is considered freestream pressure.
6. There is an infinite number of blades (30).

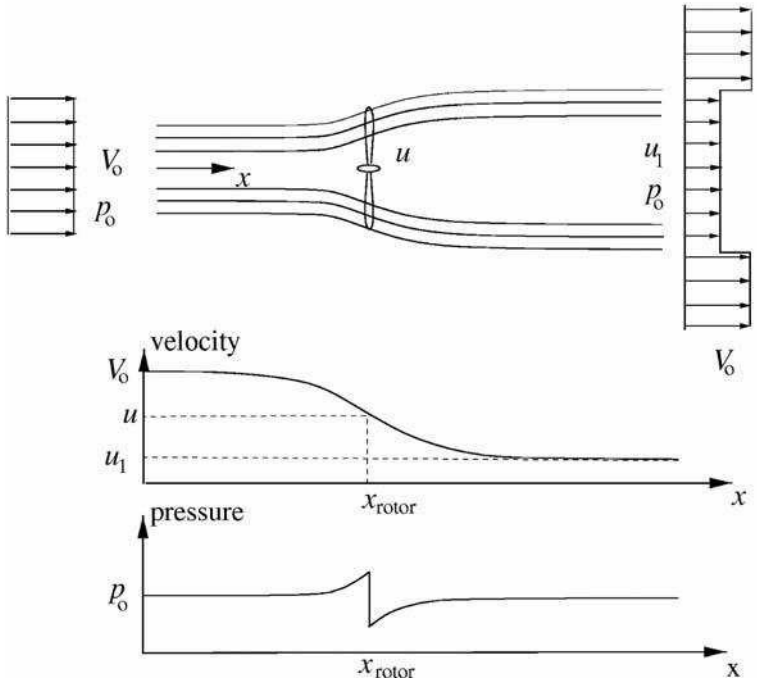

Figure 2.1: An illustration of the air flow within the propeller plane (31)

The conservation of energy principle states that the total energy of an isolated system is conserved over time. The Bernoulli Equation derives from the conservation of energy principle, and it is applicable to the flow problem illustrated in Figure 2.1. The incompressible fluid passes through a stream tube of varying cross-section past a propeller. The total energy (and density) of the fluid for a streamline in the centre of the tube remains constant. The flow area expands when it passes the propeller because of the decrease in flow velocity. The wind's kinetic energy is used to power the wind turbine, which leads to a decrease in the flow velocity in the wake. The continuity equation explains why the decrease in velocity causes the cross-sectional area of the flow to increase. The Bernoulli equation can also be used to calculate the change in pressure through the stream tube. It is also used to work out the aerodynamic loads acting on aerofoils.

The thrust of the propeller is equal to change in momentum as shown in Equation 2.1. The thrust force is denoted by T, the density is ρ, V_o is the inflow velocity and u_1 the outflow velocity, and the cross-sectional area of the actuator disc/rotor, A and the velocity at the rotor is u.

$$T = \rho \cdot u \cdot A\,(V_0 - u_1)$$

Equation 2.1

The mathematical relationship between the thrust, power, and swept area of the propeller is given by Equation 2.2.

$$P = \sqrt{\frac{T^3}{2\rho A}}$$

Equation 2.2

Assuming zero gravity, the pressures at the inlet and outlet would be considered constant. The Bernoulli Equation defines the behaviour of an incompressible fluid within a control volume in terms of velocity, density, and pressure. The static pressure is denoted as p, and u is the velocity experienced at the rotor.

$$p + \frac{1}{2}\rho u^2 = \text{constant}$$

Equation 2.3

The average of the inflow and outflow velocity is given by Equation 2.4:

$$\frac{u_1 + V_o}{2} = u$$

Equation 2.4

The pressure change across the actuator disc is given by:

$$\Delta p = \frac{1}{2}\rho\,({V_o}^2 - {u_1}^2)$$

Equation 2.5

The power output of the propeller is equal to the rate of work done by the fluid.

$$P = \frac{1}{2}\rho A u\left({V_o}^2 - {u_1}^2\right)$$

Equation 2.6

The axial induction factor, a, is the fractional decrease in wind velocity between the freestream and the rotor. u_1= (1-2a)V_0, is placed in Equation 2.6 and equals the following:

$$P = 2\rho {V_o}^3 a(1-a)^2 A$$

Equation 2.7

The pressure in the flow can be expressed as a non-dimensional parameter, the power coefficient C_p:

$$C_p = \frac{P}{\frac{1}{2}\rho {V_o}^3 A}$$

Equation 2.8

Using Equation 2.7 and 2.8 a simple expression for the ideal expression coefficient, C_p, can be derived :

$$C_p = 4a(1-a)^2$$

Equation 2.9

Differentiating Equation 2.9 with respect to a show that the maximum energy extracted occurs when a=1/3.

$$\frac{dC_p}{da} = 4(1-a)(1-3a)$$

Equation 2.10

When a = 1/3 the ideal power coefficient, C_p, reaches its theoretical maximum of 59.3% which is known as Betz's limit.

The coefficient of thrust is given by Equation 2.11:

$$C_T = \frac{T}{\frac{1}{2}\rho {V_o}^2 A}$$

Equation 2.11

When the thrust is expressed in terms of the axial induction factor the equation for coefficient of thrust becomes:

$$C_T = 4a\,(1-a)$$

Equation 2.12

The value of the thrust coefficient giving the theoretical maximum power coefficient is C_T=8/9 when a = 1/3. Figure 2.2 shows C_p and C_T plotted against the axial induction factor.

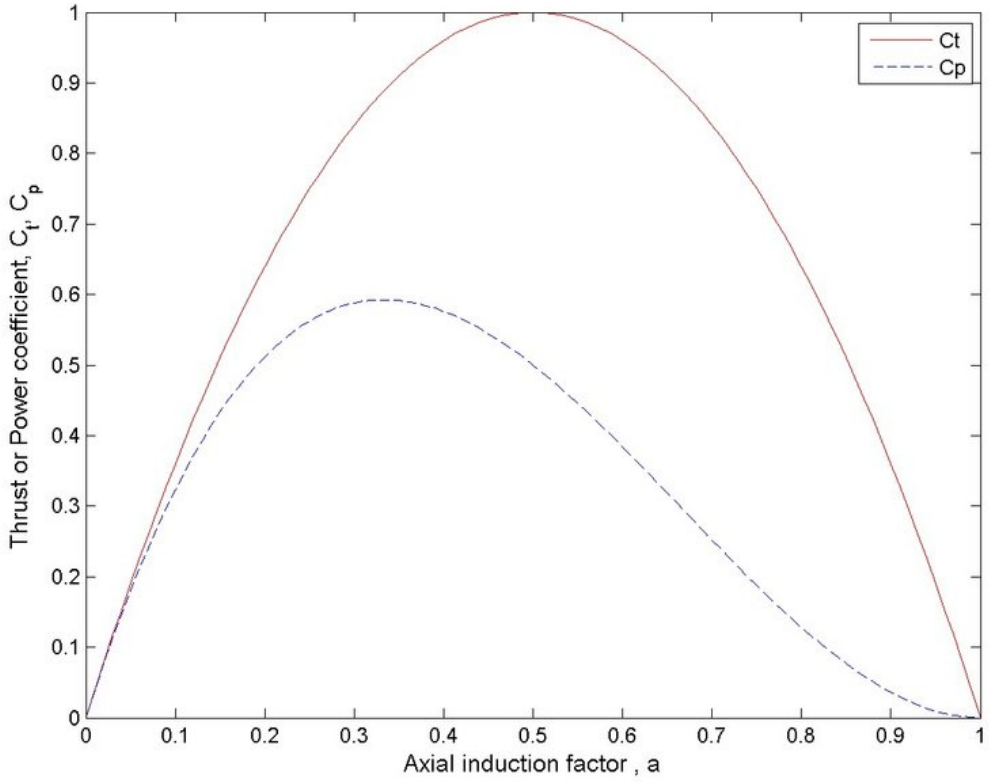

Figure 2.2: The power and thrust coefficients C_p and C_T as a function of the axial induction factor a for the ideal HAWT (32)

2.2.1 Tip-Speed Ratio

The tip speed ratio (TSR) is the ratio between the tangential speed of the tip of a turbine blade and the actual wind speed. It can mathematically be defined as:

$$\lambda = \frac{\Omega R}{V_\infty}$$

Equation 2.13

The Ω is the rotational speed of the rotor; R is the radius of the rotor, V_∞ is the freestream velocity of the wind, and λ is the TSR . The TSR is an important design parameter for wind engineers to consider, the WT should operate in such a way that it captures the maximum amount of wind energy possible. If the rotor should spin too slowly the wind will pass uncaptured, and if the rotors rotate too fast then the turbine will not be able to utilise the wind's kinetic energy. The optimum TSR is contingent on the number of blades of the WT, the fewer the number of blades the faster the rotor will need to rotate to produce optimal power. A well-designed aerofoil rotor blade has higher optimum values and operates at the

designated tip blade speed which improves the aerodynamic efficiency of a WT. Figure 2.3 illustrates the relationship between the power coefficient and TSR in relation to various WT configurations. The Glauert plot shows that the peak efficiency of the ideal WT rises exponentially when $\lambda < 4$ and plateaus when the $6 \leq \lambda$.

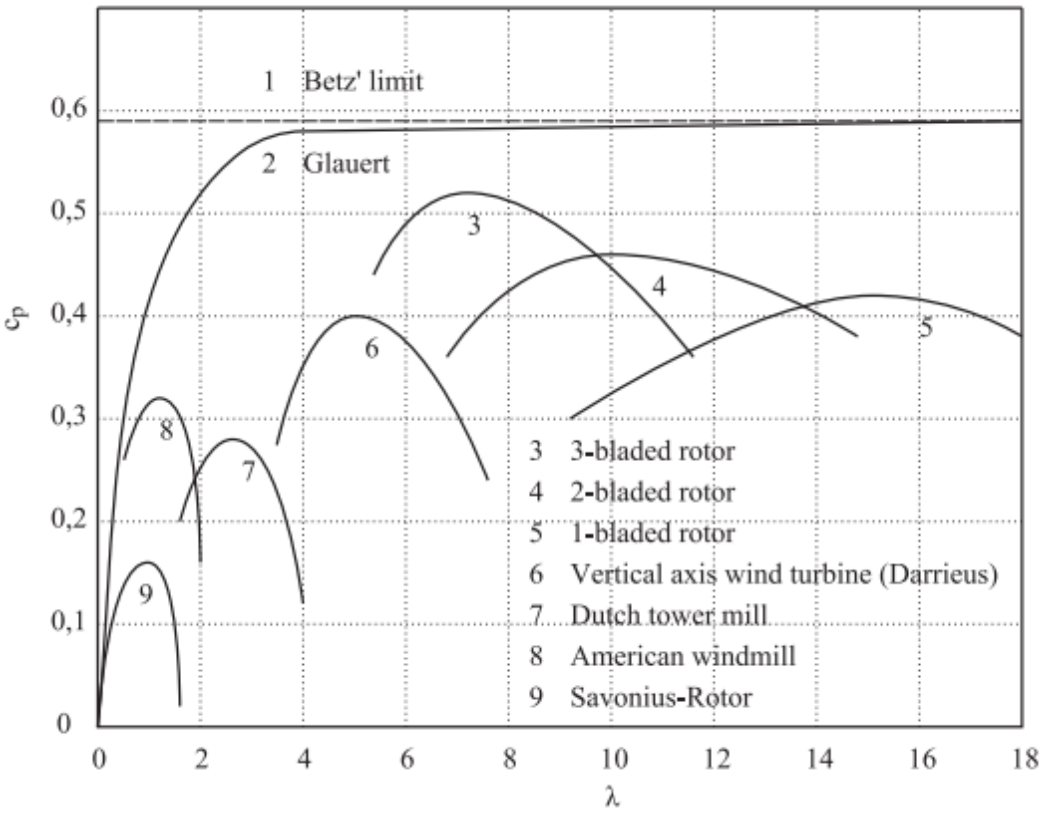

Figure 2.3: Power coefficient as a function of TSR with regards to various WT configurations (33)

N.E. Joukowsky and A. Betz validated the momentum theory and independently confirmed that the maximum c_p of the ideal WT is 59.3% (23). It is not possible to extract 100% of the kinetic energy present in the wind, if such a thing were to occur hypothetically speaking it would result in the complete stoppage of the wind and would prevent airflow downstream from the actuator disc. Furthermore, it would contradict the actuator disk theory which is predicated on laws of conservation and posits that the velocity at the rotor is the average of the velocities far upstream and downstream. The actuator disc model is a useful abstraction for understanding WT aerodynamics and it is used widely within the renewable energy industry for rotor blade design and analysis (34).

2.2.2 Generalized Momentum Theory

Glauert (35) formulated a simple model for analysing the performance of the optimum rotor which includes the effects of rotational velocities. In his method, the rotor is modelled as a rotating axisymmetric actuator disc, which corresponds to a rotor with an infinite number of blades. The main approximation in Glauert's theory is to ignore the effects of azimuthal pressure and velocity (36). This model is called the Generalized Momentum Theory; it is used to calculate the aerodynamic characteristics of the different annular sections of the rotor. The key assumptions of the theory are the flow upstream is unaffected by the disc rotation; and behind the actuator disc a tangential flow is imparted to the downstream wake. Figure 2.4 shows the rotation of the flow in the wake.

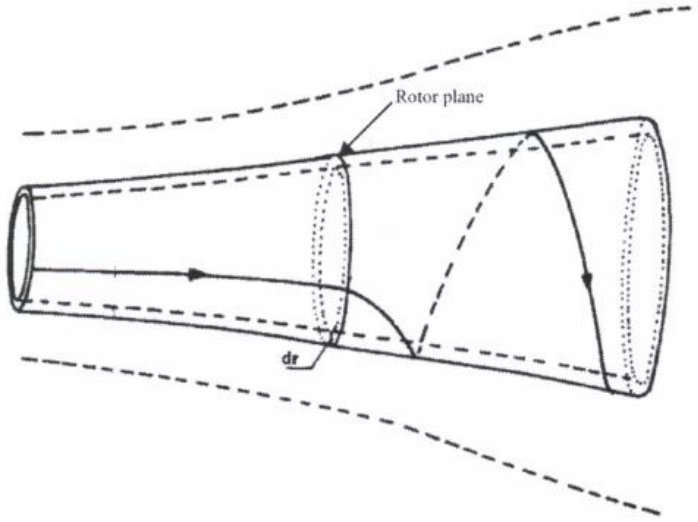

Figure 2.4 An illustration of the flow field downstream from the rotating actuator disc (37)

The azimuthal interference factor can be defined as:

$$a' = \frac{\omega}{2\Omega}$$

Equation 2.14

The ω is defined as the angular velocity imparted to the wake. The local tip speed ratio is given as $\lambda_r = \Omega r/U$ where r is the distance from the axis of rotation. r/R = x is the dimensionless radius. Using Euler's turbine equation for power the following expression can be derived:

$$P = 4\pi\rho\Omega^2 V_o \int_0^1 a'(1-a)x^3 dx$$

Equation 2.15

And for the coefficient of power:

$$C_p = 8\lambda^2 \int_0^1 a'(1-a)x^3\, dx$$

Equation 2.16

The maximum c_p is found by optimizing the integrand of Equation 2.16. Defining the azimuthal interference factor in relation to the axial induction factor gives the following equation :

$$a' = \frac{1-3a}{4a-1}$$

Equation 2.17

To determine the value of a for the optimum rotor the following equation is used:

$$16a^3 - 24a^2 + 3a(3-\lambda^2 x^2) - 1 + \lambda^2 x^2 = 0$$

Equation 2.18

To determine the axial induction factor, a, for a given TSR Equation 2.18 is used. Once a is known the azimuthal interference factor a' can be deduced from Equation 2.17 and the c_p is calculated using Equation 2.16. The optimum axial induction factor is typically reached between 1/4 < a < 1/3 this is due to the occurrence of swirl losses. The maximal c_p is a function of the TSR and from Figure 2.3 it can be seen that it plateaus when λ =7.

2.3 Aerodynamic Principles

2.3.1 Kutta-Joukowski theorem

In this chapter's prolegomenon, it is stated that La Cour was cognisant of aerofoil aerodynamics (the suction force acting on the blade) though he could not explain it theoretically (38). The Bernoulli principle provides a general explanation for the induction of aerodynamic forces on a blade aerofoil. However, it does not describe how the pressure

differential across the blade is formed and makes a few assumptions. To understand the basic mechanism behind the operation of the HAWT, it is necessary to consider general 2-D aerodynamic principles. The Kutta-Joukowski theorem was conceptualized in the 20th century by two engineers named Martin Kutta and Nikolai Joukowski, who sought to explicate how lift forces are generated with regard to air flow (39). The development of the lift theorem allowed aerodynamicists to calculate the lift force acting on two-dimensional shapes and has improved the understanding of blade aerodynamics. The lift theorem considers the blade section of an aerofoil moving through the air in a 2D plane. The body shape and the flow field are assumed to be uniform in the vertical plane, which is parallel to the flow. The wingspan is considered infinite in the y-direction and the rotational vortices induced when analysing a finite wing in a three-dimensional plane are ignored. Figure 2.5 shows the wingspan of a blade in a 3D plane, and a 2D plane relative to the flow velocity.

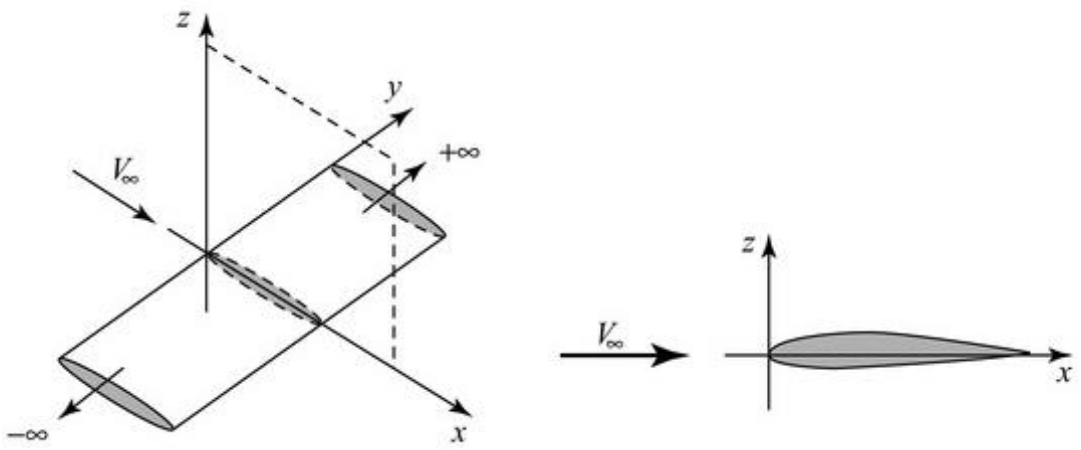

Figure 2.5 Wing and aerofoil coordinate notation (40)

Ludwig Prandtl (41) advanced the boundary layer theory, which postulates that the starting mechanism to produce lift is the viscous boundary layer which carries the circulation around the aerofoil. The veracity of his theory was later established through experimental tests by Bryant et al. (42). The process of circulation formation can be described in the following way. At the initial stage, there are two stagnation points: one at the leading edge and the other at the trailing edge. The motion of the fluid around the aerofoil is steady and irrotational. The fluid moves from the trailing edge on the lower surface to the upper surface, which results in an extremely low pressure at the trailing edge. The viscosity and the pressure gradient cause a back flow which initiates the formation of a vortex on the upper surface (known as the starting vortex) at which point the flow starts to separate from

the aerofoil. The stagnation point that was originally near the trailing edge on the upper surface moves away from it. This is described as the Kutta's condition (43). The displacement of the stagnation point occurs because a circulation of equal magnitude, but opposite direction is established from the trailing edge. The circulation around the contour of the aerofoil creates the pressure differential that gives rise to the lift and drag forces acting on the aerofoil. These forces are two orthogonal components of the resultant force acting on the blade, the lift force is normal to the freestream direction, and the drag force is produced parallel to the airflow. Figure 2.6 illustrates the fluid dynamics during the circulation-formation process.

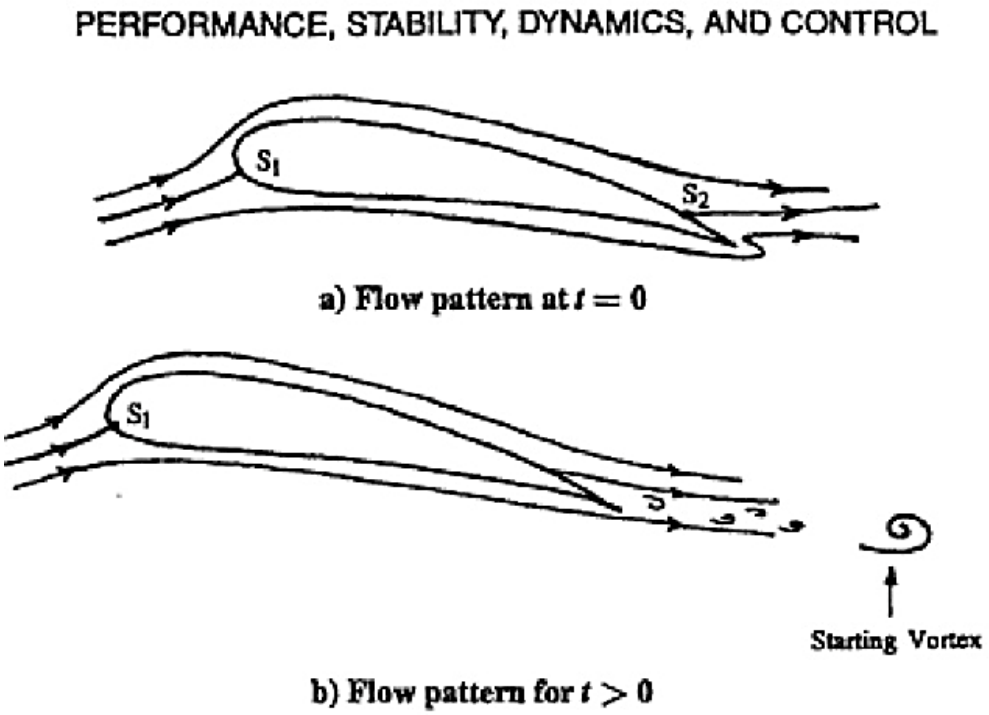

Figure 2.6: The fluid dynamics during the circulation-formation process (44)

The lift force produced by a 2D aerofoil is calculated using the Kutta-Joukowski formula.

$$L' = -\rho_\infty V_\infty \Gamma, \quad \Gamma = \oint_c u \cdot t dl = \int_s \omega dS,$$

Equation 2.19

The freestream density and velocity of the flow field is represented as ρ_∞ and V_∞, respectively. The incoming flow has contour, C, surrounding the aerofoil, and S is the total area occupied by C. The angular velocity is given by ω, the unit tangent vector is t, u is the

velocity vector, and *dl* is the infinitesimal length segment of contour C. Γ is the circulation around the aerofoil, $\Gamma > 0$ when counted counterclockwise . The velocity on the surface area is zero ($V_\infty = 0$) due to the no-slip condition. As the velocity increases, so too does the viscosity within the boundary layer; the freestream velocity is reached outside the boundary layer upstream of the aerofoil surface (41).

Figure 2.7a shows the aerodynamic loads produced by airflow passing over a blade aerofoil. According to Newton's third law, the force exerted by the wind on the blade is requited with an equal and opposing force by the blade on the wind. The torque (dFt) causes the rotor to move in the plane of the rotation at a velocity $r\Omega\ (1 + a')$ as shown in the vector diagram (Figure 2.7b). The other component of the resultant force acting on the blade is the normal force (thrust), which acts parallel to the rotor axis and in the same direction as the free stream velocity. The thrust force is absorbed by the WT structure as an aerodynamic load (45). The relative velocity of the wind (U_{rel}) impinges on the blade at an AoA (α) from the chord line, the twist flow angle (θ) and the inflow angle (ϕ) are incident from the plane of blade rotation. The vector diagram shows the induced velocities as a component of the relative velocity and expresses the velocities in terms of the axial induction factor.

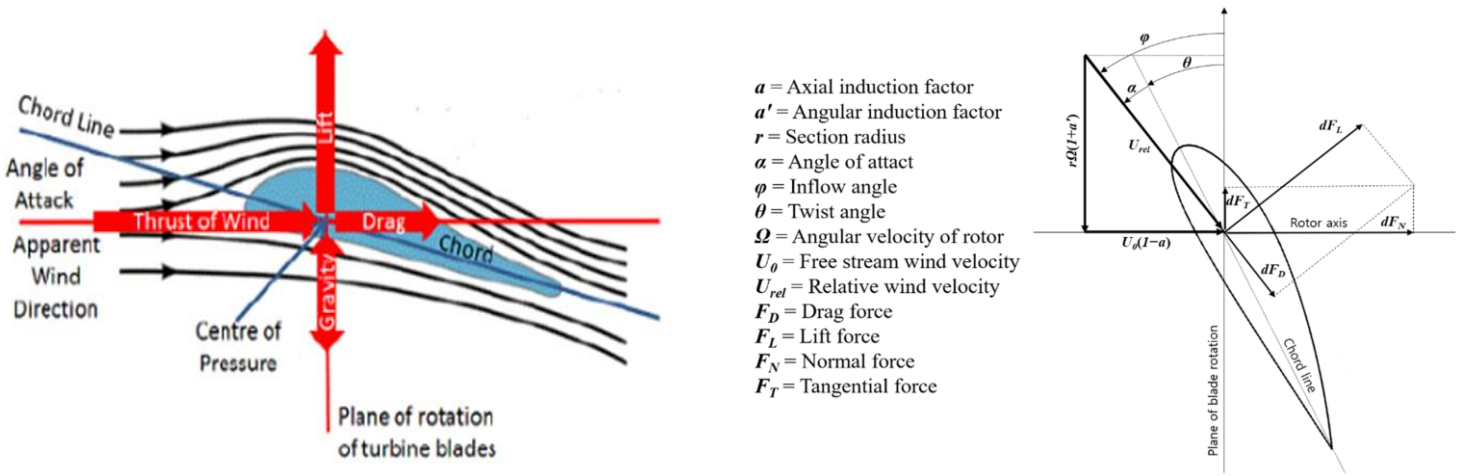

A **b**

Figure 2.7: (a) The aerodynamic forces acting on the blade aerofoil (b) and the wind velocities induced by airflow over a 2D blade (46) (47)

2.3.2 Rotor aerodynamics

Rotor aerodynamics is the branch of fluid mechanics that analyses the forces and moments acting on a blade aerofoil moving through the air. It is the oldest scientific discipline in wind energy and is particularly useful for modelling and predicting the performance of a turbine (26). For the turbine's blade to produce maximal electrical energy, the design must conform to aerodynamic requirements that optimise lift forces and mitigate drag forces. Hence, blade designers place great emphasis on the aerodynamic shape of the blade, ensuring that the most efficient design is chosen through experimental analysis. Predicting the aerodynamic coefficients of aerofoils is mathematically complex, designers typically rely on software such as XFOIL to produce accurate results (48). The lift-to-drag ratio is the most important design parameter affecting turbine performance. For a large HAWT, maximum efficiency is reached when $\lambda_{opt} > 8$ and the L/D ratio is usually between 100 and 120 (49). Design constraints such as construction costs and other economic considerations affect blade design. For example, the blade at the root is usually designed thicker than the aerodynamic optimum where stresses due to bending are highest.

Lift to drag ratio:

$$Lift\ to\ drag\ ratio = \frac{Coefficient\ of\ lift}{Coefficient\ of\ drag} = \frac{C_L}{C_D}$$

Equation 2.20

The coefficient of lift is calculated:

$$C_L = \frac{L}{0.5A\rho v^2}$$

Equation 2.21

The coefficient of drag is given by:

$$C_D = \frac{D}{0.5A\rho v^2}$$

Equation 2.22

The streamlined shape of a blade aerofoil is specifically designed with aerodynamic forces in mind, the lift-to-drag ratio is a function of the geometric shape of the aerofoil, and it is modified in accordance with its application. Turbine blades are manufactured with a rounded leading edge which enables it to generate lift and rotate at the designated velocity. The thickness of the aerofoil reaches its maximum between the quarter and

halfpoint of the chord length (50). The cross section of the aerofoil tapers towards the trailing edge, where the airflow reconvenes after being separated at the leading edge. The camber is added to the aerofoil to maximize the lift produced by the blade. The lift and drag properties of a blade moving through the air varies with the profile of the aerofoil and with the angle of attack (AoA). The angle between the velocity vector and the chord line of the aerofoil is called the AoA. The AoA increases in a quasi-linear manner until the stalling point is reached, which is typically around 12°-15° (51). An adverse pressure gradient is formed at the boundary layer, once the critical AoA is exceeded flow separation occurs. The airflow over the upper surface ceases to flow smoothly and becomes turbulent, greatly reducing the lift whilst increasing the drag. The point at which the critical AoA is attained is dependent on the aerofoil configuration. The performance of aerofoil configurations is characterized by design parameters such as AoA, C_L/C_D, and the thickness of the aerofoil as a percentage of the chord length. Figure 2.8 shows the drag and lift polar curves for NACA63XX aerofoils of various thicknesses at different AoAs.

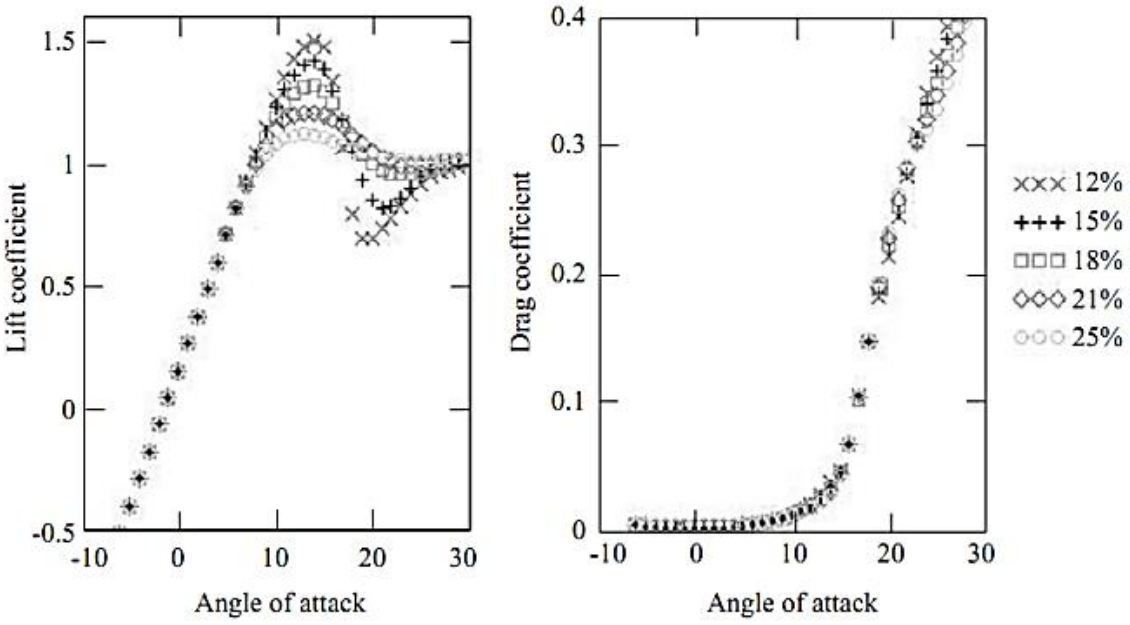

Figure 2.8: Polar curves for NACA63XX aerofoil series of various aerofoil thickness levels (45)

The Reynolds Number (Re) is a dimensionless ratio that is used to characterize the flow regime of different fluids. It measures the force of a flow against the viscosity, and it is an important parameter to consider as it affects aerodynamic performance. Modern HAWTS are designed with a power rating that ranges from 1kW (around 2m rotor diameter) to 5MW (around 125m rotor diameter). According to Christian Bak's study (52) the smaller HAWTs experience flows with Re $\leq$ 200,000 and the larger ones operate at heights where

the $6x10^6 \leq$ Re (52). The size of the rotors and thereby the chord length of each blade aerofoil varies with the turbine size and thus the aerofoil performance. Figures 2.9a and 2.9b are juxtaposed together to illustrate how the flow regime of the air and blade aerofoil influences the aerodynamic performance of HAWTs.

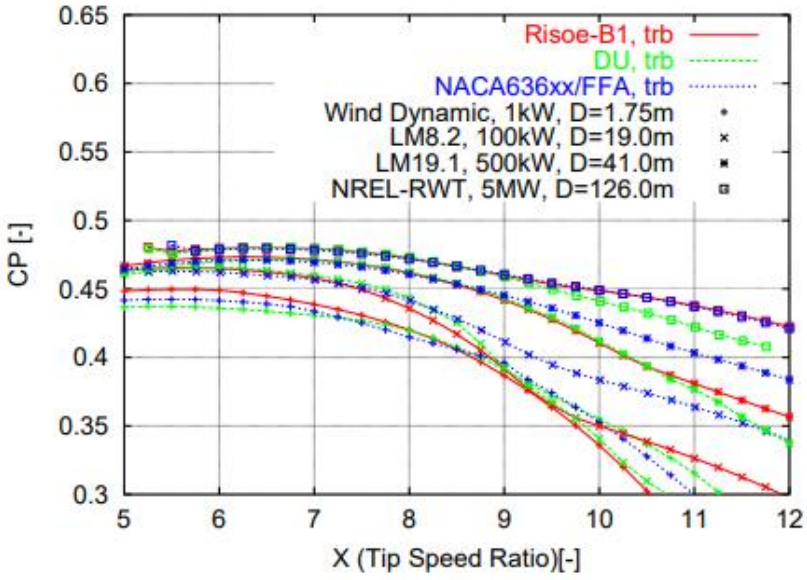

Figure 2.9a: C_p versus TSR, for four different sizes of rotor and three different kinds of aerofoils families assuming fully turbulent flows (52)

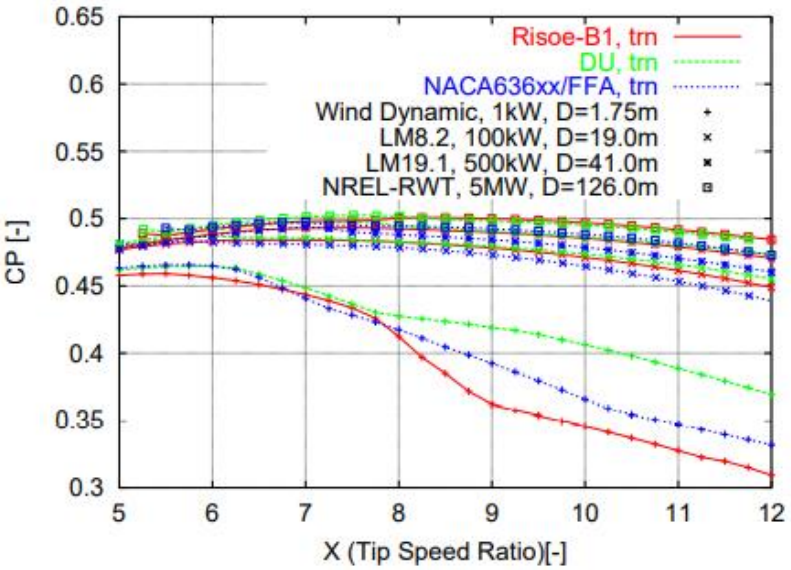

Figure 2.9b: C_p versus TSR for four different sizes of rotors and three different kinds of aerofoil families assuming free transition on aerofoils (52)

Bak (52) analysed three blade aerofoils of different geometric dimensions, each with a different thickness corresponding to the rotor size and Re number. The difference in aerodynamic performance with regards to blade design is miniscule; the NACA 636xx is better for turbulent flows and the Risoe-B1 for transitional flows. For the fully turbulent flow, the maximum c_p is reached at lower TSRs, when the TSR > 8 the peak efficiency decreases precipitously. As aforesaid, a TSR that is too high affects aerodynamic performance and acts as a blockade to air flow, the decrease in maximum efficiency at higher TSRs reflects this fact. Whereas in Figure 2.9b, the line graph shows that the HAWTs have a consistent maximum efficiency between 45% and 50% even at the higher TSRs (excluding the Wind Dynamic turbine). This demonstrates that transitional flow is more auspicious for harnessing wind energy than unsteady turbulent flow. The undulating motion of eddies in the flow produces fluctuations in velocity and pressure that affects electricity production (53). Another salient factor affecting rotor performance is rotor solidity, which can be defined as the ratio of the total area of turbine blades (in the wind direction) to the total wind-swept disc area. This is defined mathematically as:

$$\sigma = \frac{N_B c}{\pi r}$$

Equation 2.23

The σ is rotor solidity, N_B is the number of blades, and c is the chord length, and r is the radius. A low-solid wind rotor will typically have between one to three blades, and a HAWT with a high solidity ratio may have up to twelve blades. High wind solidity does not lead to greater wind efficiency because the blades act as resistance to air flow, part of the wind flow circumvents the rotor swept area, thus the energy obtained from the wind is reduced. The WTs with a very high solidity ratio not only hinder the passage of the airflow but also induce vortices and turbulence in the wake of the rotating blades, which has a similar effect on WT efficiency. The WTs with low solidity are typically situated in places with high windspeeds whence all the blades can sweep through most of the airflow, which allows the blades to rotate faster and operate with greater efficiency. Khan et al. (54) demonstrated that the optimal solidity ratio for a three-bladed HAWT is between 5%-7% when λ =5-7. Thus, three-bladed HAWTs are designed to be slender; the limited solidity also limits the thickness of the blades. On the other hand, if the blade is too thin, it may be susceptible to fatigue loading. Figure 2.10 shows the power coefficient against the TSR for HAWTs. The Zawadzki et al. study (55) demonstrates that as the solidity increases the maximal c_p

increases for a given rotor blade geometry up until the λ becomes too great at which point the c_p decreases.

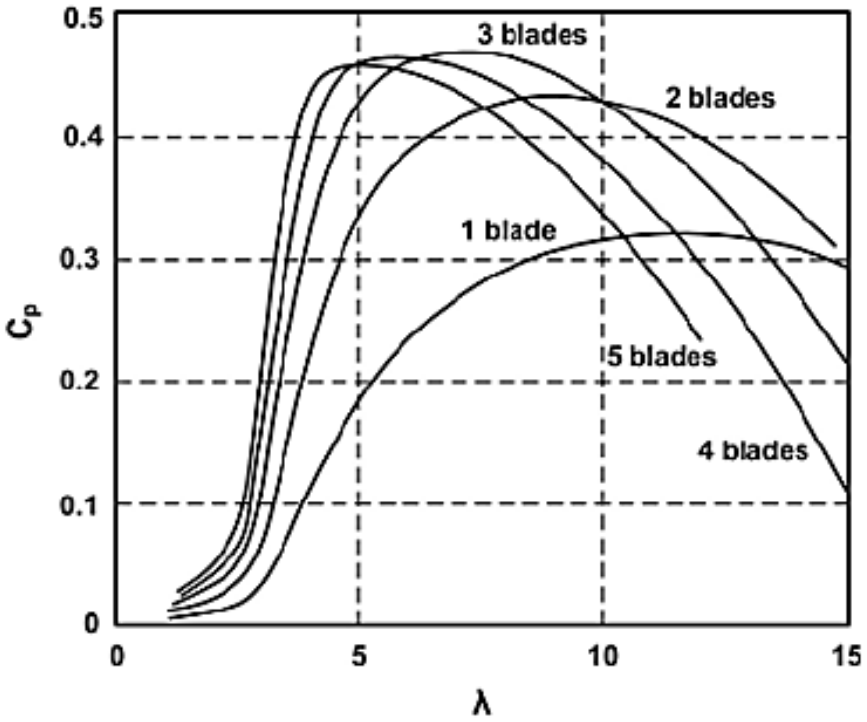

Figure 2.10: Power coefficient against TSR curves for HAWTs (56)

From the power coefficient curve, it is seen that the curves labelled 3, 4 and 5 blades have a higher maximum c_p, however, the 4 and 5 bladed turbines have a smaller TSR range. The primary benefit of a wider TSR range is that a higher c_p can be obtained at a variety of wind speeds. Moreover, the efficient HAWTs can utilise the speed of the turbine rotor (without overreliance on the gearbox's speed-increasing ratio). The 2-, 3-, and 4-bladed HAWTs have a high-power efficiency when operating at high TSRs. Zawadzki et al. (55) found that when small HAWTs (with 2 to 4 blades) have a greater number of blades, they produce a greater amount of torque, which is directly correlated with the amount of power produced. However, the 3-bladed HAWT is generally preferred to other configurations because of its wider TSR range and because it is considered more aesthetical than the 2-bladed HAWT. Multi-bladed HAWTs (with 5-8 blades) are better suited to environments where there are low wind speeds and they can efficiently utilise the wind's energy.

2.3.3 Aerofoil designs

The US National Advisory Committee for Aeronautics (NACA) has developed numerous aerofoil designs for commercial HAWTs. There are different aerofoil families that are used

within the turbine industry, each of the designs are categorised according to their geometric or aerodynamic properties. The 4-digits and 5-digits NACA aerofoil series were designed using polynomial equations which describe the geometry of the blade section: the camber (curvature) of the mean-line, the chord of the aerofoil section, as well as the thickness distribution along the length of the aerofoil (57). The 5-digit aerofoil series has similar thickness characteristics to the 4-digit aerofoils, except for the camber line near the leading edge. The main difference between the two aerofoil profiles is the reflexed camber line that was introduced to the 5-digit aerofoil to produce a zero-pitching moment (58). The NACA 63-415 aerofoil is one of the most commonly used commercial WT blade profiles (59). It has been extensively studied within wind literature and compared with the NACA 63-412 aerofoil using CFD tools (60). Figure 2.11 shows the comparison between the two referenced cambered aerofoils. The last two digit represent the thickness of the aerofoil, the NACA 63-415 and 63-412 have a thickness of 15% and 12%, respectively.

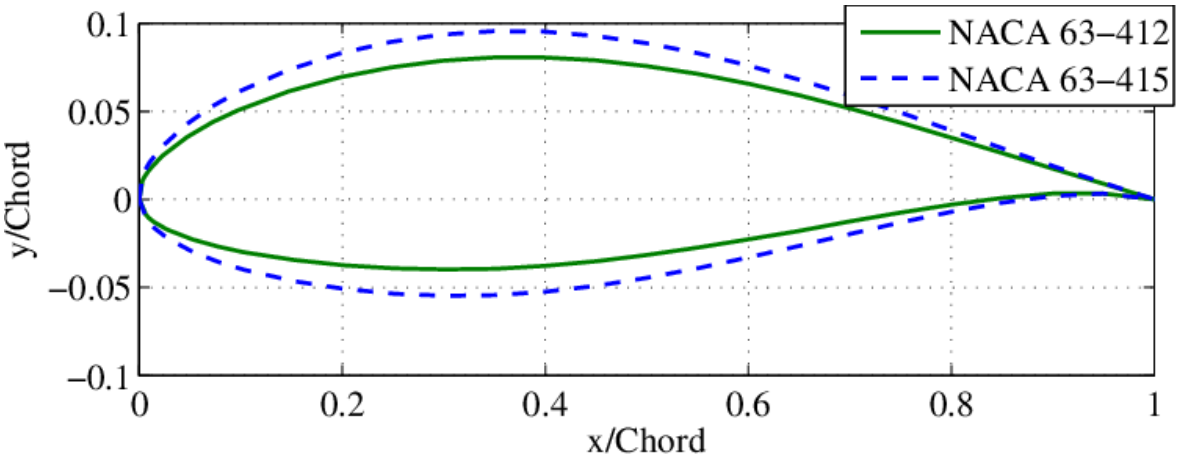

Figure 2.11: A comparison between the NACA 63-412 and NACA 63-415 (58)

The study by Chaudhary et al. (58), shows that the thinner aerofoil, NACA 63-412, performs better at a lower Re (between $5x10^4$ and $2x10^5$). This is due to the stronger pressure gradient that is formed across the aerofoils. The thicker aerofoil, NACA 63-415, produced a larger C_L/C_D when the flow had a higher Reynolds number (between $5x10^5$ and $1x10^6$). ANSYS Fluent software was used to analyse the flow (at Re =$1x10^6$) around the aerofoil, which was turbulent and unsteady. To resolve the turbulent flow, the Reynolds stresses were calculated using the SST k-ω turbulence equation. The NACA 63-415 was shown to perform better at a Re of $1x10^6$ than the NACA 63-412 producing a greater C_L/C_D. Figure 2:12 shows the performance of the NACA 63-415 at an AOA of 5.25° in comparison to the NACA 63-412 with an AOA of 4.25°.

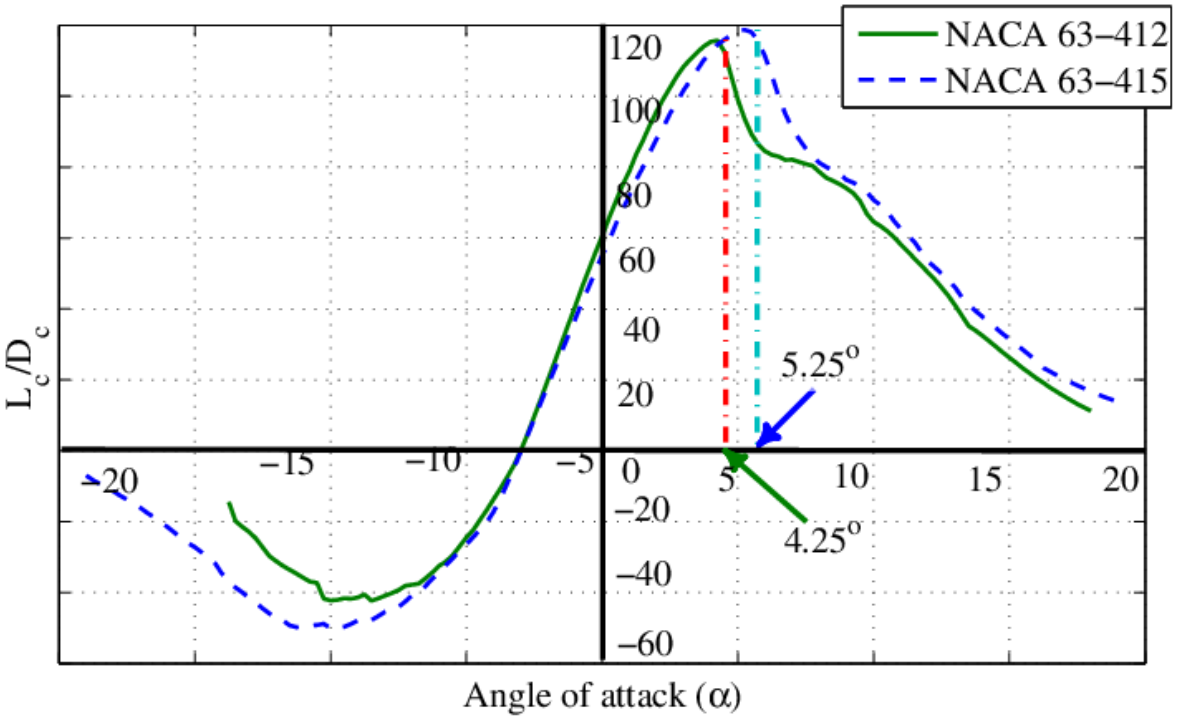

Figure 2.12: Comparison of lift-to-drag versus angle-of-attack for NACA 63-412 and NACA 63-415 aerofoil (Re= 1x10^6) (58)

2.4 Blade Element Momentum (BEM)

The Blade Element Momentum (BEM) theory is the cornerstone of WT analysis and is the most frequently used method for calculating induced velocities acting on a turbine blade (61). It is an extension of the 1D momentum theory, which was conceptualised by Rankine and Froude in the late 19th century. Glauert developed the BEM theory in 1935 (35), which is a synthesis of the momentum theory and blade element theory. The blade element theory disaggregates the rotor blade into several elements and considers the aerodynamic loads acting on each element in a two-dimensional plane (according to local flow conditions). The aerodynamic forces exerted on the constituent parts are added together to determine the total forces and moments acting on the turbine blade. The momentum theory postulates that the power rating of the rotor is equal to the work done by the airflow passing through the rotor plane, and that by using this theorem to calculate the induced velocities acting on an aerofoil, one can work out the aerodynamic loads exerted on the turbine rotor. The BEM method is a theoretical framework for understanding and predicting the performance under different conditions, including unsteady and steady flow conditions (62). This makes BEM a useful tool for the design and optimisation of WTs.

The main advantages of the BEM model are (63):

1. It is an accurate and reliable method for resolving flow problems and designing turbine blades with a long history of experimental validation.
2. Faster computation of flow problems because of less detailed analysis (approximations).
3. Can be integrated with aero-elastic codes which take structural factors into consideration.
4. It does not necessitate a large amount of computational power.

The original BEM model has a few limitations:

1. There is no radial dependency, i.e., each element is individual and is unaffected by the other elements. The flow problem is treated as 2D rather than 3D.
2. The airflow over the annular elements is assumed to be steady (non-turbulent).
3. No modelling of hub or tip vortices and their effects on induced velocities and an inability to account for skewed inflow (61).
4. Requires a series of engineering corrections to model unsteady aerodynamic phenomena.
5. Under prediction of power performance in stalling conditions (63).

Figure 2.13 shows the blade element of a turbine in rotation with its induced velocities.

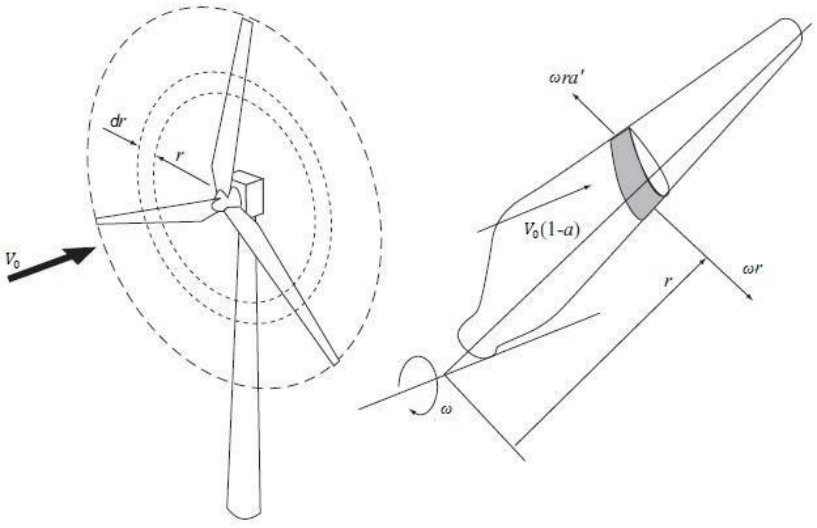

Figure 2.13: A blade sweeps out an annular ring (64)

The thrust and torque for each of the blade elements are expressed in terms of the axial and tangential induction factor:

$$dQ = 4\pi r^3 \rho V_\infty \Omega(1-a)a' dr$$

Equation 2.24

$$dT = 4\pi r \rho {V_\infty}^2 (1-a)a\, dr$$

Equation 2.25

2.4.1 Tip Loss Correction

The tip loss factor was introduced by Prandtl (65) to correct the assumption of an infinite number of blades. A rotor with a finite number of blades will induce strong tip vortices and straight vortices at the root region. For this reason, a rotor with a finite number of blades is treated differently, the helical patterns in the wake are modelled as vortex sheets (64). The induced vortices affect the amount of power that the turbine produces. Prandtl's model improves the accuracy of BEM as it accounts for the reduction of blade forces at the tip. The tip loss factor, F, is defined in the following way:

$$F_{tip} = \frac{2}{\pi}\, cos^{-1}(\exp\left(-\frac{N_B(R-r)}{2r\, sin\phi}\right))$$

Equation 2.26

2.4.2 Glauert Correction

One of the limitations of the BEM theory is that once a > 0.4, then the theorem becomes invalid. This occurs when the TSR becomes high and the rotor begins to experience a phenomenon known as the turbulent wake state where some of the flow in the far wake starts to reverse and travel upstream, which is contrary to BEM's fundamental assumptions. The flow is made more turbulent when flow from outside the wake rushes in and becomes highly unpredictable. Glauert developed a method for calculating the thrust coefficient by measuring helicopter rotors with large, induced velocities (66). The Glauert empirical correction factor gives an appropriate measure of the C_T, when the induced velocities are great, and the tip losses are large. Buhl (67) expresses the coefficient of thrust as a function of the axial induction factor, which gives the following equation:

$$C_T = \frac{8}{9} + \left(4F - \frac{40}{9}\right)a + (\frac{50}{9} - 4F)a^2$$

Equation 2.27

Figure 2.14 plots the axial force coefficient and the axial induction factor with the empirical correlation lines of Glauert and Buhl.

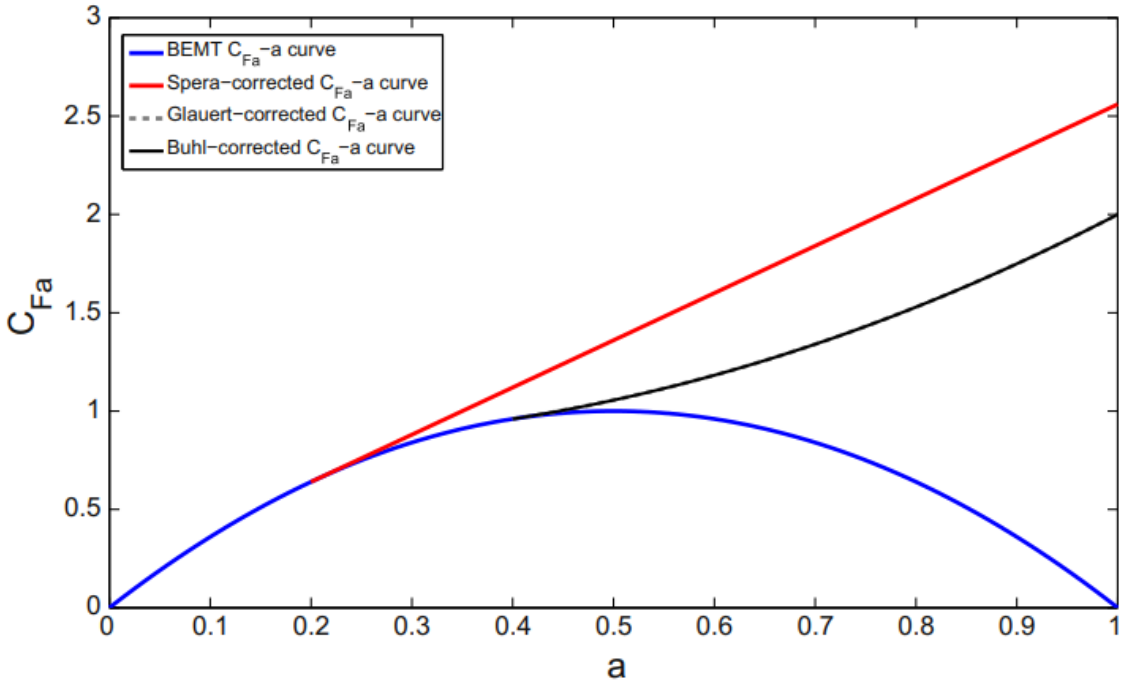

Figure 2.14: The axial force (thrust) coefficient plotted against a, Glauert and Buhl's correction with loss factor F = 0.8 (68)

2.4.3 Numerical modelling

This section aims to highlight some of the studies where the BEM model has been used to predict the performance of WTs in unsteady flow conditions, and to discuss the numerical methods used for WT analysis. The BEM model is widely used in wind literature for the evaluation of HAWT performance in different operating conditions. Although, a preponderance of the studies conducted within the wind engineering field are focused on WTs in a steady environment, a few researchers have begun to turn their attention to HAWTs in unsteady conditions. Wekesa et al. (69) used the BEM model to assess the functionality of VAWTs in unsteady wind; the empirical results that were obtained and validated against CFD simulations were found to be in close agreement. A structured mesh

was used for the computational domain, and the commercial CFD software package ANSYS FLUENT was used to resolve the flow problem. The BEM model overpredicted the power density of the VAWTs at two sites in rural Kenya marginally by 17% and 4%.

Can (31) investigated the performance of a 5MW NREL WT, the author used unsteady Navier-Stokes equations to simulate and solve the flow problem for a 2D aerofoil. These CFD simulations were performed through an OpenFOAM solver and compared with the BEM solutions which were provided through QBlade, and the discrepancies in the power output of the single rotor were found to be within the acceptable limit. Aljuhashy (70) also used CFD simulations to validate the performance of the NREL phase VI HAWT in unsteady wind at various tip speeds and compared it with BEM solutions. The CFD results were shown to be congruent with the BEM solutions provided by Qblade. A structured mesh was used for the blade geometry and an unstructured mesh for the computational domain. The performance of the HAWT in steady state conditions with a velocity of 6 m/s yielded a C_p= 0.4245 in comparison to the multiple unsteady simulations with different fluctuating amplitudes (7%, 15%, 25%, 45%) with an average C_p= 0.432, 0.425, 0.403, 0.352 at f=1Hz. The results showed that unsteady simulations generated more power when the fluctuations in wind velocity were of a smaller amplitude. Moreover, a higher frequency of oscillations was also shown to be beneficial (when velocity was kept constant).

Lanzafame et al. (71) demonstrated that the BEM theory could be used to evaluate a HAWT when used in conjunction with a fifth-order logarithmic polynomial. The lift distribution of the NACA 63_x- 2xx was interpolated to account for stall conditions and compared with 3D CFD results. The 1D BEM code showed good compatibility with the 3D CFD results when empirical corrections were used. The greatest difference occurs at a wind speed of 16.5m/s, at which point the numerical simulation differs from the experimental data by 6.6%. Another study by Hamlaoui et al. (72) shows that the BEM model is a cost-effective way of predicting the power output of a HAWT. A corrective engineering model is introduced, rather than using 2D lift coefficient the study uses 3D lift coefficients through a computer code written in Matlab to predict the power output of HAWT in comparison to the experimental data of the NREL Phase VI turbine. For freestream velocities above 16m/s, the conventional models are unable to predict the power output, accounting for 3D effects (such as tip loss) gives a more accurate prediction.

Prince et al. (73) used a computer code based on the blade element momentum theory (BEMT) to simulate the power performance of the Nordtank NTK 500kW HAWT; the Glauert and tip loss correction was factored in to give a more accurate prediction of power capabilities. The Nordtank turbine is a 3-bladed HAWT, stall regulated, fixed pitch design

with a tip-to-tip diameter of 41m and a hub height of 35m, with a fixed rotational speed of 27 rpm. The full specification of the Nordtank turbine and its experimental data are detailed within this reference (74). The aerodynamic coefficients C_L and C_D were obtained for angles within the incidence range of - 90° < ∝ < 90°. The BEMT code was found to accurately predict the power efficiency of the HAWT when 32 elements were used across the blade to estimate blade geometry and performance. The BEMT simulation was demonstrated to be in close agreement with the experimental data for wind speeds up to 15 m/s. However, beyond that there is a 5% difference in power output predicted by BEMT and the experimental data. This is because the BEMT solution did not factor in the effects of radial outflow which caused stall and boundary layer separation which led to an underprediction in power output. The BEMT's model's predictive accuracy makes it a useful tool for comparing and assessing the power output of a wind turbine when flow control strategies are applied. Figure 2.15 shows a comparison of experimentally measured and theoretical prediction of the power output/coefficient of the Nordtank NTK 500/41 wind turbine.

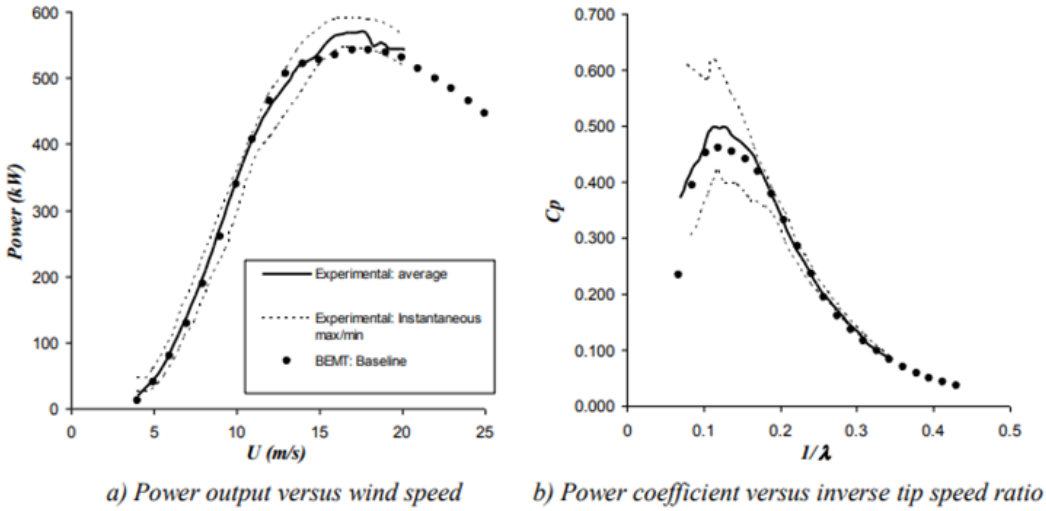

Figure 2.15: Comparison between experimentally measured and theoretical prediction (BEMT) for the baseline Nordtank NTK 500/41 wind turbine (73)

Numerical modelling has its own advantages: it shortens development cycles, lessens concomitant risks, and is an inexpensive method of performance analysis. This is especially true for the BEM model, which is used extensively throughout the wind industry for HAWT design and validation; this semi-empirical method is a straightforward technique for obtaining performance predictions. The examples cited within this section provide reasonable justification for the use of the BEM model within this thesis. However, the limitations that were aforementioned: failure to account for radial flow, over-predictions of power in stall, and simplifying assumptions, affect the accuracy of the BEM methodology.

Recent advances in CFD have made it the preferred method for HAWT analysis. Although both methods are frequently used together to predict and validate the performance of HAWT machines, CFD models can be used to resolve turbulence and provide a more accurate solution for a flow problem. Additionally, CFD enables flow visualisation, which allows engineers to examine regions of interest, and simulations can be performed relatively quickly and inexpensively.

2.5 Computational Fluid Dynamics (CFD)

CFD is an engineering tool that is used to model and predict the behaviour of fluid flows. For single-phase flows, it employs a set of numerical equations called the Navier-Stokes equations (75). These partial differential equations (PDEs) accurately describe the motion of viscous fluids according to their properties such as pressure, velocity, temperature, and density. The Navier-Stokes equations are derived from the fundamental principles of the conservation of momentum, mass, and energy. The fluids are modelled as a continuum rather than discrete particles. The Navier-Stokes equations for a 3D incompressible flow can be expressed in the following way.

The conservation of mass equation:

$$\frac{\partial u}{\partial x}+\frac{\partial v}{\partial y}+\frac{\partial w}{\partial z}=0$$

Equation 2.28

The momentum conservation equations in the x, y, and z direction:

$$\rho\left(\frac{\partial u}{\partial t}+u\frac{\partial u}{\partial x}+v\frac{\partial u}{\partial y}+w\frac{\partial u}{\partial z}\right)=-\frac{\partial p}{\partial x}+\mu\left(\frac{\partial^2 u}{\partial x^2}+\frac{\partial^2 u}{\partial y^2}+\frac{\partial^2 u}{\partial z^2}\right)+\rho g_x$$

$$\rho\left(\frac{\partial v}{\partial t}+u\frac{\partial v}{\partial x}+v\frac{\partial v}{\partial y}+w\frac{\partial v}{\partial z}\right)=-\frac{\partial p}{\partial y}+\mu\left(\frac{\partial^2 v}{\partial x^2}+\frac{\partial^2 v}{\partial y^2}+\frac{\partial^2 v}{\partial z^2}\right)+\rho g_y$$

$$\rho\left(\frac{\partial w}{\partial t}+u\frac{\partial w}{\partial x}+v\frac{\partial w}{\partial y}+w\frac{\partial w}{\partial z}\right)=-\frac{\partial p}{dz}+\mu\left(\frac{\partial^2 w}{\partial x^2}+\frac{\partial^2 w}{\partial y^2}+\frac{\partial^2 w}{\partial z^2}\right)+\rho g_z$$

Equations 2.29

The four independent variables in the equation are the spatial coordinates: x,y and z, and the time t. The six primary variables in the complete Navier-Stokes system are: pressure p, density ρ, temperature (T, from the energy equation), and the three velocity components (u, v, w). The left-hand side of the momentum equations has the convection terms; and the right-hand side represents the internal forces, the pressure gradient and viscous forces, and the external forces applied to the fluid. Changes in fluid properties, such as temperature and density, are determined by solving the governing conservation equations which couple these variables to the velocity field. CFD applications use efficient algorithms to solve the nonlinear PDEs which makes solving flow problems under dynamic and steady conditions easier (76). The equations for unsteady turbulent flow are complex, and as such, there is no exact analytical solution to these equations. Thus, the numerical solution that is generated is averaged to produce aerodynamic quantities such as drag and lift from a pressure-based solver.

A Newtonian fluid, like air, is modelled as an incompressible 3D flow with a constant density. The speed of the flow is below the Mach number limit ($M_\infty < 0.3$). For the physical modelling of the flow problem, it is necessary to create a control volume which applies the equations of the fluid's motion, laws of conservation, and the boundary conditions (77). PDEs are mathematical equations which can be solved through computational analysis; they are used to compute the behaviour of airflow within a control volume. Several discretization methods can be used to subdivide the flow domain; however, the most popular methods are the finite volume method, the finite element method, and the finite difference method. The FVM is the most common method of analysis used in the CFD approach, it is an efficient and accurate way of generating a solution for high Reynolds number turbulent flows (77) (78).

The Reynolds-Averaged Navier Stokes (RANS) equations are time-averaged equations of fluid flow that are used to describe turbulent flows. Because RANS requires fewer computational resources than DNS or LES, it is preferred over other computational methods (79). Time-averaging is used to reduce a complex series of differentials into simpler forms by decomposing the flow into mean and fluctuating components. However, in the case of unsteady flow, the RANS uses a solution that incorporates the time-dependent mean flow velocity and time-varying fluctuations (80). The averaging process over time produces Reynolds stresses, and the use of turbulence models (like k-omega & k-epsilon) helps to resolve turbulence flows and model turbulence-induced stress. Despite being computationally intensive, CFD methods provide accurate and practical predictions for turbulent flows in engineering applications.

2.5.1 Turbulence Models

Turbulence models are used in engineering applications to close the RANS equation by modelling the Reynolds Stress that is incurred by fluctuations in the fluid's flow. The Spalart-Allmaras (S-A), k–ε (k–epsilon), k–ω (k–omega) and k–ω SST (Shear Stress Transport) models are used most frequently because of their low computational cost and accuracy (81) (82). The S-A model is a one-equation model that is used to resolve the turbulence viscosity equation, it factors in wall-bounded flows and gives good results when the boundary layers are subjected to adverse pressure gradients. The k–ε model is the most commonly used model in CFD; it captures turbulent flow using two equation models and is appropriate for flows that are wall-bounded with limited adverse pressure gradients or separation (82). The k–ω model is an oft-used model for simulating turbulent flows, it is a two-equation that solves transport equations for turbulent kinetic energy and specific dissipation rate. It is best used for flows that require near-wall treatment and performs better than other models at complex boundary layers. The k–ω SST uses k–ε in freestream and is therefore less sensitive to inlet conditions, it is a better predictor of flow separation than other RANS models. Table 2.1 contains a list of the advantages and disadvantages of the various eddy viscosity models.

Table 2.1: The advantages and disadvantages of Eddy Viscosity Models (83)

Models	Advantages	Disadvantages
S-A	• Fast simulation • Good convergence • Allowance of poor-quality mesh	• No wall functions • Under-prediction of stall. • Not good for shear flows
k–ε	• Performs well away from walls. • Reasonable accuracy • Good for external flows	• Poor performance for flows with strong separation & large pressure gradients • Cannot be calculated near wall without wall functions.
k–ω	• Omega used as it is easier to solve than epsilon. • Uses wall functions.	• Difficult to converge and sensitive to initial conditions. • Issues with freestream flows

	• Good convergence and low memory requirements. • Improved accuracy for internal flows.	• Over predicts separation
k–ω SST	• Wall functions • Combination of k-ε (outer boundary layer) and k-ω (inner boundary layer). • Accurately predicts separated flows and jets.	• Difficult to converge. • Does not factor in buoyancy. • Requires limiters to improve prediction of stagnant regions.

A comparative study of the eddy viscosity models was undertaken by Muiruri et al. (84) for the power efficiency of an NREL 5MW HAWT using ANSYS FLUENT and the k–ω SST showed the most remarkable agreement with numerical simulation results. Eboibi et al. (85) also found the k-ω SST to be the best model for predicting dynamic stall from their Particle Image Velocimetry (PIV) experimental study. Hendriana et al. (86) used k-ω SST to simulate the performance of a HAWT; the power efficiency of the HAWT was optimised using the OpenFoam software. According to these studies, the best eddy viscosity model for measuring the performance of HAWT in unsteady wind is the k-ω SST.

2.6 Passive Flow Control Methods

Flow control devices are low-cost addendums that boost the energy capture of the turbine blades without compromising the structural integrity of the turbine. Flow control systems are broadly classified into two types: passive and active control solutions. Passive flow control (PFC) devices operate without an actuating mechanism to enhance the lift-to-drag ratio of the rotor blade and prevent flow separation from occurring at the boundary layer. Active flow control devices perform the same function; however, they require an auxiliary energy source to operate. Engineering research has been used to produce active flow control devices such as ailerons, stall ribs, and mechanical tabs throughout the last decade (87). The aim is to manage the flow over the turbine blade by mitigating the vibration that the blade aerofoil experiences in dynamic conditions. Active flow control devices are typically more costly than PFC devices and they require more maintenance. In any case, the purpose of this thesis is to understand how effective PFC solutions are in improving aerodynamic performance; active flow control methods are beyond the scope of this thesis.

PFC methods have attracted the interest of researchers due to their low cost and high energy capture. These devices can promote mixing, delay flow transitions, and reduce fluctuations, all of which improve the rotor blade's power efficiency. The modifications made to the blade profile improve the aerodynamic properties of the rotor blade by regulating the flow characteristics in the boundary layer and controlling mixing in the separated shear layer. Stationary components such as riblets, vortex generators, micro tabs, and Gurney flaps are utilised in PFC strategies to improve turbine performance. These addendums have undergone experimental and numerical analysis to determine their effectiveness in optimising turbine performance. This section will examine the literature on various PFC methods and evaluate their respective benefits.

2.6.1 Riblets

The concept of riblets is abstracted from the natural features found in certain animals, such as the surface of shark skin and the structure of bird beaks. These biological features operate in a similar way to engineered riblets, enhancing drag reduction in turbulent flow regimes which allows for smoother movement through fluids (88). Riblets are made up of small grooves that are positioned on the blade's surface and oriented in the direction of the wind. A study by Debisschop and Nieuwstadt found that ribleted aerofoils can reduce the skin friction coefficient in an adverse pressure gradient (89). This is achieved by modifying the turbulent flow structure in the boundary layer. Choi's (90) seminal study found that the entire velocity profile can be moved from the viscous sublayer to the outer layer due to riblets increasing the viscous sublayer thickness. The resultant effects are the reduction of turbulent energy production; the mitigation of turbulence intensity and reduction of turbulence drag in the near-wall region. Sundram et al. (91) study demonstrated that riblets could reduce drag on an aerofoil by up to 16% on a standard symmetric aerofoil whilst the drag reduction for an asymmetric aerofoil was between 4%-6%. Charmorro et al. (92) investigated riblet effectiveness on a large asymmetric HAWT blades and found a drag reduction of 6%. Figure 2.16 shows the riblet configurations that are used to improve aerodynamic performance.

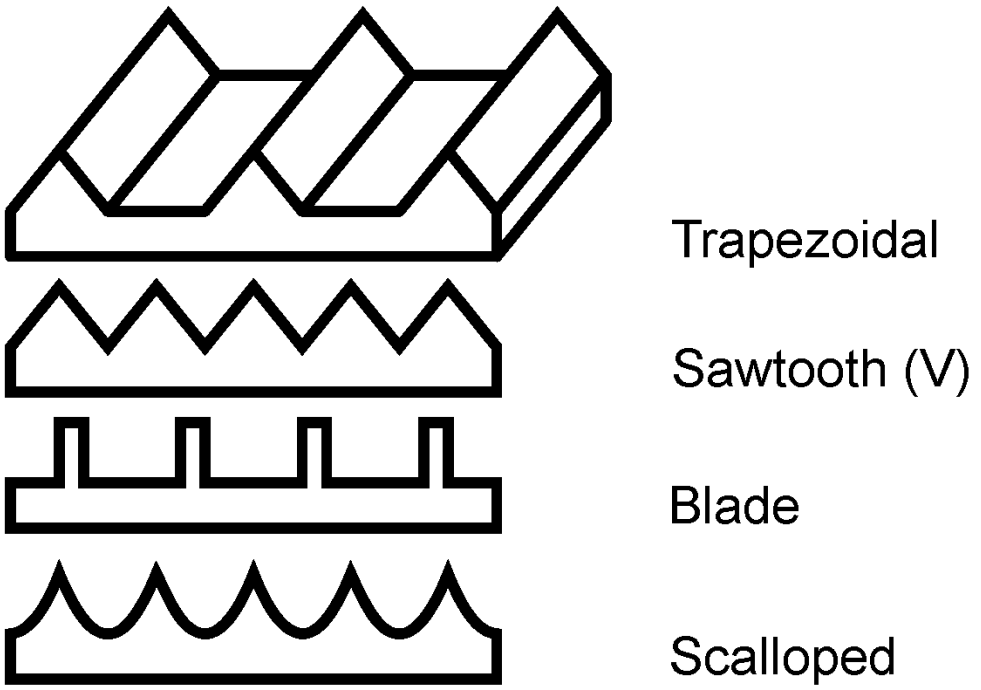

Figure 2.16: Riblet configurations used to improve aerodynamic performance (93)

There are several factors determining riblet effectiveness which require consideration such as Reynolds number, AOA, riblet spacing, and riblet size. These parameters have been the subject of recent riblet studies although, studies of this nature are limited in number. Sareen et al. (94) showed that riblets could reduce drag up to 5% when configured optimally, however, it could also increase drag by a maximum of 12% when the riblet size is non-optimal. The study investigates riblet performance over three Reynolds numbers and finds that drag reduction increases, ceteris paribus, as the flow became less turbulent. The optimal riblet size were found to be 62 μm for the range of Reynolds numbers (1×10^6, 1.5×10^6, and 1.85×10^6) at which tests were conducted. A study by Gatti and Quadrio confirms an increase in drag reduction for low-Reynolds-number flows (95).

To optimise drag reduction the riblet geometry must be correctly dimensioned with adequate spacing to prevent the formation of vortices in the near-wall region. Conversely, if the riblet spacing is made too large, vortices will form in-between the riblets, increasing contact with the riblet surface thus increasing drag. The question of the optimal design of ribleted aerofoils is one which academics have addressed ad nauseam (96) (97). Linnayer found that trapezoidal riblets were most effective when there was a height-to-spacing ratio approaching 0.50 (98). Whereas riblets with semi-circular grooves were shown to require a height-to-spacing ratio around 0.7 to maximise drag reduction (99). Furthermore, riblets with a saw-tooth cross section angled at 60 degrees were found to maximise drag reduction

(increasing it by 5.5%) with a 0.9 h/s ratio, demonstrating that riblet performance is a function of incidence and spacing (99). Tiainen et al. (100) investigated riblet effectiveness by examining the NACA 024 aerofoil performance at two different Reynolds number. The numerical results showed that riblets could reduce drag at the designed incidence by 6.8 %. Tiainen's study conceded that the height-to-spacing ratio and trapezoidal shape were bigger factors for drag reduction than the incidence of riblets and optimizing the incidence could reduce wall shear stress and Reynolds stress and raise the entire velocity profile.

2.6.2 Vortex Generators

The vortex generator has several configurations which are deployed for lift enhancement: namely, the steady air jet blowing, pulsed blowing, synthetic jets, and the vane-vortex generator. These flow control devices operate in different ways but perform the same function; they reenergise the boundary layer by encouraging mixing and the prevention of flow separation. The Vane – vortex generator technique is an effective method for the enhancement of lift and suppression of drag forces. The vane is affixed to the blade's surface close to its leading edge and within the boundary layer of the streamwise flow. The vortex generator is usually positioned at an angle incident to the local airflow which creates a tip vortex effect, thus the vortices in the freestream entrain into the boundary layer and becomes enmeshed with it. This is a desirable outcome as a turbulent boundary layer has less chance of detaching from the surface or forming regions of recirculation. The passive vortex generator method is therefore an effective technique for flow control as it is capable of increasing energy capture in unsteady wind conditions. Figure 2.17 shows the geometry of a VVG when applied to a blade surface.

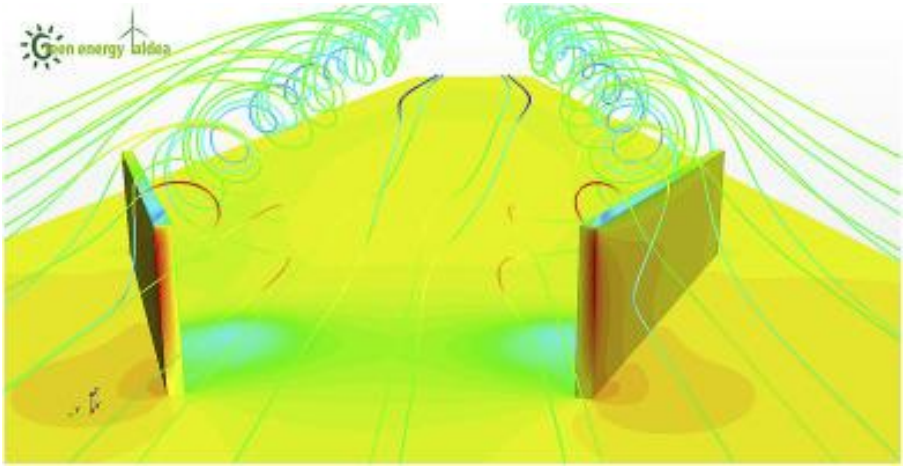

Figure 2.17 A low-profile vortex generator and the streamwise flow within the local boundary layer (101)

An experimental study undertaken by Sullivan (102) exemplifies the effect that VGs can have on HAWT performance in unsteady wind. It investigates the effect that different VGs have on the power efficiency of a two-bladed NASA turbine with a power rating of 2.5 MW. The VVG was applied from the 20% span to the tip and boosted the annual energy capture by 20% whilst requiring a wind velocity that is 3 ms^{-1} less to produce the rated power. Corrigan and Savino's (103) approach to VVG analysis involved full-scale wind tunnel testing of the NASA Mod-0; the VVG was applied to the turbine blade tip section (at 7.31m) of a 39m diameter 100kW HAWT. The findings demonstrated that the net torque was increased by 30% due to the installation of VVGs, with a maximum of 30% increased power output achieved with a wind speed of 6 ms^{-1}.

Prince et al (73) demonstrated the effectiveness of VGs in preventing dynamic stall and enhancing power efficiency through numerical analysis. Prince's theoretical study investigated the improvements that could be made to Nordtank turbine through the application of VGs. The modifications made to the blade were postulated to boost C_L by 5% in unsteady airflow conditions. Figure 2.17 shows the estimated increase in turbine performance due to the attachment of passive air jets to the blade surface. The plotted lines represent the blade turbine when air jets are applied across the blade span in three different configurations. The black BEMT line represents the air jets that are applied across the blade span; the red and green line shows the power generated by the turbine when the air jets are placed at the 50% inboard and outboard section, respectively. The experimental average is higher for wind speeds <15ms^{-1} than the theoretical BEMT power generated which indicates that PAJVGs is less effective at higher wind speeds. Overall, the results show the auspicious effects that VGs can have at moderate wind speeds; the PAJVGs can boost the power generated whilst mitigating the effects of stall. It was suggested within Prince's study that vane generators could have a similar effect on turbine performance, utilising wind energy in turbulent conditions especially at intermediate wind speeds.

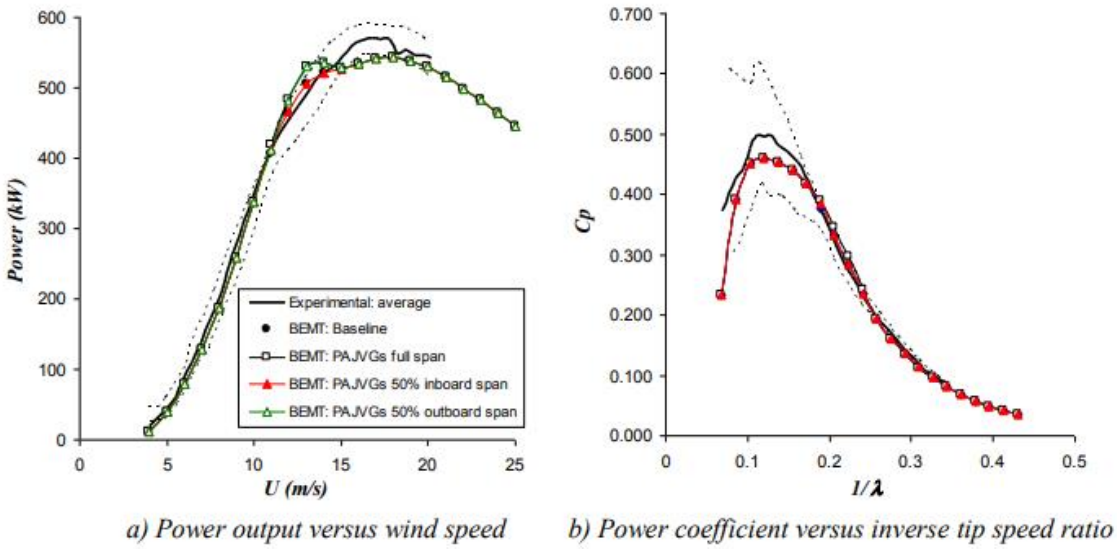

Figure 2.18 The estimated effect of passive air jets on turbine performance when applied to the Nordtank NTK 500/41 wind turbine for three air jet configurations (73)

A numerical investigation was conducted by Filgueira et al (101) to examine the optimal profile of vortex generators for energy generation. The study analyses the vortexes produced within the local boundary region when various VVGs of differing heights are adduced to a flat plate which are incident at an angle of 18.5° to the flow. The StarCCM+ CFD code was used to simulate the motion performance of the flow downstream from the VVG. A solution for the flow problem was found using the RANS equations; and k-ω SST was used to model the turbulence. The QUICK scheme was applied to discretise the convective terms and ensure an accurate solution is reached. The VVG has a rectangular shape with heights equal or lower than the boundary layer thickness: h1 =0.2m, h2=0.15m, h3=0.1m, h4=0.05m. The study found that the vortex path followed downstream of VGs with h1,h2, and h3 were similar. H4=0.05m, the smallest VVG, was demonstrated to be most effective in diminishing associated drag and circulation-formation. The explanation for this is that the path followed by the vortex is different laterally and vertically for H4 than other VGs. The smallest VG was most effective owing to its smaller profile and proximity to the wall; it interferes with the inner side of the boundary layer where the viscous stress is most prevalent to encourage mixing.

Research studies show VGs to be an effective supplement to turbine blades, as aforementioned flow control devices have been demonstrated to delay flow separation and aerodynamic stalling. Moon et al. (104) numerical study measures the improvement in turbine performance when VGs are applied using CFD analysis. A 2.3 MW HAWT was analysed using the CFX software in ANSYS which was then compared to aerodynamic

performance data obtained using the SCADA system. The RANS equation K- ω SST model was used to simulate the turbulent flow problem. The results demonstrated an improvement in power production of 2.80% at the rated wind speed of 10 m/s when the VVG pairs were attached to the turbine blade, compared to the experimentally measured improvement of 4.83%. The effect on the annual energy production was estimated to be a 0.81% increase due to VGs when the wind speed is between 4-11 m/s; the SCADA system measured 1.87% increase in annual energy capture. Overall, the results indicate that VGs are capable of modifying vortex behaviour and enhancing turbine performance.

2.6.3 Gurney Flaps

The Gurney flap is a microtab positioned at the trailing edge of a wing perpendicular to the pressure-surface of the aerofoil. It was created by Dan Gurney as an amendment to the trailing edge of the rear wing of his race car in the 1970s. This innovation improved the traction of the race car, allowing for better handling (105). The Gurney flap was later applied within the aeronautical industry for lift enhancement and load alleviation. It has become popular within the field of engineering because it is a simple device to analyse and manufacture, yet effective in enhancing performance. The flow physics of the Gurney flap is rather straightforward; a recirculation region is formed upstream of the Gurney flap due to the adverse pressure gradient which leads to an increase in pressure at the lower surface. Furthermore, two recirculation regions form downstream of the Gurney flap which creates a suction pressure region there. The Gurney flap alters the Kutta condition at the trailing edge and moves the stagnation point to the lower edge of the flap, essentially increasing the camber length of the aerofoil. The effect of the Gurney flap on vortex dynamics has been studied computationally and experimentally (106), it has been shown that the flow field is influenced by the technological device. The flow velocity over the aerofoil increases whilst the flow over the lower surface reduces, this corresponds with the increased pressure difference across the aerofoil which results in increased lift and drag coefficients. Figure 2.19 shows the geometry of the GF and its effect on the chordwise flow.

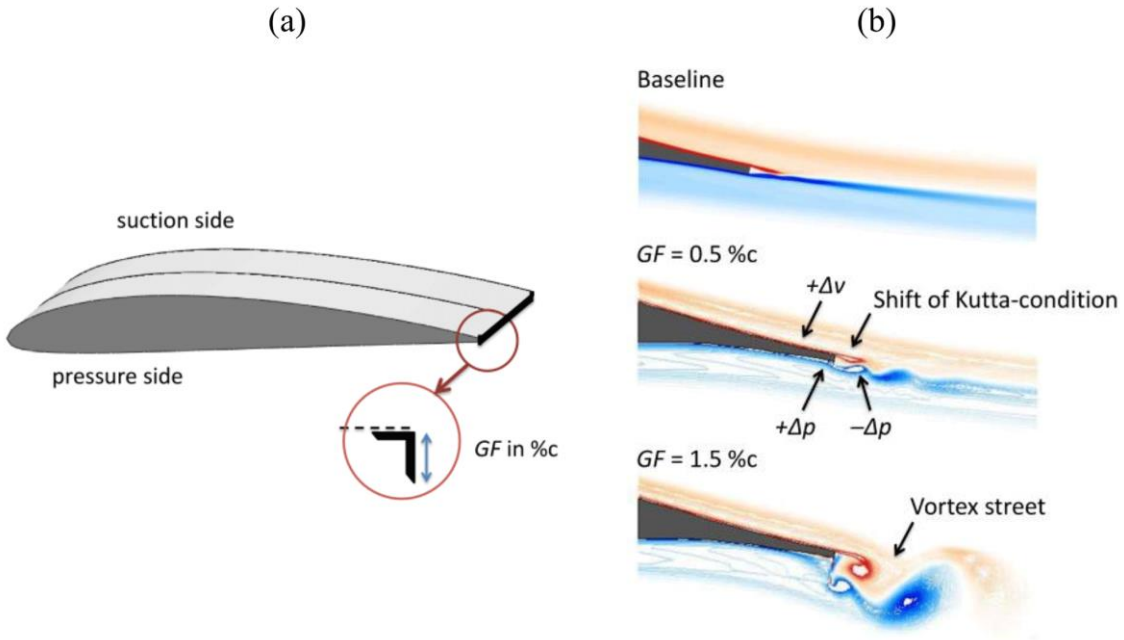

Figure 2.19 :a) Position of the Gurney Flap at the trailing edge of an aerofoil b) The effect of different GFs on chordwise flow (107)

Research has shown the Gurney flap to have good aerodynamic properties, a Gurney flap with a chord length of 2% can yield an increase in CL_{max} of 30% (105). A parametric study conducted by Jain et al. (108) analysed the effect of the Gurney flap on aerofoil aerodynamics. ANSYS ICEM CFD was used to assess the NACA 0012 aerofoil and investigate the flow control effectiveness of a GF based on several factors (Re number, flap height, position, mounting angle, configuration, etc.) in comparison with experimental results. The author found that there is a correlation between the GF height and $C_{L\,max}$, at an AoA of 10° as the GF height increases so too does the $C_{L\,max}$. The same trend occurs with the drag coefficient and GF height, however, if the AOA becomes too great then there is an exponential increase in drag coefficient. The lift-to-drag ratio was found to be optimal when the GF height was sized at 2% and a greater drag penalty was incurred at greater sizes.

Maughmer and Bramesfeld's (109) experimental research into the optimal size and location of GFs demonstrated that there is a linear correlation between lift enhancement and the chordwise location of the GF. Furthermore, the study showed that the best placement for GFs were closer to the trailing edge where the flow device could attenuate the build-up of adverse pressure gradients. At higher AOAs, the GF is more effective in influencing flow topology. Likewise, Jain et al. (108) explored the relation between C_L and the positioning of the GF on the chord. The study examined the effect of the GF on a number of chordwise locations S = 0%, 4%, 10%, 15% and 20%; the results showed that lift

enhancement capability reduced as the GF flap was moved further upstream away from the trailing edge.

Li-Shu Hao and Yong-Wei Gao (110) explored the effect of a GF's geometry on aerodynamic enhancement by using CFD++ (Metacomp) software for numerical simulation in comparison to experimental data. The steady Reynolds-Averaged Navier Stokes (RANS) equation was used to perform the analysis for the influence of the GF on the S809 aerodynamic performance with regards to its height and shape. The results showed an increase in the lift-to-drag ratio and a considerable increase in lift for the linear and nonlinear sections. This is demonstrated in the study, wherein the effect of GFs on turbine performance is examined. The GF with widths of 0.2c%, 0.6c% and 1.0c% are found to increase C_L by 102.33%, 91.79% and 89.23% respectively at an AOA= 1.03° with respect to the original aerofoil. When raised to an AOA =7.1° the rise in C_L is 28.33%, 26.97% and 23.36% respectively. Thus, the GF generates greater lift as its thickness decreases. In addition, the pitching moment and drag are increased. Another factor which this study considers is shape, it demonstrates that triangular GFs are substantially better than rectangular GFs in increasing lift, the triangular GFs obtained C_{Lmax} of 28.42% in comparison to the rectangular which was 16.31%.

2.6.4 Microtabs

The microtab (MT) resembles the GF in that both are small tabs normal to the blade surface, with a height of 1-2% of the chord, effectively immersed within the boundary layer. It is typically deployed upstream of the trailing edge on the pressure side of the blade where it can affect vortex dynamics, maximizing lift gains and mitigating drag forces. The MT operates in much the same way that the GF does, except that the recirculation zone forms under the pressure side of the blade which effectively moves the flow separation zone to boost lift. The MT and GF are the most frequently used flow strategies because of their effectiveness in controlling vortex behaviour and mechanical simplicity (111). However, the MT has a slight advantage over the GF as it is marginally more efficient for load reduction at higher AOAs (112).

A number of computational and wind tunnel experiments were conducted by Van Dam et al. (113) to determine the optimal height and distribution of the MT. The results indicated that the best configuration for a MT is situate the lower surface tab at 0.95 c, with a height of 0.01c, and the upper surface tab at 0.90 c. This placement of the MT was shown to be the best position for lift and drag optimization. Chow and Van Dam's (114) numerically simulated the unsteady flow over an S809 aerofoil with a MT the height of 0.01c deployed at 0.95c using OVERFLOW solver for analysis demonstrated that MTs are effective for

cambered aerofoils and retain their effectiveness even at higher AOAs. Furthermore, the active MTs were found to be as effective in generating lift as the passive ones. Abbas Ebrahimi and Mohammadreza Movahhedi (115) performed a 3D numerical analysis on a NREL Phase VI WT to ascertain the feasibility of using MT as a flow control strategy. The authors used the CFD RANS approach to show that the MT could improve energy efficiency by 17% relative to the Betz limit.

Deployment location and MT height are two factors which have a substantial influence on MT performance. Matthew Lennie et al. (116) examined the NACA0021 aerofoil by conducting wind tunnel tests which analysed the effectiveness of MTs in unsteady flow. By modifying parametric factors relating to MTs the authors were able to determine the variables that had the most considerable impact on aerodynamic efficiency. The findings demonstrated that as the AOA was increased the aerodynamic coefficient increased proportionately (up until the stalling point). In addition, the study investigated the chordwise positioning of MTs to analyse the influence of tab positioning on flow control effectiveness starting from the 0.9c to the trailing edge. The effect of this modification was a small pressure increase and increased aerodynamic damping measured as instantaneous values, C_m, when at 0.9c. Another variable which the study analysed was the effect of tab height on flow control effectiveness. A similar effect is evidenced when the tab height is increased, there is a commensurate increase in instantaneous damping. The larger MTs are able to overcome the smaller flow perturbations and enhance flow control. Figure 2.20 illustrates the recirculation region when a MT is affixed to a turbine blade.

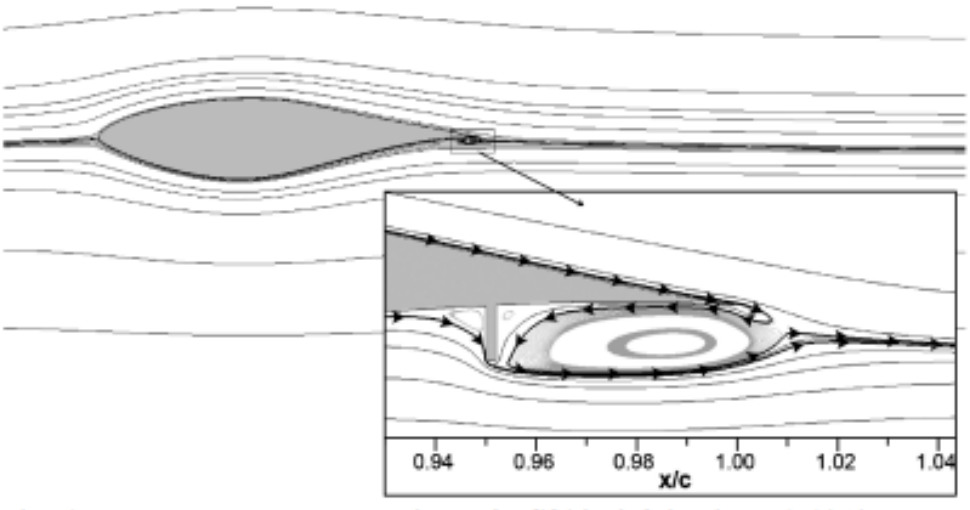

Figure 2.20: Instantaneous streamlines of a S809 aerofoil with a 1.10c% microtab at 0.95 x/c (114)

2.7 Summary

Unsteady wind is known to affect blade inflow conditions negatively and thus prevent the effective conversion of the wind's kinetic energy into electrical energy. Blade optimization studies have been hugely beneficial for the development of the HAWT machine thus far; further refinement would require an understanding of advanced concepts in relation to wind turbine aerodynamics and observation of best engineering practises in regard to simulation and analysis. This literature review discusses the fundamentals of wind turbine aerodynamics and mentions some of the important works done by researchers to understand and improve the performance of HAWTs in unsteady wind. The URANS CFD software and the eddy viscosity model k–ω SST are identified as useful methods for measuring the performance of HAWTs in unsteady wind.

In addition, a critical evaluation of passive flow devices is undertaken within this chapter so that the benefits of these methods can be properly understood. To provide a comprehensive understanding of the passive flow control landscape, this review examines major PFC devices used in wind turbine applications. However, the computational analysis within this study specifically focuses on riblets, microtabs, and Gurney flaps, which are most suitable for the NREL Phase VI blade geometry and the unsteady flow conditions under investigation.

Research into the effects of unsteady wind on the performance of HAWTs is still in its infancy; more numerical studies are needed to develop an episteme and provide verification of performance-enhancing solutions. The overarching aim of this project is to propose a more effective blade geometry that incorporates passive flow control techniques which enhances the HAWT's ability to operate in dynamic conditions. This study addresses the identified research gap through extensive numerical evaluation of the baseline blade and the above-mentioned PFCs .

3 NUMERICAL TECHNIQUES FOR CFD VALIDATION

3.1 Introduction

The main purpose of this chapter is to outline the methodology used to perform numerical analysis within this thesis and to elucidate on the simulation techniques used to measure the aerodynamic efficiency of the NREL Phase VI wind turbine. The unique numerical framework provided within this chapter provides a clear foundation for the accurate predictions of aerodynamic performance, enabling a comprehensive evaluation of the complex flow field and the resulting power characteristics under various operating conditions.

CFD analysis is sometimes called a “virtual wind tunnel” because the conceptual model is rigorously tested through iterative simulation. The function of CFD within turbine design is to characterize flow regimes in and around the HAWT detailing the shear stress, pressure and aerodynamic loads the turbine blade undergoes. From these results, the aerodynamic performance of the NREL Phase VI turbine in different wind conditions can be obtained. Researchers have used CFD to predict HAWT performance within the industry for several decades. The low costs of simulation and reasonable processing time of CFD make it a useful analytical tool.

The Qblade software was developed by a team of engineers at the TU Berlin University in 2010 for the design and analysis of WTs. The basis of the program is the BEM method which has a long history of application within turbine research. This open-source platform utilises XFOIL software developed by Drela and Giles at MIT, to analyse and compute the flow around subsonic aerofoils (25). Once these values have been obtained, the turbine blade can be designed and optimized to improve blade performance. XFOIL is seamlessly integrated with Qblade, its main function is to predict the aerodynamic coefficients at various angles (both pre-stall and post-stall). A stall-controlled HAWT can experience dynamic changes in its AOA, therefore, it is necessary to simulate the turbine performance over the full 360° range. The lift and drag polar values are extrapolated from XFOIL software and fed into the Qblade program where the effects associated with 3D flow are factored in through semi-empirical correction models.

Once the rotor geometry and design parameters have been specified then the power output of the HAWT can be predicted by Qblade. Weinzerl (117) utilized Qblade to execute parametric investigations into the functionality of an active trailing edge flap for load alleviation of WTs. Additionally, Mueller-Vahl (118) used Qblade to predict the power output of a HAWT when VGs are adduced to the blade by using experimental polar data

extrapolated from wind tunnel tests. The BEM algorithm of the Qblade software has been validated against experimental data and other BEM-based commercial software such as Flex5 by DTU and the GL-certified WT_Perf from NWTC (25). The congruence of Qblade with other commercial software and experimental data demonstrates that it is a reliable tool for the prediction of HAWT performance.

3.2 General simulation setup

Having already expounded on the physical assumptions and equations in previous chapters, this section lays out the basic procedures that are used to solve the flow problem. Computational simulations are frequently deployed in the early design phases to evaluate power efficiency and optimise turbine performance within the industry. Figure 3.1 shows the multistep process of CFD simulation that is utilised within this numerical setup for the validation of experimental data. To ensure an accurate CFD solution is reached, the protocols in each stage are followed meticulously. Broadly speaking, there are four stages involved in computational analysis: preprocessing, CFD modelling, simulation, and postprocessing. The geometry is imported into ANSYS Fluent, which is then used for the meshing, modelling, and analysis of the flow problem. The final stage is the post-processing stage which, is essential for the comparison and verification of simulation results with experimental data.

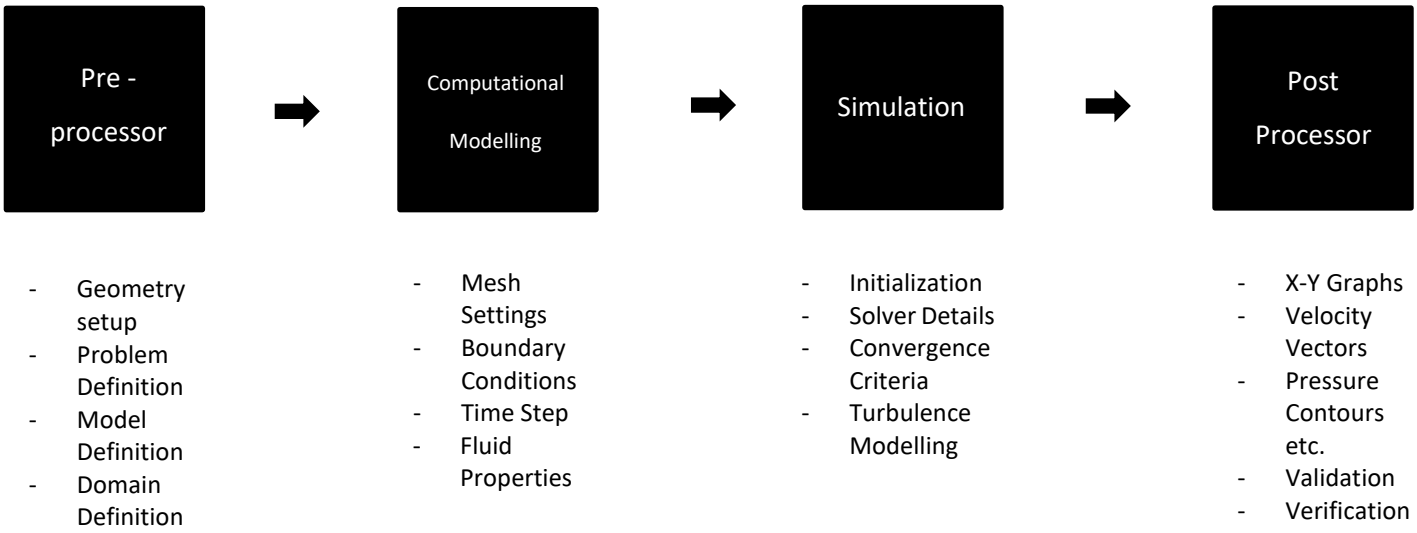

Figure 3.1 CFD Simulation Process

There are several software programs involved in the simulation and visualisation of the flow problem presented within this research project. The 3D geometry is imported from SolidWorks into ANSYS FLUENT, and the geometry is reoriented in Design Modeller with the fluid flow direction in the positive Z-axis with the blade axis along the Y-direction. The computational domain and rotor geometry are discretised within the ANSYS meshing software using an equations discretisation process such as the FVM, and the mesh is generated. The details pertaining to the simulation setup, such as the convergence criteria, turbulence model, and fluid properties, are inputted into ANSYS 2023 R2 software before a solution is generated. The post-processing work is done on the ANSYS platform; the numerical results are exported to Excel to produce graphs from which comparative analyses are conducted. Also, contour plots are produced from the solution generated to the flow problem for visualization. The postprocessing step is completed through the validation of the simulation results with experimental data.

The HAWT geometry chosen for computational analysis is the NREL Phase VI turbine because it is a well-studied HAWT with lots of information published about it. An experimental study was conducted by the NREL to examine the aerodynamic behaviour of the HAWT. These wind tunnel tests were designed to characterise its performance in dynamic conditions. The NREL Phase VI WT was evaluated at the NASA Ames Research Centre, which has the dimensions 24.4m x 36.6m with a turbine of hub height 12.2m. Figure 3.2 shows the NREL Phase VI WT geometry within the computational domain and Figure 3.3 illustrates the dimensions of the rotating domain.

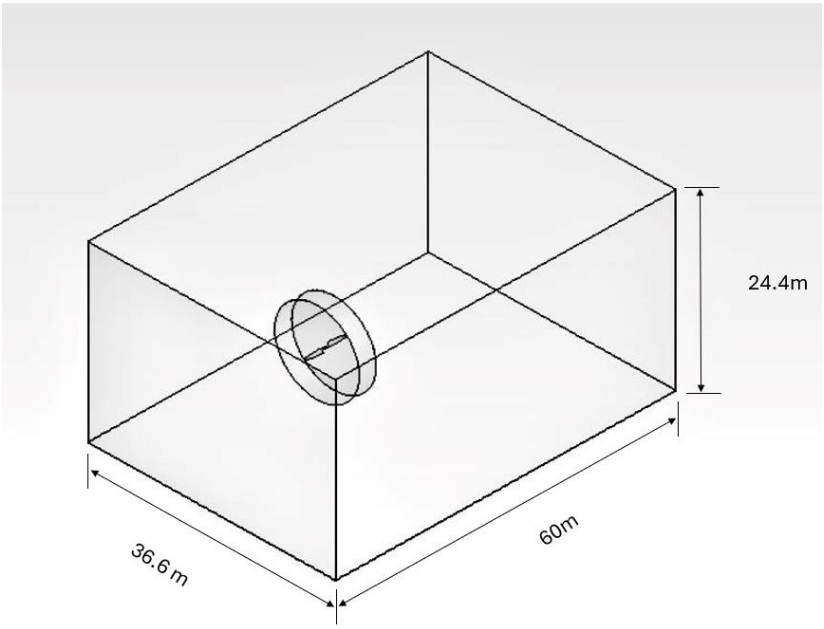

Figure 3.2: NREL Phase VI rotor within computational domain

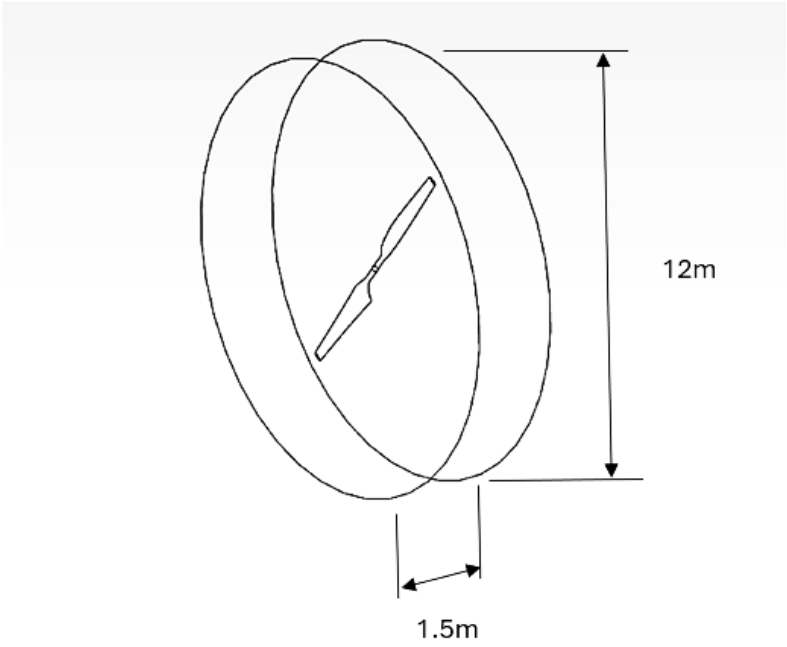

Figure 3.3: Dimensions of the rotating domain

3.3 Design Parameters

CFD software is used to analyse the NREL Phase VI WT and to model the aerodynamic loads exerted on the turbine blades. A 3D CAD model with a 19.8kW power rating is used to simulate the performance of the NREL Phase VI turbine. Table 3.1 shows the design features of the NREL Phase VI turbine analysed in ANSYS FLUENT.

Table 3.1: Design parameters of the NREL Phase VI

Number of blades	2
Diameter of blade	10.058m
Power Rating	19.8 kW
Chord Length	0.356m-0.737m
Angular velocity	7.54 rad s^{-1}
Tip Pitch Angle	3°

Local Twist Angle	Non-linear twist distribution
Blade profile	S809
Blade Thickness	20.95%

The 3D CAD model is of a two-bladed upwind HAWT that operates at 7.54 rad s^{-1}. The aerofoil thickness is 20.95% of the chord, it remains constant irrespective of radial position. The chord is designed with high thickness which permits it to deal with the large bending moments that the long blade undergoes. The total diameter of the blade is 10.058m. The chord length at the root is 0.737 m, and at the tip, it is the shortest, measuring 0.356m. The tip pitch angle of the HAWT is 3°, and there's no cone angle. Figure 3.4 illustrates the 3D HAWT model from tip-to-tip and the 2D blade aerofoil of the NASA Phase VI turbine.

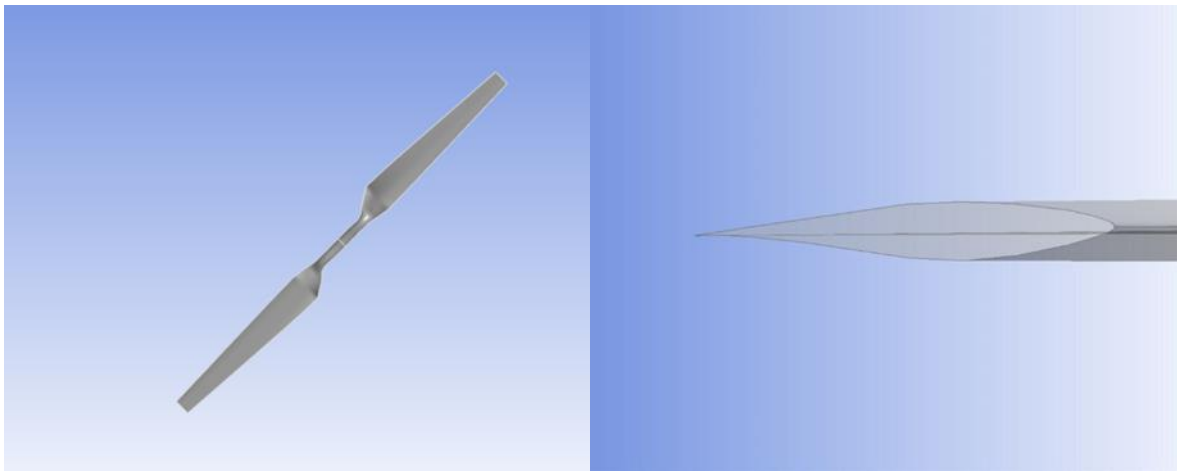

Figure 3.4: 3D model of NREL Phase VI turbine from tip-to-tip (left) and the cross-section of the blade aerofoil (right)

3.3.1 Reynolds Number

The Reynolds number is a nondimensional quantity that measures the ratio of inertial forces to viscous forces. It is an important parameter for describing the flow pattern of a fluid. When the flow is laminar, then the air molecules move smoothly over one another with minimal perturbations. However, when the flow is turbulent, then the motion of the eddies is often erratic, unsteady, and random. Equation 3.1 shows the Reynolds Equation.

$$Re = \frac{\rho v_{rel} c}{\mu}$$

Equation 3.1

The density and relative velocity of the fluid are symbolised by ρ and v_{rel}, respectively; c is the chord length and μ is the dynamic viscosity of air. For external flows, such as airflow over aerofoil, the flow can be categorised as turbulent when Re>500,000 (119). Table 3.2 shows the Reynolds number for different inlet velocities. The Reynolds numbers are sufficiently high in each instance for the flow regime to be modelled as turbulent. TSR measures tip speed blade in relation to freestream velocity; it is an important parameter as it has a significant bearing on the power efficiency of a HAWT. It has already been established that power efficiency is at its greatest when the TSR is between 8 and 12 for a 2-bladed HAWT. Research also shows that the pitch angle also affects c_p of HAWTs (120).

Table 3.2: The Reynolds Number at different inlet velocities

Inlet Velocity (m/s)	Tip Speed Ratios	Reynolds Number (at root)	Reynolds Number (at the tip)
5	7.58	524,333	915,570
7	5.42	570,962	922,280
10	3.79	656,284	936,177
13	2.92	754,008	954,628
15	2.53	822,960	969,244

3.3.2 Turbine control systems

The NREL Phase VI is a stall-regulated turbine, so it operates by limiting power in high operational winds through moderation of the rotor speed and blade angle. As the wind speed increases, the stall-regulated turbine controls power generation by steepening the flow angle of the turbine blade in relation to the incoming wind. The blades automatically incline, and this limits the amount of power being produced to acceptable levels without the introduction of any control device. The chief advantage of this is that the blade becomes stalled above the rated wind speed; the effect is less fluctuations in blade loading and output power (121). In stall control, the rotor speed is kept constant through the connection of the electric generator to the grid. In contrast, the pitch-controlled HAWTs operate by reorienting the turbine blades to regulate the power generated by the turbine.

This process involves the pitching of blades via the active control system in the right direction to achieve the desired output power. Although the systems differ in their modes of operation, they essentially achieve the same objective of power regulation.

Most modern HAWTs no longer use fixed speed control systems; rather, they operate using a variable speed system. The variable speed system operates by matching the rotor speed to the wind speed; this enables the HAWT to maintain the best flow geometry to achieve rated power. This type of system confers several advantages, namely, improved power efficiency and increased energy capture. In addition, the variable system helps to provide load alleviation, mitigate pitch system activity, and improve output power reliability. The variable system is able to function more efficiently at high wind speeds (15 m/s to 25 m/s) and is less likely to suffer significant power losses, which is why variable speed turbines are the most predominant type used within the industry.

3.3.3 Tip pitch angle

For a fixed-pitch turbine such as the NREL Phase VI turbine, the tip pitch angle is kept constant. The local AOA is defined as α, the angle between the chord line of the aerofoil and the resultant velocity of the wind acting on the turbine blade. At any radial location, the local AOA is equivalent to the sum of the flow angle, ϕ, minus the local twist angle θ_T, and the tip pitch angle, θ_{cp} . The relationship between these angles is expressed in Equation 3.2.

$$\alpha\,(r) = \phi\,(r) - [\theta_T\,(r) + \theta_{cp}]$$

Equation 3.2

The wind turbine blade is designed such that the built-in twist distribution C_L/C_D is as close to the maximum as possible. The lift-to-drag ratio is largely contingent on the AOA of the turbine blade. Therefore, the design angle is an important parameter that the turbine designer must take into consideration when assessing the performance of a stall-regulated HAWT. The lift force acts orthogonal to the direction of the wind, and the drag force is exerted in the opposite direction of the wind's vector. The tangential force acts in the plane of rotation, and the normal force acts perpendicular to the plane of rotation. For a detailed description of the local twist distribution of the NREL Phase VI wind turbine, please refer to Appendix A.

Figure 3.5 illustrates the angles of attack of the blade turbine at different wind speeds. From the graph it can be seen that the turbine blade requires a higher AOA to generate lift

at greater wind speeds. As the blade moves out from the centre (increasing r/R) the tangential velocity of the blade increases. At the high wind speeds, the flow over the blade can sometimes experience dynamic stall, which affects the flow over the blade and can lead to flow separation and a drastic decrease in lift generation. The blade twist design at the root allows the turbine blade to generate the required lift but a much lower AOA is necessary at the tip. The centrifugal force acting on the blade causes the airflow to move out over the blade surface from the root to the tip. When the centrifugal force is dominant, the flow will stay attached to the suction side of the blade which enhances aerodynamic stability.

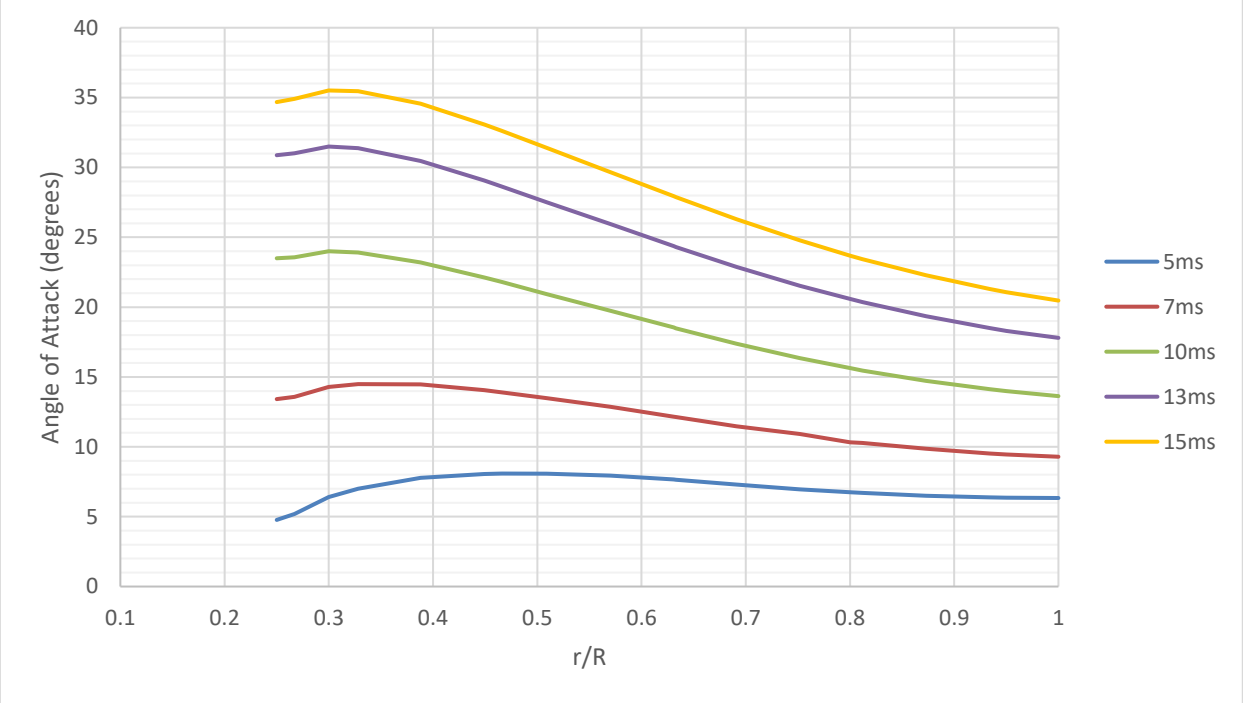

Figure 3.5: The angle of attack from the root to the tip of the turbine blade

3.4 Methodology

3.4.1 Geometric Model

NREL's landmark study provides experimentally measured data for the aerodynamic performance of the Phase VI turbine at different wind speeds between 5 m/s and 25 m/s. The published data from the wind tunnel tests allows researchers to measure the accuracy and reliability of QBlade and CFD simulations through comparison. The computational analysis of the turbine blade is an integral part of the design and optimisation of the blade

turbine; it allows the engineer to characterise the flow field and improve the aerodynamic performance of the turbine within the design phase, thus saving time and money.

The NREL Phase VI turbine blade is designed with 13 S809 aerofoils at equidistance from the root to the tip (0.459 m to 5.029 m). The blade aerofoil has a sharp trailing edge and a rounded leading edge; it is made less sensitive to surface roughness at the leading edge to improve the turbine output power. As aforementioned, the CFD model has the same dimensions as the actual NREL turbine rotor. The hub and the tower are excised from the CFD model to reduce the computational time of simulation. Since the effects of the hub and tower on turbine performance have been demonstrated to be negligible, removing it from the CFD model will not greatly affect the accuracy of the CFD simulations (122). Li et al. (123) demonstrated that the tower affects flow aerodynamics and creates a separation between the nacelle and itself; this induces vertical vortices, which evolve into hairpin vortices as the wind speed increases. However, the CFD result showed that the presence of a tower within the CFD model had a relatively small effect.

The computational domain is the region of space where the solution for the CFD simulation is generated. The outer domain defines the limit of the computational space and determines the physical conditions wherein the flow problem is solved. The inlet, outlet, and walls define the boundary regions, and the inner domain encloses the turbine as shown in Figure 3.2. The fluid domain is rotating at a velocity of 7.54 rad/s; the shape of the domain is cylindrical, and the appropriate size is designed to be large enough to avoid the influence of the domain on turbine performance. The inner domain enclosing the turbine rotor has a width of 12m with a thickness of 1.5 m; it is stationed 20m from the inlet and 40 m from the outlet.

The computational domain is made large enough to accommodate the HAWT geometry and to measure its performance in various wind conditions. An adequate size is given to the domain so as to accurately trace air flow around the rotor blade, excluding the effects of flow perturbations. The accuracy of the solution produced is largely contingent on domain size and shape. In this instance, a rectangular prism is preferred because of the lower computational time required and the relative ease of meshing and simulation. An oversized control volume would waste time and resources and would not improve the accuracy or reliability of the CFD analysis. A compromise between the domain size and the number of mesh elements is the best approach for achieving an accurate CFD solution. In this instance, the computational domain size is made to be the same size as the wind tunnel testing centre with dimensions 36.6 m × 24.4 m × 60 m. The computational domain is made large enough in the Z-direction to avoid the formation of vortexes and recirculation regions

downstream from the HAWT which could lead to inaccurate measurements of the power capacity of the HAWT.

3.4.2 Boundary Conditions

The boundary conditions of the computational domain are an important aspect deciding the accuracy and the reliability of the flow solution, and therefore it requires careful consideration. This section sets out the parameters used for the numerical simulations performed within the next chapter. Table 3.3 contains the boundary conditions for the simulations performed in ANSYS Fluent.

Table 3.3: Boundary Conditions for the NREL Phase VI Turbine

Boundary	Boundary Conditions (velocity)	Boundary Conditions (pressure)
Inlet	Fixed Value	Zero Gradient
Domain Walls	Slip Wall	Fixed Value
Outlet	Pressure Outlet	Zero Gradient
Turbine Blade	No-slip wall	Zero Gradient

The inlet velocity is one of the parameters used to define the wind conditions that the turbine blade experiences. This input variable is set between 5 m/s and 15 m/s within ANSYS FLUENT so that the aerodynamic performance of the NREL Phase VI can be examined at different wind speeds. Since the flow case is incompressible, the inlet and outlet surface-averaged gauge pressure is set at zero, and the freestream pressure is assumed to be equivalent to the standard atmospheric pressure (101,325 Pa). The stagnation pressure of the fluid flow will rise as the flow velocity increases. The official report uses a turbulent intensity and length of 0.1% and 0.02m, respectively (124).

The boundary wall regions of the flow domain are defined as a slip wall; the walls are modelled as a frictionless surface, therefore its effect on the flow field is ignored. An interface is formed between the inner and outer domain for data transmission, the outer domain is subject to the operating conditions abovementioned, whereas the inner domain holding the turbine blade is designated a rotating wall with an angular velocity of 7.54 $rads^{-1}$. It has a no-slip boundary condition which means that the effect of the fluid viscosity on

the turbine blade is taken into consideration. The moving reference frame (MRF) has been shown to be a useful technique for simulating turbine performance within steady flow fields. This method uses Navier-Stokes equations for the rotating flow whilst keeping the mesh fixed. (125). However, the sliding mesh technique is the most accurate method for simulating unsteady rotating flows even though it is more computationally demanding (126).

3.4.3 Mesh Generation

The mesh generation process is one the most important preprocessing stages in numerical simulation. This stage involves subdividing the flow domain into elements using a discretisation method. ANSYS uses the FVM to discretise the mesh which consists of several elements and nodes. For incompressible fluids, the physical quantity in the control volume are defined at the centre point of the element in contrast to a compressible fluid for which the value in the element is averaged. The basic differential equations governing the behaviour of the fluid flow are integrated in the elements constituting the computational domain. This is followed by the discretisation of the terms in the integrated equation representing the flow over the NREL Phase VI geometry. This changes the integral equations into a set of algebraic equations. The ANSYS FLUENT software is deployed to solve these algebraic equations and to simulate complex flow phenomena (127).

The FVM is widely used in CFD applications for complex geometries and large-scale turbulent flows. The constituent mesh elements have different shapes which are used to capture information about the flow structure. The most common elements used to discretise 3D geometries are tetrahedrons, hexahedrons, triangular prisms and quadrilateral prisms. For 2D geometries, the elements are usually in the shape of extruded triangles and quadrilaterals. Meshes can be categorised into two groups: unstructured and structured meshes. A structured mesh can be defined by its interior nodes which have an equal number of adjoining elements. These meshes are typically comprised of hexahedral or quadrilateral elements which are arranged in a spatially efficient manner. Structured meshes are either orthogonal or non-orthogonal, examples of orthogonal meshes include Cartesian, spherical and cylindrical meshes (128). The structured meshes with orthogonal coordinates have a better convergence and higher resolution than unstructured meshes.

Unstructured meshes are usually composed of a number of triangular and tetrahedral elements, the tessellations may also use quadrilateral and hexahedral elements to make up the mesh. The connectivity between the constituent elements are irregular and their size and shapes differ accordingly. Unstructured meshes are often used to discretise complex geometries because they allow for flexibility in the mapping of cells across the

computational domain. This is an essential advantage when dealing with geometries with sharp edges, curved boundaries et cetera, as it helps provide a more accurate solution. However, structured meshes incur a lower computational cost because they require less memory to generate a numerical solution which means it can be generated faster. The ease of meshing makes the structured mesh an attractive option for computational simulation.

For this numerical study, a structured mesh is used to discretise the outer domain as this method is most suitable for simple geometries. The inner domain houses the rotor blade, and a finer mesh is used to capture the flow physics in the region near the turbine blade. The trailing edge of the NREL Phase VI is known to be sharp therefore irregular elements are needed to discretise the flow in the near-wall region. An unstructured mesh is used within the moving frame reference to capture the pressure and velocity gradients at the boundary region for better accuracy and reliability in assessing the turbine's performance. Figures 3.6 and 3.7 show the mesh topography of the inner and outer domain. The outer domain is discretised using a body-fitted cartesian grid and the inner domain uses the patch conforming method to tesselate the rotating domain which is comprised of tetrahedrons. Figure 3.8 shows the front and lateral view of the mesh interface, and the mesh layers added to the blade aerofoil.

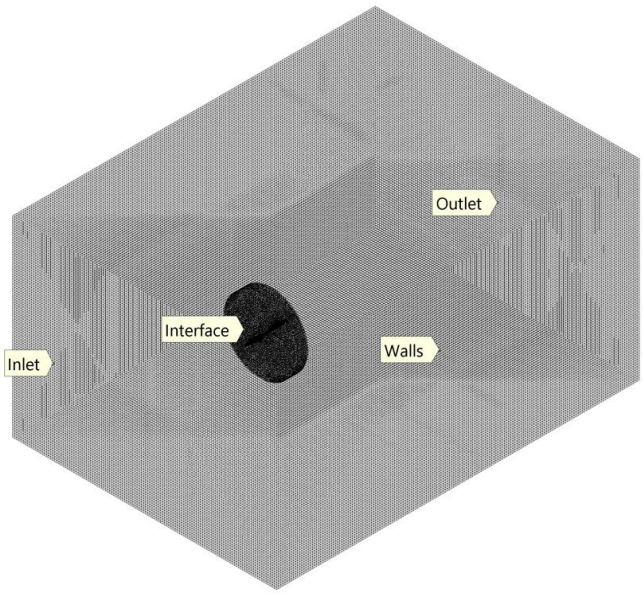

Figure 3.6: A full display of the generated mesh domain

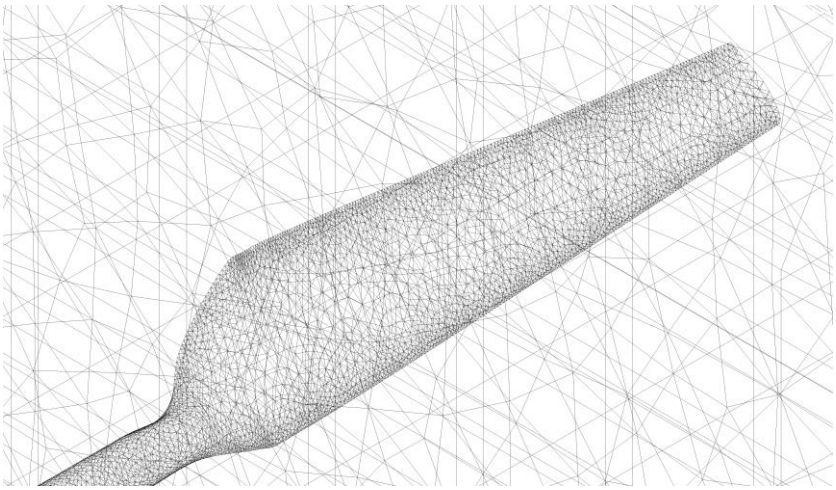

Figure 3.7: The unstructured mesh for the turbine blade within the rotating domain

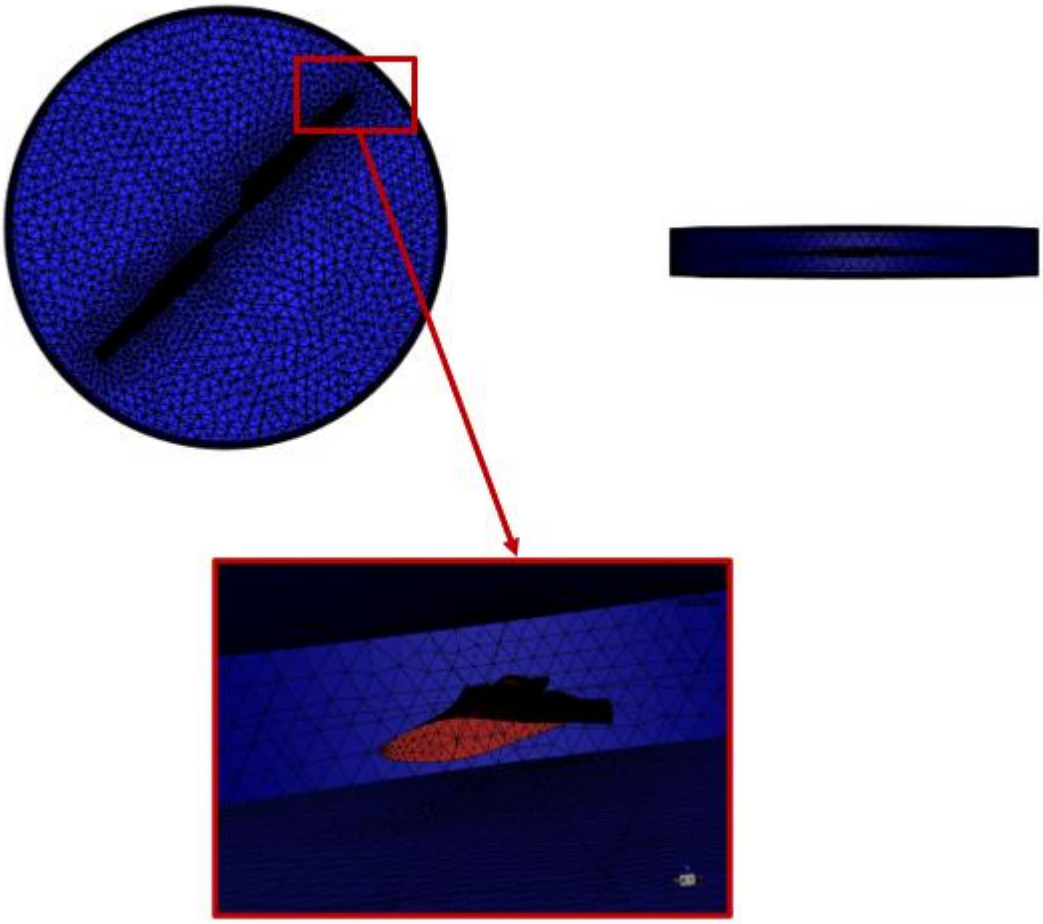

Figure 3.8: A front and lateral view of the mesh layers on the blade aerofoil

Creating a quality mesh is an essential aspect of reaching an accurate numerical solution, there are a few criterions by which to judge the mesh quality such as the mesh skewness, aspect ratio and size distribution of cells. ANSYS Fluent allows the fluid dynamicists to analyse the quality of the mesh by monitoring the skewness of the cells; highly skewed cells can lead to difficulties in convergence of residuals and decrease the accuracy of the numerical solution. The ideal skewness for a mesh cell is zero, however an average value below 0.5 is still within an acceptable range. The aspect ratio is defined as the measurement of how stretched an element is, this is calculated by dividing the maximum distance between the cell centroid and the nodes by the minimum distance. A good aspect ratio for the freestream region of the flow field is 5:1; in the boundary layers the aspect ratio may be a little higher at 10:1, an aspect ratio nearer to 1 is generally indicative of a good quality mesh. To obtain accurate results the smoothness of mesh elements must be taken into consideration; a sudden increase in cells size would introduce errors at the nearby nodes. All of these factors, smoothness, skewness and aspect ratio are important determinants in reaching a credible and accurate numerical solution.

The onset profile and mesh structure together determine the accuracy of performance predictions. The onset profile defines the wind conditions, such as the wind shear and turbulence that the rotor blade experiences ; if this profile is inaccurate, the simulation will fail to account for the uneven structural loads and torque fluctuations that cause mechanical wear. Meanwhile, the mesh structure serves as the basis for these calculations. A high-quality, refined mesh is fundamental near the blade surfaces to correctly model the boundary layer and flow separation, ensuring that lift and drag are calculated precisely. Ultimately, a detailed onset profile provides the correct input data, while a robust mesh ensures the processing of that data, it captures the complex physics of power generation and wake development.

When a flow becomes turbulent a separate boundary layer is formed over the surface of the wall and a non-uniform velocity gradient is created adjacent to the wall. The viscous sub-layer is the immediate layer over the wall which is dominated by viscous effects induced by the turbulence above the viscous sublayer. The buffer layer is a transition region where the flow is partially dominated by viscous and turbulent forces, these forces are of similar magnitude, the flow profile is complex as such it is not easily defined. The logarithmic region is the aspect of the boundary layer where the turbulence stress dominates the fluid flow. Once the y+ value is established - the dimensionless unit measuring the distance from the wall - then the first layer height can be deduced. The value of first layer height has to be at the correct length to give a detailed resolution of the boundary layer region. Inflation layers are added to the boundary layer region to enhance

resolution of the flow physics and ensure an accurate prediction of the flow region. Figure 3.9 shows the velocity profile within the boundary layer region.

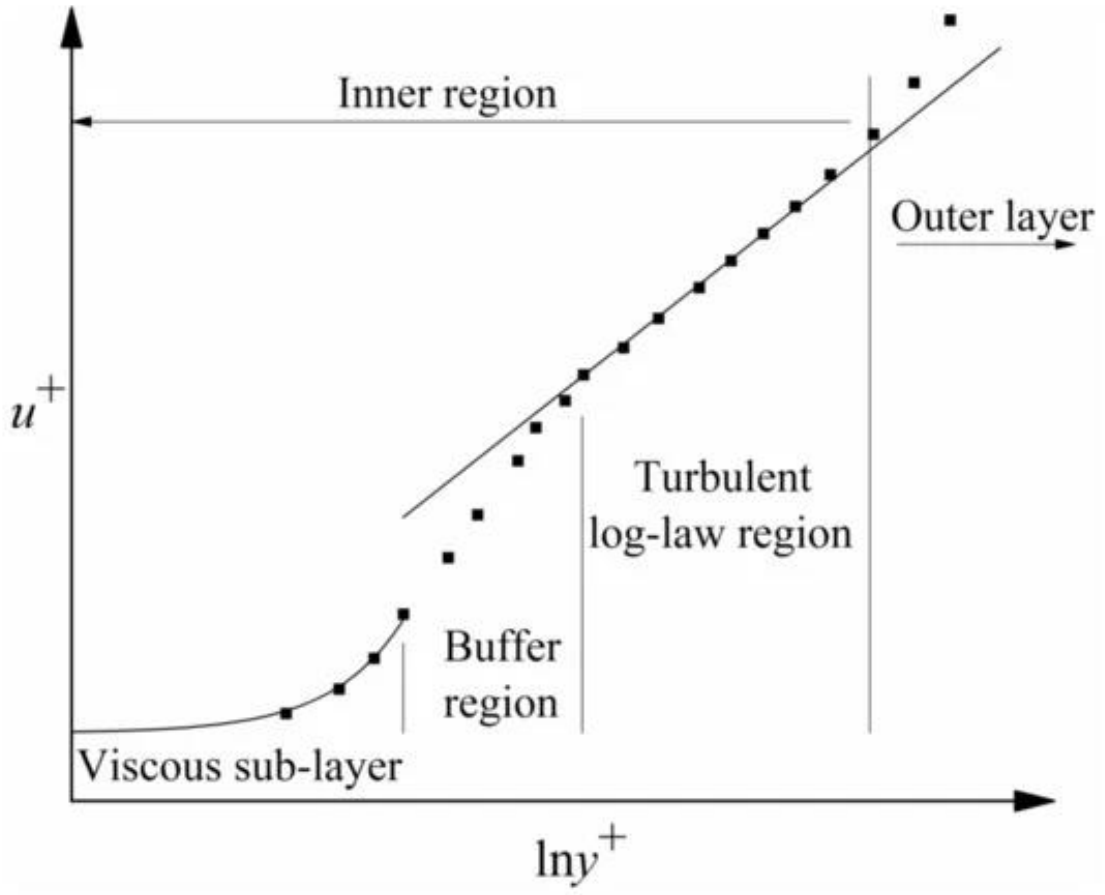

Figure 3.9: The velocity distribution in the boundary layer region (129)

The operating principle behind the use of wall functions is the law of the wall which axiomatizes that the average velocity of the turbulent flow is proportional to the logarithm of the distance to the boundary of the fluid region. The wall induces vortices and turbulence within the flow field which affects the flow profile, using the log-law method the velocity profile and stresses near the wall can be predicted. Thus, a wall function is used to model the effects of turbulence on the flow field with the first cell centre being placed in the logarithmic region (where $30 < y^+ < 300$). Even though modelling the turbulence in this way is computationally demanding, it is effective when measuring the forces acting near the wall. Another approach involves modelling the turbulence in the near-wall region using turbulence models to simulate the effects of perturbations in the flow field. To ensure an accurate numerical solution is reached the first cell centre is established in the viscous sub-layer (for $y^+ = 1$). The benefit of using wall functions is that it obviates the need to modify the RANS model to resolve the boundary layer, therefore less mesh elements are required

for computational simulation. Table 3.4 shows the turbulence models used to resolve wall-bounded flows in accordance with their y^+ value.

Table 3.4: shows the acceptable range of y+ value for given turbulence models

	Turbulence Models	Y+ values
Low – Re flows	K-omega, K-omega SST, Spalart Allmaras	$y^+ < 5$
High – Re Flows	Realizable k-epsilon, standard k-epsilon, RNG k-epsilon	$30 < y^+ < 300$

The y+ for the k-omega SST is usually set between 1 and 5 for accuracy in near-wall modelling. Using this turbulence model will enable an accurate resolution of the flow problem in the viscous sublayer. This approach allows for a coarser mesh to be utilized without compromising the accuracy of the solution. When the first layer height is kept constant at $1x10^{-5}$ m, thus the y+ value ranges are << 5.

3.4.4 Solver Setup

The first order upwind scheme is used to discretise the convection term in the momentum and energy equations. It is widely used within research due to its stability; however it may be prone to false diffusion if the mesh is not properly refined (130). The second-order upwind scheme is generally preferred for RANS modelling as it offers improved accuracy when solving for the convection term. The second-order upwind scheme is used within this numerical study to solve the governing equations. The flow field within the computational domain is expressed through the incompressible Navier Stokes Equation. There exists within ANSYS Fluent several numerical methods for solving these equations such as the SIMPLE, SIMPLEC, PISO and Coupled algorithm. The SIMPLE, SIMPLEC and PISO algorithm uses pressure-based segregated algorithms, whereas the Coupled uses the pressure-based coupled solver. The differences in the numerical schemes are explicated below:

- The SIMPLE algorithm uses a relationship between velocity and pressure corrections to obtain the pressure field.

- The SIMPLEC algorithm is an improvement of the SIMPLE algorithm, it helps to reduce convergence difficulties when simulating with skewed meshes.
- The PISO algorithm is part of the SIMPLE family of algorithms; however, it is more efficient in calculation through two additional corrections: neighbour correction and skewness correction.
- The Coupled algorithm is robust and efficient for single phase flows with better performance in comparison to the segregated solution schemes. The coupled scheme solves the momentum and pressure-based continuity equations together.

The numerical approach for the simulations performed within the ANSYS Fluent setup are detailed in table 3.5.

Table 3.5: Numerical parameters for the simulations performed within ANSYS FLUENT.

Algorithm	Numerical Parameters
Turbulence Model	SST k-w
Turbulence Intensity	0.1%
Length Scale	0.02 m
Pressure-Velocity Coupling Method	COUPLED
Wind Velocity	$v = 5$ ms^{-1} – 15 ms^{-1}
Operating Pressure	$p = 1\ atm$
Discretisation Scheme	Second Order Upwind

There are two different discrete solvers, the pressure-based solvers and the density-based solver. Each of these solvers makes use of control-volume methods. The pressure-based solver is designed to solve incompressible flows; however, it also has the capacity to solve compressible flows by utilizing the coupled algorithm. Both discrete solvers are capable of dealing with a wide range of flows however the density based-solver is better at handling compressible flow regimes. The pressure-based approach is particularly good at dealing with the incompressible flows and will give a more accurate solution to the flow problems presented within this report.

The calculation of unsteady flow development and wake interaction relies on solving the URANS equations, which incorporates a time-dependent momentum term to account for the fluid's inertia as it reacts to moving blade rows. These terms account for the phenomena of unsteadiness and wake propagation. Blade designers' factor in the occurrence of unsteadiness by designing the blade with enough structural integrity to withstand mechanical resonance and aerostatic flutter.

The LES method is most effective when handling complex flow cases with significant large-scale turbulence. In this respect, it is more effective than the RANS models which prioritises efficiency over complexity. Although, the LES method requires greater computational effort to model the flow field it has a higher degree of accuracy than the RANS method. It is capable of modelling turbulent structures and predicting instances of vortex shedding and flow recirculation. The Navier-Stokes Equations is filtered to represent the LES Equations. Equation 3.3 measures the effect of the larger eddies in the fluid, which create the turbulent structures in the flow field. Equation 3.4 is the sub-grid scale component which models the smaller eddies and averages out it effects. The density within the fluid flow is assumed to be constant with no divergence.

The LES-filtered Navier-Stokes Equation for incompressible flows is expressed as:

$$\frac{\partial \bar{u}_i}{\partial t} + \frac{\partial \bar{u}_\iota \, \bar{u}_j}{\partial x_j} = -\frac{1}{\rho}\frac{\partial \bar{p}}{\partial x_i} + \frac{\partial}{\partial x_j}\left(v\frac{\partial \bar{u}_\iota}{\partial x_j}\right) - \frac{\partial \tau_{ij}}{\partial x_j}$$

Equation 3.3

$$\tau_{ij} = \overline{u_\iota u_j} - \overline{u_\iota}\,\overline{u_j}$$

Equation 3.4

The filtered pressure field is $\bar{p}$, and $\frac{\partial \tau_{ij}}{\partial x_j}$ is the rate of stress tensor, the nonlinear filtered advection term is symbolized by $\overline{u_\iota u_j}$. The modelling of the τ_{ij} is done through the sub grid scale models, the stress tensor is used to represent all of the unclosed terms. An empirical turbulence model is then selected to model the smaller unresolved scales.

3.4.5 Turbulence modelling

A turbulence model is required to solve the flow problem in the viscous sublayer of the boundary region. The k-ω SST is widely used in fluid mechanics to accurately model turbulence and predict flow separation. It is an ideal algorithm for incompressible flows with a high Reynolds number, which makes it an appropriate choice for the flow problem

presented in this paper. Equation 3.5 and Equation 3.6 shows the two equations that the SST k-ω uses to capture the behaviour of the viscous sublayer:

$$\frac{d}{dt}(pk) + \frac{d}{dx_i}(pkv_i) = \frac{d}{dx_j}\left(\Gamma_k \frac{dk}{d_j}\right) + \tilde{G}_k - Y_k + S_k u$$

Equation 3.5

$$\frac{d}{dt}(p\omega) + \frac{d}{dx_i}(pwv_i) = \frac{d}{dx_j}\left(\Gamma_\omega \frac{d_\omega}{dx_j}\right) + \tilde{G}_\omega - Y_\omega + D_\omega + S_w$$

Equations 3.6

Equation 3.5 measures the turbulent kinetic energy and Equation 3.6 refers to the specific dissipation rate. Y_k and Y_ω are the dissipation of k and ω due to turbulence. G_k is the generation of turbulence kinetic energy (TKE) due to mean velocity gradients and G_ω is the generation of ω. Γ_ω and Γ_k are the effective diffusivity of ω and k, respectively. D_ω stands for cross diffusion and S_k and S_ω are the optional sources in the model.

4 A COMPARATIVE ANALYSIS OF THE NREL PHASE VI HAWT

4.1 Introduction

The benchmark data published in the NREL report is a useful tool for the validation and verification of CFD simulations. The experimental datasets are compared with CFD simulations and used to measure the accuracy and reliability of the numerical solutions presented within this chapter. Authenticating the CFD model through comparison with benchmark data helps to validate the methodology and measure the simulation modelling error. One of the chief benefits of validating the CFD methodology is that it can be used in future applications for research and development purposes, especially when shown to be reliable and accurate. The application of the BEM-based software, Qblade, within this study is for cross-analysis and the validation of the CFD results.

4.2 Mesh Independence Study

The mesh independence study is an integral part of obtaining an accurate solution when performing computational simulations. Initially, a coarse mesh is used to analyse the flow problem and then the mesh is refined until the solution is deemed accurate enough; when the convergence criteria is reached and the residual errors are sufficiently small. The RMS residuals is considered converged when the residual levels are as low as 10^{-6}, although it may not be always feasible to reach such a high fidelity. Table 4.1 shows the mesh sizes used for the analysis of NREL Phase VI turbine.

Table 4.1: Torque and Power rating of the NREL Phase VI turbine at different mesh sizes

Elements	Nodes	Torque (Nm)	Power (kW)
749,181	171,339	238.86	1.80
1,045,104	233,565	260.26	1.96
2,290,526	746,330	285.70	2.15
5,011,846	2,557,627	295.30	2.23

The numerical parameters for the simulations performed in the mesh independence study are stipulated in Table 3.5. Up to four meshes are used to perform the mesh independence study and the mesh refinement study is conducted by examining the change in the values

of torque and power as the number of mesh elements increases. The torque and power are quantities of interest because they directly relate to the power efficiency of the turbine. Other parameters such as the static pressure and pressure coefficient are also examined. In addition, the relaxation factors are reduced to account for the high turbulence in the flow field. The pressure is set to 0.2, momentum is 0.5, turbulence KE 0.5, specific dissipation rate 0.5. Reducing the relaxation factors usually makes the solution take longer to converge thus each simulation is allowed to run for 5,000 iterations. Each simulation is steady-state, and the moving frame motion is activated to simulate the rotational speed of the blade. The mesh could be refined further, however, the computational time for the simulations would be excessive. The mesh is considered adequately refined when the residuals have asymptotically converged indicating that the solution presented is accurate. The residual levels reached 10^{-4} for the last simulation which means that the solution is reasonably accurate. Figure 4.1 and Figure 4.2 shows the RMS residual levels of the finest mesh and the torque of the NREL Phase VI turbine after 5,000 iterations.

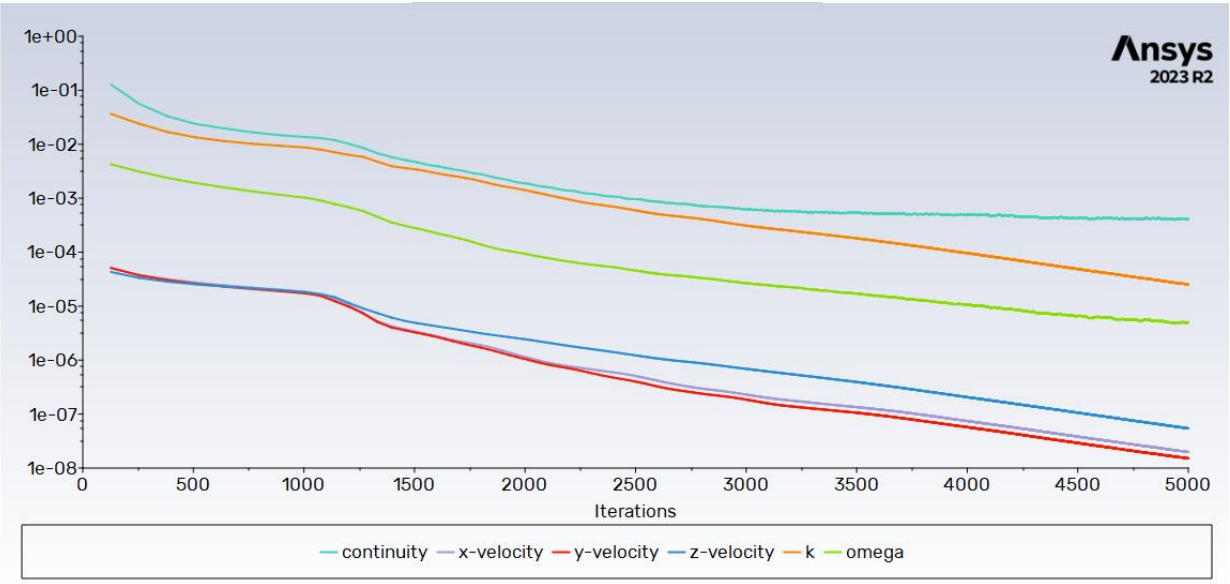

Figure 4.1: RMS residuals for a steady state simulation

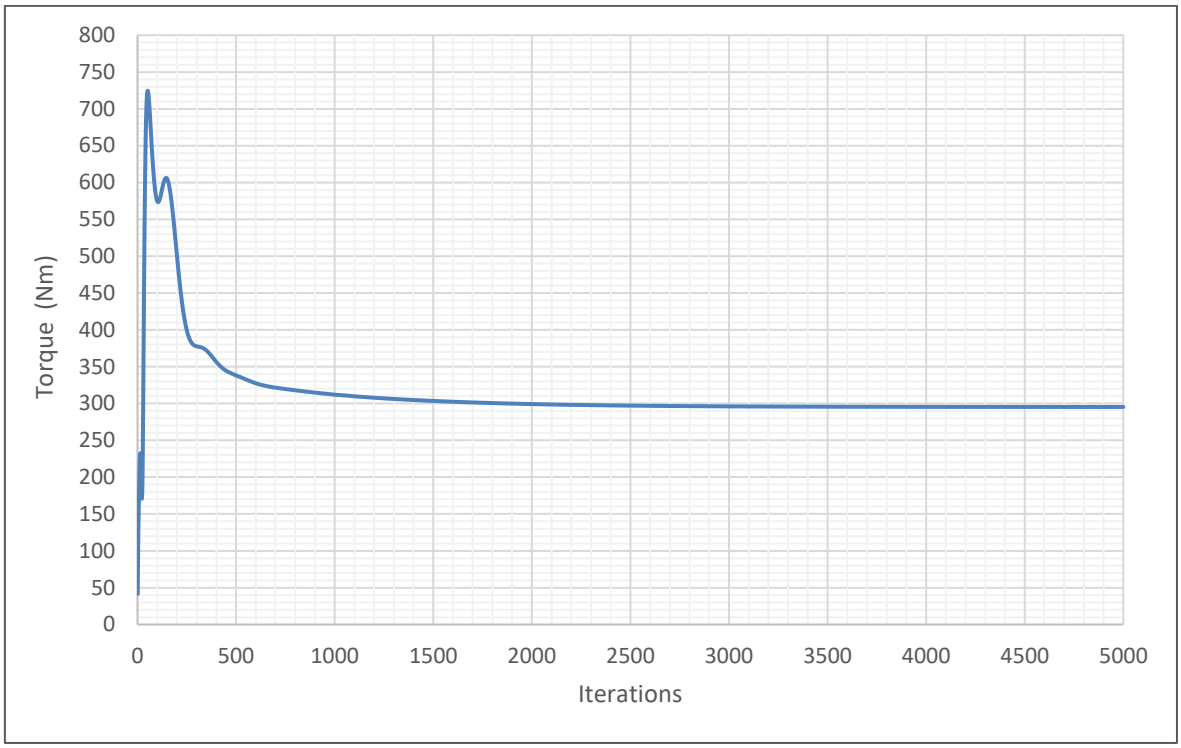

Figure 4.2: The torque generated after 5,000 iterations

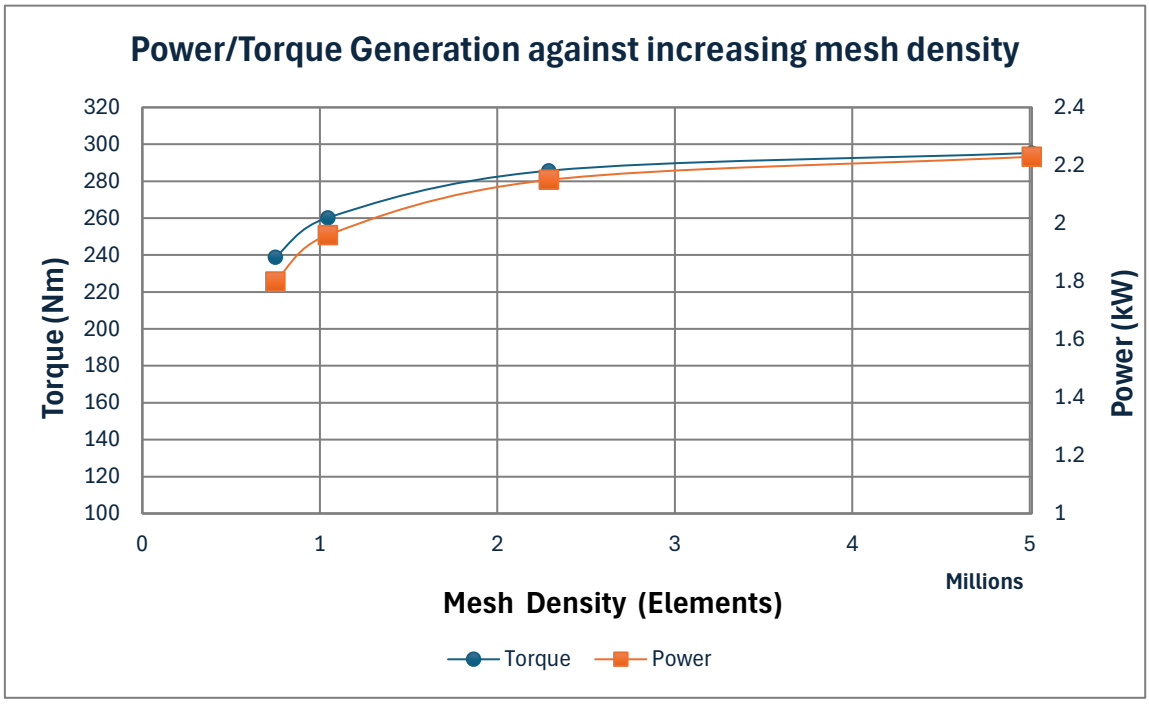

Figure 4.3: Effect of increasing mesh density on power/torque generation

Figure 4.3 shows that the CFD solution converges as the mesh density is increased. Therefore, the mesh is deemed to have sufficient resolution to capture the flow physics in the computational domain. Mesh independence is reached at the third iteration of the simulation; however, the 5 million grid is used for better resolution of the flow problem.

4.3 Steady Simulations

4.3.1 Power and Torque

The CFD solver was used to simulate the performance of the NREL Phase VI turbine and generate results for its aerodynamic performance under different inlet conditions. Table 4.2 shows the torque generated by the CFD solver in comparison to the experimental data published in the NREL report.

Table 4.2: The torque generated by CFD solver in comparison to experimental data

Wind Speed	CFD Simulation (Steady) Torque (Nm)	Experimental Torque (Nm)	Percentage Difference
5 m/s	295.30	299	1.24%
7 m/s	823.41	835	1.39%
10 m/s	1492.1	1289	15.76%
13 m/s	1653.0	1297	27.45%
15 m/s	1265.2	1267	0.16%

The computational model used for these simulations generated a relatively accurate result, the percentage difference for each simulation is within 2% of the experimental results, except the simulations for which the inlet velocities are set at 10 and 13 m/s. The overprediction of the moment of the force or the torque generated by the HAWT is evidence that the flow experiences what is known as flow separation – the boundary layer begins to separate due to the adverse pressure gradient that is formed on the suction side of the turbine blade. Therefore, the pressure differential across the blade is overestimated by the CFD solver which causes an overestimation of the torque generated by the turbine. In addition, the k-ω SST model is susceptible to overpredicting the torque when the flow is turbulent; the most plausible explanandum for this is that the model exaggerates

turbulence production in the near-wall region. This phenomenon usually occurs when the shear stress around the turbine blade becomes excessive. Different turbulence models are used to solve the flow problem to assess whether they have better predictive capabilities. The experimental data for torque validation is extracted from Dias and Camacho's report (131). Figure 4.4 shows a comparison between the experimental data against different turbulence models.

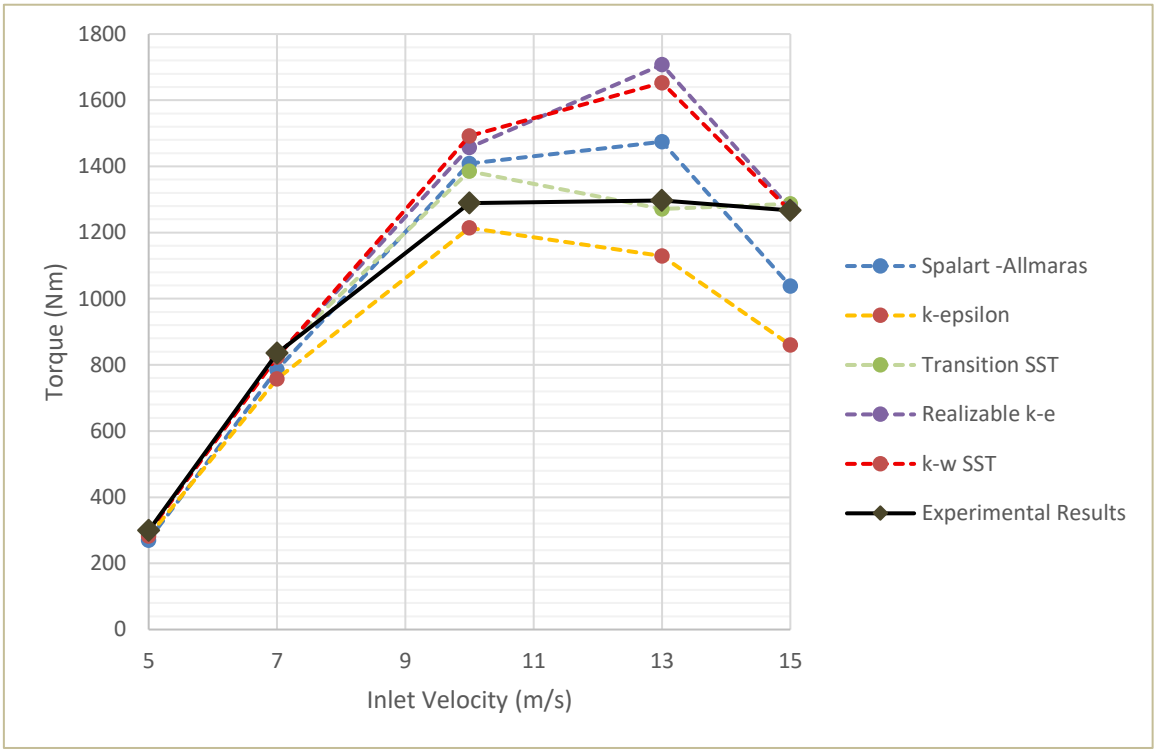

Figure 4.4: A comparison between the experimental torque data and different numerical turbulence models

The turbulence models used in these simulations show good agreement with the experimental data. However, the realizable k-Ɛ model is greatly disparate from the experimental results when the inlet speed is set at 13 m/s. The results are similar to the ones obtained when the k-ω SST method was used. The inaccuracies at higher wind speed are indicative that the steady state simulations do not accurately capture the effects of flow perturbations (like vortex shedding) effectively. The k-Ɛ model proved to be a useful mathematical scheme for modelling the turbulence, although it generally underpredicted the aerodynamic performance of the turbine across the different wind speeds.

The Spalart-Allmaras model produced a reasonable prediction of the flow problem, without being as accurate as some of the other models (particularly at the wind speeds of 5, 7 and

15m/s) which were used for simulations. The Transition SST model demonstrated to be the most useful algorithm for modelling turbulence in the flow field as the most accurate results were produced when these models were used for the steady state cases on average. (Other CFD approaches may have yielded similar or even better results, but they were not considered within this context due to time constraints). Figure 4.5 presents the coefficient of power for the NREL Phase VI for steady state simulations juxtaposed against experimental data.

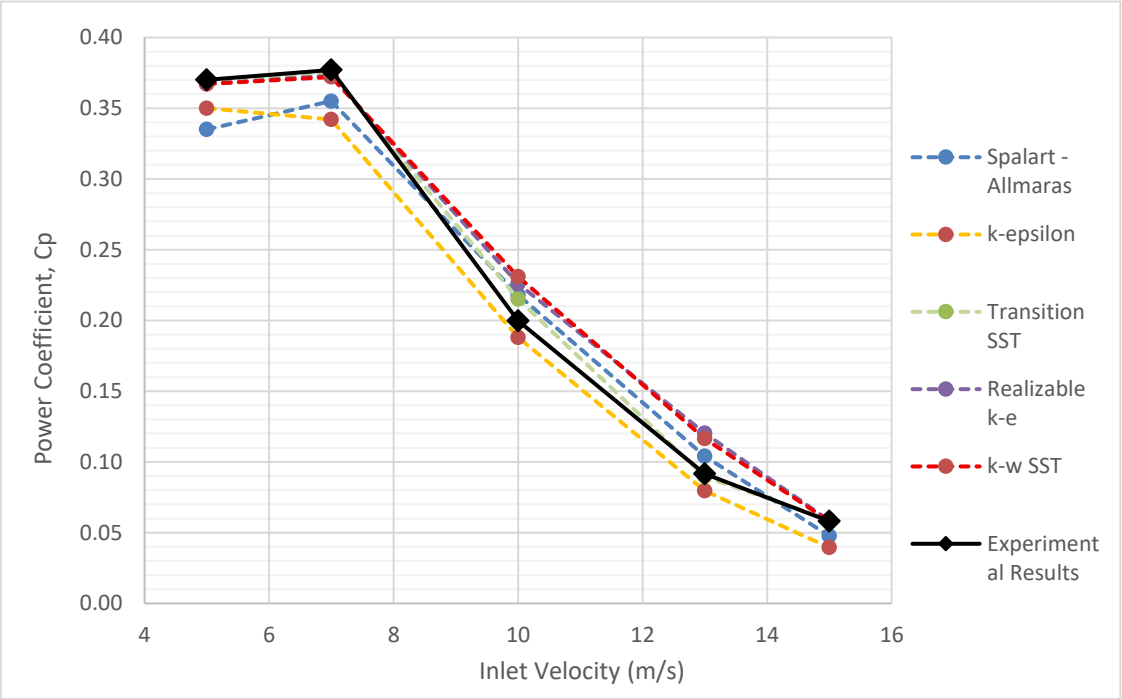

Figure 4.5: Power coefficient of NREL Phase VI (steady state simulations) across different wind speeds against experimental data

The graph above illustrates how power efficiency decreases with an increase in wind velocity. Blade efficiency tends to be at its highest point when it is between 5-7 ms^{-1} and in a steady state, whilst there is a precipitous decline in efficiency as the inlet velocity increases. The Transition SST tracks well with the experimental data due to the fact that is able to predict boundary layer transitions better than the other algorithms. The K-Ɛ and Spalart-Allmaras are the most incongruous at the lower velocities because of their proclivity to overestimate eddy viscosity near the blade surface which impacts the prediction of lift. K-ω SST and realizable k-Ɛ generally overpredicts the aerodynamic performance of the NREL Phase VI at the higher velocities. In summary, the numerical algorithms used are relatively accurate estimating the power efficiency of the turbine.

Figure 4.6 illustrates the power generated by the NREL Phase VI turbine across different wind speeds.

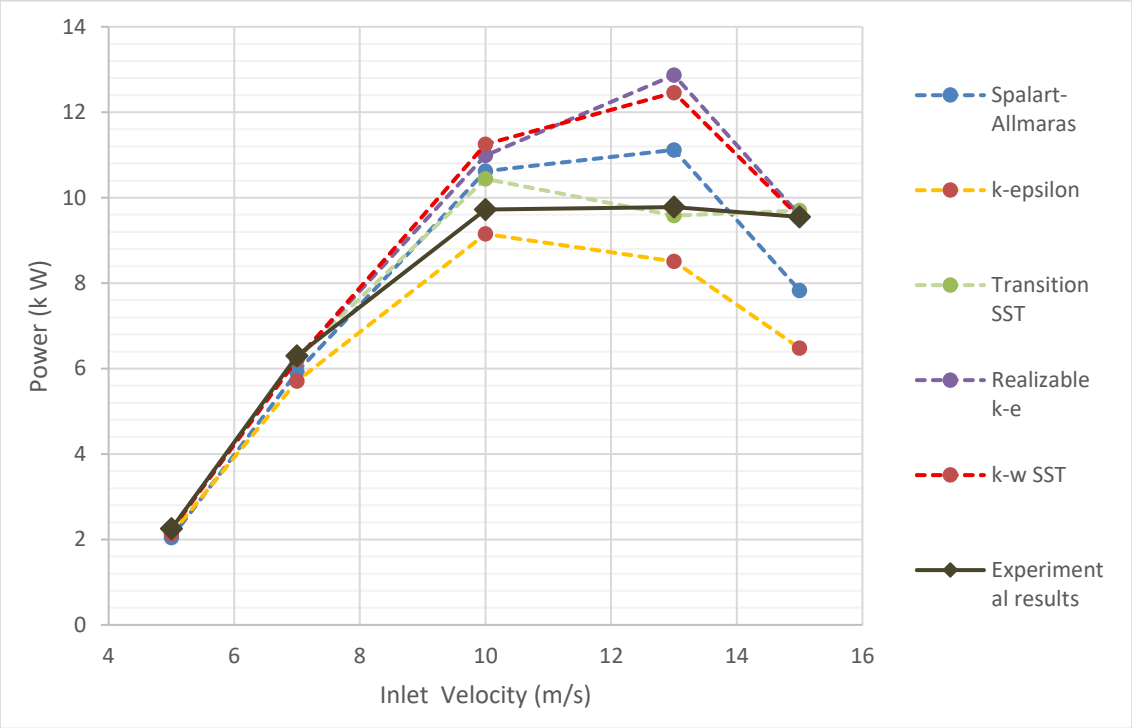

Figure 4.6: Power generated by the NREL Phase VI turbine across different wind speeds (steady state)

From the graph, it can be seen that greater power is generated at the higher wind speeds (10 m/s – 15m/s). At the lower TSRs between (2.53 -3.79) and the NREL Phase VI is able to produce its highest power output according to steady-state simulations. Although, the turbine is less efficient at the higher wind speeds, there is a much greater amount of energy available as per the cubic wind speed law. This means that even though the efficiency is greater at lower speeds the power output is maximized at the higher wind speeds.

4.3.2 Velocity Profile

The velocity readings at different spanwise positions gives an indication of the local inflow conditions which the blade experiences. At the higher wind speeds the blade assumes higher AOAs which can sometimes lead to dynamic stall, examining the behaviour of the flow allows the researcher to understand the flow physics around the blade under different inlet conditions. Figures 4.7 to Figure 4.11 show the velocity profile in boundary region of the blade.

5 m/s λ = 7.58

Figure 4.7 shows the variation in velocity magnitudes at different radial positions, illustrating the flow pattern across the blade. Several vortex structures are generated at the root of the blade r/R= 0.3 which increases radially outward at a higher velocity. The velocity contours are tighter in the mid-span indicating stronger and more immediate blade loading. Stagnation points form at the leading edge, whilst a low-velocity wake develops downstream of the trailing edge. This phenomenon is more pronounced at r/R = 0.95 due to the greater tangential speed.

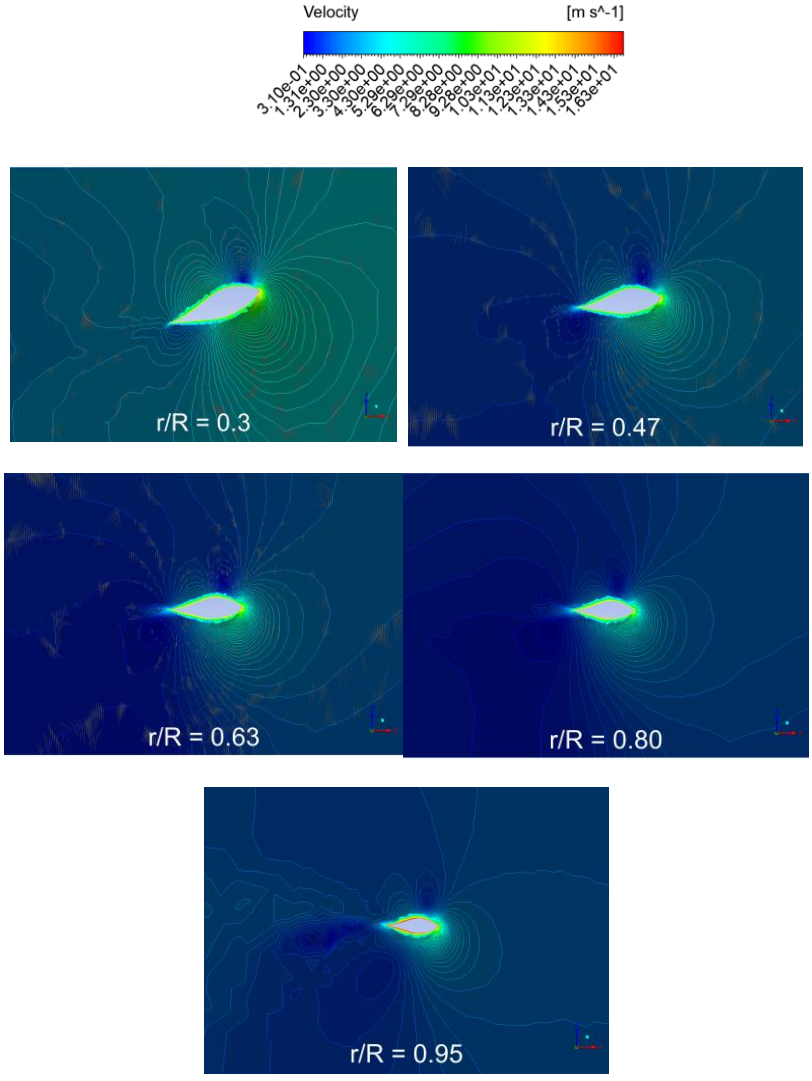

Figure 4.7: Velocity magnitude contours at various spanwise locations for λ = 7.58

7 m/s λ = 5.42

Figure 4.8 shows that the velocity magnitude increases outward radially (from r/R = 0.3 to r/R=0.95) which is expected for a rotating turbine due to the increase in tangential velocity. Towards the outer span, the tip vortices grow in strength and definition, accompanied with an expansion of the wake region downstream from the trailing edge.

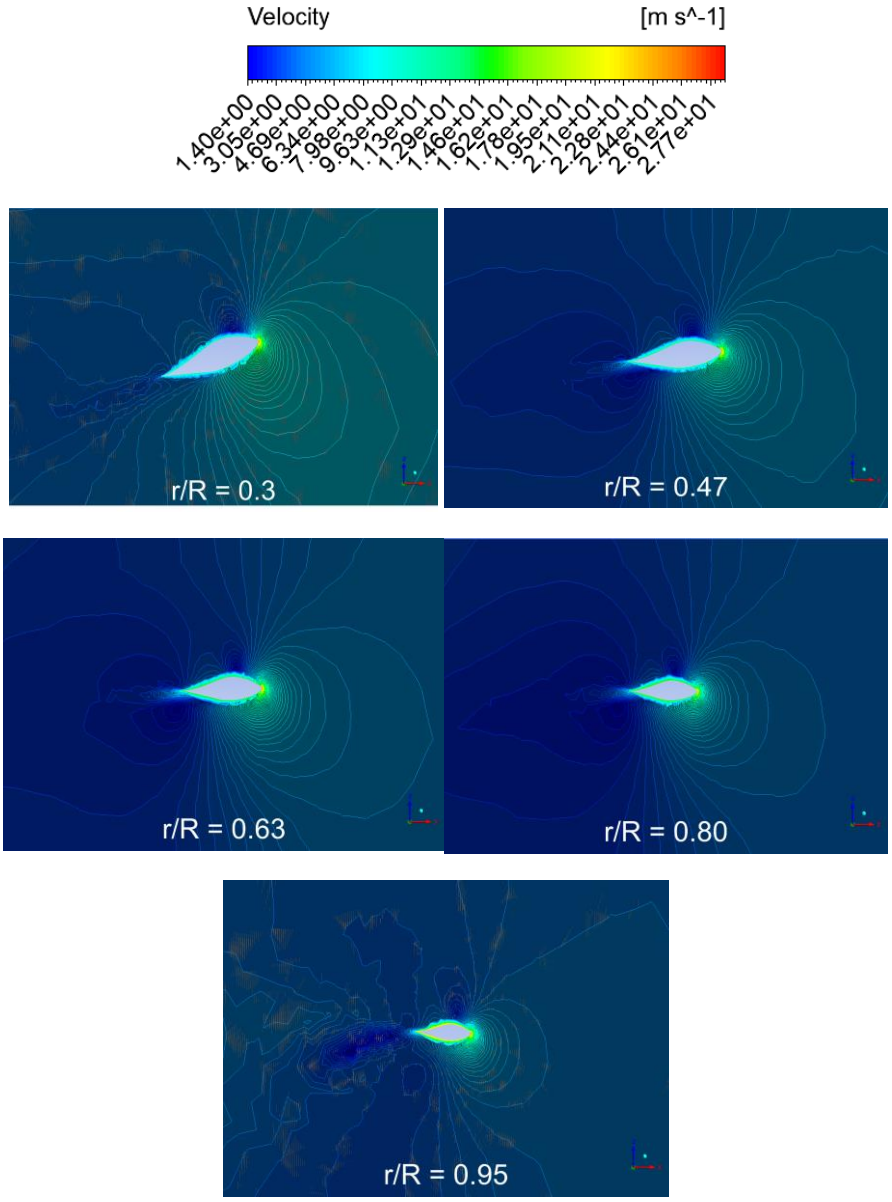

Figure 4.8: Velocity magnitude contours at various spanwise locations for λ = 5.42

10 m/s λ = 3.79

Figure 4.9 shows the rising velocity across the blade from the root to the tip(r/R=0.30 to r/R=0.95). The near-wall velocity gradient increases, and the higher AOA facilitates greater torque production. However, at the root, the blade is in deep stall and flow separation is evident in this region which is shown by strong wake formation. The stagnation pressure increases near the leading edge; followed by flow acceleration along the blade surface towards the trailing edge.

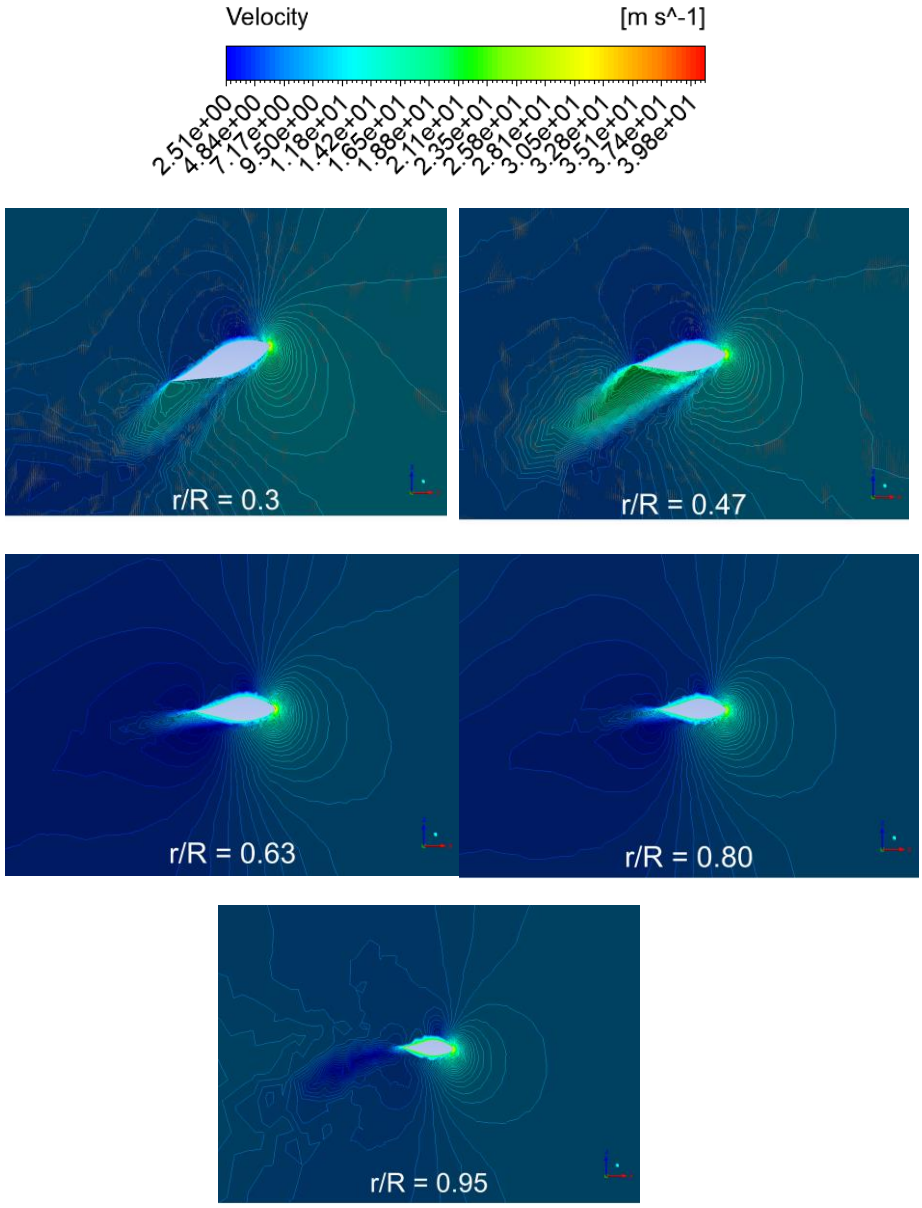

Figure 4.9: Velocity magnitude contours at different spanwise locations for λ = 3.79

13 m/s λ = 2.92

Figure 4.10 shows a moderate acceleration over the blade with a low velocity wake downstream. At the mid-span, greater acceleration over the blade is observed, with increasingly unsteady 3D behaviour. Nearer the tip at (r/R=0.80) and (r/R =0.95) a stagnation region forms at the leading edge, and larger tip vortices develop in this region, resulting in an expanded wake downstream.

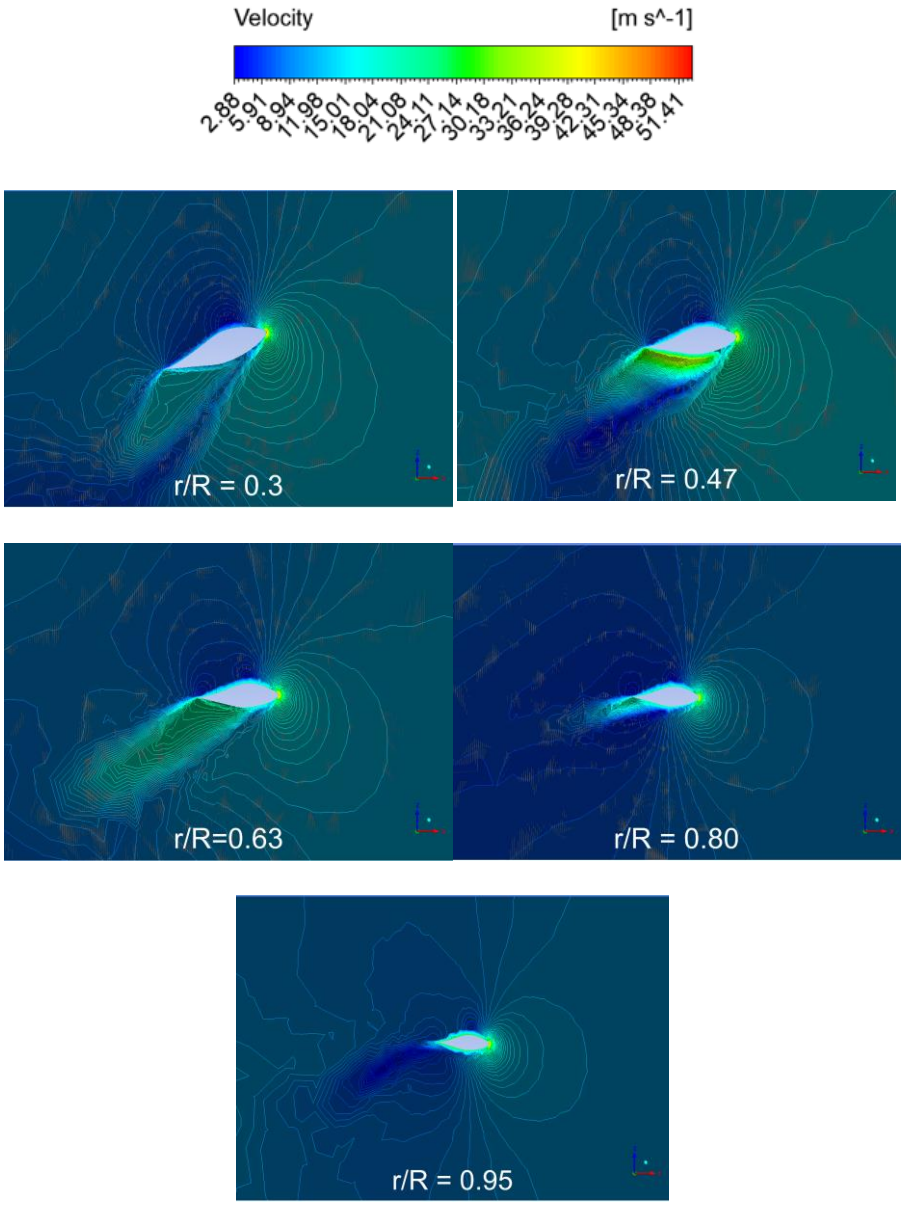

Figure 4.10: Velocity magnitude contours at different spanwise locations for λ = 2.92

15 m/s λ=2.53

Figure 4.11 illustrates the stronger near-wall velocity gradients. The acceleration at the root section (r/R =0.30) is less due to a lower tangential velocity. At the mid-span (r/R =0.47-0.63) a higher AOA leads to less effective conversion of energy. The strong wake patterns in this region occur due to large flow separation. Closer to the tip, the tangential velocity is at its highest, and the wake in the tip region has become more pronounced.

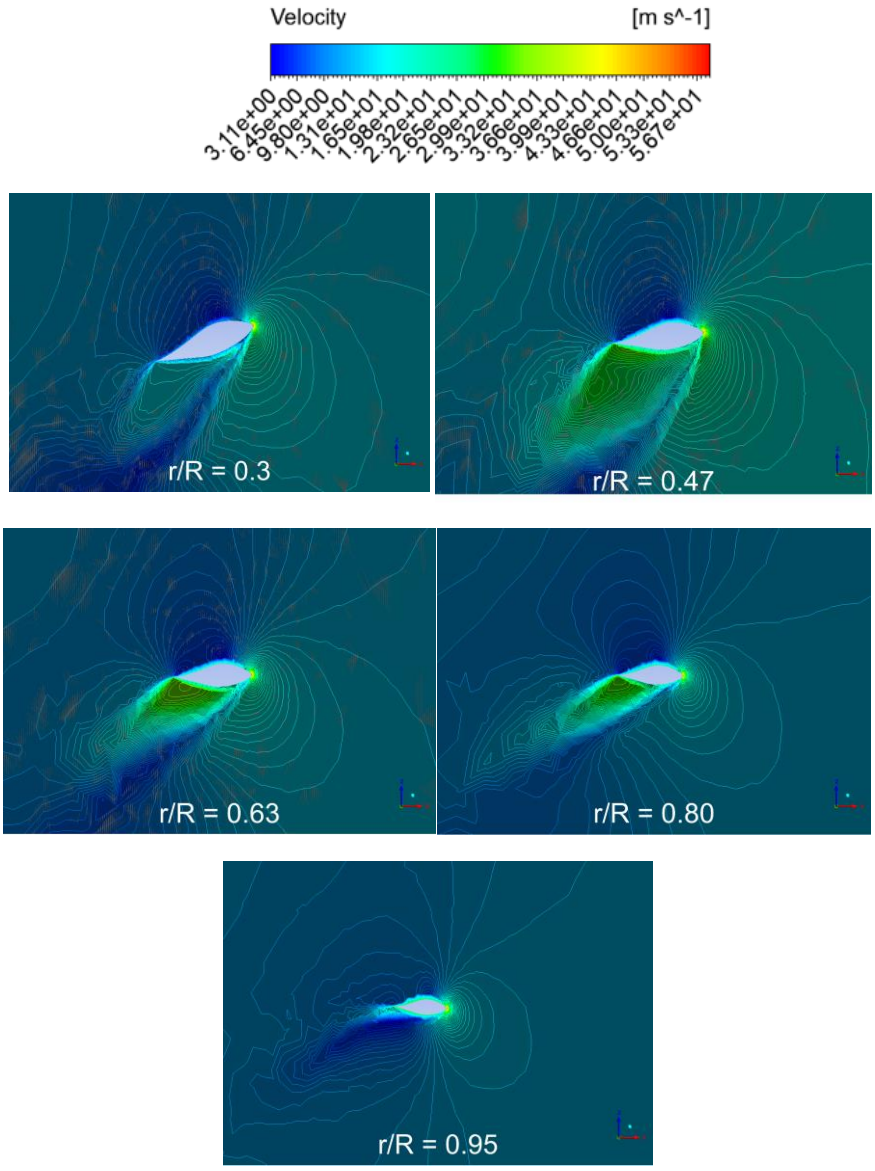

Figure 4.11: The velocity over the turbine blade at different spanwise locations for λ = 2.53

4.3.3 Surface Streamlines

Figure 4.12 displays the spanwise flow patterns inlet velocities from u =7 m/s to u =15 m/s. The surface streamlines indicate the wall shear where the flow interacts with the turbine blade. At 7 m/s it can be seen the flow is attached to the blade with mild curvature (near the root). At 10 m/s the effects of root separation can be seen more visibly on the blade and the 3D effects are adequately visualized. At 13 m/s, the variegated contours indicate a strong velocity gradient in which the crossflow fluctuations can be seen clearly. At 15 m/s the 3D effects are more robust, there is significant spanwise flow which covers most of the blade accompanied with root separation.

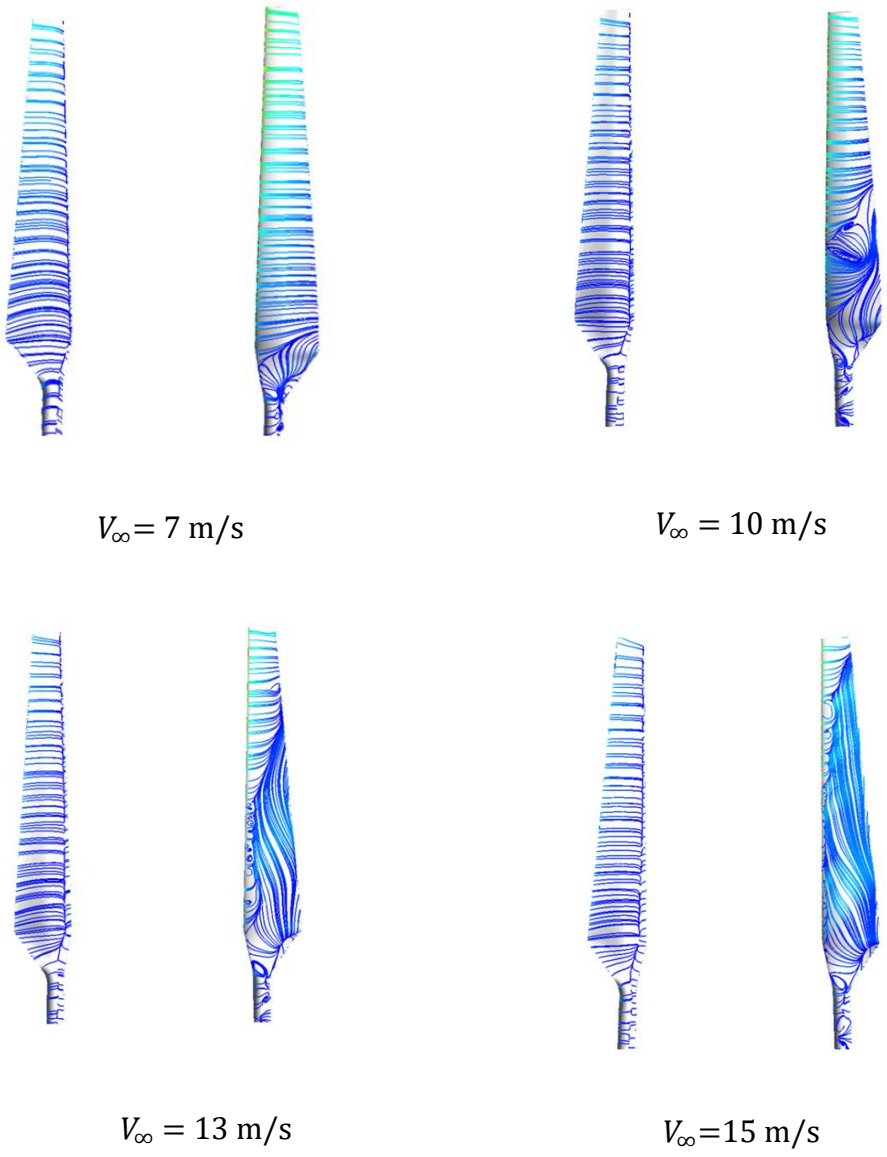

Figure 4.12: Surface streamlines on the turbine blade on the pressure side (left) and suction side (right) when U= 7 m/s to U = 15 m/s

4.4 Unsteady Simulations

It is important to consider the real-life operating conditions under which HAWTs function, especially the fluctuations and turbulence that the turbine blades experience. Capturing the unsteady effects of the wind enables an accurate prediction of the aerodynamic performance of the turbine. To accomplish this, a time step is introduced to the governing equations in order to represent the vicissitudes of airflow mathematically. The time step can be defined as the increment of time over which the solver advances a simulation. A smaller time step may produce more accurate results but typically requires greater computational effort and time. On the other hand, if the time step is made too large the solution produced may lack precision. The discrete time step is usually determined based on the angle of rotation. Alipour's numerical study (132) investigating the power efficiency of a proposed Savonius turbine found that there was no difference between the outcome when the degree of rotation was set between 0.5 and 1.5. Aljuhashy (70) demonstrated in his research that accurate results could be produced when the degree of rotation was either set at 0.5 or 1.0. For the simulation setup the degree of rotation was set at 1.0 and 20 iterations per time step was chosen with a time step size of 0.002s.

The unsteady simulations were completed using the University of Sheffield's High-Performance Computer (HPC) system which provides the computational capacity required to resolve the unsteady simulations. Stanage is the University of Sheffield's HPC cluster which has a greater number of cores available and was used to perform the unsteady simulations. The scaled residuals converged at 10^{-5} which means that an accurate solution was reached. For turbulence modelling, the LES method was introduced, and the WALE model was used for resolving the subgrid scale because of its effectiveness in predictive near wall behaviour and separation than other numerical models. The bounded central differencing method was used when solving the momentum equations to produce an accurate and physically stable solution. The second order implicit transient formulation was used for both the LES and URANS simulations to improve temporal accuracy, and to capture unsteady flow structures.

4.4.1 Power and Torque

Figure 4.13 compares the CFD torque prediction under steady and unsteady conditions. At the lower velocities. The results show that both solvers are capable of predicting the torque output with a high amount of accuracy. However, as the flow becomes more turbulent and the blade begins to experience dynamic stall the flow starts to detach from the blade surface. This phenomenon reduces the amount of energy converted to mechanical power.

The CFD solver's failure to account for this sufficiently is probably the reason why the discrepancy between the simulated power at 10 m/s and 13 m/s is relatively large.

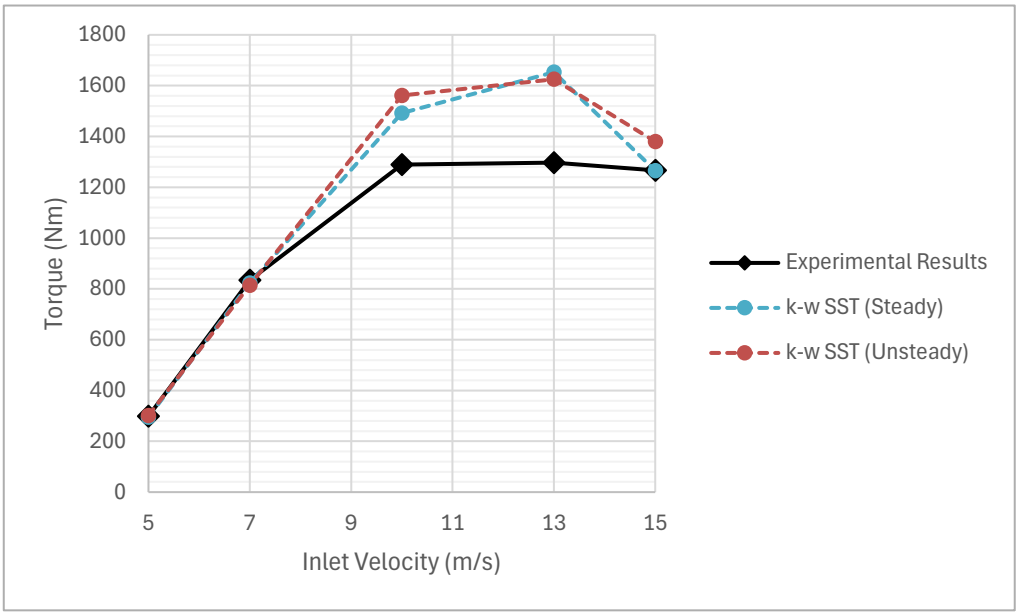

Figure 4.13: Comparison between the torque output of the NREL Phase VI under different conditions

Table 4.3 shows the unsteady state simulations when compared with the experimental data.

Table 4.3: The torque generated by CFD solver in comparison to experimental data (unsteady state)

Wind Speed	CFD Simulation (Unsteady) Torque (Nm)	Experimental Torque (Nm)	Percentage Difference
5 m/s	301.79	299	0.93%
7 m/s	814.32	835	2.48%
10 m/s	1561.35	1289	21.12%
13 m/s	1625.07	1297	25.29%
15 m/s	1379.62	1267	8.89%

The Transition SST and K-Ɛ algorithm was found to be unsuitable for the present unsteady simulation, as they failed to provide stable and accurate predictions. Other turbulence models were used to simulate the NREL Phase VI performance in unsteady wind to see

whether they would yield more accurate results such as the LES and realizable k-Ɛ. Figures 4.14 and 4.15 displays the torque and power generated by the NREL Phase VI in unsteady conditions using several turbulence models. Figure 4.16 shows the power efficiency for unsteady simulations.

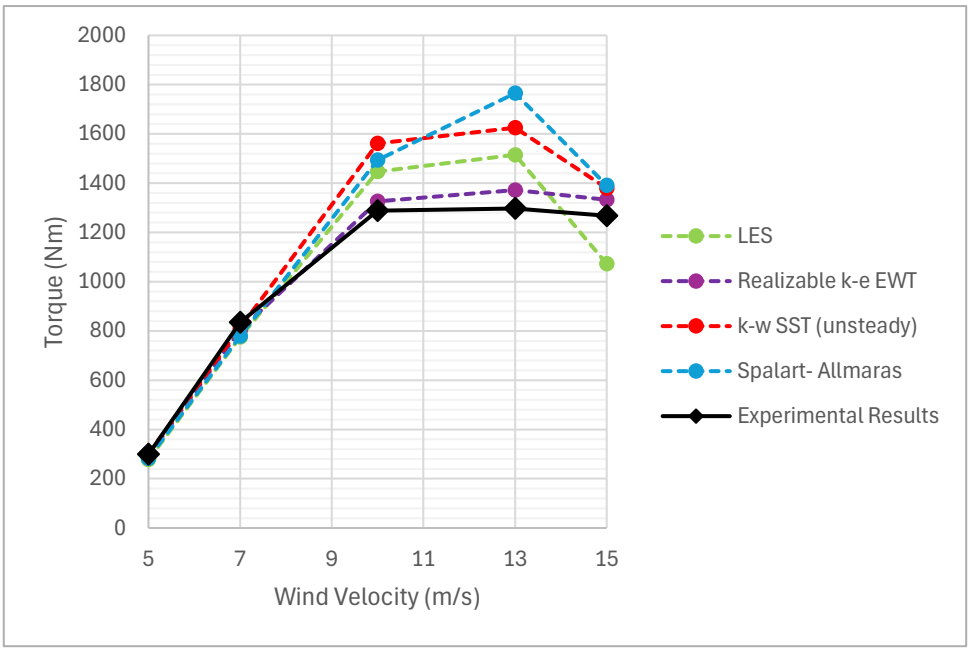

Figure 4.14: Torque predictions using different numerical algorithms for the unsteady state simulations

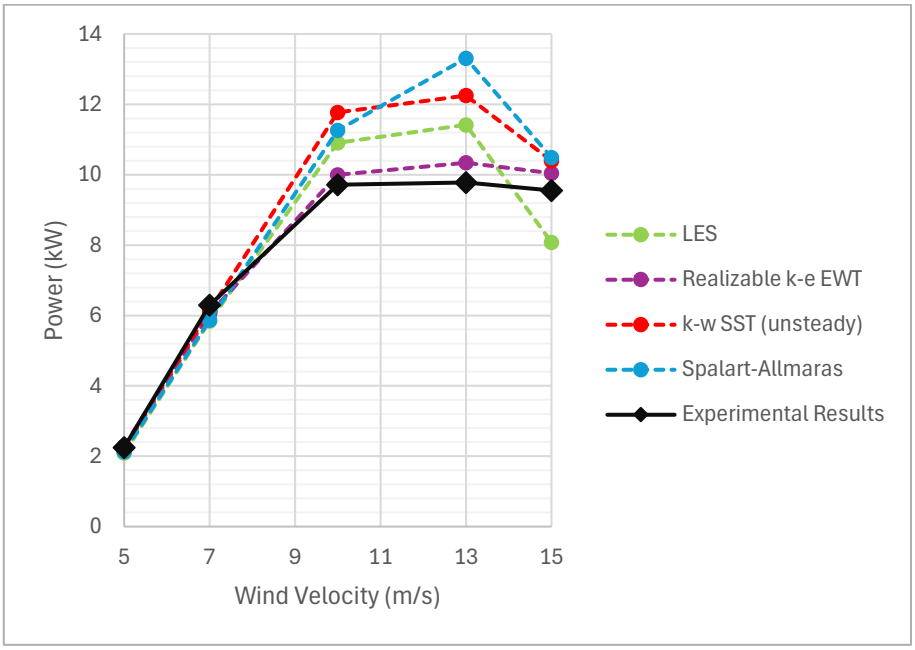

Figure 4.15: Power prediction of the NREL Phase VI under unsteady conditions

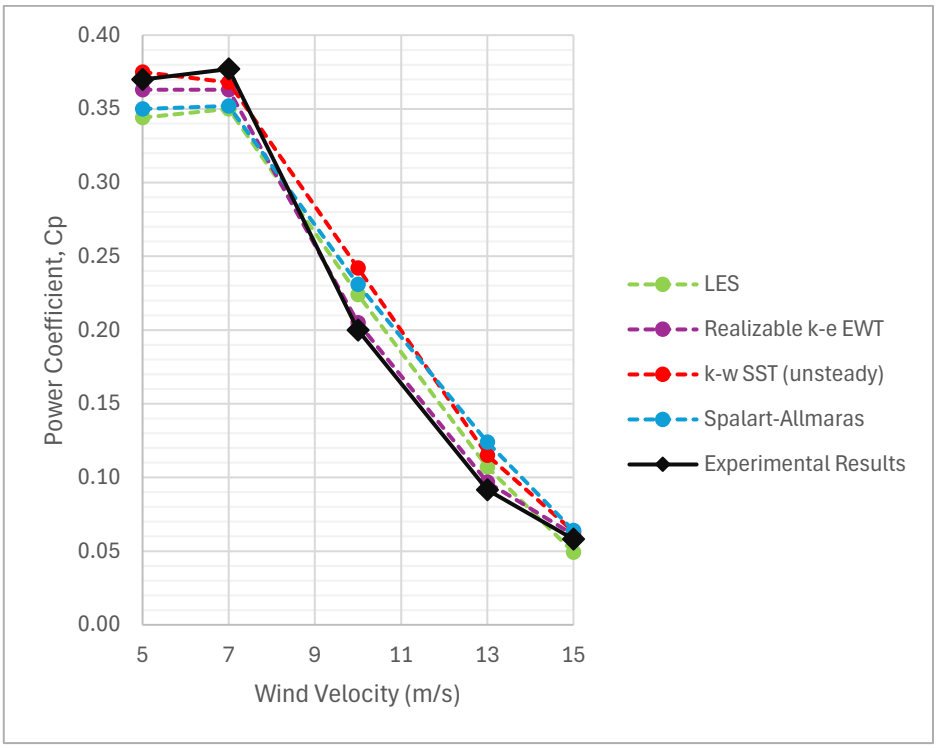

Figure 4.16: Coefficient of power for unsteady state simulations

Figure 4.17 compares the numerical results produced in this study to other notable CFD studies.

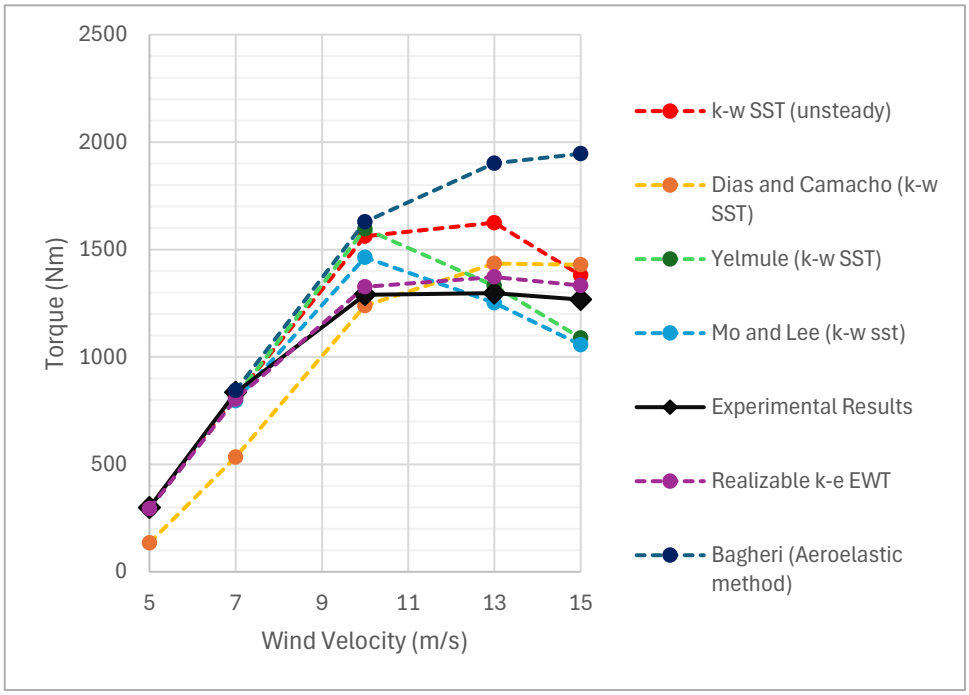

Figure 4.17: Comparison of torque prediction within present study with other notable CFD studies for the NREL Phase VI

The solution presented within this work is shown to be accurate especially when compared to studies such as Dias and Camacho (131), Yelmule and Anjuri (133), Mo and Lee (134) and Bagheri and Nejat (135). The K –ω SST shows a high degree of accuracy in the non-stall conditions, however, when dynamic stall ensues there is a slight overprediction of torque at 10 ms^{-1}, which increases at 13 ms^{-1} and then closely aligns with the experimental results at 15 ms^{-1}. CFD methods exhibit a proclivity to overpredict the torque generated in dynamic stall. The other numerical studies exemplify the same trend with their overestimation at 10 ms^{-1}.

4.4.2 Measurements of Static Pressure and Pressure Coefficient

The static pressure describes the thermodynamic pressure of the fluid at the blade's surface. It is an important parameter to consider as it gives insight into the aerodynamic loading on the blade and the energy that can potentially be harnessed by the blade. A larger pressure differential across the blade generates greater lift force, enabling more energy extraction from the wind. The static pressure referenced in the following figures is measured relative to the atmospheric pressure which is set at 101325 Pa. The positive values indicate a higher value than the ambient pressure and the negative values represent a lower value.

The pressure coefficient, C_p, is a nondimensional parameter of interest because it informs the researcher of how the flow is behaving at the surface boundary. It normalizes the pressure acting on the turbine blade and measures it relative to freestream dynamic pressure. A negative pressure coefficient on the suction side, combined with positive pressure on the pressure side, creates the pressure differential that generates lift.

$$C_p = \frac{p - p_\infty}{\frac{1}{2}\rho {V_\infty}^2}$$

Equation 4.1

The local pressure is defined as p, the freestream pressure is p_∞, and the V_∞ is the freestream velocity.

5 m/s

On the pressure side, the upper part of the blade experiences higher pressure, especially at the leading edge of the blade. The pressure decreases towards the trailing edge

evidenced by yellow and green contouring. The pressure contours are smooth and continuous which indicates even aerodynamic loading, and the flow is attached to the turbine blade which allows for efficient conversion of wind energy. At the suction side the green contouring in the upper section represents a low-pressure zone. The pressure distribution ranges from slightly over 800 Pa to -1900 Pa. Figure 4.18 illustrates the pressure distribution across the turbine blade when the freestream velocity is at 5 m/s.

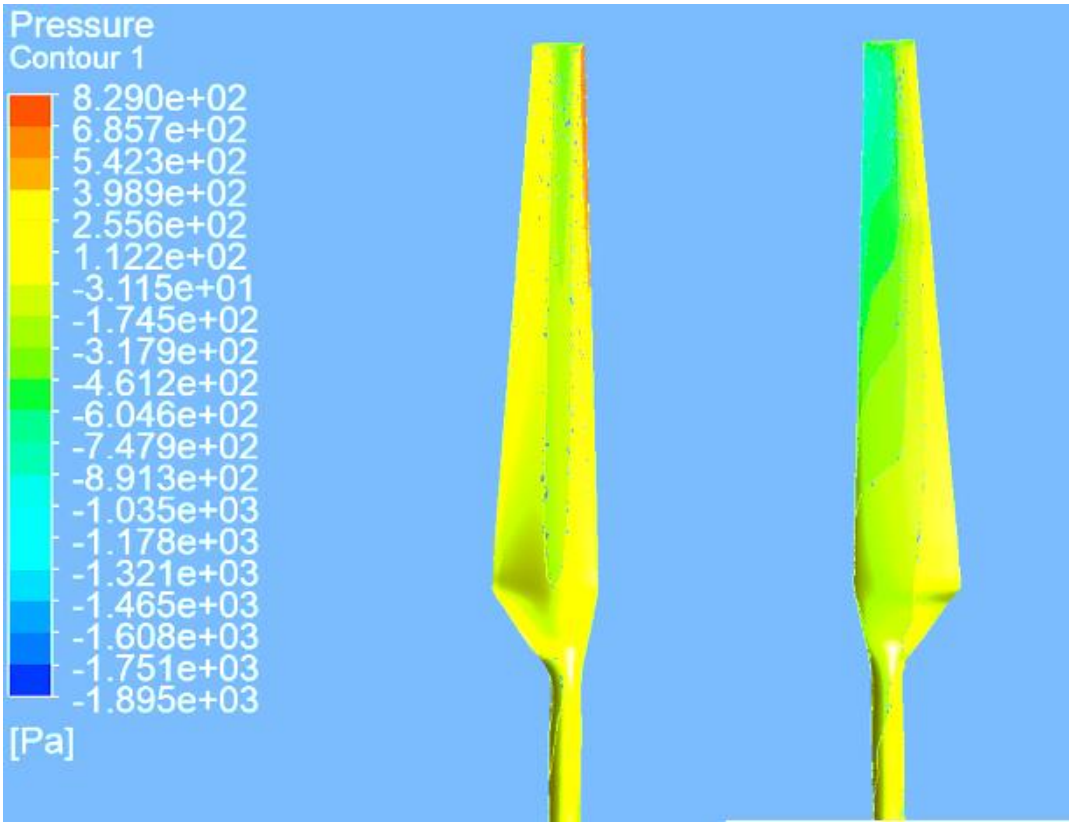

Figure 4.18: Surface static pressure at freestream velocity (V_∞ = 5m/s)

Figure 4.19 displays the pressure coefficient across the blade chord and compares the experimental data with CFD results. The graph plots C_p against the abscissa, x/c, at different radial positions across the blade. The CFD results show good accuracy nearer to the root of the blade. At the mid-span (r/R = 0.47 - 0.63) the $k-\omega\ SST$ turbulence model underestimates suction this is likely due to 3D effects such as tangential velocity and radial flows which are not fully captured by the RANS solver. At the tip, the experimental results indicate a lower negative pressure coefficient, and this aligns with the simulation results produced by CFD. The pressure coefficient exhibits a sharp decrease (higher negative values) on the suction side closer to the leading edge of the blade, followed by a steep

pressure recovery towards the trailing edge of the blade. In summary, the CFD results can accurately predict the pressure coefficient across the spanwise stations of the blade.

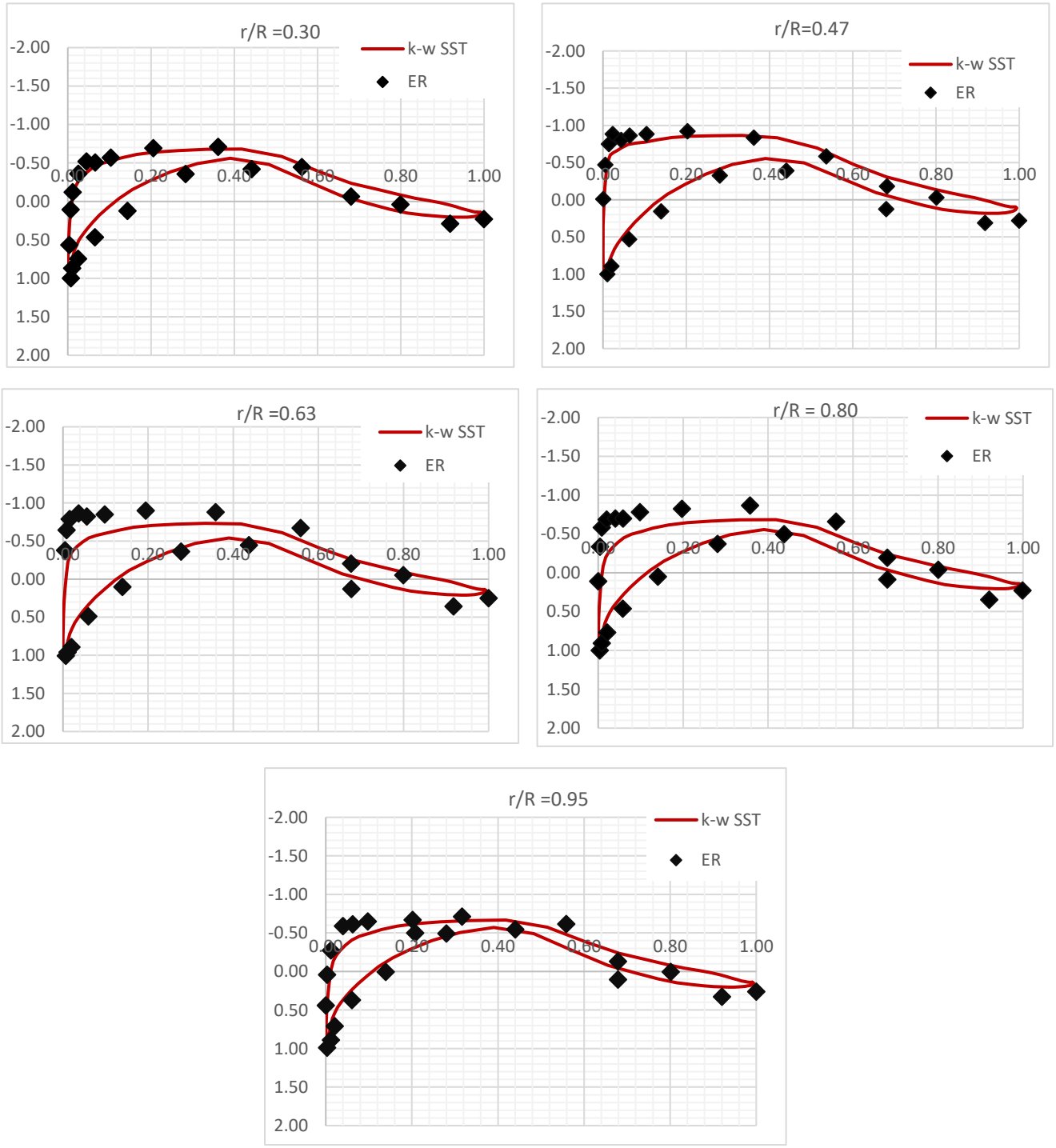

Figure 4.19: Pressure coefficient comparison at spanwise locations for wind speed = 5 m/s

7 m/s

There is a greater concentration of red contouring at the leading edge of the blade (pressure side). The red streaks are due to a strong build-up of pressure due to faster incoming flow. The pressure decreases across the chord which is indicated by the heavy yellow contouring in the midsection of the radial chord. On the suction side, the pressure transition from green to yellow once again, which implies a lower pressure zone. Figure 4.20 displays the pressure distribution at the freestream velocity (V_∞ = 7 m/s).

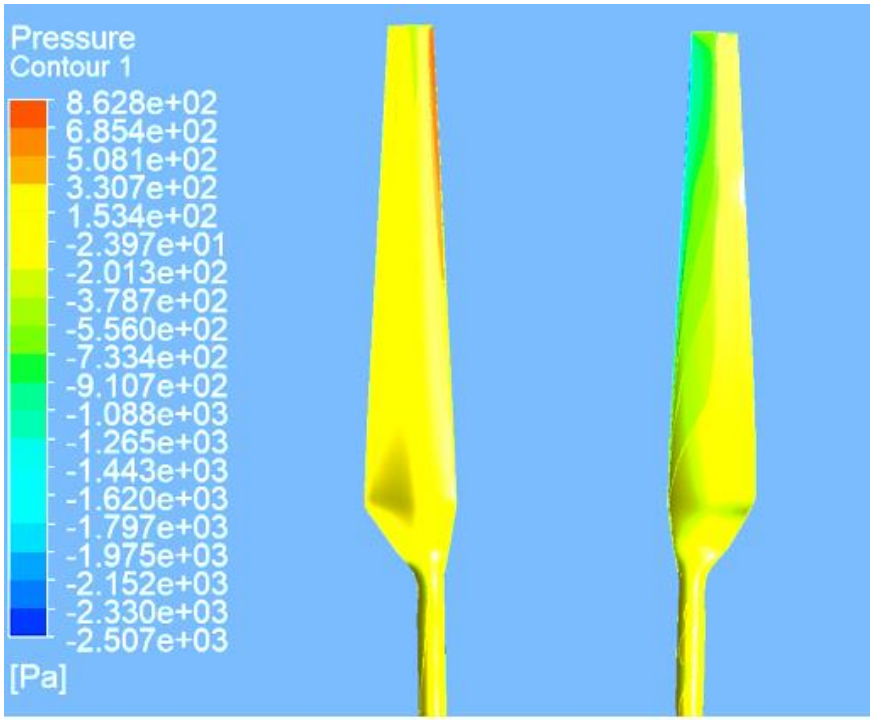

Figure 4.20: Surface static pressure at freestream velocity (V_∞ = 7 m/s)

Figure 4.21 measures the pressure coefficient against the chordwise position for a freestream velocity of 7 m/s. At the r/R = 0.30 location there is a higher suction pressure indicating that a greater amount of power is generated there. The turbine blade has a greater AOA at the root which enables it to harness greater amounts of energy. The suction pressure coefficient becomes less negative nearer to the tip, and less power is produced at r/R = 0.95. The CFD results are accurate, however, the simulation results predict a larger pressure differential at the leading edge consistently. The discrepancy between the computational results and the experimental data is likely due to the flow separation that takes place at the leading edge of the blade.

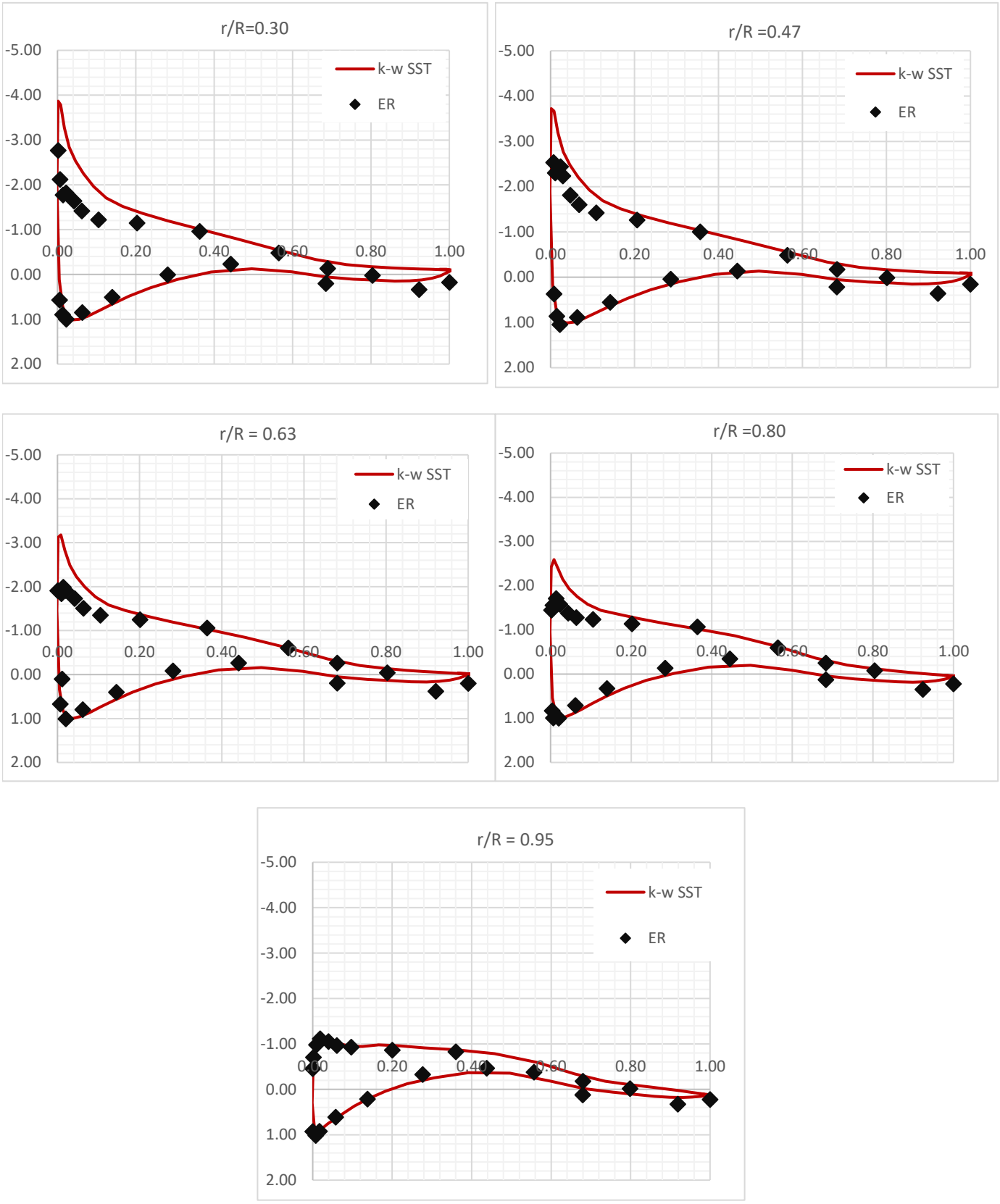

Figure 4.21: Pressure coefficient comparison at spanwise locations for wind speed = 7 m/s

10 m/s

The pressure side of the blade is covered in orange with red streaks at the leading edge which illustrates high static pressure along the blade chord. This means that there is a deceleration in the flow velocity over the blade. The pressure differential across the blade from orange to green (suction side) is in marked contrast to the pattern seen at the lower velocities. A stronger adverse pressure differential shows that flow separation is likely to occur at this point. Figure 4.22 displays the pressure distribution across the blade when the freestream velocity (V_∞= 10 m/s).

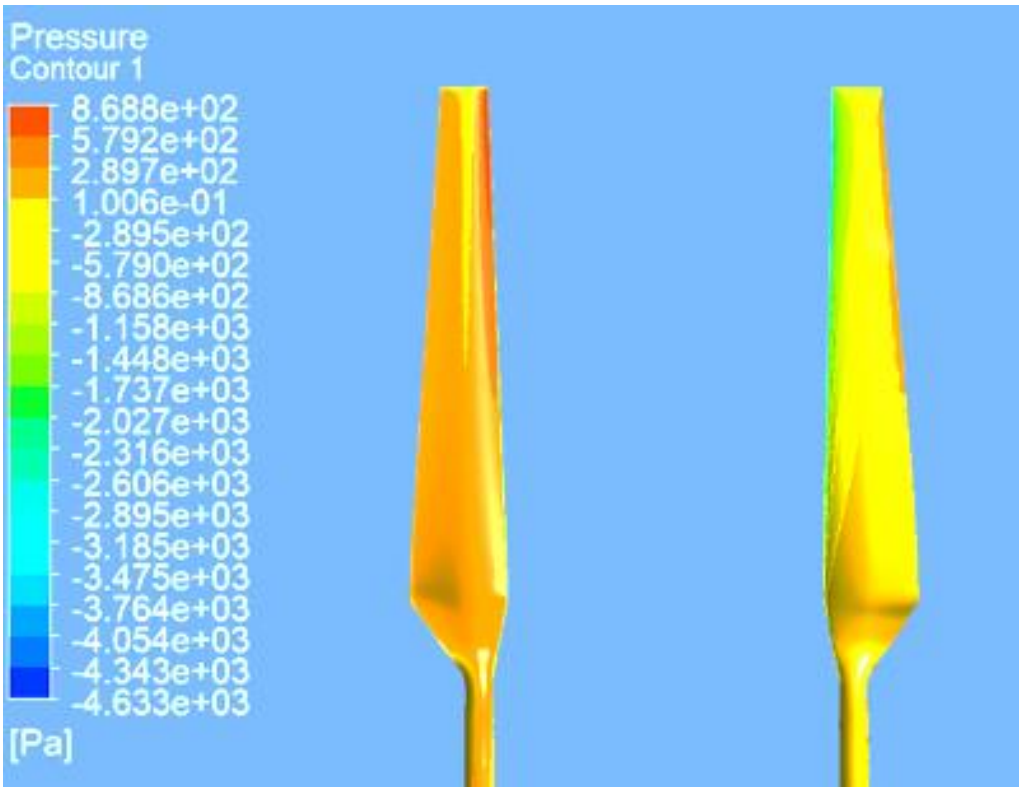

Figure 4.22: Surface static pressure at freestream velocity (V_∞ = 10 m/s)

Figure 4.23 shows the pressure coefficient comparison for the 10 m/s flow case where the turbine blade is in dynamic stall. The computational results are largely congruent with the experimental data. Flow separation takes place at the leading edge where there is a slight overprediction of the magnitude of the suction pressure at r/R =0.47 and r/R =0.95. As the flow becomes more turbulent the probability of misprediction increases as the flow behaves in ways that is difficult for the CFD solver to predict.

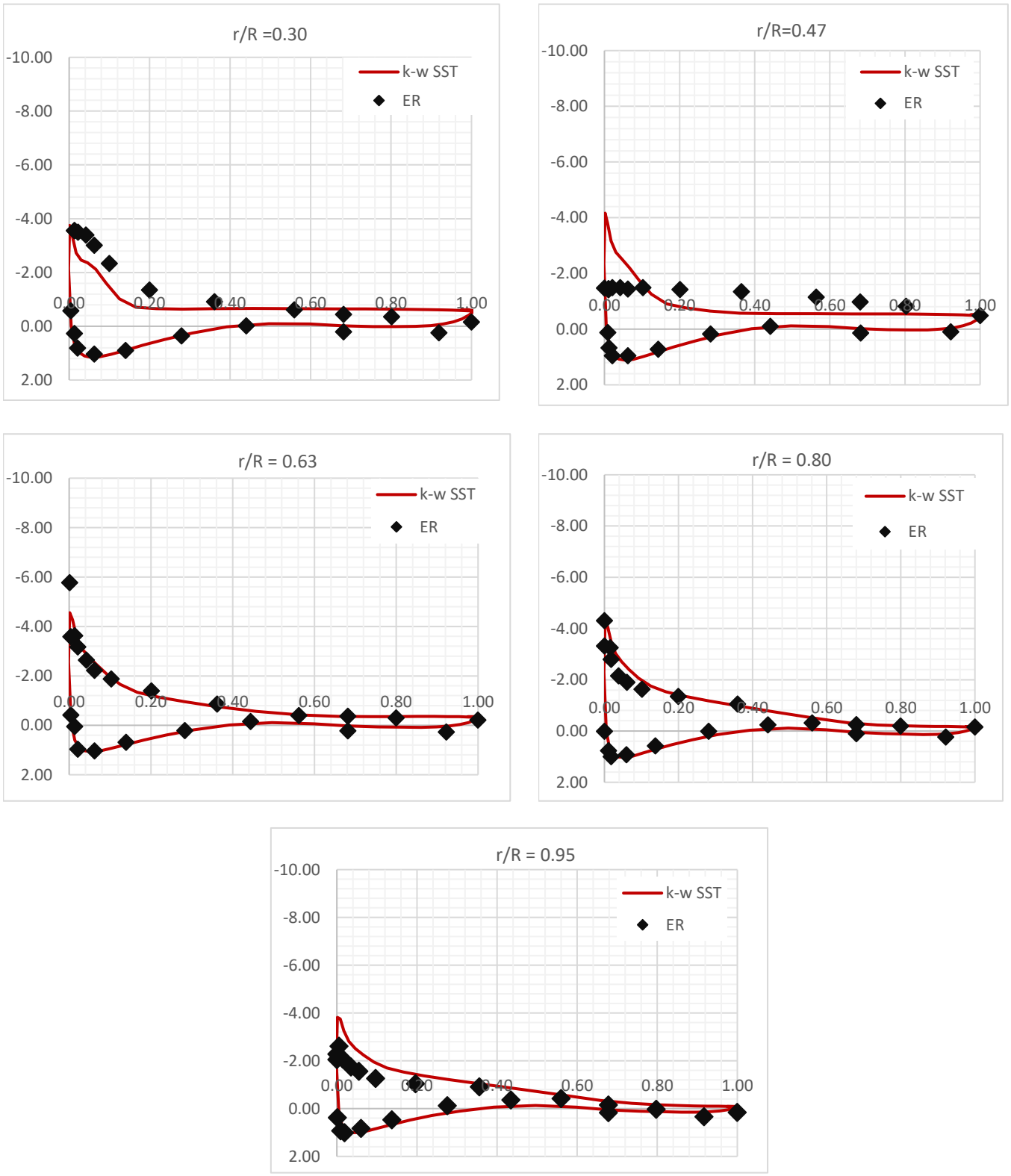

Figure 4.23: Pressure coefficient comparison at spanwise locations for wind speed = 10 m/s

13 m/s

The entire blade is covered in orange and dark red streaks indicating higher pressure, particularly at the leading and trailing edge of the blade. The flow has stalled at this point, creating stagnation points at the edge of blade. On the suction side, an adverse pressure gradient has formed which suggests flow separation has occurred at this point. Figure 4.24 illustrates the pressure contours when the freestream velocity is at 13 m/s.

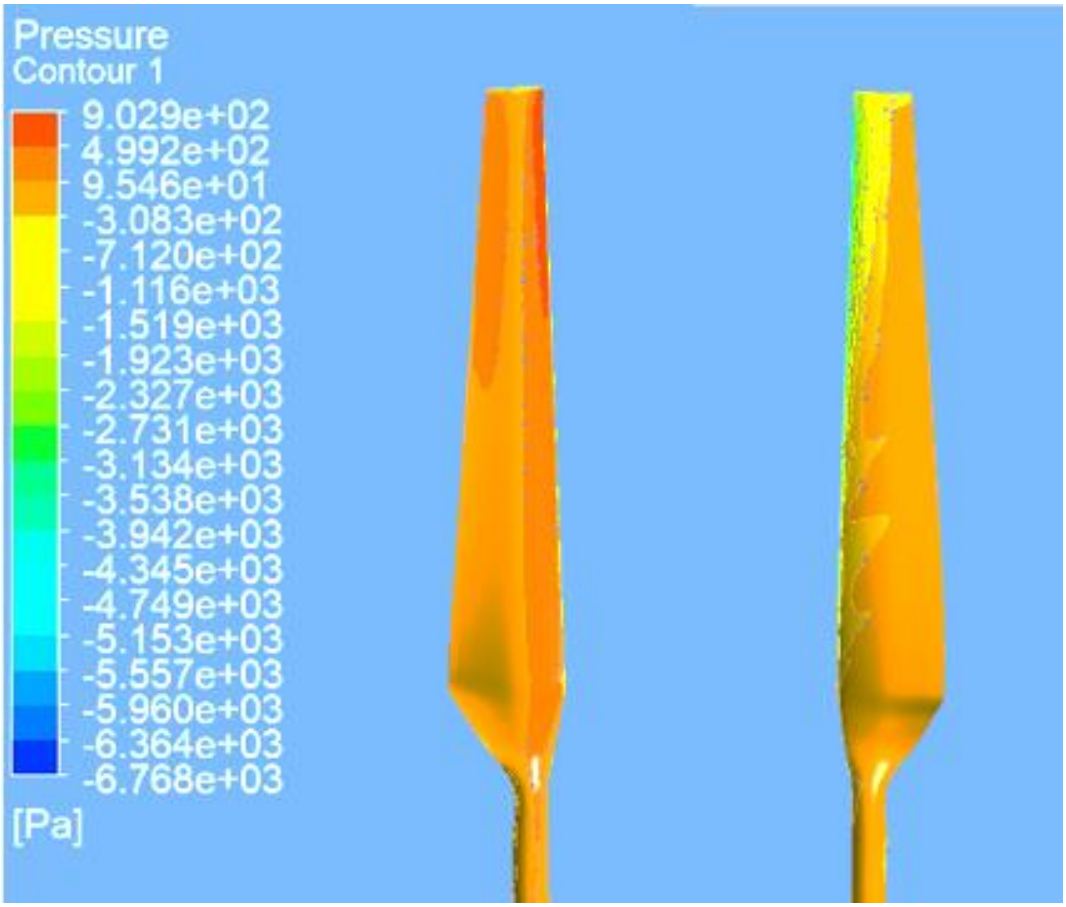

Figure 4.24: Surface static pressure at freestream velocity (V_∞ = 13 m/s)

Figure 4.25 compares the pressure coefficient at 13m/s at which point large flow separation begins to occur. At the root there is a large discrepancy between the computed results and the experimental data. The underprediction of the negative suction pressure at r/R = 0.30 and r/R =0.80 and the overprediction at the leading edge of the suction side at r/R = 0.63 and r/R is evidence of uneven blade loading and flow topology. For this case, the blade has stalled and flow separation has taken place across most of the blade.

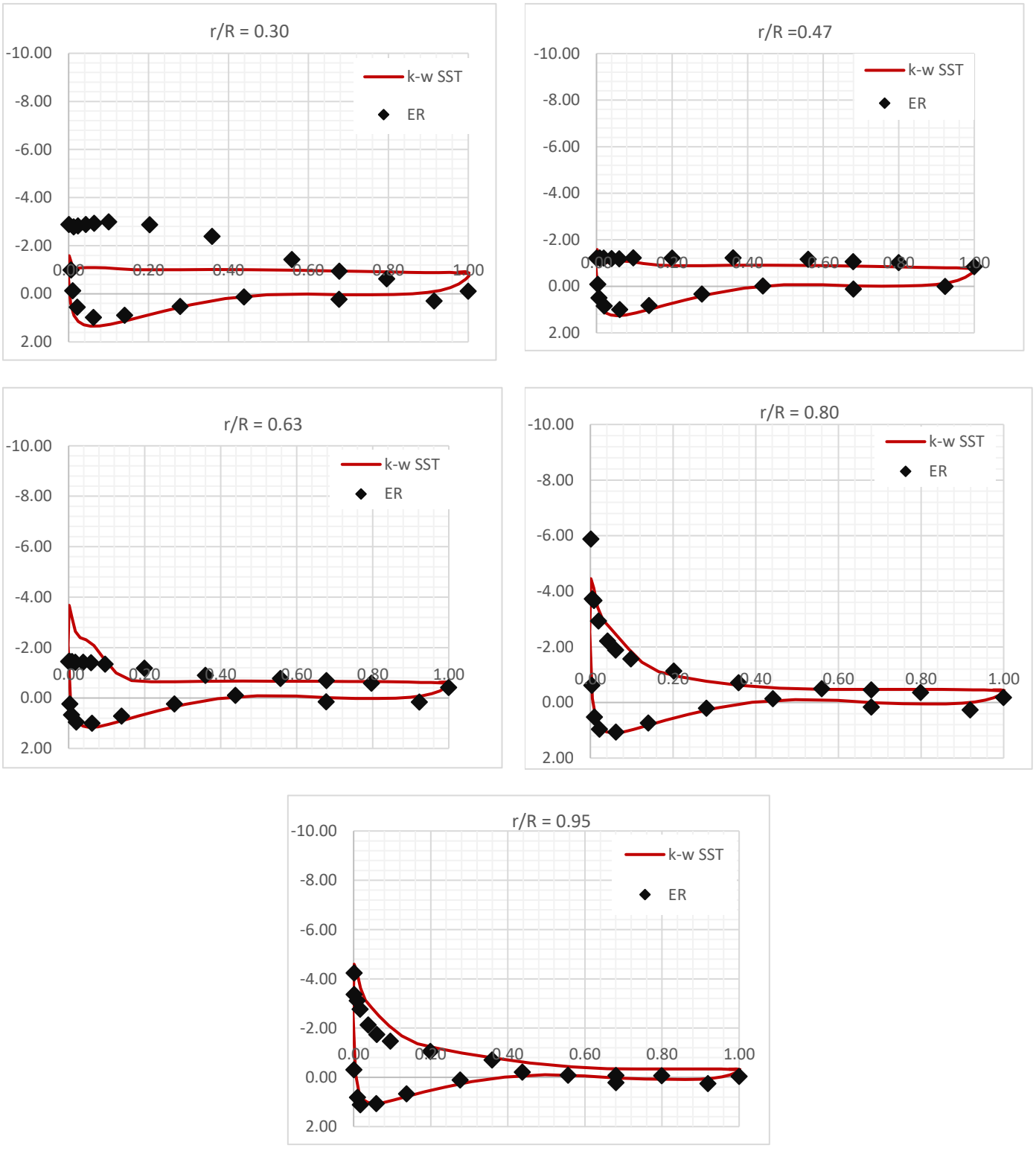

Figure 4.25: Pressure coefficient comparison at spanwise locations for wind speed = 13 m/s

15 m/s

The dark red sections at both edges of the chord are dark red which evinces a high-pressure zone where the flow has stagnated. On the suction side, there is once again an adverse pressure gradient which is indicative of flow separation. Figure 4.26 displays the pressure contour for the turbine blade for a freestream velocity of 15 m/s.

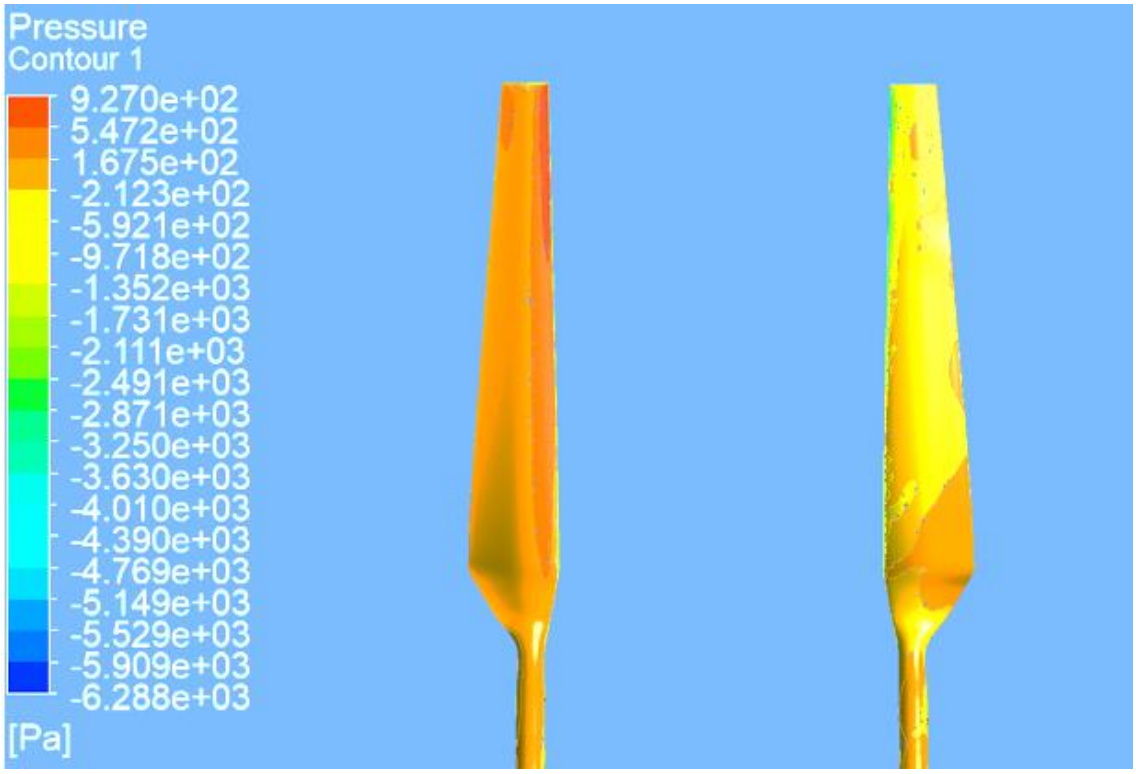

Figure 4.26: Surface static pressure at freestream velocity (V_∞ = 15 m/s)

Figure 4.27 shows that the blade has fully stalled and large flow separation has occurred over most of the blade. The CFD results are once again greatly disparate from the experimental data at r/R =0.30. The computational results show a relatively low negative suction pressure except at the tip of the blade where r/R =0.95. The capacity of the blade to generate lift has decreased when compared with the other high wind speed cases. The blade's high AOA means that the blade is no longer harnessing the wind's energy, and its power efficiency has suffered a precipitous decline.

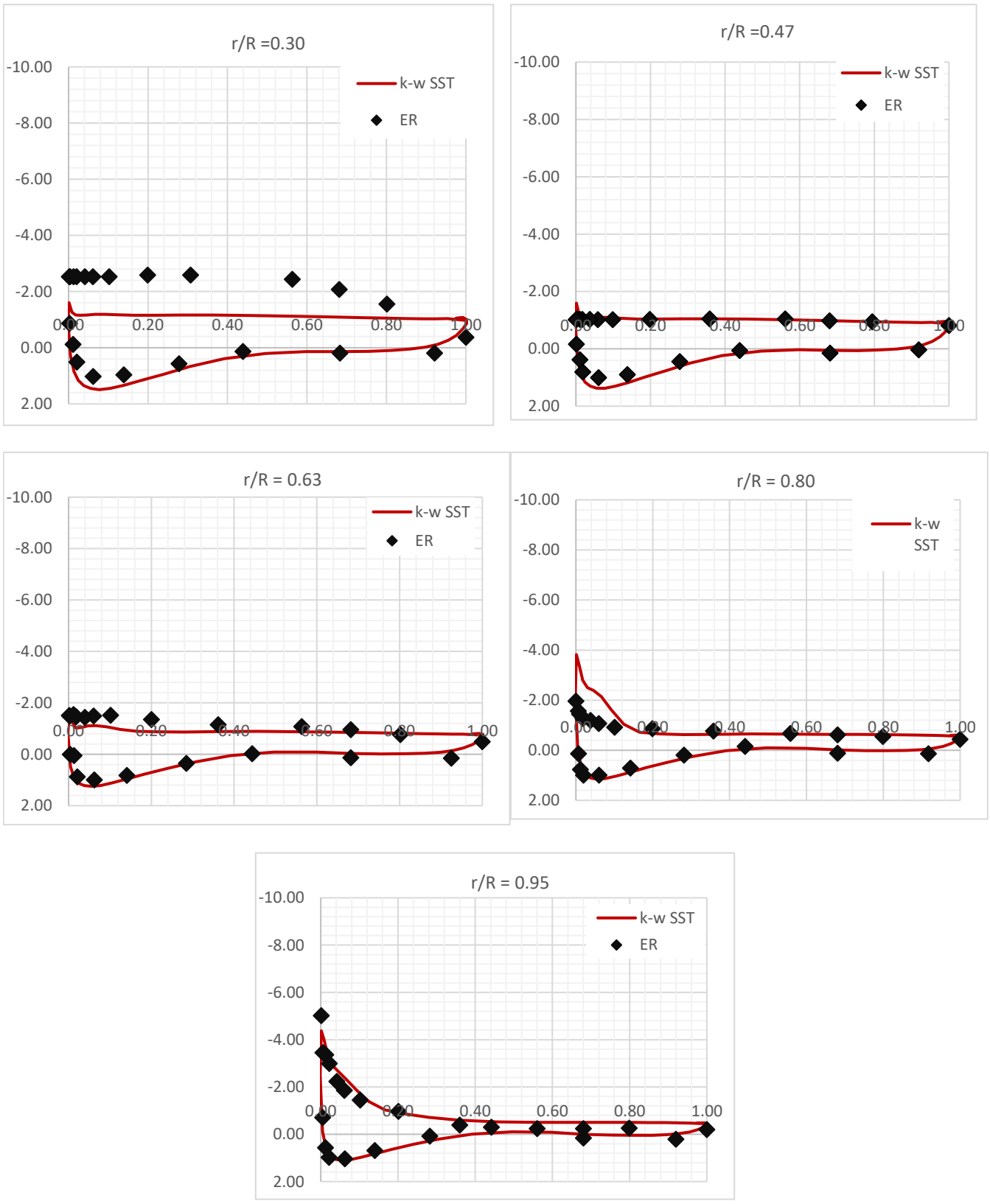

Figure 4.27: Pressure coefficient comparison at spanwise locations for wind speed = 15 m/s

4.4.3 Skin Friction Coefficient

The skin friction coefficient, C_f, is a dimensionless variable that gauges the frictional resistance of a fluid against a surface. It is a measure of how strongly the fluid flow is slowed down by the surface due to viscous effects. It has a direct relationship with the drag force acting on the blade. A larger C_f indicates higher wall stress and greater viscous (frictional) losses. The equation for the skin friction coefficient is defined as:

$$C_f = \frac{\tau_w}{\frac{1}{2}\rho {V_\infty}^2}$$

Equation 4.2

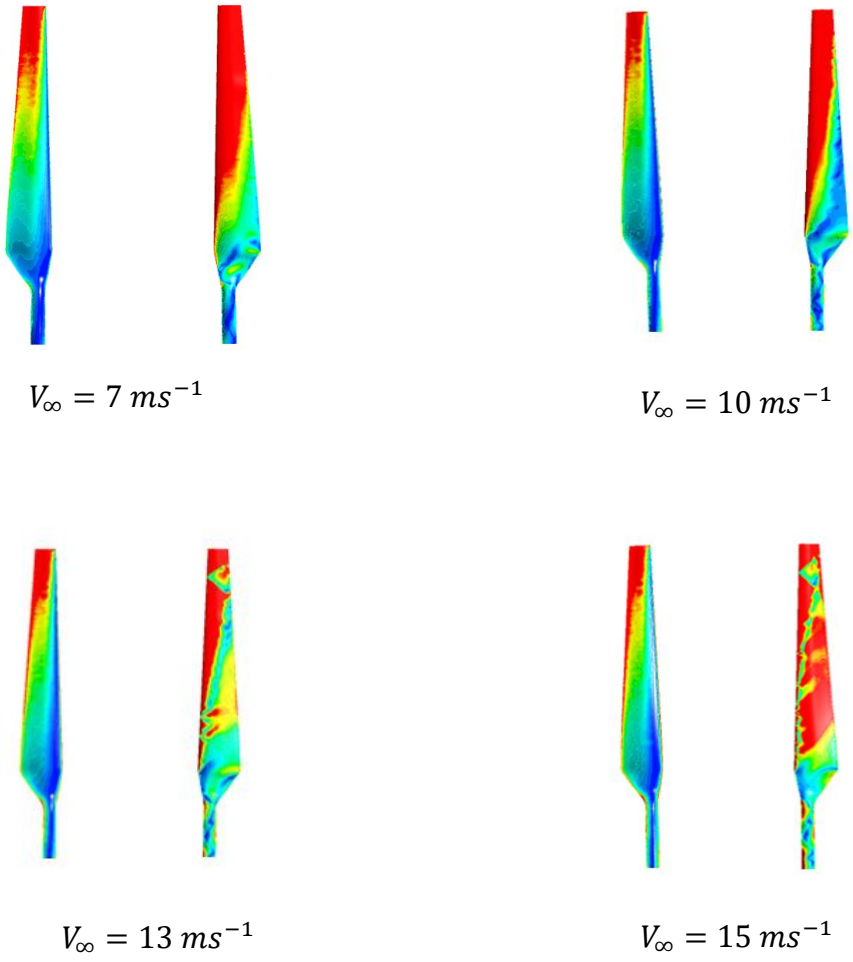

Figure 4.28: Normalised skin-friction coefficient for flow cases V∞ = 7,10,13, and 15; pressure side (left) and suction side (right)

Figure 4.28 displays the normalised skin friction coefficient contours, providing a visualization of fluid behaviour in the boundary layer. These plots show the magnitude of the wall shear that the turbine blade encounters (the direction is illustrated as surface streamlines in a previous figure). The red region of the turbine blade is the area which experiences the most wall shear, starting at the leading edge it expands downstream into the mid-section of the chord. As the flow increases the red region covers a greater area of the blade which suggests greater frictional losses. For the 7 m/s flow case, the pressure side shows a lower C_f which means that the flow is attached and lesser frictional forces affect the flow. In contrast, on the suction side the colour contours vary from red (high wall shear, attached flow) to green and blue (low wall shear), indicating flow separation in these regions. For the 10 m/s flow case a similar pattern occurs with thicker red streaks. The flow separation and spanwise flow pattern is visualised on the suction side of the blade and can be seen for $V_\infty = 13$, it becomes more apparent for $V_\infty = 15$ m/s. Overall, higher flow velocities result in higher peak wall shear stresses in attached flow regions, but also promote earlier and more extensive flow separation.

4.5 Qblade Validation

The BEM simulations were performed using QBlade CE v2.0.9. software which was then used to investigate the aerodynamic performance of the NREL Phase VI under steady and unsteady flow conditions. The process involved building the geometry using the S809 blade aerofoil, generating the aerofoil aerodynamic polars, and defining the operational characteristics of the rotor turbine. The turbine is defined as 2-bladed upwind rotor with an operating speed of 72 rpm, an illustration of the turbine is displayed in Appendix B. The Prandtl tip loss correction and 3D Snel correction were applied to give more accurate results. Instead of applying the Glauert correction the DTU Poly Bem correction factor is used to give a better prediction of power and thrust. The steady and unsteady BEM simulations provide a useful validation of the CFD results that were produced in ANSYS Fluent and proves that the results are accurate and reliable. To capture the effects of unsteadiness on power production at the higher speeds the Øye dynamic stall model within QBlade Unsteady Solver was utilised. As the wind speed increases the local AOA increases and the turbine blade becomes more susceptible to dynamic stall.

Figures 4.29 and 4.30 contrasts the power generated using the BEM method and compares it to the CFD simulations performed in this chapter and the experimental data published by the NREL. The graphs show the solutions that were arrived at using QBlade, are closely aligned with the CFD simulations and therefore provides validation of the results. QBlade overpredicted the power generated at λ=2.53 and λ=2.92 even though a stall model was

utilized when the simulations were performed. This underscores the limitations of the BEM method in deep stall conditions at higher wind speeds.

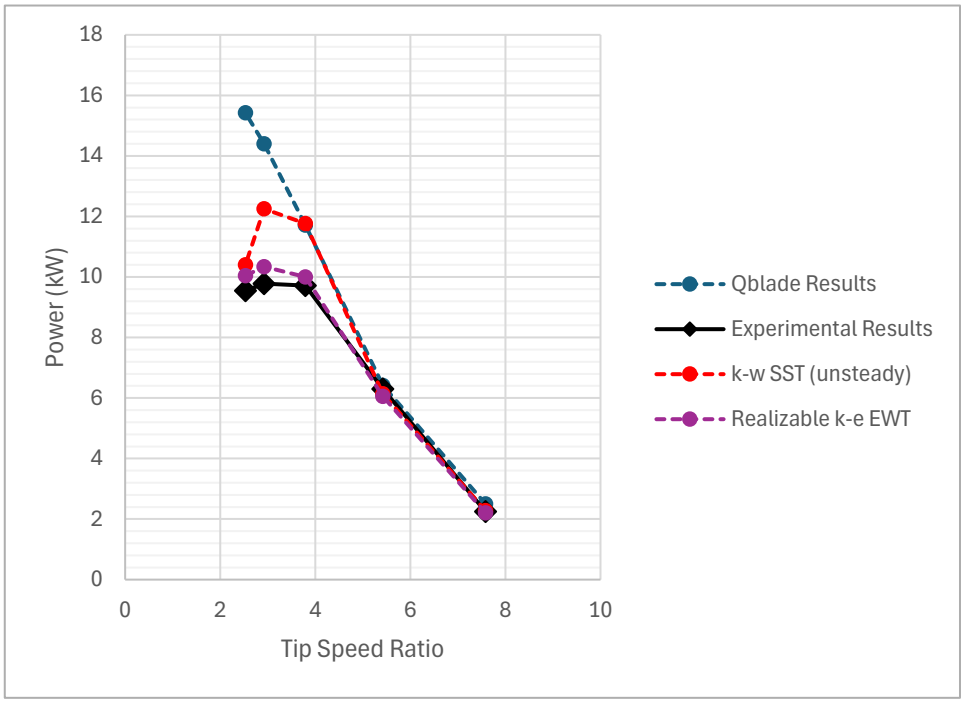

Figure 4.29: Comparison of power generation under transient conditions with QBlade

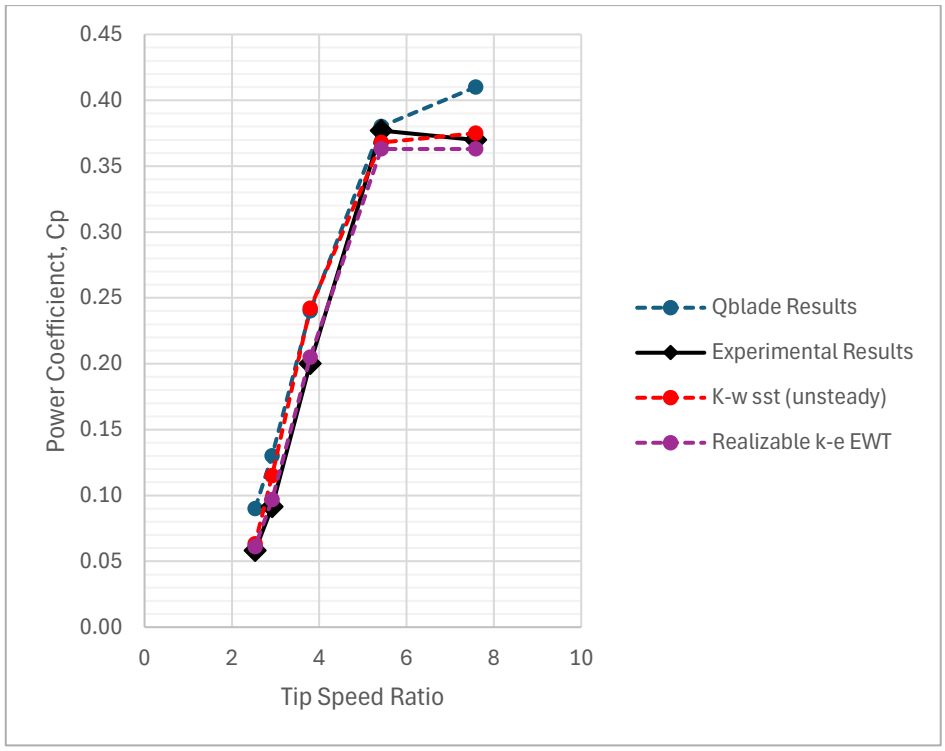

Figure 4.30: Comparison of the power efficiency of the NREL Phase VI with QBlade

4.6 Summary of the Chapter

This chapter investigates the aerodynamic performance of the stall-regulated NREL Phase VI using CFD and QBlade software under different physical conditions. The first aim was to provide a quantitative analysis of the performance of the turbine under both steady and transient conditions. The CFD solver accurately predicted the performance of the HAWT under non-stall conditions for both solvers. The margin of difference in both of these flow cases (5 and 7m/s) can be considered negligible. The greatest inaccuracies can be found at the higher AOAs at 10 m/s and 13m/s where there is a difference of 21.12% and 25.29% respectively. These results are consistent with the numerical results produced in the CFD studies of the NREL Phase VI by other researchers. At a wind speed of 15 m/s, under deep stall conditions, CFD predictions demonstrate improved agreement with experimental data compared to performance at mid-range wind speeds.

The accuracy of the turbulence models used in the steady and unsteady state simulations evinces the importance of selecting the appropriate turbulence model for computational analysis. For instance, the Transition SST was found to be excellent for predicting performance in steady conditions, however, it was unable to produce results for the unsteady simulations. Likewise, the Spalart-Allmaras algorithm predicted the power produced in steady conditions but in stall conditions it overpredicted the power generated by the turbine. From this study, it can be seen that the k-ω SST and Realizable k-Ɛ EWT are the best methods because they provide the most accurate solutions when considering their performance under different conditions.

The BEM method featured in this chapter as a means of validating the CFD simulations and verifying whether the CFD results showed a sufficient degree of fidelity to the experimental data so as to be considered a superior method. At the lower TSRs, CFD shows a far greater accuracy than QBlade, and at the higher TSRs the difference is more marginal even though CFD still yielded more accurate results. For the BEM technique, the lift and drag coefficients at specific Reynolds number must be interpolated to estimate the power this can sometimes lead to imprecision in the estimation of power as it is not always exact.

In summary, the increase in power efficiency is correlated with a general increase in the TSR, even though the total amount of power generated is at its lowest point when λ=7.58. Conversely, at λ=2.53 the lowest amount of power efficiency is recorded but a greater amount of power is produced. This demonstrates that while higher wind speeds enable greater absolute power generation, the turbine operates less efficiently at low tip-speed ratios due to stall conditions, limiting the proportion of available wind energy that can be converted to mechanical power. These numerical results provide a greater understanding

of the flow physics which is critical for optimizing turbine performance and is a useful contribution to the field of wind energy research.

5 CFD VALIDATION OF THE NREL PHASE VI WITH PASSIVE FLOW CONTROL SOLUTIONS

5.1 Introduction

PFC methods and their respective benefits have been discussed at length in section 2.6. As mentioned above, the main function of PFCs is to control the flow around the blade aerofoil by encouraging mixing and preventing flow separation. Flow control devices act to boost the lift-to-drag ratio, ultimately increasing the energy harvested by the blade turbine. This chapter focuses on PFC methods and their effect on aerodynamic performance. Different passive flow solutions were utilized to enhance the aerodynamic performance of the NREL Phase VI.

5.2 3D Parametric Study on Riblets

The purpose and function of riblets have been described in detail in earlier sections. Riblets reduce drag by altering the velocity profile within the boundary layer. Their effectiveness is influenced by several factors, including Reynolds number, AOA, riblet spacing, and riblet size. This study focuses on how the Reynolds number and riblet height affect aerodynamic performance. The primary role of riblets is to manipulate near-wall vortices within the viscous sublayer. If riblets are made too large, they can increase drag; however, when properly dimensioned, they modify near-wall turbulent structures to reduce skin friction drag and thus improve power generation. Using the equations listed in Appendix C the size of the viscous sublayer, σ_v, can be obtained. The viscous sublayer tends to be smaller the greater the flow velocity is. In the literature review, it was mentioned that a ratio of h/s =0.5 is optimal for riblets; generally speaking, a h+ of 8-15 is effective for drag reduction (136). The cross-sectional angle α is set at 53.1˚ for the triangular riblets (thus h = d). These heuristics are a useful starting point for the sizing of the riblet geometry. Table 5.1 contains the dimensions of riblet geometries used within this parametric study.

Table 5.1: Dimensions of riblet geometries

	H(mm)	h+	S (mm)	S+
Riblet Geometry I	0.10mm	2-4	0.20mm	4-8
Riblet Geometry II	0.20mm	5-9	0.40mm	10-18
Riblet Geometry III	0.35mm	8-15	0.70mm	16-30

The riblets are applied to the suction side of the blade in each case as this is where it is most likely to have the greatest effect on the flow aerodynamics. The boundary layer is typically thinner on the suction side of the aerofoil, especially in instances where an adverse pressure gradient is formed, the flow on the upper side of the blade surface begins to detach because of the flow on the upper side of the blade surface begins to detach because of the adverse pressure gradient and reduced near-wall momentum. A boundary layer with high wall shear stress is well-suited for riblets operating in their optimal h+ range, allowing them to reduce turbulent drag and improve blade efficiency. A similar approach was taken by Bliamis et al. (137) when modelling riblets on a blade surface, they found that the riblets were effective in boosting power efficiency when placed nearer to the trailing edge and closer to the tip. At a higher AOA, when the blade is in dynamic stall, the riblets become less effective. Figure 5.1 presents the geometrical parameters of the riblet configuration.

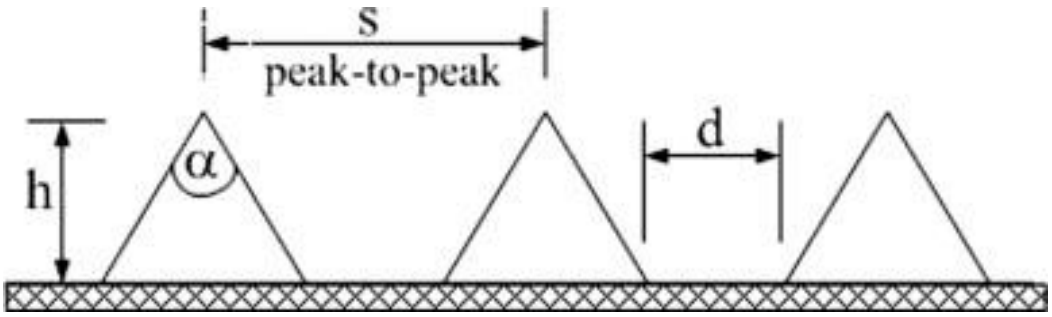

Figure 5.1: Geometrical parameters of riblet configuration (138)

5.2.1 Computational Setup

The slip length effectively models the behaviour of the fluid at the wall boundary in the riblet region. The riblet grooves act by altering the near-wall momentum transfer and reducing skin-friction, this is accurately represented using a Navier slip-length boundary condition applied via a User-Defined Function (UDF). Mele and Tognaccini (139) demonstrated the effectiveness of the slip-length modelling strategy in their numerical study, which showed that riblets could be represented by using a Navier slip boundary condition with slip length being proportional to the riblet height. The geometrical parameters of the riblet are factored into the slip length. The results showed good agreement when a RANS solver was used to simulate the effects of riblets on aerodynamic performance. The riblets showed the ability to reduce friction and drag as well as to

improve pressure recovery by delaying separation. Equation 5.1 describes the relationship between the slip length and the dimensionless length in wall units, l_+:

$$l_+ = \frac{L_s\, u^*}{v}$$

Equation 5.1

The frictional velocity u^* and the kinematic velocity v that the riblets experience directly corresponds to the slip length which is itself proportional to the dimensionless wall units. The slip length technique is a more advanced technique of dealing with 3D oscillating flows, offering greater accuracy than modelling the riblets as a single roughness problem. Although, the slip-length model is not as detailed as Direct Numerical Simulations, this numerical approach captures the essential drag reduction mechanism of the riblet by modelling the shift of the viscous sublayer and the concomitant change in the overall drag in a computationally feasible manner. The effect of the riblets on the wall-bounded flow is modelled through a UDF that factors in the slip length. The slip length modifies the near-wall momentum boundary condition without changing the turbulence model parameters. The slip boundary is best represented by Equation 5.2:

$$\tau_{w,t} = \frac{\mu}{L_s} u_t$$

Equation 5.2

u_t is the tangential velocity at the wall, μ is the dynamic viscosity, L_s is the prescribed slip length used to represent the aerodynamic effect of riblets, and the tangential wall shear denoted as $\tau_{w,t}$. The effects of the riblets on the velocity profile is a shift of the turbulent boundary layer in the wall region. The presence of the riblets shifts the velocity profile from the viscous sublayer, the drag reduction is proportional to the slip length in the streamwise direction, and the upward shift is modelled by Equation 5.3:

$$U^+ = \frac{1}{k}\ln\,(y^+) + B - \Delta U^+$$

Equation 5.3

U^+ is the upward shift, k is the Kármán constant, $B = 5$ is the smooth-wall constant, and the superscript $+$ indicates non-dimensional quantities. The slip length is proportional to the upward shift in the log-law profile.

A finer mesh is required to adequately discretise the blade surface and capture the changes in flow aerodynamics in the boundary layer. For an accurate resolution of the riblets, a face sizing is applied as well as 30 inflation layers. The geometry model has the same configuration as the one laid-out in the methodology. The first layer height is set at 10 µm. It is optimal when $y^+ \leq 1$ so that it can capture the effects of turbulence in the viscous sublayer, however, a $y^+ \leq 5$ will provide a relatively accurate solution. Considering the scale of the riblets and their effect on local aerodynamics it is imperative that the mesh topology has sufficient near-wall refinement and gradual expansion into the outer flow to ensure the accurate prediction of turbulence generation and shear stress distribution. Figure 5.2 shows the y+ distribution for the turbine blade.

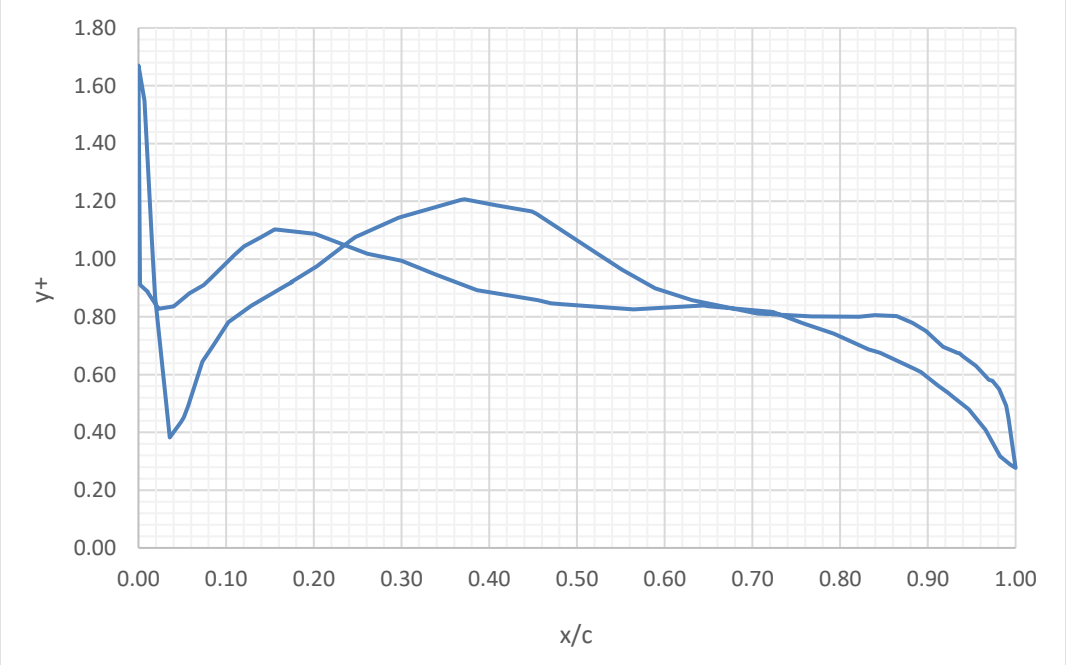

Figure 5.2: The y+ distribution for the turbine blade

The realizable k-ε EWT has demonstrated remarkable accuracy in predicting aerodynamic performance across a wide range of speeds. It is selected for the following simulations because of its robustness and capability to resolve near-wall regions down to $y^+ = 1$. It accurately captures the shear-layer gradients and surface pressure distributions over the riblet geometry, at a lower computational cost without compromising on accuracy. Figure

5.3 displays the riblet region at the trailing edge of the turbine blade, extending from r/R = 0.25 to r/R = 0.90 and covering the trailing edge from x/c = 0.80 to x/c = 1.0.

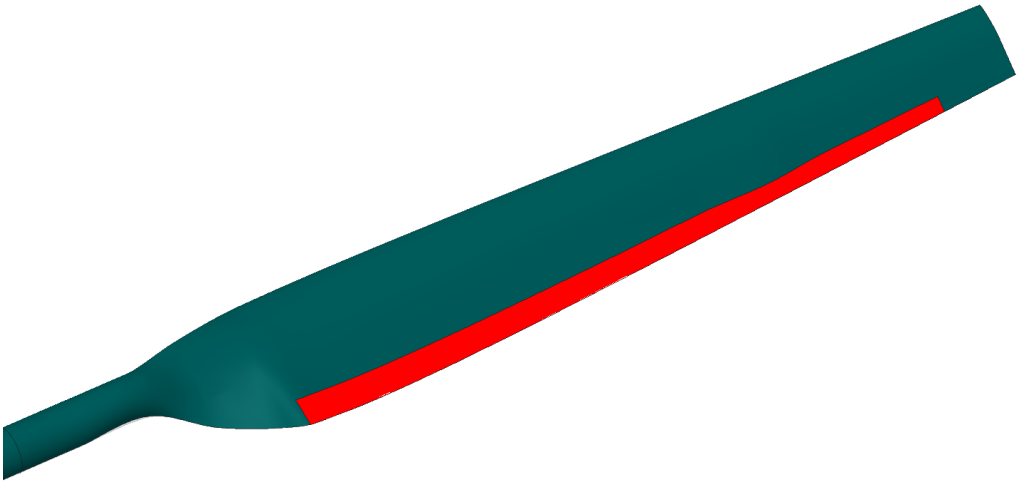

Figure 5.3: The designated riblet region on the turbine blade

The CFD simulations performed within this section predict the aerodynamic performance of the NREL Phase VI with the riblet geometries. The torque and power measurements are boosted through the utilization of the riblet geometries, with Riblet Geometry III showing the most marked increase within the operating ranges. The torque generated increases with riblet height, with only a few percent difference between the power output for each of the riblet geometries. This demonstrates the effectiveness of using the riblet geometry on the suction side and how it acts to prevent flow separation by shifting the streamwise flow away from the surface. Therefore, wall momentum is reduced by the displacement which results in the decrease in wall shear stress and friction. Figures 5.4–5.6 present the power measurements, whereas Figures 5.7 and 5.8 illustrate the reduction in turbulent kinetic energy and skin-friction drag within the riblet region.

Increasing riblet height within the viscous sublayer suppresses near-wall turbulence energy. The reduction in turbulent energy (shown in Figure 5.8) signifies a decrease in Reynolds shear stress, confirming a reduction in skin friction drag. Figure 5.9 shows the improvement in pressure distribution within the riblet region for the given geometries. The turbulent kinetic energy increases with wind speed for all geometries, which evidences the higher turbulence production at elevated Reynolds number. The rate of increase in the TKE is largely dependent on the riblet geometry which modifies the total amount produced.

Riblet Geometry I exhibits the steepest rise in TKE from 5–15 m/s, indicating that the smallest riblet height is insufficient to suppress the dominant near-wall structures and spanwise motions that drive turbulence production. In contrast, Riblet Geometries II and III show lower TKE and a reduced growth rate with wind speed, consistent with better stabilization of the near-wall flow and reduction of crossflow fluctuations within the riblet region. Geometry III provides the greatest suppression across 10–15 m/s, suggesting it is the most effective of the tested heights for limiting near-wall turbulence development in this operating range.

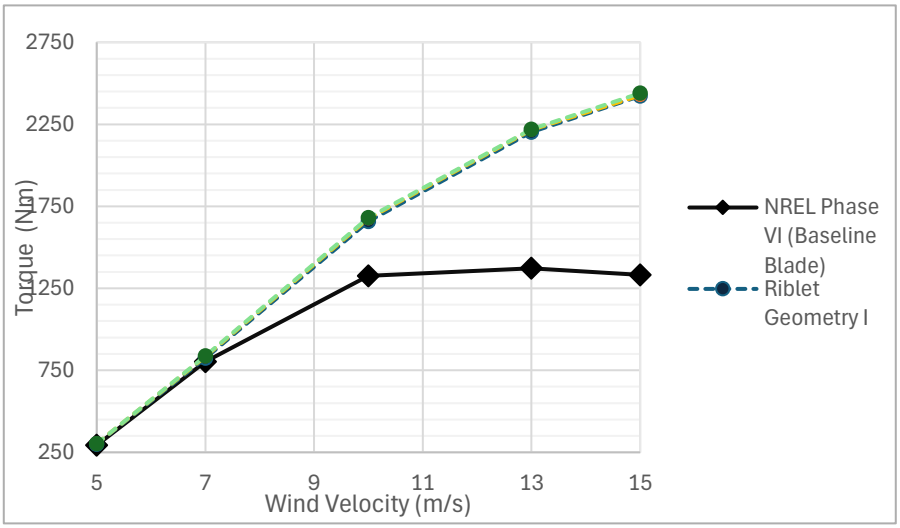

Figure 5.4: Torque prediction for NREL Phase VI with different riblet geometries

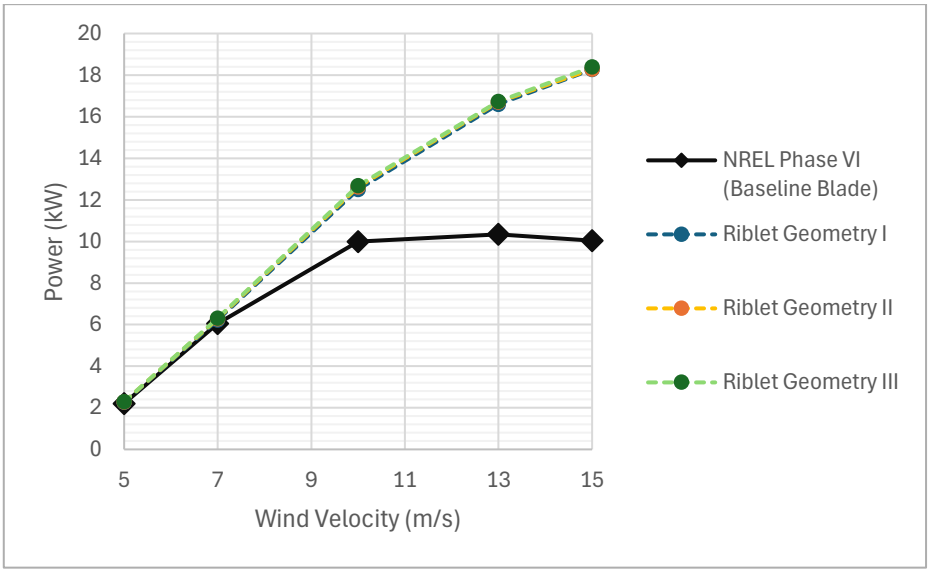

Figure 5.5: Power prediction of NREL Phase VI with different riblet geometries

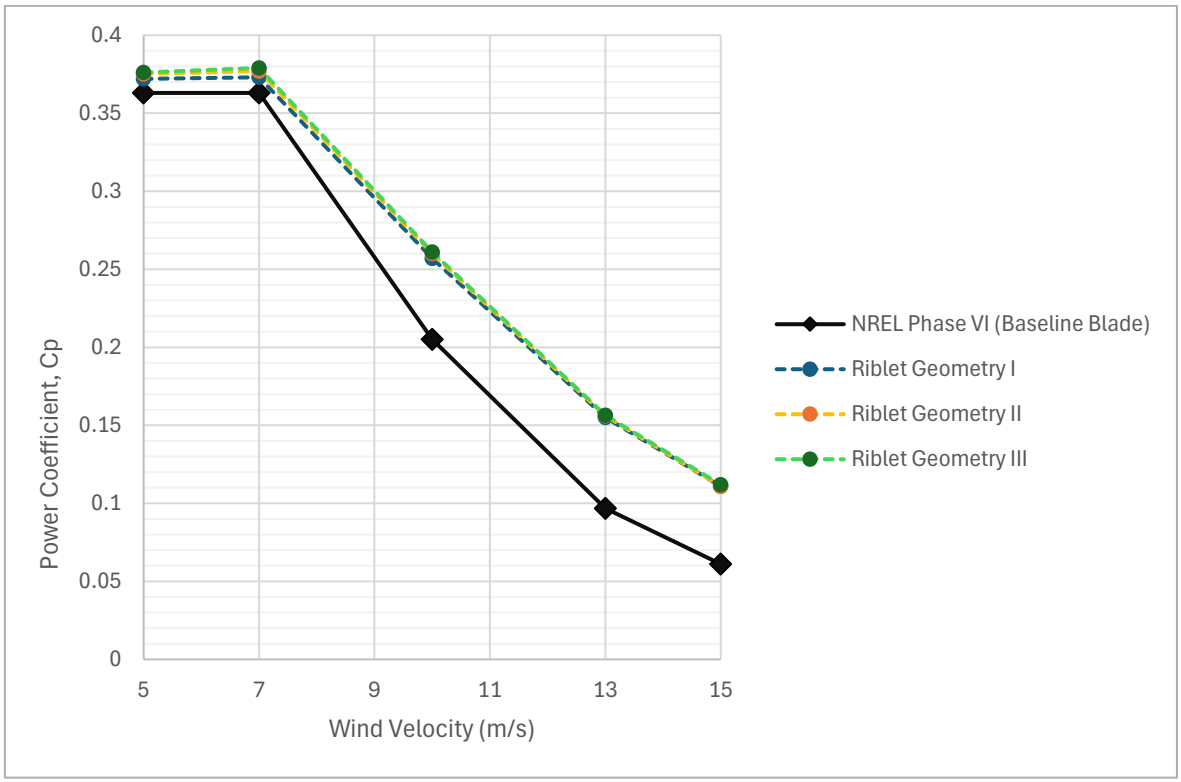

Figure 5.6: Comparison of power efficiencies for NREL Phase VI with riblet geometries

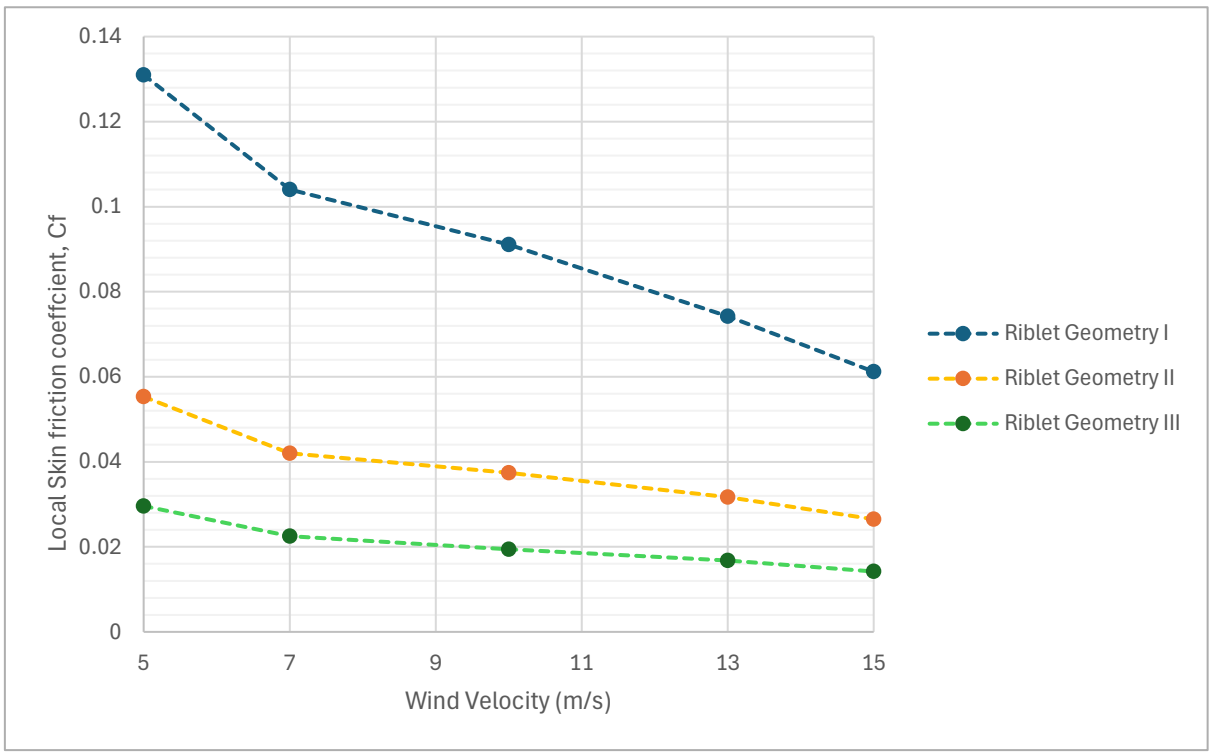

Figure 5.7: The local skin friction coefficient of the designated riblet region

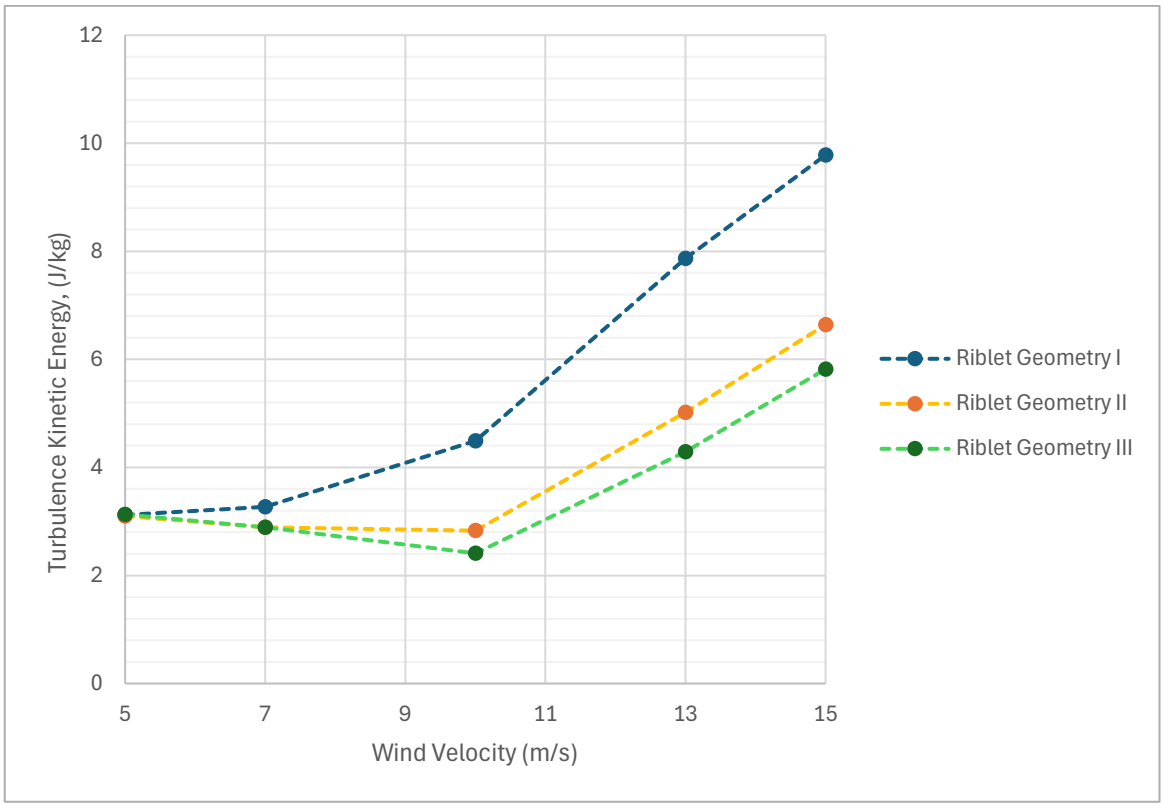

Figure 5.8: The turbulence kinetic energy generated within the local riblet region

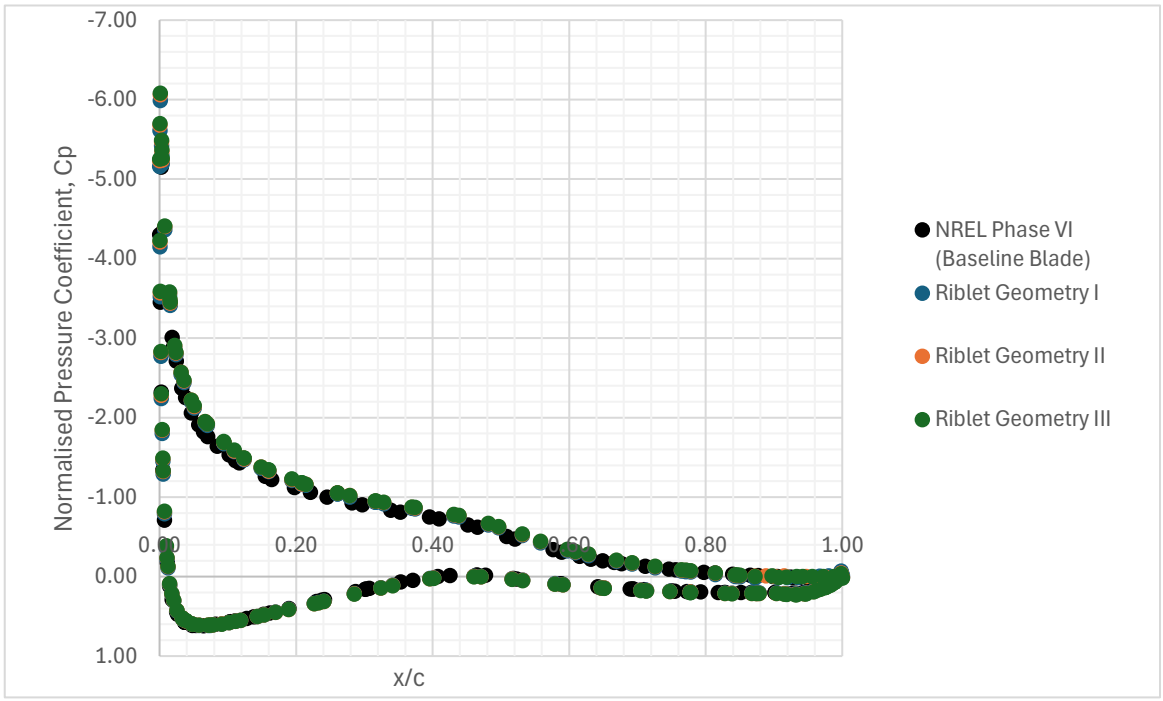

Figure 5.9: The pressure distribution at spanwise location (r/R =0.63) of the NREL Phase VI with different riblet geometries

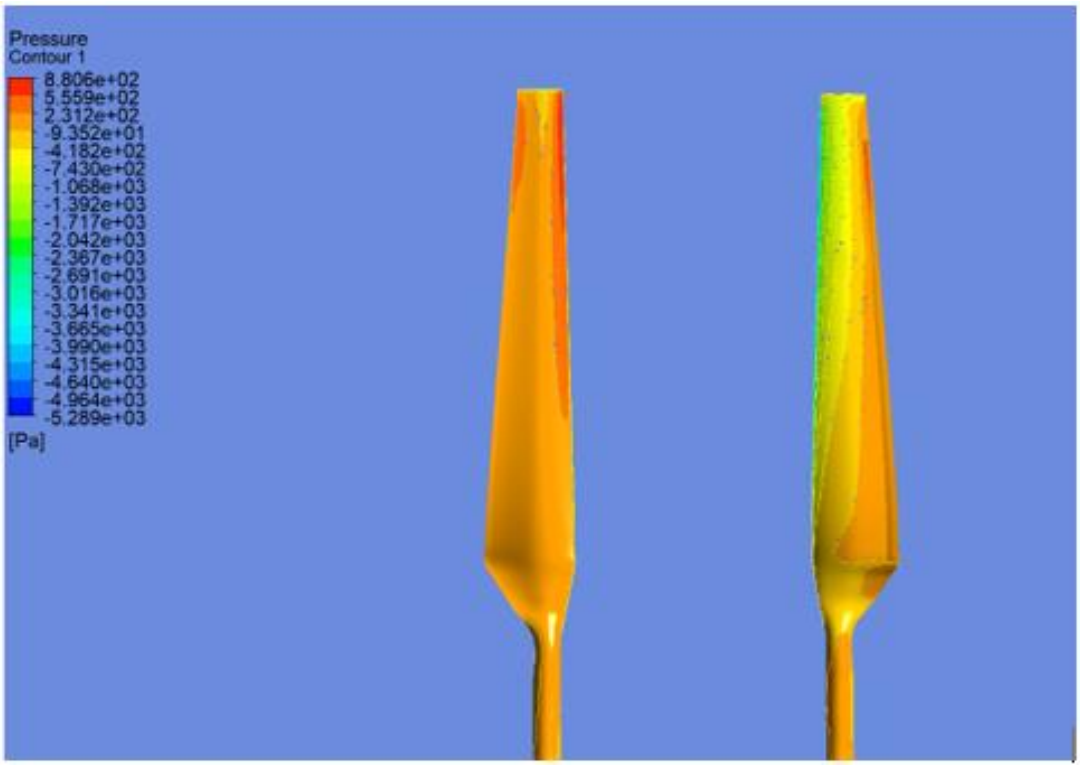

Figure 5.10: : Surface static pressure for ribleted NREL Phase VI (at V_∞ = 10 m/s)

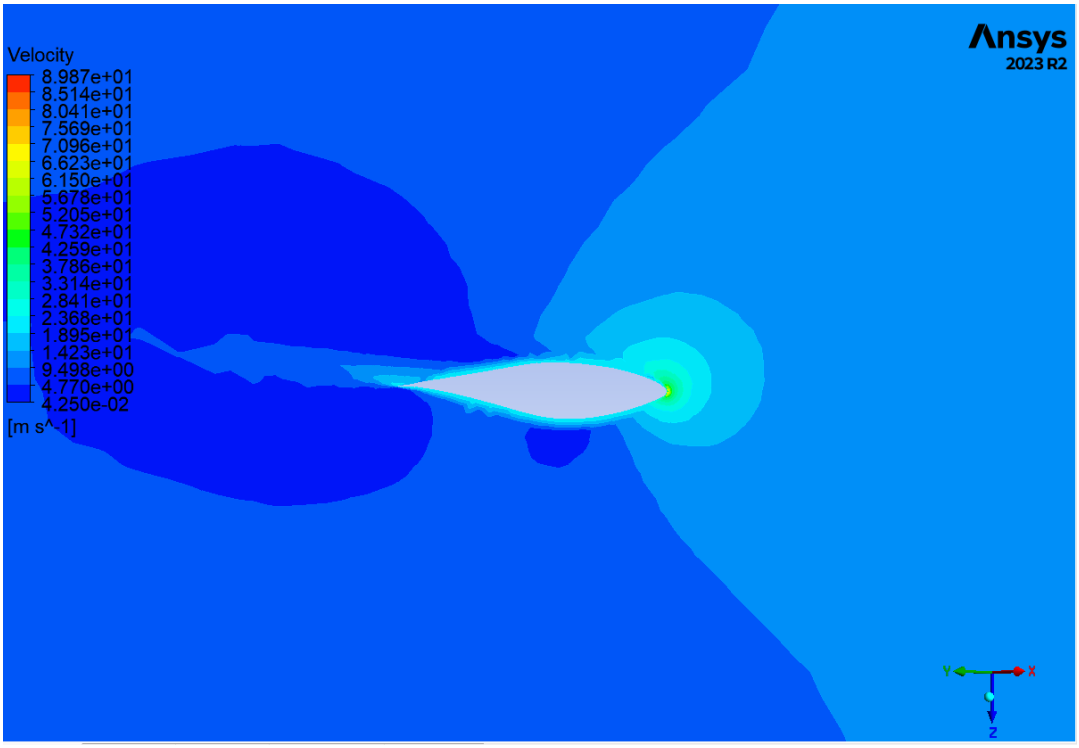

Figure 5.11: Velocity profile at spanwise location (r/R =0.63) for the ribleted blade (at V_∞ = 10 m/s)

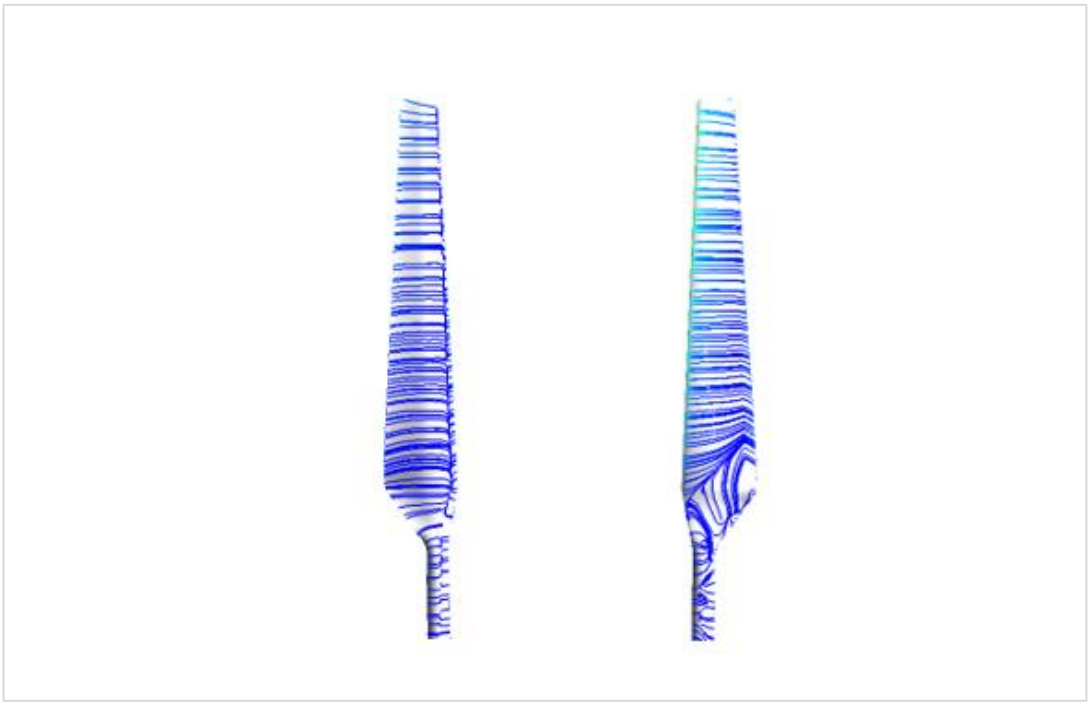

Figure 5.12: Wall shear streamlines for ribleted NREL Phase VI (at V_∞ = 10 m/s)

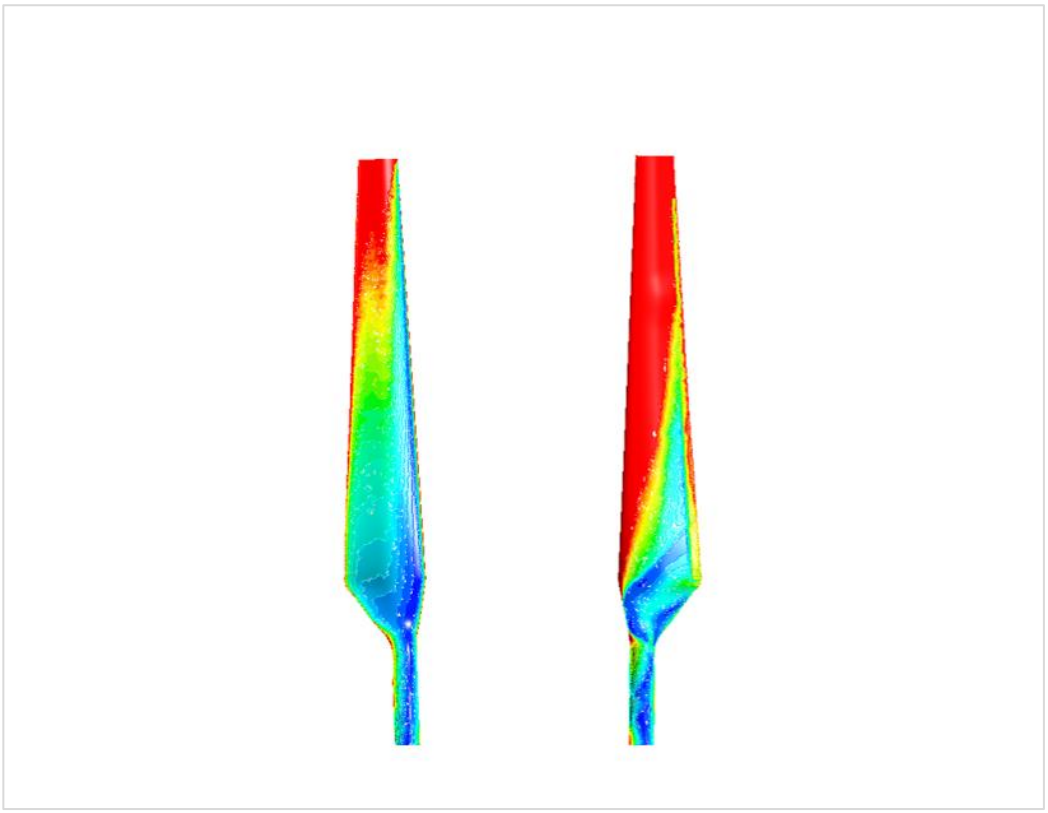

Figure 5.13: The skin friction coefficient of the ribleted turbine blade (at V_∞ = 10 m/s)

The effect of the riblets on aerodynamic performance is evidenced in the above figures, Figure 5.10 to Figure 5.13. The contour plots detail the effects of Riblet Geometry III in improving the aerodynamic performance of the NREL Phase VI. The pressure plot illustrates a stronger adverse pressure gradient (when V_∞ = 10 m/s); there is a greater concentration of pressure at the trailing edge. The riblets act to improve pressure recovery and therefore delay flow separation. The resultant effect is that torque is boosted considerably for this flow case. Figure 5.11 gives a sectional view of the ribleted blade, the flow velocity is greatest at the leading edge where the flow accelerates and produces a local maximum velocity point adjacent to the nose of the blade. There is a gradual decrease in velocity as the flow progresses along the blade surface toward the trailing edge, influenced by the riblets, which results in a low-speed wake downstream from the turbine blade.

The wall shear plot shows reduced spanwise flow when compared with Figure 4.12, demonstrating that the riblets damp crossflow fluctuations and suppress spanwise shear. Although root separation is evident from the contour plot (Figure 5.12), the riblets act to keep the streamwise flow attached. Figure 5.13 shows the contour plot on the suction side of the turbine blade. There is a general decrease in the observed C_f especially in the mid-span portion of the suction side at the trailing edge. Towards the leading-edge high values of C_f persist which exemplifies that the riblets are unable to reduce viscous drag in this area. The average C_f of the turbine blade decreases as the riblet height increases, indicating that the viscous drag has reduced on the suction side of the blade which results in a substantial torque increase. These results indicate that the primary contributor to the observed torque increase is the mitigation of spanwise crossflow on the suction side, which delays separation in pre-stall regimes. The reduction in viscous drag alone is therefore insufficient to explain the performance gains.

The overall effect of riblet microstructures is modelled through the slip concept which captures the effect of the riblet on the turbulent boundary layer with its ability to lift the velocity profile in the near-wall region. In pre-stall conditions, the RANS solver demonstrates greater predictive accuracy and the computed increases in torque are congruent with the results shown in other numerical studies. Abbasi and Ketabdari's (140) work assessing the aerodynamic performance of a riblet covered turbine blade showed an increase of 18.36% in torque and 16.82% in power efficiency. In post-stall conditions ($V_\infty \geq$ 13 m/s), torque predictions exceed expected values due to pronounced spanwise flow and flow separation at higher Reynolds numbers. The slip model concept makes the simplifying assumption that the flow is fully attached; consequently, it does not fully account for the drag penalties and vortex shedding associated with the flow regimes at these velocities.

5.3 Numerical Study on Microtabs and Gurney Flaps

The MT is a well-studied method for optimizing the power efficiency of the turbine blade, it is widely recognised as one of the most effective techniques for controlling the flow around the blade aerofoil. The MT is typically positioned near the trailing edge of the blade aerofoil; it acts to shift the stagnation point so that flow separation takes place away from the blade. This allows for the effective conversion of the wind's energy into mechanical power. It is best deployed on the pressure side of the blade according to researchers as this is where the lift can be maximized. The deployment location and height of the MT are crucial factors influencing its effectiveness. The literature review indicates that the optimal placement for the MT is on the outboard section, and this yielded the best results. The MT extends from 70% to 95% radial span region at 0.90c with a height 2.5%c and thickness of 0.025%c.

The GF operates in a similar way to the MT by extending the camber of the aerofoil and delaying flow separation through Kutta's condition, except that the GF is usually attached to the trailing edge rather than the pressure side of the blade surface. For this study, the GF is positioned at 0.95c closer to the trailing edge from 0.65 r/R to 0.90 r/R. The best sizing for the GF was explored within the literature review, and it evidenced the fact that the GF with smaller widths were generally more effective in boosting lift even at higher AOAs. Determining the thickness of the GF means balancing efficiency with manufacturing feasibility. If the GF is made too thin it may be difficult to produce and may even be sub-optimal for maximizing efficiency, however, if it is made too thick then it would not be a useful control strategy. The literature survey suggests that a GF width of 0.1%c and a height of 2% represent a reasonable compromise.

By examining the contour plots at 80% and 95% span, the effect of the passive flow devices on local pressure distribution is ascertained. Both devices augment lift and this is clearly seen by the red contouring at the trailing edge. The GF and MT induce pressure changes by altering the camber which induces a low-pressure region on the suction side of the blade, and a high-pressure region at the pressure side. The increased pressure differential across the blade allows produces greater lift. At higher wind speeds a greater pressure differential is created across the blade causing larger amounts of power to be generated. The velocity plots show the effects that the PFCs have on local aerodynamic loading by illustrating how the flow accelerates over the suction side and redirects around the modified trailing-edge geometry, thereby facilitating circulation and sectional lift. The velocity contour plots detail the flow at the spanwise locations (of r/R =0.30, 0.47,0.63,0.80 and 0.95). Figure 5.14 to

Figure 5.43 show the pressure and velocity contour plots, and numerical results for the simulations performed within this section.

Microtab

7 m/s

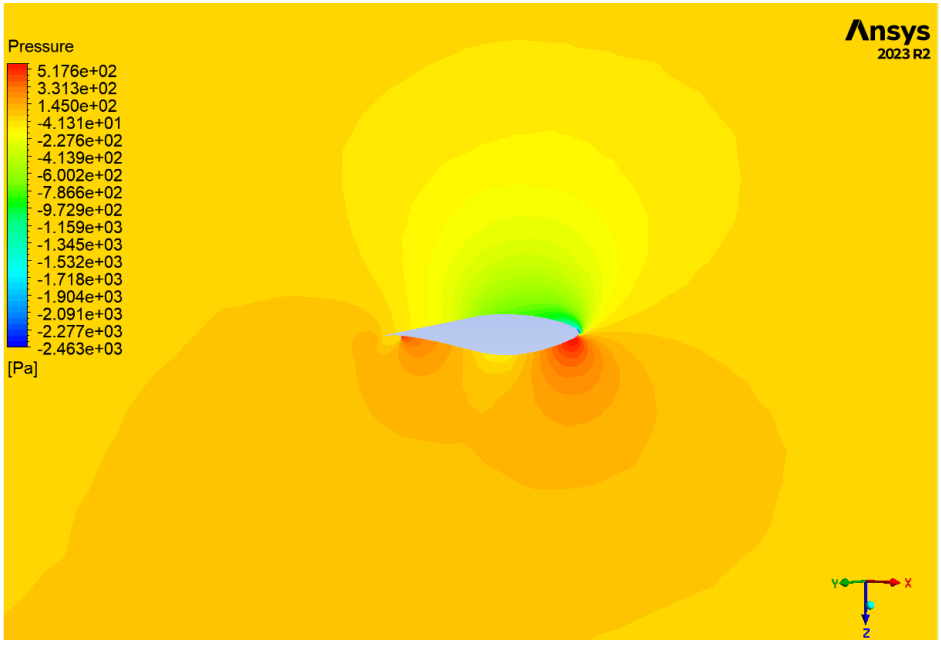

Figure 5.14: The pressure contour of the NREL Phase VI with the microtab at 80% spanwise location for (V_∞ = 7 m/s)

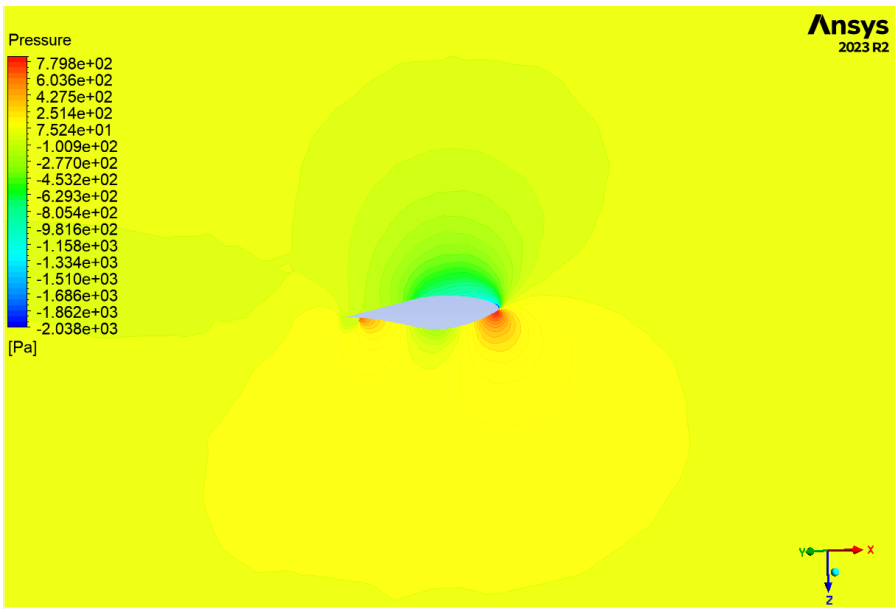

Figure 5.15: The pressure contour of NREL Phase VI with the microtab at 95% spanwise location for (V_∞ = 7 m/s)

10 m/s

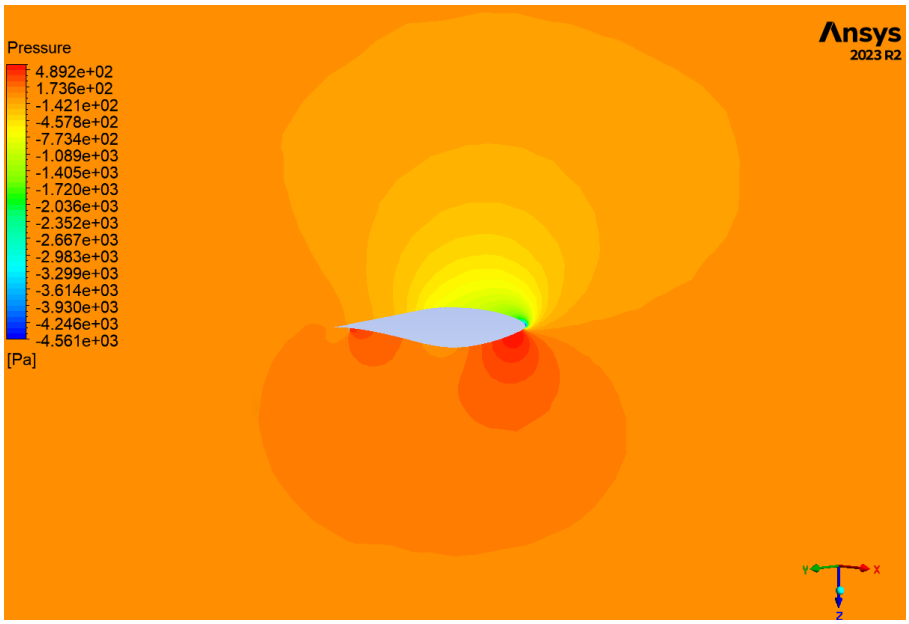

Figure 5.16: The pressure contour of the NREL Phase VI with the microtab at 80% spanwise location for (V_∞ = 10 m/s)

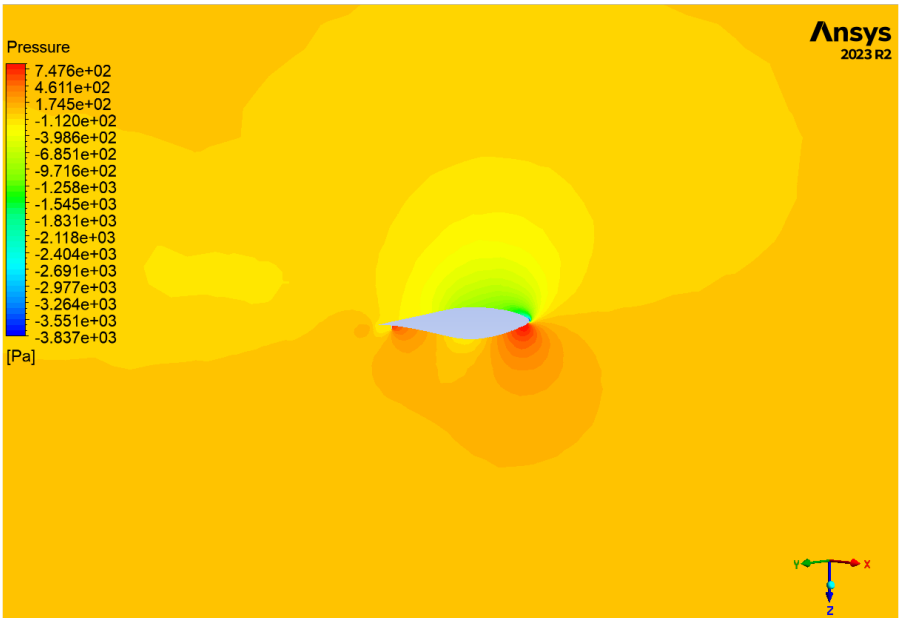

Figure 5.17: The pressure contour of the NREL Phase VI with the microtab at 95% spanwise location for (V_∞ = 10 m/s)

13 m/s

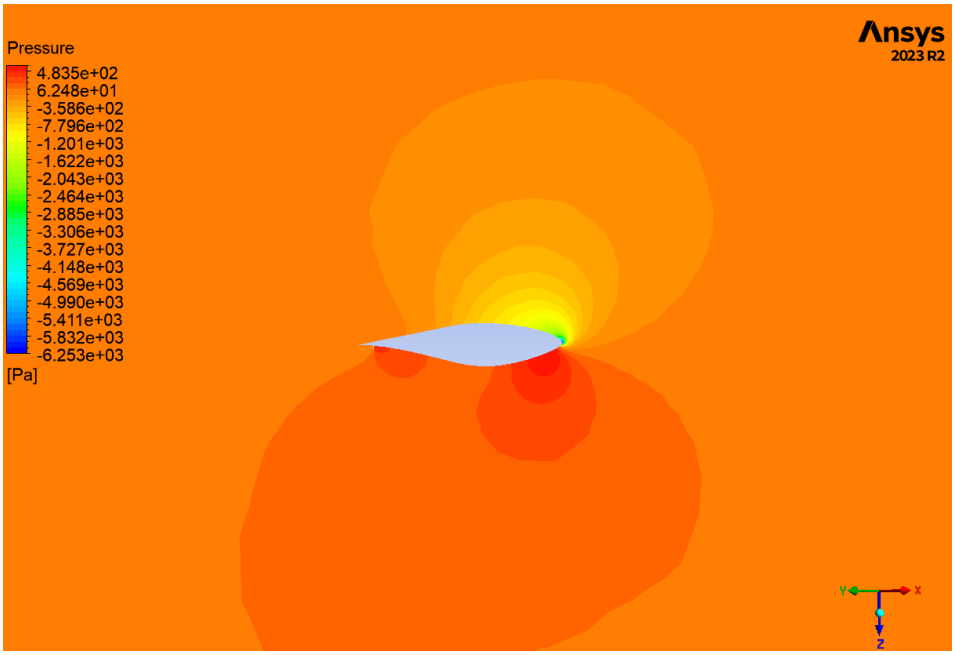

Figure 5.18: The pressure contour of the NREL Phase VI with the microtab at 80% spanwise location for (V_∞ = 13 m/s)

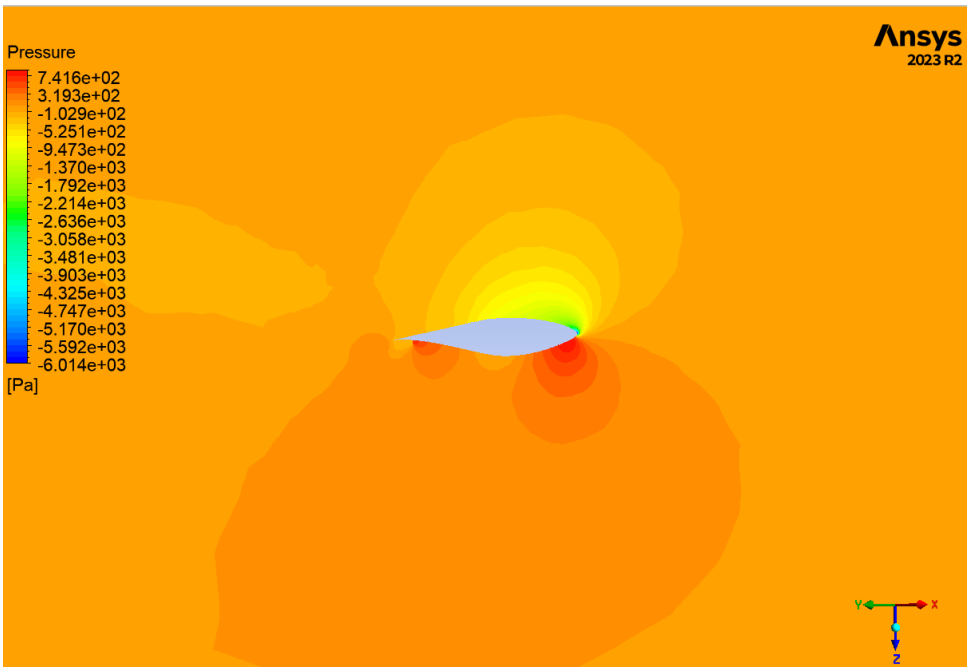

Figure 5.19: The pressure contour of the NREL Phase VI with the microtab at 95% spanwise location for (V_∞ = 13 m/s)

15 m/s

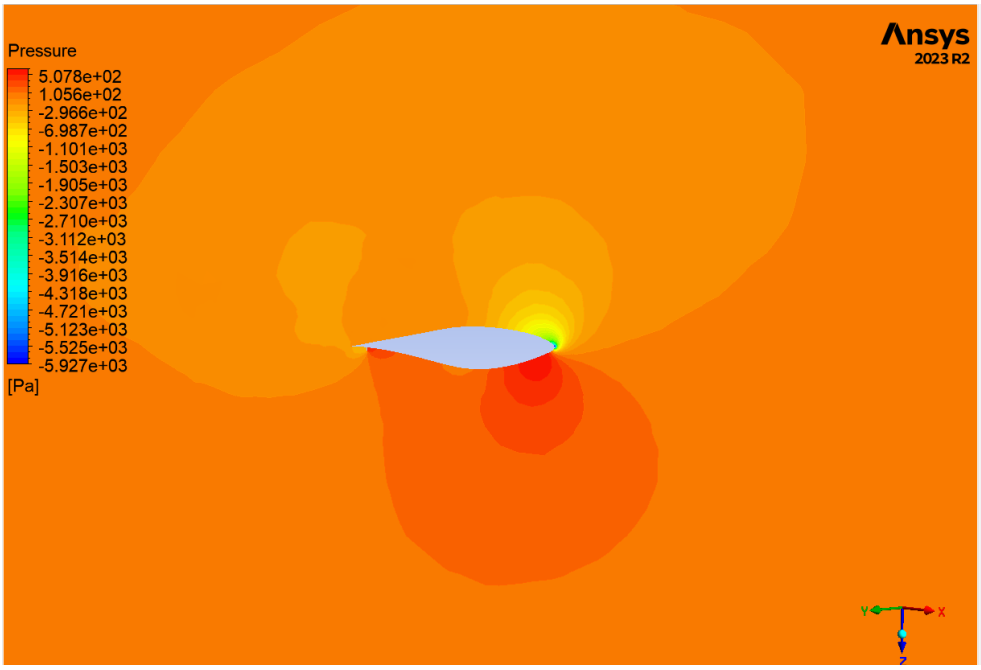

Figure 5.20: The pressure contour of the NREL Phase VI with microtab at 80% spanwise location for (V_∞ = 15 m/s)

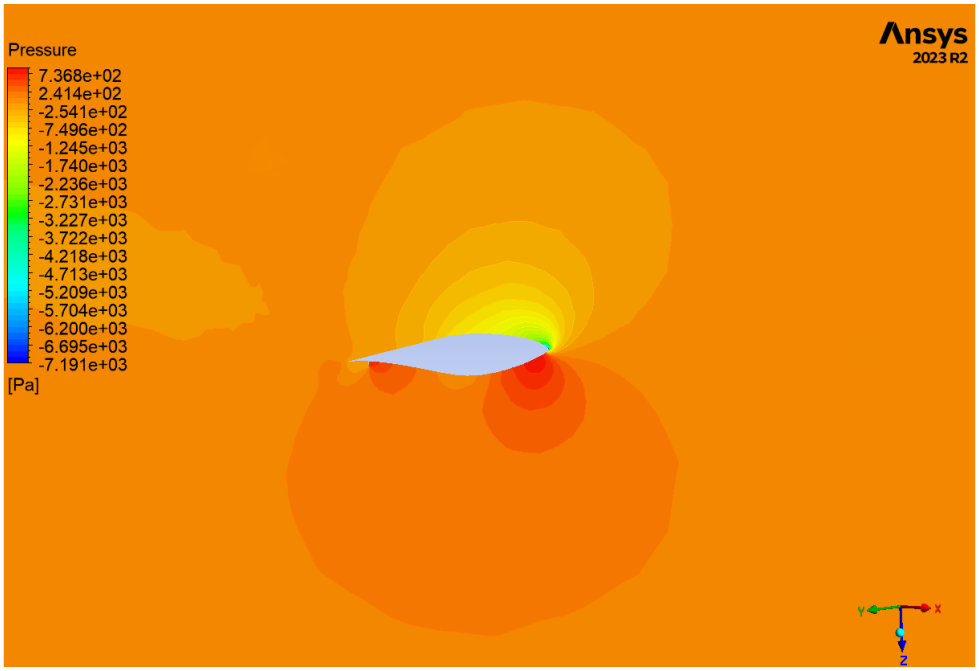

Figure 5.21: The pressure contour of the NREL Phase VI with the microtab at 95% spanwise location for (V_∞ = 15 m/s)

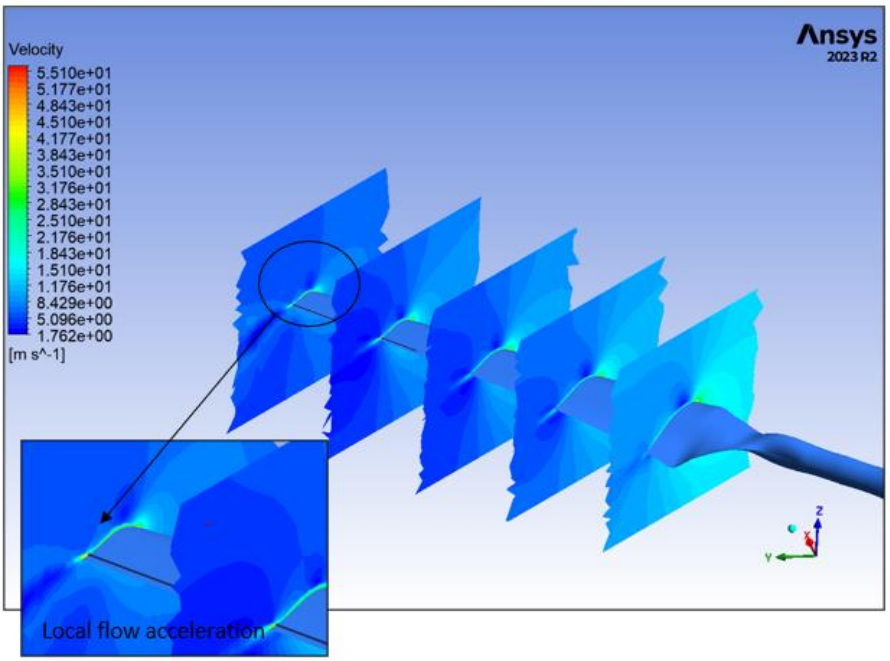

Figure 5.22: Velocity contour of the NREL Phase VI with the microtab at spanwise locations for V_∞ = 7 m/s

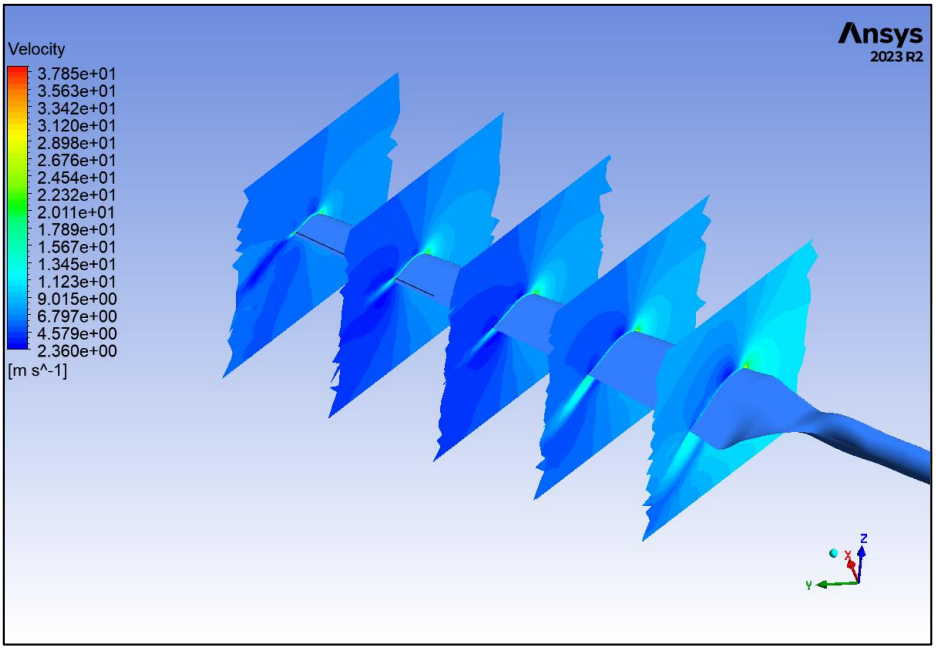

Figure 5.23: Velocity contour of the NREL Phase VI with the microtab at spanwise locations for V_∞ = 10 m/s

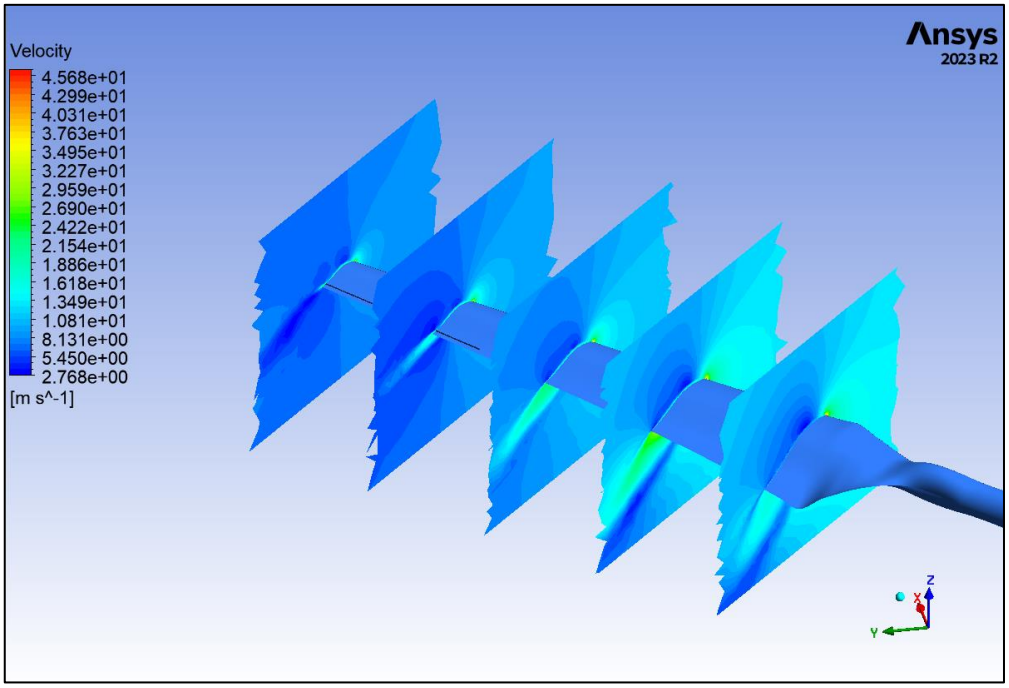

Figure 5.24: Velocity contour of the NREL Phase VI with the microtab at spanwise locations for V_∞ = 13m/s

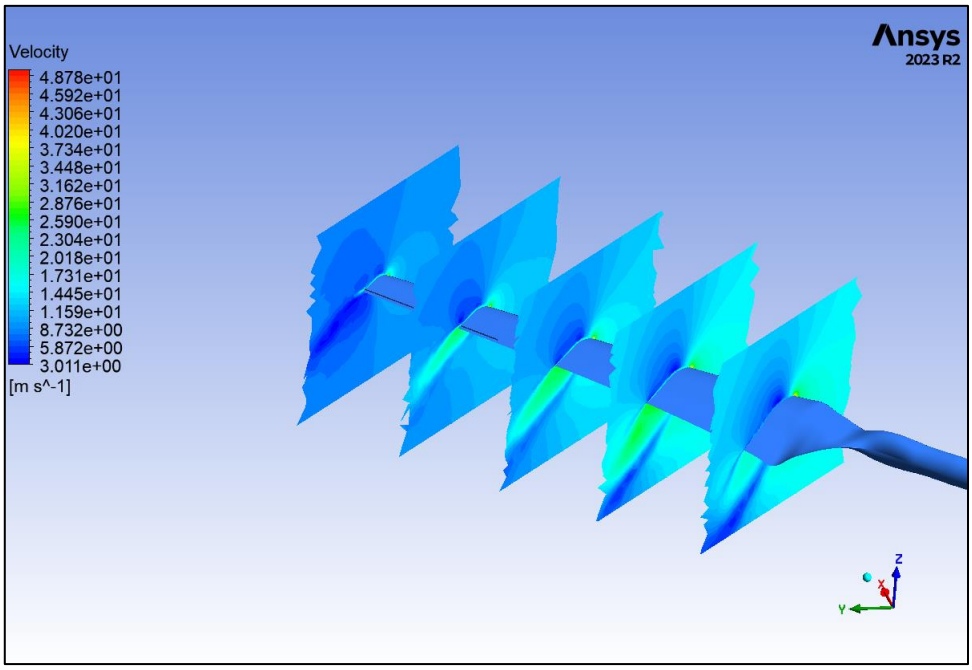

Figure 5.25: Velocity contour of the NREL Phase VI with the microtab at spanwise locations for V_∞ = 15 m/s

Gurney Flap

7 m/s

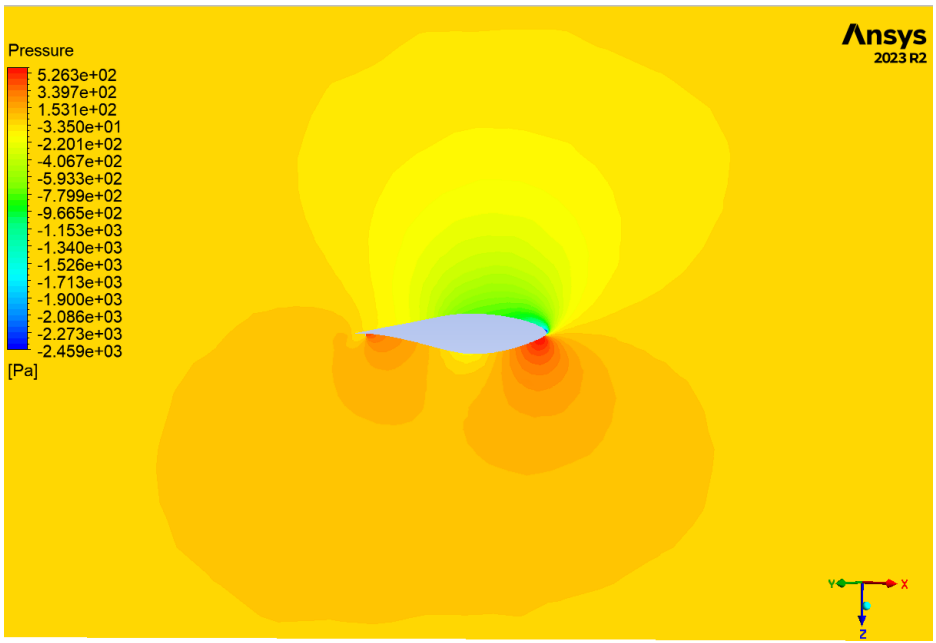

Figure 5.26: The pressure contour of the NREL Phase VI with the Gurney flap at 80% spanwise location for (V_∞ = 7 m/s)

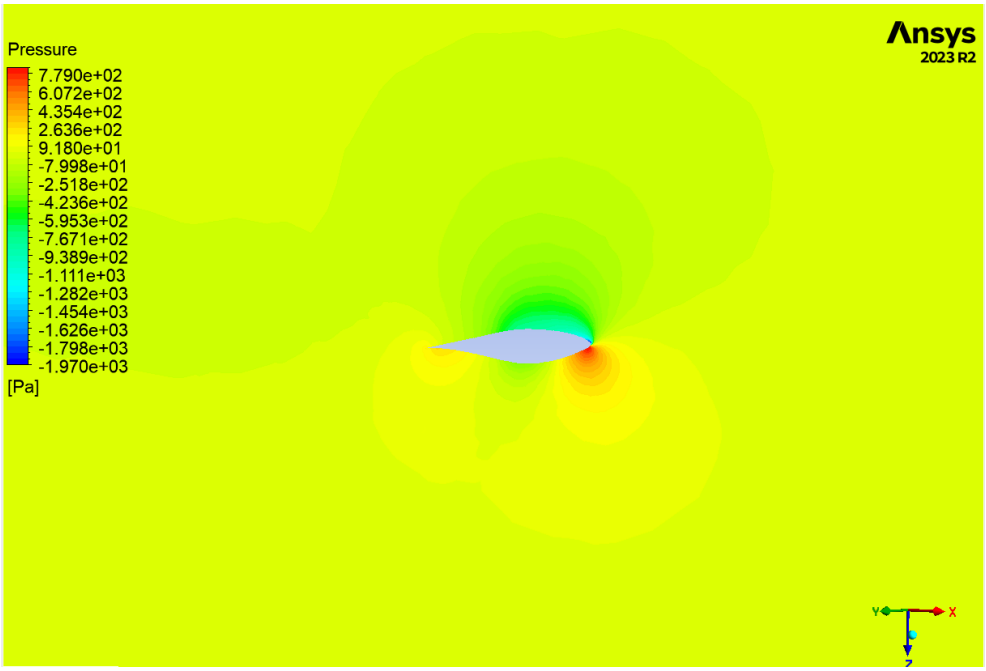

Figure 5.27: The pressure contour of the NREL Phase VI with the Gurney flap at 95% spanwise location for (V_∞ = 7 m/s)

10 m/s

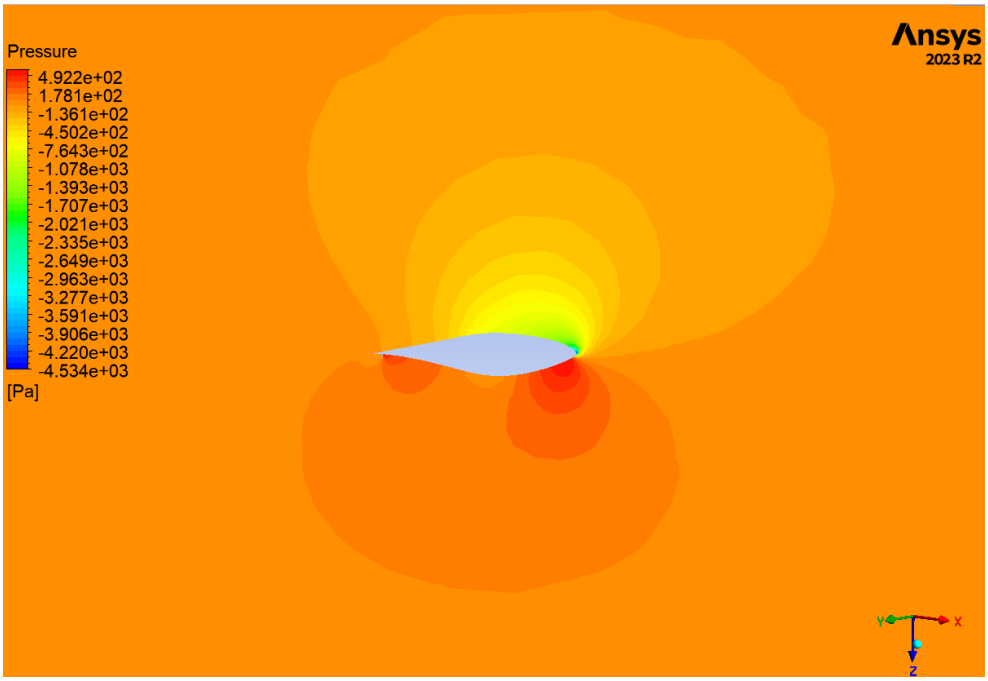

Figure 5.28: The pressure contour of the NREL Phase VI with the Gurney flap at 80% spanwise location for (V_∞ = 10 m/s)

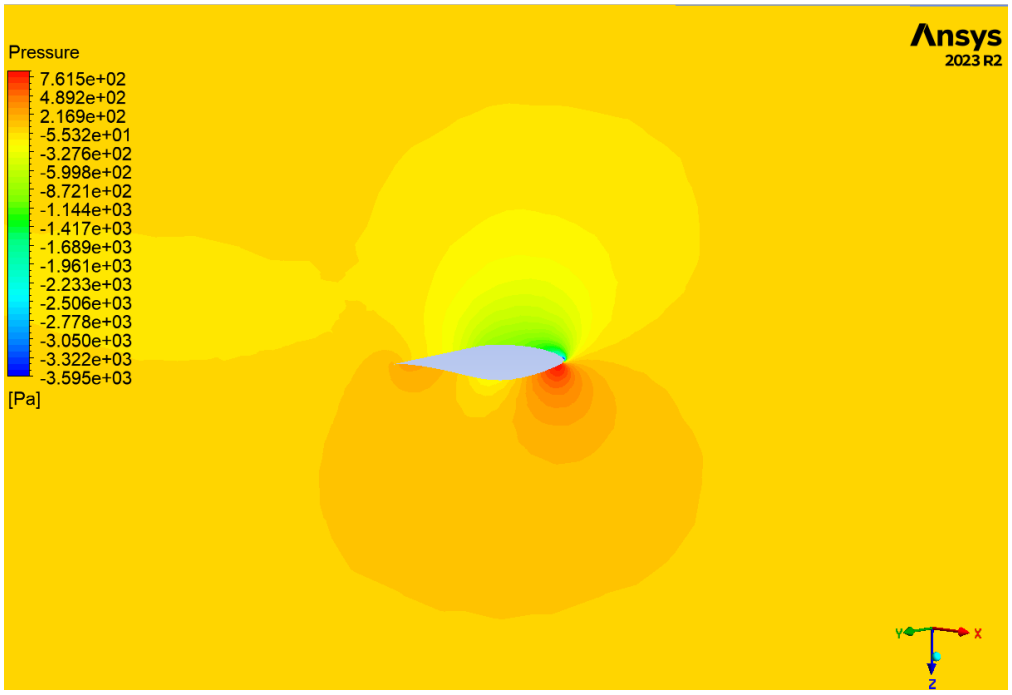

Figure 5.29: The pressure contour of the NREL Phase VI with the Gurney flap at 95% spanwise location for (V_∞ = 10 m/s)

13 m/s

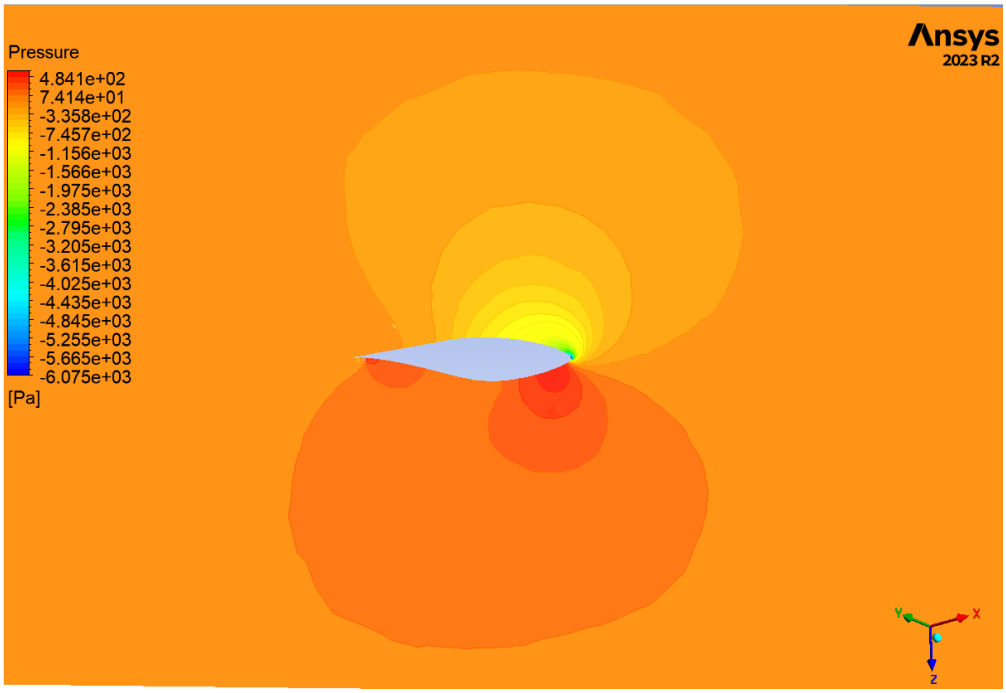

Figure 5.30: The pressure contour of the NREL Phase VI with the Gurney flap at 80% spanwise location for (V_∞ = 13 m/s)

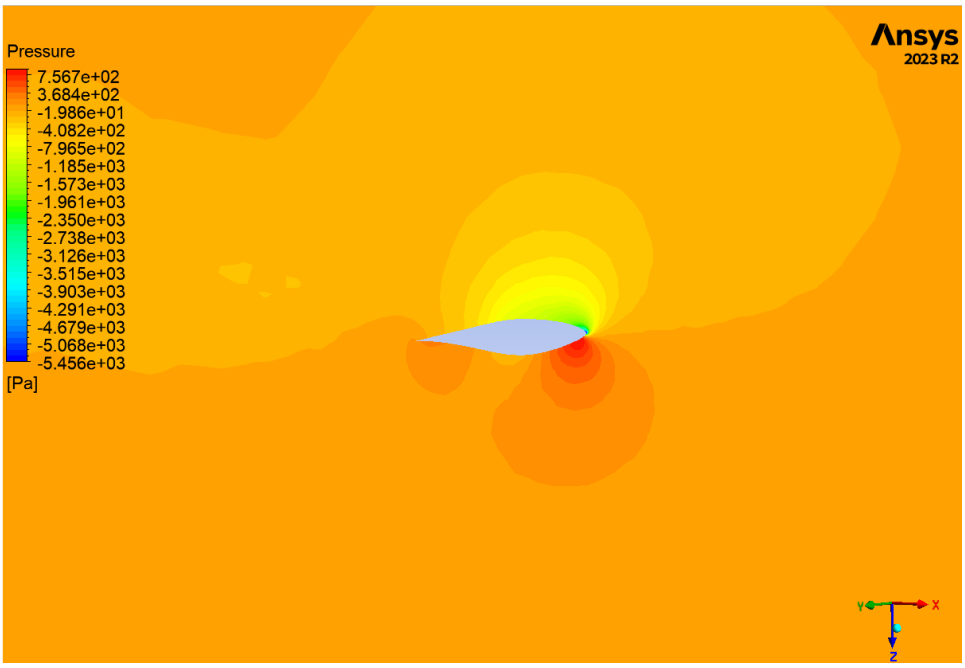

Figure 5.31: The pressure contour of the NREL Phase VI with the Gurney flap at 95% spanwise location for (V_∞ = 13 m/s)

15 m/s

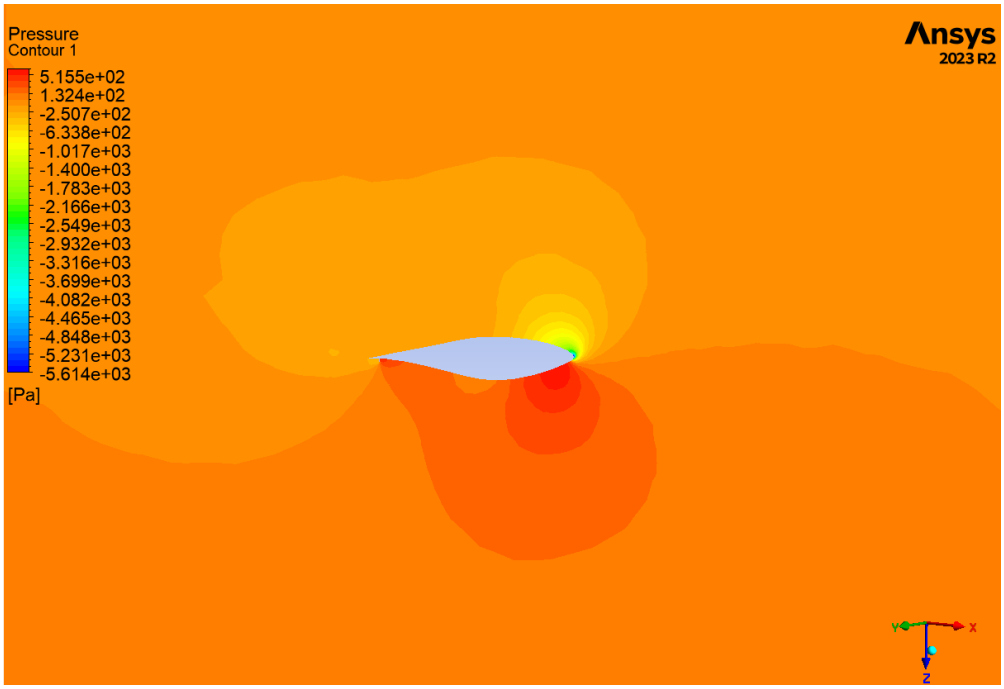

Figure 5.32: The pressure contour of the NREL Phase VI with the Gurney flap at 80% spanwise location for (V_∞ = 15 m/s)

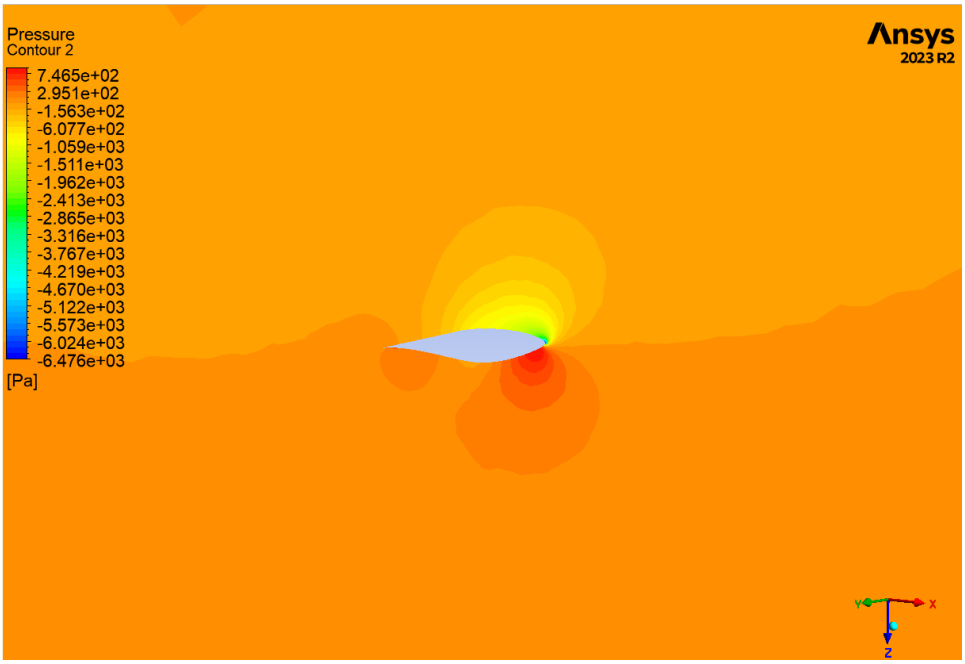

Figure 5.33: The pressure contour of the NREL Phase VI with the Gurney flap at 95% spanwise location for (V_∞ = 15 m/s)

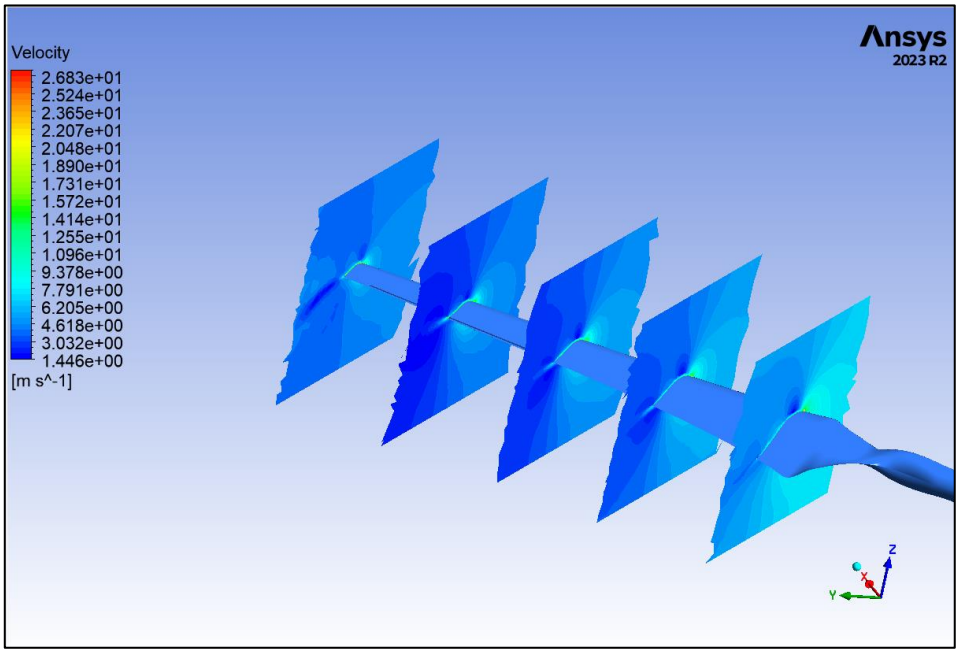

Figure 5.34: Velocity contour of the NREL Phase VI with the Gurney flap at spanwise locations for V_∞ = 7 m/s

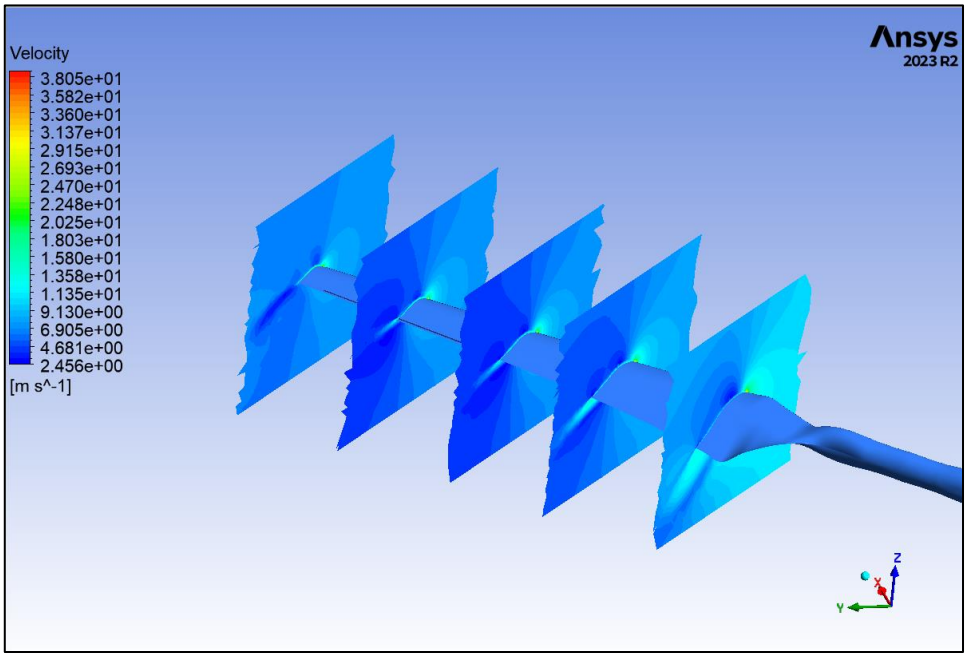

Figure 5.35: Velocity contour of the NREL Phase VI with the Gurney flap at spanwise locations for V_∞ = 10 m/s

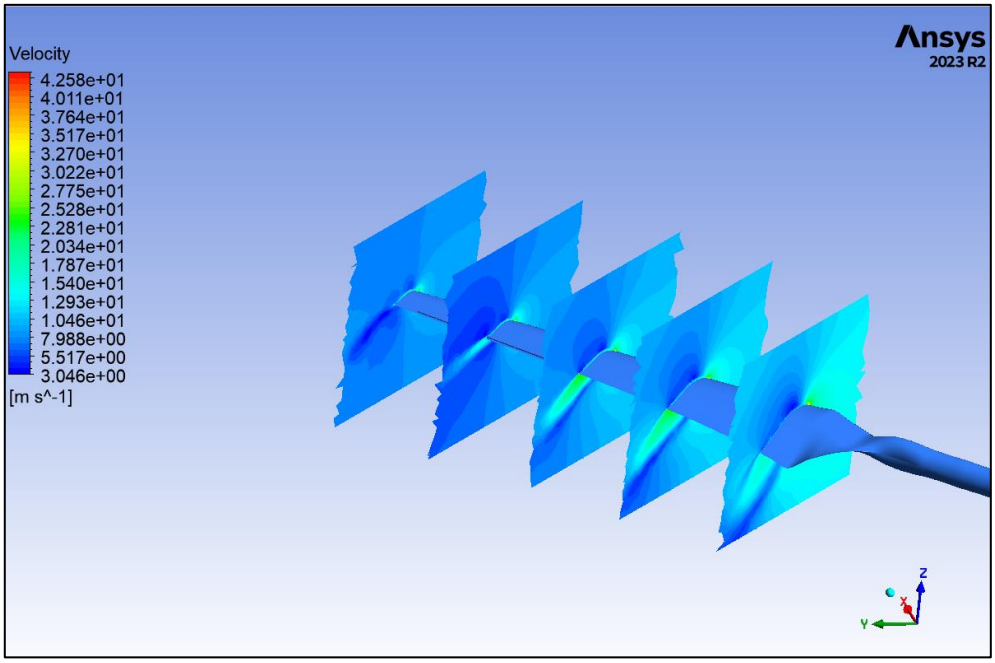

Figure 5.36: Velocity contour of the NREL Phase VI with the Gurney flap at spanwise locations for V_∞ = 13 m/s

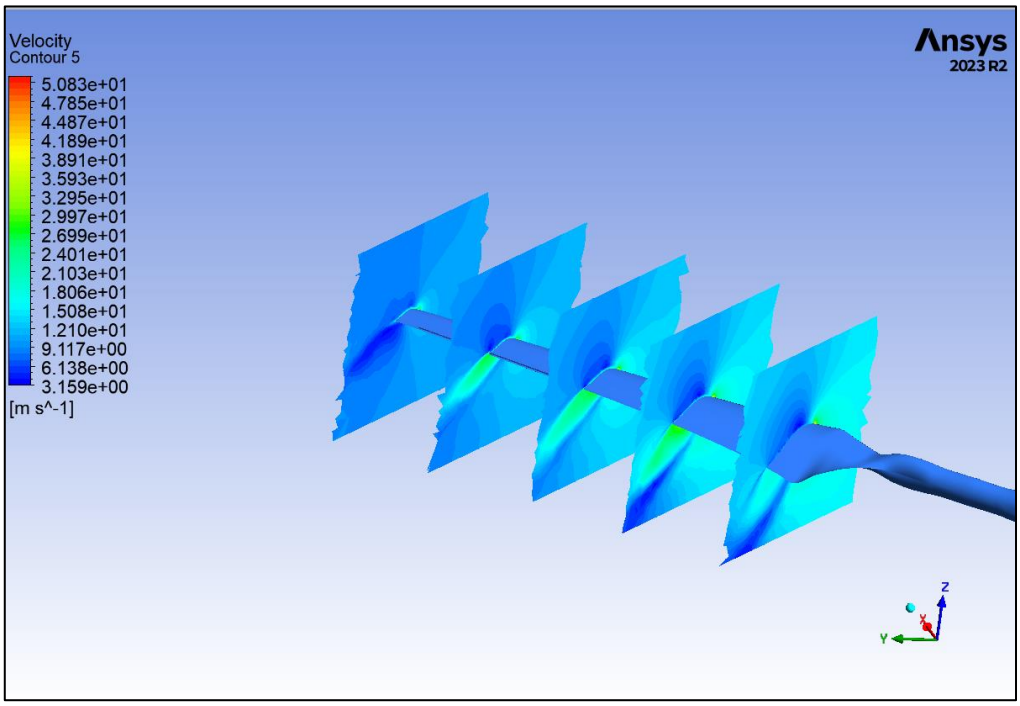

Figure 5.37: Velocity contour of the NREL Phase VI with the Gurney flap at spanwise locations for V_∞ = 15 m/s

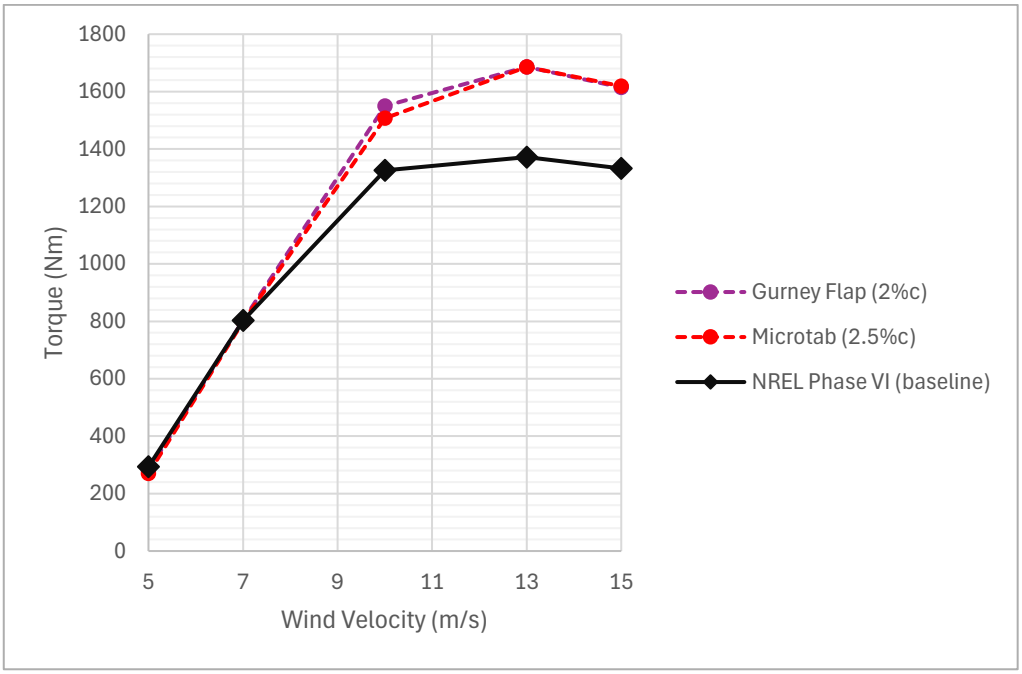

Figure 5.38: : A comparison between the torque generated when PFCs are utilized against the baseline NREL Phase VI blade

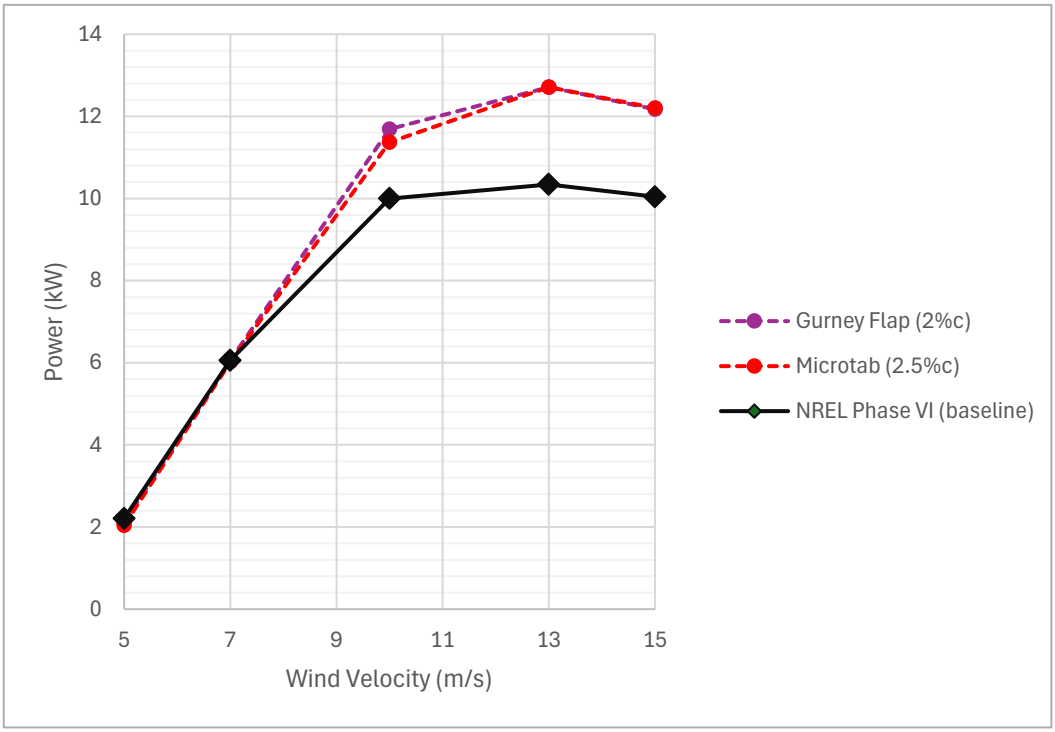

Figure 5.39: A comparison between the power generated when PFCs are utilized against the baseline NREL Phase VI blade

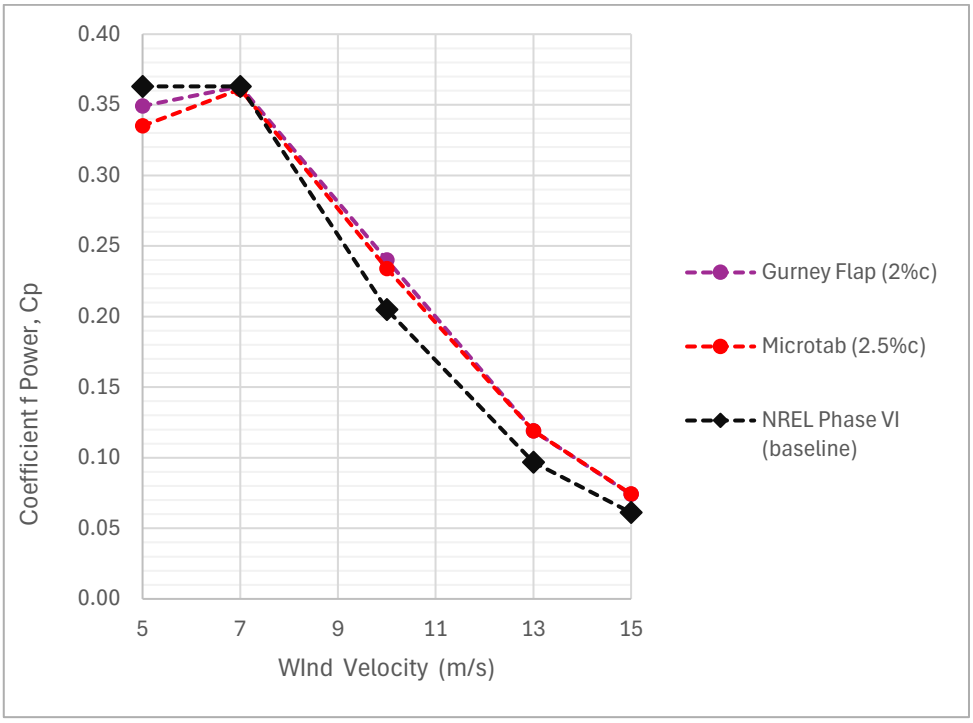

Figure 5.40: Measurement of the coefficients of power for the modified NREL Phase VI blades against baseline blade

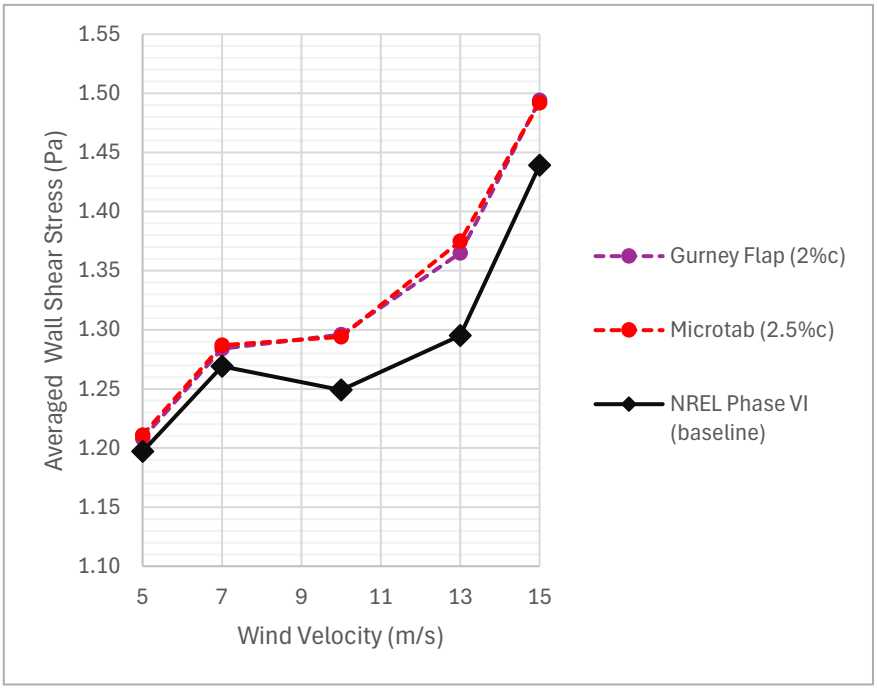

Figure 5.41: The average wall shear surface across the turbine blade for the different blade geometries

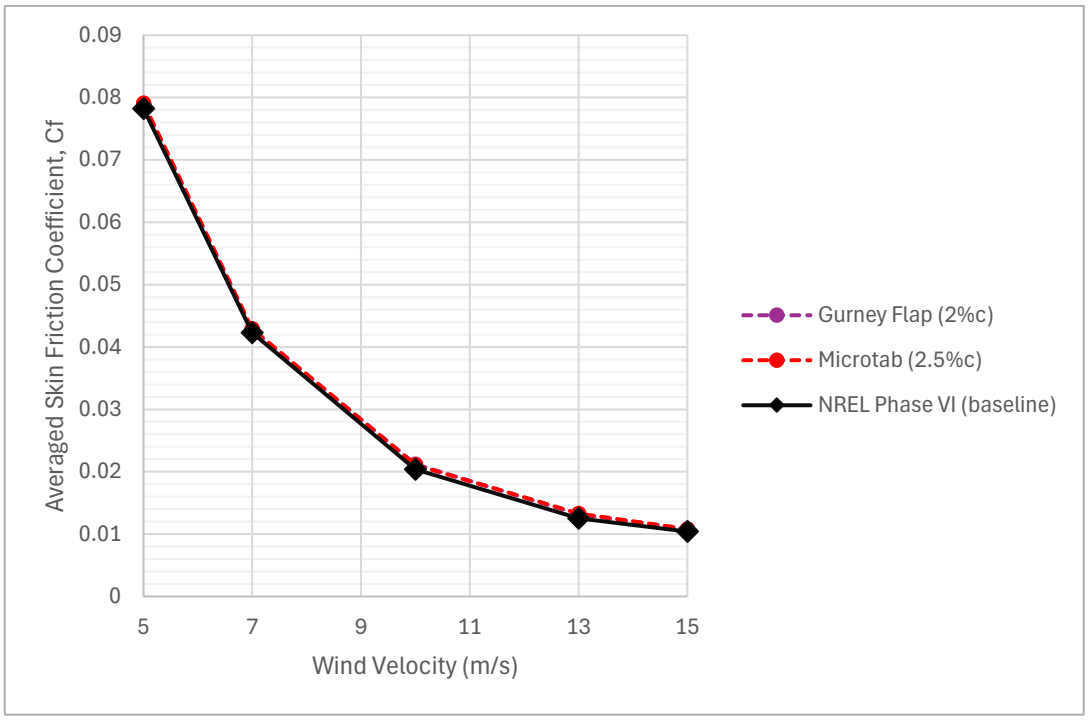

Figure 5.42: The average skin friction coefficient across the turbine blade for the different blade geometries

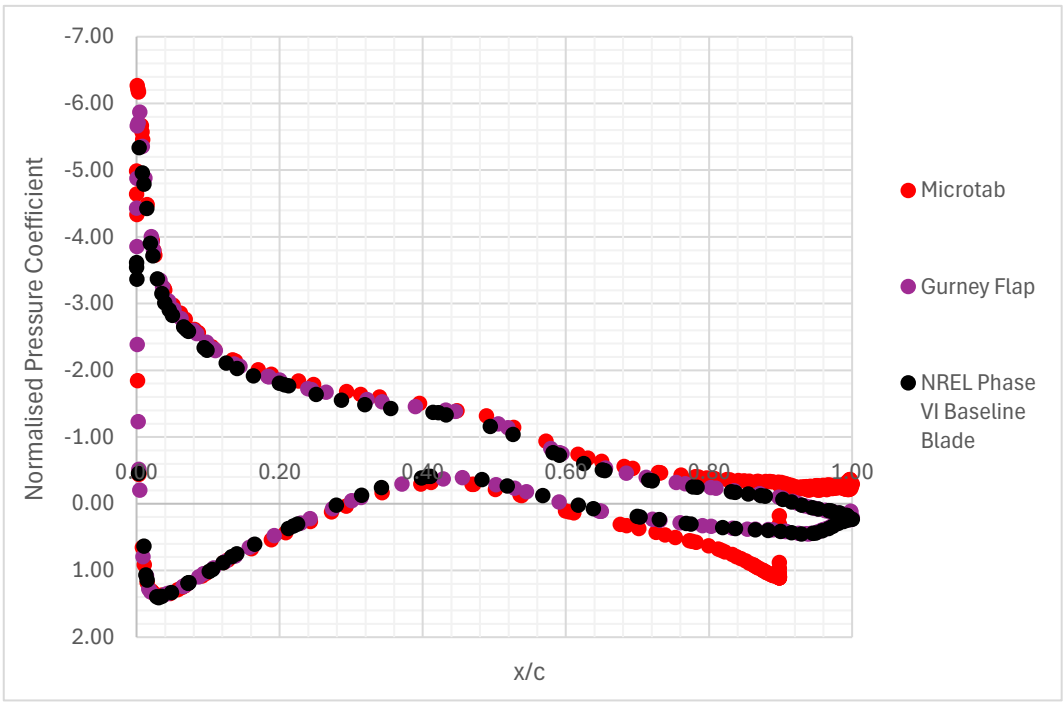

Figure 5.43: Normalised pressure coefficient at spanwise location (r/R = 0.95) for V_∞ = 10 m/s

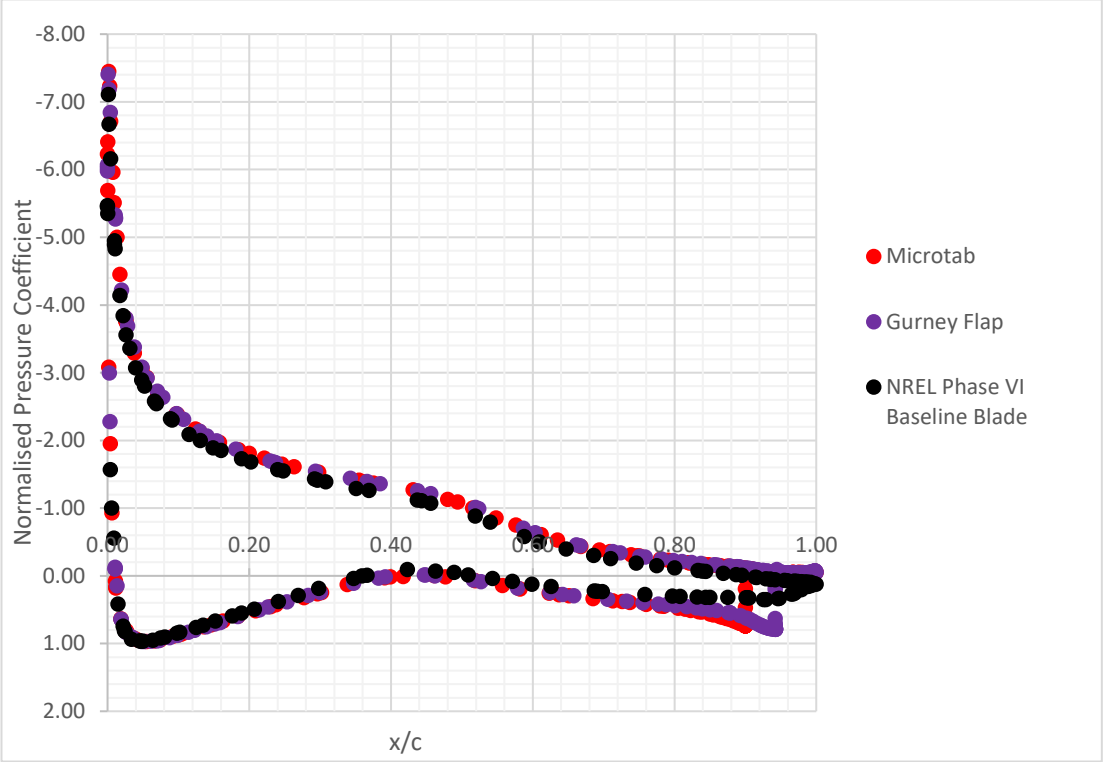

Figure 6.44: Normalised pressure coefficient at spanwise location (r/R = 0.80) for V_∞ = 10 m/s

The velocity contour plots in the tip region demonstrate the local acceleration that takes place in the boundary layer which energizes the flow and increases the energy capture of the turbine blade. As a result, more energy is extracted from the flow, reducing the kinetic energy in the downstream wake. The increase in overall power efficiency at 10 m/s for the GF is 3.5%, and for the MT is 2.9%. This indicates the usefulness of these passive devices particularly at the moderate to higher speeds. The average wall shear stress increases when the passive technologies are utilized, owing to enhanced turbulent mixing in the near-wall region (as shown in Figure 5.41). The enhanced flow momentum results in increased power and there is a noticeable increase at the higher velocities. Figure 5.42 shows the averaged skin friction coefficient across the turbine blade for the different blade geometries. The normalised pressure coefficient distribution shown in Figure 5.43 compares the baseline blade with the microtab and Gurney flap configurations at the 95% spanwise location. Both devices show a greater adverse pressure gradient than the baseline, which indicates increased circulation and greater potential for lift generation. Although, the Gurney flap is positioned in the outboard section, the residual effect of the device is evident in the tip region. For the microtab case, the pressure recovery occurs upstream from the trailing edge at x/c = 0.90 where the microtab is located.

Figure 5.44 illustrates the effect of the microtab and Gurney Flap at the 80% spanwise location along the blade chord. Both devices increase the pressure differential compared with the baseline NREL Phase VI blade, indicating enhanced aerodynamic loading. The devices effectively alter the camber of the aerofoil, with pressure recovery occurring near the trailing edge at approximately x/c = 0.90 for the microtab and x/c = 0.95 for the Gurney flap. Figure 5.45 shows the change in power generation in the pre-stall phase relative to the baseline blade.

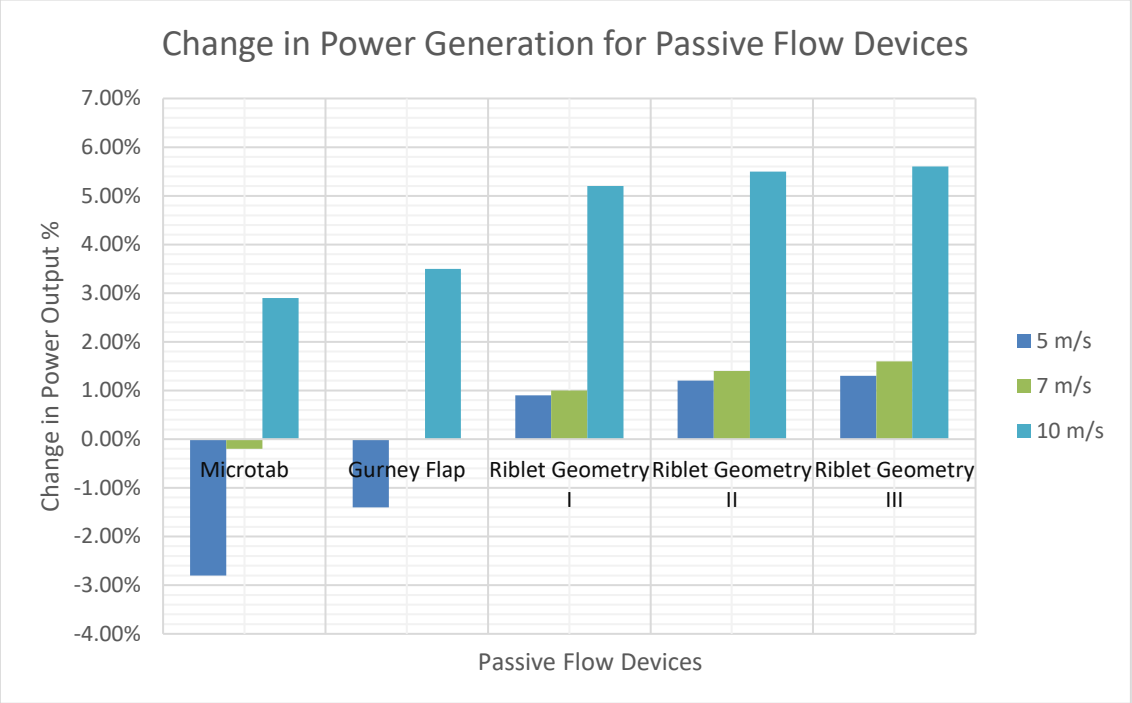

Figure 5.45: Percentage change in power output relative to the baseline blade for different passive flow-control devices at wind speeds of 5, 7, and 10 m/s.

5.4 Summary of the Chapter

This chapter investigates the effectiveness of passive flow control solutions comparing the change in power efficiency to the baseline turbine blade. The numerical approach taken when analysing the aerodynamic performance of the riblets differs from the other passive technologies. The effect of the riblets on boundary layer flow showed that the best geometry for optimizing performance is Riblet Geometry III. It had the capacity to suppress local TKE and C_f across the given wind speeds which resulted in optimized aerodynamic performance. Riblet Geometry III shows a marked improvement in the pre-stall and stall phases as shown in Figure 5.44. This side-by-side comparison shows the effectiveness of riblets in improving turbine blade especially in low wind speed regimes.

The microtab and the Gurney flap were appended onto the NREL Phase VI at different spanwise and chordwise locations. They both improved the aerodynamic performance of the original blade in stall conditions by energizing the boundary layer and encouraging circulation which led to increased loading and recovery of aerodynamic losses. The improvement in torque generation occurred primarily at the higher wind speeds, specifically at the wind speeds of 10,13, and 15 m/s. The increase at 13 m/s was the largest at 22.89%, followed by 21.49% at 15 m/s for the microtab. In contrast, the geometry with the Gurney flap registered an improvement of 22.91% and 21.20% at 13 m/s and 15 m/s, respectively. The decrease in torque for the microtab at 5 m/s was 8.03% and at 7 m/s it 0.51%. The Gurney flap only decreased in torque at 5 m/s by 4.2% and increased by 0.15% at 7 m/s; its superior low-speed effectiveness can be attributed to its placement.

The microtab incurred a greater drag penalty at the lower wind speeds and rather than energizing the boundary layer it blocked the movement of flow slightly. The decrease in aerodynamic performance for the passive flow devices at 5 m/s and 7 m/s is relatively marginal and the overall effect of the technology can be considered to be good. The contour plots show the localized effect of the flow technologies and how they affect the boundary layer, there is a general increase in the pressure differential and acceleration at the wall boundary which results in the prevention of flow separation and greater power generation. The increase in average wall shear stress and skin friction coefficient is a positive trend; it indicates that the passive flow devices act to prevent flow separation and therefore boost power efficiency. The skin friction drag may increase slightly but the pressure drag would have decreased substantially.

6 CONCLUSION

Increasingly, commercial wind companies and research institutes are striving to develop larger wind systems capable of utilising the energy reserves available in the troposphere. However, the concomitant challenges of developing larger blades that operate at higher altitudes include greater exposure to wind shear and turbulence. To characterize and manage the higher aerodynamic loads that the turbine blade undergoes in unsteady conditions, researchers are developing advanced solutions to optimise efficiency and mitigate aerodynamic losses. Key innovations include the use of prestressed concrete rather than steel for structural components, and the implementation of variable speed and pitch control systems allowing for the regulation of direction and angle of the blade, which are effective in optimising HAWT performance. Alongside these innovations in the wind industry is the development of technologies with a greater power capacity – such as generators and converters – which are important for effective transmission of energy. Amongst the proposed solutions, the PFC techniques are one of the most cost-effective methods of making HAWTs more eco-friendly and energy efficient.

The effects of unsteadiness in the ABL on HAWT performance are an understudied phenomena within wind literature. This study investigated the effects of unsteadiness on HAWT performance by modelling it using the URANS equations and comparing it to the steady-state results. The solution showed that the prediction of the URANS solver was more accurate at the lower wind speeds (λ = 7.58 and 5.42) when using the k-ω SST algorithm. At λ = 3.79 discrepancies begin to occur between the experimental and the computed results irrespective of the turbulence model. This is a normal occurrence in CFD simulations and flow separation begins to occur. It is at this point that k-ω SST stops giving the most accurate results, instead k-Ɛ realizable EWT gives a more accurate prediction. Interestingly, the unsteady k-ω SST gives a better prediction than the steady-state solver at λ = 2.92 but not at λ = 2.53 when the flow is in deep stall and the effects of tip vortex and root separation have become more pronounced – there is a clear overestimation. At the higher wind speeds, the k-Ɛ realizable EWT is able to give a more accurate prediction. Chapter 4 also presents measurements of static pressure and the pressure distribution across the blade at different wind speed. As the flow velocity increased there was greater static pressure on the blade surface indicating that there was more potential energy available for conversion. However, an adverse gradient could be seen on the suction side which implies flow separation has occurred. The computed results show good agreement with the experimental data at the lower wind speeds λ = 7.58 and 5.42. The pressure coefficient showed higher suction peaks at the wind speeds of 10 m/s and 13m/s , however,

at the radial positions' r/R =0.30 and r/R =0.47 the line plateaus which indicates leading edge separation. At 15 m/s the flow is essentially stagnant all over the flow and this is represented by the flat line which occurs from r/R = 0.30 to r/R = 0.80.

The numerical simulations performed in chapter 5 show a general improvement in the power generation of the NREL Phase VI at greater wind speeds when PFCs are utilized. The overall power efficiency of the turbine improved considerably with the addition of the Gurney Flap and microtab. The Gurney Flap showed superior performance overall owing to its position in the outboard region, being further upstream, it was able to boost overall performance over a greater range of wind speeds. The macroscopic effects of the riblets are represented in this study using the slip length concept which shows the benefits of reducing the shear stress of the blade to optimize aerodynamic performance. The reduction of viscous drag and wall shear stress is associated with measurable improvements in power generation for both the pre-stall and near-stall flow regimes. The simulation results show that the riblet acts to delay separation at 10 m/s. Figure 5.44 presents a direct comparison between the effectiveness of the different passive devices in the pre-stall phase and shows that the riblets improve the aerodynamic efficiency at the lower speeds, unlike the other passive technologies which incur a small drag penalty at these speeds. The Gurney Flap was found to be the most effective in the deep-stall phases when compared to the microtab. To fully capture the complex effects of fluid interactions with riblet geometries in deep-stall phases would require DNS investigation.

This work has effectively characterized the aerodynamic performance of the NREL Phase VI with PFC solutions under different physical conditions. The modifications made to the baseline blade produced significant improvements in each instance. The optimal configuration of the riblet geometry for the turbine blade was investigated in the parametric study. The results showed that viscous drag was sizably reduced when h+ was increased, and the resultant effect was an improvement in power generation. The parametric study shows the effects that riblets have on a full turbine blade under rotating conditions across a range of TSRs, providing valuable insight into the utility of riblets. The use of the slip length model improves the current understanding of the effects of riblets on turbine performance and produces accurate numerical results which are useful for the optimization of blade geometries. The numerical results produced in this work demonstrate excellent agreement with experimental data and enable a comprehensive analysis of multiple PFC devices.

6.1 Recommendations for future studies

The present work provides valuable insight into the ability of PFCs in enhancing aerodynamic performance and gives a greater understanding of the numerical methods that can be used to predict the effect of riblet technology. It lays a good methodological and theoretical framework for future numerical studies investigating this subject.

The following recommendations are made for future studies:

- Further investigation using higher-fidelity numerical methods, such as DNS or wall-resolved LES, would be valuable for assessing PFC performance under high wind speed and deep stall conditions.
- There remains a scarcity of validated 2D and 3D numerical studies assessing riblet performance on HAWTs, particularly against benchmark experimental data. Additional numerical and experimental studies are required to fully characterise the aerodynamic benefits of riblet technology. Related flow control concepts such as vortex generators, winglets, and trailing-edge serrations should also be examined.
- Additional parametric studies examining optimal riblet spacing, groove height, and number are needed to understand the relationship with aerodynamic performance under rotating conditions.
- The prognosticated increase in wind turbine height implies that turbine blades will be subjected to greater aerodynamic loads than previously experienced. Therefore, future research should focus on the mitigation of aerodynamic loading in order to improve structural reliability and service life.

REFERENCES

1. *The Aerodynamics of Wind Turbines.* **J.N. Sørensen, R. Mikkelsen, N. Troldborg, V.L. Okulov, and W.Z. Shen.** 1, Technical University of Denmark : Springer Dordrecht, 2013. 978-94-007-5967-1.

2. **Georgios Nikitas, Subhamoy Bhattacharya, Nathan Vimalan, Hasan Emre Demirci, Nikolaos Nikitas, Prashant Kumar.** 10 - Wind power: A sustainable way to limit climate change. [book auth.] Trevor M. Letcher. *Managing Global Warming.* s.l. : Academic Press, 2019.

3. **Center for Sustainable Systems.** *"Wind Energy Factsheet".* s.l. : University of Michigan , 2021. CSS07-09.

4. **Wind Energy Technologies Office.** *Land-Based Wind Market Reports: 2021 Edition.* Washington : U.S. Department of Energy, 2021.

5. *Grand challenges in the science of wind energy.* **Paul Veers, Katherine Dykes, Eric Lantz,Stephan Barth, Carlo L. Bottasso, Ola Carlson,Andrew Clifton, Johney Green, Peter Green, Hannele Holttinen, Daniel Laird, Ville Lehtomäki,Julie K. Lundquist, James Manwell, Melinda Marquis, Charles Meneveau, etc.** 6464, s.l. : American Association for the Advancement of Science, 2019, Vol. 366. 0036-8075.

6. **National Centers for Environmental Information.** *State of the Climate: Global Climate Report for Annual 2020.* s.l. : NOAA, 2021.

7. **Hannah Ritchie, Max Roser and Pablo Rosado.** CO_2 and Greenhouse Gas Emissions. *Our World in Data.* 2020.

8. **International Renewable Energy Agency.** *Future of wind: Deployment, investment, technology, grid integration and socio-economic aspects.* Abu Dhabi : IRENA , 2019. 978-92-9260-155-3.

9. **The International Renewable Energy Agency.** *Renewable Energy Statistics 2021.* Abu Dhabi : IRENA (2021), 2021. 978-92-9260-356-4.

10. **IEA (2021).** *Renewables 2021.* Paris : IEA, 2021.

11. **IRENA.** World Adds Record New Renewable Energy Capacity in 2020. *Irena.org.* [Online] International Renewable Energy Agency, 5 April 2021. [Cited: 6 April 2022.] https://www.irena.org/newsroom/pressreleases/2021/Apr/World-Adds-Record-New-Renewable-Energy-Capacity-in-2020.

12. *Geophysical potential for wind energy over the open oceans.* **Anna Possner, Ken Caldeira.** 43, Stanford : PNAS, 2017, Vol. 114.

13. **Office of Energy Efficiency & Renewable Energy.** How Do Wind Turbines Survive Severe Storms? *Energy.Gov.* [Online] 30 Jun2 2017. [Cited: 19 April 2022.] https://www.energy.gov/eere/articles/how-do-wind-turbines-survive-severe-storms.

14. **R. Wiser, M. Bolinger,.** *2017 wind technologies market report.* Washington : Wind Energy Technologies Office, 2018.

15. **wind.energy.gov.** Wind Gallery. *Wind Energy Technologies Office.* [Online] Office of Energy Efficiency & Renewable Energy. [Cited: 12 May 2022.] https://www.energy.gov/eere/wind/photos/wind-gallery.

16. *Advanced Science Letters.* **Guo, Lanhui, et al.** 3, s.l. : ResearchGate, 2011, Vol. IV. 1936-6612.

17. **GE Renewable Energy.** Haliade-X offshore wind turbine. *GE Renewable Energy.* [Online] General Electric. [Cited: 21 May 2022.] https://www.ge.com/renewableenergy/wind-energy/offshore-wind/haliade-x-offshore-turbine#:~:text=Power%20meets%20efficiency,-The%20combination%20of&text=One%20Haliade%2DX%2014%20MW,typical%20German%20North%20Sea%20site..

18. **Hoen, B.D., Diffendorfer, J.E., Rand, J.T., Kramer, L.A., Garrity, C.P., and Hunt, H.E.** Science Base Catalog. *United States Wind Turbine Database.* [Online] U.S. Geological Survey, American Clean Power (ACP) Association, and Lawrence Berkeley National Laboratory data release, 19 April 2018. [Cited: 03 April 2022.] https://doi.org/10.5066/F7TX3DN0.

19. *Steady and Unsteady Wind Loading of Buildings and Structures.* **Scruton, C., E. W. E. Rogers, J. B. Menzies, and R. S. Scorer.** 1199, s.l. : Royal Society, 1971, Vol. 269. 0080-4614.

20. **Camuffo, Dario.** Atmospheric Stability and Pollutant Dispersion. *Microclimate for Cultural Heritage (Second Edition).* s.l. : Elsevier, 2014.

21. **Craig MacEachern, İlhami Yıldız.** 1.16 Wind Energy. [book auth.] Ibrahim Dincer. *Comprehensive Energy Systems.* s.l. : Elsevier, 2018, Vol. 1.

22. *An Unsteady Aerodynamic Model for HAWT Performance Including Tower Shadow.* **Coton, Tongguang Wang and Frank N.** 5, s.l. : Sage Publications Ltd., 1999, Vol. 23. 0309524X.

23. **Valery L. Okulov, Gijs A. M. van Kuik.** *The Betz–Joukowsky limit: on the contribution to rotor aerodynamics by the British, German and Russian scientific schools.* s.l. : Wiley Online Library, 2011.

24. **C. Strangfeld, C. L. Rumsey, H. Muller-Vahl, D. Greenblatt, C. N. Nayeri, C. O. Paschereit.** *Unsteady wind turbine blade aerodynamics: Experiments, computation and theory.* Dallas : Research Gate, 2015.

25. *QBLADE: An Open Source Tool for Design and Simulation of Horizontal and Vertical Axis Wind Turbines.* **D. Marten, J. Wendler, G. Pechlivanoglou, C. N. Nayeri, C.O. Paschereit.** 3, s.l. : International Journal of Emerging Technology and Advanced Engineering, 2013, Vol. 3. 2250-2459.

26. *The Aerodynamics of Wind Turbines.* **J.N. Sørensen, R. Mikkelsen, N. Troldborg, V.L. Okulov, and W.Z. Shen.** 1, Technical University of Denmark : Springer Dordrecht, 2013. 978-94-007-5967-1.

27. **Arnfred, J. T.** Developments and Potential Improvements in Wind Power Utilization. *Renewable Energy.* s.l. : Routledge, 2011.

28. **Paul Gipe, Erik Mollerstrom.** *An overview of the history of wind turbine development: Part 1—The early wind tubines until the 1960s.* s.l. : Wind Engineering, 2022. 2048-402X.

29. *Design of Wind Power Plants in Denmark.* **United Nations Conference of New Sources of Energy.** s.l. : United Nations, 1961. Vol. 7.

30. **Bertram, Volker.** Propellers. *Practical Ship Hydrodynamics (Second Edition).* s.l. : Butterworth-Heinemann, 2012.

31. **Önel, Hüseyin Can.** *Numerical simulations of wind turbine wake interactions using actuator line and LES models, Thesis (M.S.).* Middle East Technical University : Graduate School of Natural and Applied Sciences, Aerospace Engineering, 2019.

32. **Keogh, Brad.** *Performance quantification of marine current energy converters in constrained flow fields.* s.l. : University of Southampton, Faculty of Engineering and the Environment, 2016. 393735.

33. **Schaffarczyk, Alois P.** *Aerodynamics and aeroelastics of wind turbines .* Kiel : WIT Press, 2010. 1755-8336.

34. *Computational Actuator Disc Models for Wind and Tidal Applications.* **B. Johnson, J. Francis, J. Howe, J. Whitty.** s.l. : Journal of Renewable Energy, 2014. 172461.

35. **Glauert, H.** Airplane propellers in Aerodynamic Theory. [book auth.] W.F. Durand. *Aerodynamic Theory .* s.l. : Springer, 1935, Vol. IV.

36. *Analysis and Validation of Glauert Rotor Design.* **Jens N. Sørensen, Néstor Ramos-García and Valéry L. Okulov.** s.l. : Journal of Physics: Conference Series, 2022, Vol. 2265. 2265 032047.

37. **University of Notre Dame.** *Momentum Theory.* [Online] [Cited: 5 September 2022.] https://www3.nd.edu/~tcorke/w.WindTurbineCourse/Aerodynamics_Presentation.pdf.

38. *A Short History of (Wind Turbine) Aerodynamics.* **Okulov, Jens Nørkær Sørensen and Valery.** s.l. : DTU Vindenergi, 2018.

39. **Massimo Gennaretti, Riccardo Giansante.** *Kutta–Joukowski Theorem for Unsteady Linear Aerodynamics.* Rome : AIAA Journal, 2022.

40. **Gary A. Flandro, Howard M. McMahon, Robert L. Roach.** Two-Dimensional Airfoils. *Basic Aerodynamics Incompressible Flow.* s.l. : Cambridge University Press, 2012.

41. **K. Jayanarasimhan, and V. Subramani-Mahalakshmi.** *Wind Turbines - Advances and Challenges in Design, Manufacture and Operation [Working Title].* s.l. : IntechOpen, 2022.

42. *V. An investigation of the flow of air an aërofoil of infinite span.* **L.W. Bryant, D. H. Williams, and G. I. Taylor.** s.l. : Philosophical Transactions of the Royal Society A, 1926, Vols. 225, 199.

43. **J. Y. Zhu, T. S. Liu, L. Q. Liu, S. F. Zou, J. Z. Wu.** *Causal mechanisms in airfoil-circulation formation.* s.l. : AIP Publishing LLC, 2015. 123601.

44. **Johnson, Claes.** Unphysical AIAA Lift Theory. *CJ on Mathematics and Science: Towards understanding by critical enquiry.* [Online] 23 September 2012. [Cited: 19 September 2022.] http://claesjohnson.blogspot.com/2012/09/unphysical-aiaa-lift-theory.html.

45. **Pechlivanoglou, Georgios.** *Passive and active flow control solutions for wind (Doctoral Thesis).* Berlin Institute of Technology : Institute for Fluid Mechanics and Technical Acoustics, 2013.

46. **Md. Kamal Uddin, Md. Zahidul Islam, Md. Rokunuzzaman, Robiul Islam Rubel.** *Experimental and Numerical Measurement of Lift and Drag Force of NACA 0015 Aerofoil Blade.* Department of Mechanical Engineering, Rajshahi University of Engineering& Technology, Rajshahi-6204, Bangladesh : International Conference on Mechanical, Industrial and Materials Engineering 2015, 2015.

47. *Geometry Design Optimization of a Wind Turbine Blade Considering Effects on Aerodynamic Performance by Linearization.* **Yang, K.** 9, s.l. : Energies, 2020, Vol. 13. 2320.

48. **Drela, M.** *XFoil.* Cambridge : Massachusetts Institute of Technology, 2000.

49. **Conaill Soraghan, William Leithead, Peter Jamieson.** *Influence of Lift to Drag Ratio on Optimal Aerodynamic Performance of Straight Blade Vertical Axis Wind Turbine.* s.l. : University of Strathclyde, 2013.

50. **Winarto, Hadi.** AERO 2258A THIN AEROFOIL THEORY Lecture Notes. [Online] 15 March 2004. [Cited: 5 October 2022.] https://ftp.unpad.ac.id/orari/library/library-non-ict/aero/docs/Aero2258A%20Thin%20Aerofoil%20TheoryLecture%20Notes.pdf.

51. *CFD simulations for the selection of an appropiate blade profile for improving energy efficiency in axial flow mine ventilation fans.* **Durga Charan Panigrahi, Devi Prasad Mishra.** 1, Department of Mining Engineering, Indian School of Mines (Dhanbad, Jharkhand, India) : Journal of Sustainable Mining, 2014, Vol. 13. 2300-3960 .

52. *Sensitivity of Key Parameters in Aerodynamic Wind Turbine Rotor Design on Power and Energy Performance.* **Bak, Christian.** Roskilde, Denmark : Journal of Physics: Conference Series, 2007, Vol. 75. 012008.

53. *Turbulence and wind turbines .* **Jakob Mann, Joachim Peinke, Arno J. Brand.** s.l. : Journal of Physics: Conference Series , 2011, Vol. 318. 072005.

54. *On Adapting a Small PM Wind Generator for a Multiblade, High Solidity Wind Turbine.* **K. D. Visser, M. A. Khan, P. Pillay.** 3, s.l. : IEEE TRANSACTIONS ON ENERGY CONVERSION, 2005, Vol. 30.

55. *Influence of the Solidity Ratio on the Small Wind Turbine Aerodynamics.* **Karol Zawadzki, Wojciech Śmiechowicz, Małgorzata Stępień, Anna Baszczyńska, Michał Tarkowski.** Łódź, Poland : E3S Web of Conferences, 2021, Vol. 242.

56. **C. E. A. Silva, D. S. Oliveira Jr., L. H. S. C. Barreto, R. P. T. Bascopé.** *A Novel Three-Phase Rectifier with High Power Factor for Wind Energy Conversion Systems.* Bonito : 2009 Brazilian Power Electronics Conference, 2009. 2688956.

57. *Comparison and Selection of Airfoils for Small Wind Turbine between NACA and NREL's S series Airfoil Families.* **Md. Robiul Islam, Labid Bin Bashar, Dip Kumar Saha,**

Nazmus Sowad Rafi. 2, s.l. : International Journal of Research in Electrical, Electronics and Communication Engineering, 2019, Vol. 4.

58. **Umesh Chaudhary, Praveen Tripathy, Sisir Kumar Nayak.** *Micro and Small-Scale HAWT Blades AirfoilsStudy through CFD for Low Wind Applications.* Indian Institute of Technology, Guwahati : Research Scholars Congress , 2015.

59. *Wind turbine performance under icing conditions.* **C. Hochart, G. Fortin, J. Perron, A. Ilinca,.** 4, s.l. : Wind Energy , 2008, Vol. 11.

60. *Investigation of aerodynamic performance characteristics of a wind-turbine-blade profile using the finite-volume method.* **Onur Erkana, Musa Ozkan,T. Hikmet Karakoc, Stephen J. Garrett, Peter J. Thomas.** s.l. : Renewable Energy, 2020, Vol. 161. 0960-1481.

61. **P.J. Moriarty, A.C. Hansen.** *AeroDyn Theory Manual.* s.l. : National Renewable Energy Laboratory, 2005.

62. *Unsteady Blade Element-Momentum Method Including Returning Wake Effects.* **Cláudio Tavares Silva, Maurício Vicente Donadon.** s.l. : Journal Aerospace Teachnology and Management, 2013, Vol. 5.

63. **Tang, Xinzi.** *Aerodynamic Design and Analysis of Small Horizontal Axis Wind Turbine Blades (PhD Thesis).* Preston : University of Central Lancashire , 2012.

64. **Okita W.M., Ismail K.A.R., Moura L.F.M.** *Aerodynamic performance and annual energy production of small horizontal axis windmill using different airfoils.* s.l. : Proceedings of the 10th International Conference on Rotor Dynamics– IFToMM, 2018.

65. **Prandtl, Betz.** *Vier Abhandlungen zur Hydrodynamik und Aerodynamik.* Göttingen : Universitätsverlag Göttingen, 1927. 3941875752.

66. *Tip Loss Factor Effects on Aerodynamic Performances of Horizontal Axis Wind Turbine.* **Y. El khchine, M. Sriti.** s.l. : Energy Procedia, 2017, Vol. 118. 1876-6102.

67. **Buhl, M.L.J.** *A new empirical relationship between thrust coefficient and induction factor for the turbulent windmill state.* s.l. : NREL, 2005.

68. *The Buhl correction factor applied to high induction conditions for tidal stream turbines.* **J.C. Chapman, I. Masters, M. Togneri, J.A.C. Orme,.** s.l. : Renewable Energy, 2013, Vol. 60. 0960-1481.

69. *A numerical analysis of unsteady inflow wind for site specific vertical axis wind turbine: A case study for Marsabit and Garissa in Kenya.* **David Wafula Wekesa, Cong Wang, Yingjie Wei, Joseph N. Kamau, Louis Angelo M. Danao,.** s.l. : Elsevier, 2015, Vol. 76. 0960-1481.

70. **Aljuhashy, Radwan.** *The Influence of Unsteady Wind on the Performance and Aerodynamics of Horizontal Axis Wind Turbines, PhD thesis.* s.l. : University of Sheffield, 2019.

71. *HAWT Design and Performance Evaluation: Improving the BEM Theory Mathematical Models.* **R. Lanzafame, S. Mauro, M. Messina.** s.l. : Energy Procedia, 2015, Vol. 82. 1876-6102.

72. *Improved BEM Method for HAWT Performance Predictions.* **Hamlaoui, Mohammed Nadjib, Smaili, Arezki and Fellouah, Hachimi.** s.l. : 2018 International Conference on Wind Energy and Applications in Algeria (ICWEAA), 2018.

73. *The Application of Passive Air Jet Vortex-generators to Stall Suppression on Wind Turbine Blades.* **Simon A. Prince, Carmine Badalamenti, Constantinos Regas.** 1, s.l. : Wind Energy, 2017, Vol. 20.

74. **Bak C, Fuglsang P, Sørensen NN, Madsen HA, Shen WZ, Sørensen JN.** *Airfoil characteristics for wind turbines.* s.l. : Risø National Laboratory, 1999. Risø-R-1065(EN).

75. **Benoît Chezeau, Christophe Vial.** Modeling and Simulation of the Biohydrogen Production Processes. [book auth.] S. Venkata Mohan, Jo-Shu Chang, Patrick C. Hallenbeck, Christian Larroche Ashok Pandey. *Biomass, Biofuels, Biochemicals.* s.l. : Elsevier, 2019.

76. *A Flexible Framework and Model Library for Process Simulation, Optimization and Control.* **Andrew Lee, Jaffer H. Ghouse, Qi Chen, John C. Eslick, John D. Siirola,**

Ignacio E. Grossman, David C. Miller,. s.l. : Computer Aided Chemical Engineering, Elsevier, 2018, Vol. 44. 9780444642417.

77. **Simon P. Neill, M. Reza Hashemi.** Ocean Modelling for Resource Characterization. *Fundamentals of Ocean Renewable Energy.* s.l. : Elsevier, 2018.

78. **Patankar, Suhas V.** *Numerical Heat Transfer and Fluid Flow.* s.l. : Hemisphere Publishing Corporation, 1980. 978-0891165224.

79. *A Comparison of Various Turbulence Models for Analysis of Fluid Microjet Injection into the Boundary Layer over a Flat Surface.* **Mohammad Javad Pour Razzaghi, Seyed Mojtaba Rezaei Sani, Yasin Masoumi, Guoping Huan.** s.l. : arXiv, 2022.

80. **Chris Baker, Terry Johnson, Mark Sterling, Dominic Flynn, Hassan Hemida, Andrew Quinn, David Soper.** Computational Techniques. *Train Aerodynamics .* s.l. : Elsevier, 2019.

81. **Mohammad Javad Pour Razzaghi, Seyed Mojtaba Rezaei Sani, Yasin Masoumi, Guoping Huan.** *A Comparison of Various Turbulence Models for Analysis of Fluid Microjet Injection into the Boundary Layer over a Flat Surface.* s.l. : Semantic Scholar, 2022.

82. **John Gorman, Lijing Cheng and John P. Abraham.** Turbulence Models Commonly Used in CFD. [book auth.] Suvanjan Bhattacharyya. *Applications of Computational Fluid Dynamics Simulation and Modeling.* London, United Kingdom : IntechOpen, 2021.

83. **Breunig, Jim.** Which Turbulence Model Should You Use For Your CFD Analysis? *Xceed Engineering.* [Online] 5 July 2017. [Cited: 30 October 2022.] https://www.xceed-eng.com/which-cfd-turbulence-model/.

84. *A comparative study of RANS-based turbulence models for an upscale wind turbine blade.* **Muiruri, P.I., Motsamai, O.S. & Ndeda, R.** 237, s.l. : SN Appl. Sci, 2019, Vol. 1.

85. *A numerical study of the influence of blade profile and solidity on the performance of vertical axis wind turbines.* **O. Eboibi, L.A.D.R. Howell, J.M. Edwards.** Dallas, Texas :

51st AIAA Aerospace Sciences Meeting including the New Horizons Forum and Aerospace Exposition, 2013.

86. *Design and optimisation of low speed Horizontal-Axis Wind Turbines using Openfoam.* **Dena Hendriana, Tommy Firmansyah, Joga Dharma Setiawan, Dodi Garinto.** 21, s.l. : ARPN Journal of Engineering and Applied Sciences, 2015, Vol. 10. 1819-6608.

87. *Horizontal axis wind turbines passive flow control methods: a review.* **Sudhanshu S. Manerikar, Sourabh R. Damkale, Sanjay N. Havaldar, Shubhanga V Kulkarni, Yash A. Keskar.** 1, Pune, India : IOP Publishing, 2021, Vol. 1136. 012022.

88. *A review on the use of passive flow control devices as performance enhancement of lift-type vertical axis wind turbines.* **Syawitri, T. P., Yao, Y., Yao, J., & Chandra, B.** 4, s.l. : Wiley Interdisciplinary Reviews: Energy and Environment, 2022, Vol. 11.

89. *Turbulent boundary layer in an adverse pressure gradient - Effectiveness of riblets.* **Nieuwstadt, J. R. Debisschop and F. T. M.** 5, s.l. : AIAA Journal, 1996, Vol. 34.

90. *Near-wall structure of a turbulent boundary layer with riblets.* **Choi, Kwing-So.** s.l. : Journal of Fluid Mechanics, 1989, Vol. 208.

91. *Viscous drag reduction using riblets on NACA 0012 airfoil to moderate incidence.* **Sundaram, S., Viswanath, P. R., & Rudrakumar, S.** s.l. : AIAA Journal, 1996, Vol. 34.

92. *Drag reduction of large wind turbine blades through riblets: Evaluation of riblet geometry and application strategies.* **Chamorro, L. P., Arndt, R. E., & Sotiropoulos, F. (.** s.l. : Renewable Energy, 2013, Vol. 50.

93. *Flow Control Methods and Their Applicability in Low-Reynolds-Number Centrifugal Compressors—A Review.* **Jonna Tiainen, Aki Grönman, Ahti Jaatinen-Värri, and Jari Backman.** 2, s.l. : International Journal of Turbomachinery Propulsion and Power, 2018, Vol. 3.

94. *Drag Reduction Using Riblet Film Applied to Airfoils for Wind Turbines.* **Sareen, A., Deters, R. W., Henry, S. P., and Selig, M. S.** 2, s.l. : J. Sol. Energy Eng., 2014, Vol. 136. 021007.

95. *Reynolds-number dependence of turbulent skin-friction drag reduction induced by spanwise forcing.* **Gatti, D., & Quadrio, M.** s.l. : Journal of Fluid Mechanics, 2016, Vol. 802.

96. *Experiments on drag-reducing surfaces and their optimization with an adjustable geometry.* **Bechert, D. W., Bruse, M., Hage, W., van der Hoeven, J. G. T., and Hoppe, G.** 1, s.l. : Journal of Fluid Mechanics, 1997, Vol. 338.

97. *Flow field analysis of a turbulent boundary layer over a riblet surface.* **Lee, S.-J. Lee & S.-H.** s.l. : Experiments in Fluids , 2001, Vol. 30.

98. *Recent advances in manufacturing of riblets on compressor blades and their aerodynamic impact.* **C. Lietmeyer, B. Denkena, T. Krawczyk, R. Klin, L. Overmeyer, B. Wojakowski, E. Reithmeier, R. Scheuer, T. Vynnyk, J.R. Seume.** 4, s.l. : ASME Journal of Turbomachinery, 2013, Vol. 135.

99. *Numerical Supported Design of Continuously Adapted Riblets for Viscous Drag on a NREL Wind Turbine Airfoil.* **Karsten Oehlert, Jan H. Haake, Konrad M. Hartung.** s.l. : 32nd European Conference on Modelling and Simulation,, 2018. 2522-2422.

100. *Effect of non-ideally manufactured riblets on airfoil and wind turbine performance.* **Jonna Tiainen, Aki Grönman, Ahti Jaatinen-Värri, Lauri Pyy.** s.l. : Renewable Energy, 2020, Vol. 155. 0960-1481.

101. *Parametric study of low-profile vortex generators.* **P. Martínez-Filgueira, U. Fernandez-Gamiz, E. Zulueta, I. Errasti, B. Fernandez-Gauna.** 28, s.l. : International Journal of Hydrogen Energy, 2017, Vol. 42. 0360-3199.

102. **Sullivan, T. L.** *Effect of vortex generators on the power conversion performance and structural dynamic loads of the Mod-2 wind turbine.* s.l. : NASA Lewis Research Center, 1984. DOE/NASA/20320-59; NASA-TM-83680.

103. **Corrigan, R.D., Savino, J.M.** Vortex-generators as a means for increasing rotor performance. *Proc. 20th. Inter-soc. Energy Conversion Engineering Conversion Engineering Conf.* 1985, Vol. 3.

104. *Numerical and experimental validation of vortex generator effect on power performance improvement in MW-class wind turbine blade.* **Hyeongi Moon, Junhee Jeong, Sunho Park, Kwangtae Ha, Jae-Ho Jeong.** s.l. : Renewable Energy, 2023, Vol. 212. 0960-1481.

105. **Matthew L. Wilbur, Mihir P. Mistry, Peter F. Lorber, Robert Blackwell, Silvestro Barbarino, Thomas H. Lawrence, Uwe T.P. Arnold.** Chapter 24 - Rotary Wings Morphing Technologies: State of the Art and Perspectives. [book auth.] Ignazio Dimino, Leonardo Lecce, Rosario Pecora Antonio Concilio. *Morphing Wing Technologies.* s.l. : Butterworth-Heinemann,, 2018.

106. **WANG, Jinjun and FENG, Lihao.** Gurney Flap. *Flow Control Techniques and Applications.* s.l. : Cambridge University Press, 2018.

107. *Aerodynamic effects of Gurney flaps on the rotor blades of a research wind turbine.* **Jörg Alber, Rodrigo Soto-Valle, Marinos Manolesos, Sirko Bartholomay, Christian Navid Nayeri, Marvin Schönlau, Christian Menzel, Christian Oliver Paschereit, Joachim Twele, and Jens Fortmann.** 4, s.l. : Wind Energy Science, 2020, Vol. 5. 2366-7451.

108. **Shubham Jain, Nekkanti Sitaram, Sriram Krishnaswamy.** *Computational Investigations on the Effects of Gurney Flap on Airfoil Aerodynamics.* s.l. : International scholarly research notices, 2015. 402358.

109. *Experimental Investigation of Gurney Flaps.* **Bramesfeld, Mark D. Maughmer and Götz.** 6, s.l. : Journal of Aircraft, 2008, Vol. 45. 0021-8669.

110. *Effect of Gurney Flap Geometry on a S809 Airfoil.* **Li-Shu Hao, Yong-Wei Gao.** s.l. : International Journal of Aerospace Engineering, 2019. 1687-5966.

111. *Computational Modeling of Gurney Flaps and Microtabs by POD Method.* **Fernandez-Gamiz U, Gomez-Mármol M, Chacón-Rebollo T.** 8, s.l. : Energies, 2018, Vol. 11. 2091.

112. **Bach, Alena Berit.** *Gurney Flaps and Micro-Tabs for Load Control, PhD Thesis.* s.l. : University of Berlin, 2016.

113. *Computational investigations of small deploying tabs and flaps for aerodynamic load control.* **van Dam, C.P., et al.** s.l. : J. Phys.: Conf. Ser, 2007, Vol. 75. 012027.

114. *Unsteady Computational Investigations of Deploying Load Control Microtabs.* **Raymond Chow, C. P. van Dam.** 5, s.l. : Journal of Aircraft, 2006, Vol. 43.

115. *Wind turbine power improvement utilizing passive flow control with microtab.* **Abbas Ebrahimi, Mohammadreza Movahhedi.** s.l. : Energy, 2018, Vol. 150. 0360-5442.

116. *The Unsteady Aerodynamic Response of an Airfoil with Microtabs and it's Implications for Aerodynamic Damping.* **Matthew Lennie, Alena Bach, George Pechlivanoglou, Christian Nayeri and Christian O. Paschereit.** s.l. : AIAA 34th Wind Energy Symposium, 2016.

117. **Weinzierl, G.** *A BEM based simulation-tool for wind turbine blades with active flow control elements, PhD Thesis.* s.l. : TU Berlin University, 2011.

118. *Vortex Generators for Wind Turbine Blades: A Combined Wind Tunnel and Wind Turbine Parametric Study.* **Mueller-Vahl, Pechlivanoglou, G., Nayeri, C.N., Paschereit.** s.l. : ASME IGTI Turbo Expo Proceedings 2012, 2012.

119. *Low Reynolds Number Airfoils for Small Horizontal Axis Wind Turbines.* **Philippe Giguère, Michael S. Selig.** 6, s.l. : Wind Engineering, 1997, Vol. 21.

120. *Experimental study on pitch angle effects on the performance of Sg-6043 horizontal wind turbine.* **Kukuh Mukti Wibowo, Bayu Rudiyanto, Nugroho Agung Pambudi, Basori, Rusdi Febriyanto, Riyanto, Nova Dani Setyawan.** s.l. : Journal of Physics: Conference Series, 2019, Vol. 1153. 012140.

121. *CFD Investigation on the aerodynamic characteristics of a small-sized wind turbine of NREL PHASE VI operating with a stall-regulated method.* **Young-Ho Lee, Jang-Oh Mo.** s.l. : Journal of Mechanical Science and Technology, 2012, Vol. 26.

122. **Mohamad AbdulRaouf, Essam AlBahkali, Shahid Parvez, Ammar Alnahdi, Mhamed Souli, Thamer AlBahkali.** Chapter 7 - On the investigation of the effect of tower and hub exclusion on the numerical results of a horizontal axis wind turbine.

[book auth.] Arash Soleiman Fallah and Hassan Abbas Khawaja and Mojtaba Moatamedi. *Multiphysics of Wind Turbines in Extreme Loading Conditions.* s.l. : Academic Press, 2024.

123. *Dynamic overset CFD simulations of wind turbine aerodynamics.* **Yuwei Li, Kwang-Jun Paik, Tao Xing, Pablo M. Carrica.** 1, s.l. : Renewable Energy, 2012, Vol. 37.

124. **Chen, Hao.** *Numerical Study of Trailing Edge Flow Control (PhD Thesis).* s.l. : University of Sheffield, 2016.

125. **Tabatabaei, Narges.** *Impact of Icing on Wind Turbine Aerodynamics (PhD Thesis).* s.l. : Luleå University of Technology, 2018. 1402-1544 .

126. **F. Concli, C. Gorla.** Analysis of the power losses in geared transmissions - measurements and CFD calculations based on open source codes. [book auth.] Philippe Velex. *International Gear Conference 2014: 26th-28th August 2014 .* s.l. : Chandos Publishing, 2014.

127. *Review on the numerical investigations into the design and development of Savonius wind rotors.* **Sukanta Roy, Ujjwal K. Saha.** s.l. : Renewable and Sustainable Energy Reviews, 2013, Vol. 24. 1364-0321.

128. **Eldredge, T., Vasquez, E.R.** 18 - Process modeling for hydrocarbon fuel conversion. [book auth.] M. Rashid Khan. *Advances in Clean Hydrocarbon Fuel Processing.* s.l. : Woodhead Publishing, 2011.

129. *Comparison of Methods for Bed Shear Stress Estimation in Complex Flow Field of Bend.* **Zhang, L., Zhang, F., Cai, A., Song, Z., & Tong, S.** 10, s.l. : Water, 2020, Vol. 12.

130. *Investigation approaches to quantify wind-induced load and response of tall buildings: A review.* **Fangwei Hou, Mohammad Jafari.** s.l. : Sustainable Cities and Society, 2020, Vol. 62. 2210-6707.

131. *Optimization of NREL phase VI wind turbine by introducing blade sweep, using CFD integrated with genetic algorithms.* **Ramirez Camacho, Dias, Marcelo M. G.** 2, s.l. : Journal of the Brazilian Society of Mechanical Sciences and Engineering, 2022, Vol. 44.

132. *Performance improvement of a new proposed Savonius hydrokinetic turbine: a numerical investigation.* **Ramin Alipour, Roozbeh Alipour, Farhad Fardian, Seyed Saeid, Rahimian Koloor, Michal Petrů.** s.l. : Energy Reports, 2020, Vol. 6. 2352-4847.

133. *CFD predictions of NREL Phase VI Rotor Experiments in NASA/ AMES Wind Tunnel.* **Mukesh M. Yelmule, EswaraRao Anjuri VSJ.** 2, s.l. : International Journal of Renewable Energy Research, 2013, Vol. 3.

134. *CFD Investigation on the aerodynamic characteristics of a small-sized wind turbine of NREL PHASE VI operating with a stall-regulated method.* **Jang-Oh Mo, Young-Ho LEE.** 1, s.l. : Journal of Mechanical Science and Technology, 2011, Vol. 26.

135. *Numerical aeroelastic analysis of wind turbine NREL Phase VI Rotor.* **Edris Bagheri, Amir Nejat.** 1, Tehran, Iran : Energy Equipment and Systems, 2015, Vol. 3.

136. **Viswanath, P.R.** Aircraft viscous drag reduction using riblets. *Progress in Aerospace Sciences.* 2002, Vol. 38, 6-7.

137. *CFD Aided Investigation of a Small Horizontal Wind Turbine.* **Chris Bliamis, Zinon Vlahostergios, Dimitrios Misirlis, Kyros Yakinthos.** s.l. : Chemical Engineering Transactions, 2023, Vol. 103. 2283-9216.

138. *Drag reduction of large wind turbine blades through riblets: Evaluation of riblet geometry and application strategies.* **Sotiropoulos, Leonardo P. Chamorro and R.E.A. Arndt and F.** s.l. : Renewable Energy, 2013, Vol. 50. 0960-1481.

139. *Slip Length–Based Boundary Condition for Modeling Drag Reduction Devices.* **Benedetto Mele, Renato Tognaccini.** 9, s.l. : AIAA Journal, 2018, Vol. 56.

140. *Enhancement of OWC Wells turbine efficiency and performance using riblets covered blades, a numerical study.* **Reza Abbasi, Mohammad Javad Ketabdari.** s.l. : Energy Conversion and Management, 2022, Vol. 254. 0196-8904.

APPENDICES

Appendix A: Blade Chord and Twist Distributions

Radial Distance r (m)	Span Station[1] (r/5.532 m)	Span Station[1] (r/5.029 m)	Chord Length (m)	Twist[2] (degrees)	Thickness (m)	Twist Axis (% chord)
0.0	0.0	0.0	Hub - center of rotation	Hub - center of rotation	Hub – center of rotation	Hub - center of rotation
0.508[3]	0.092	0.101	0.218 (root hub adapter)	0.0 (root hub adapter)	0.218	50 (root hub adapter)
0.660[4]	0.120	0.131	0.218[5]	0.0	0.218	50
0.883	0.160	0.176	0.183[5]	0.0	0.183	50
1.008	0.183	0.200	0.349[5]	6.7	0.163	35.9
1.067	0.193	0.212	0.441[5]	9.9	0.154	33.5
1.133	0.205	0.225	0.544[5]	13.4	0.154	31.9
1.257	0.227	0.250	0.737[5]	20.040	0.154	30
1.343	0.243	0.267	0.728	18.074	20.95% chord	30
1.510	0.273	0.300	0.711	14.292	20.95% chord	30
1.648	0.298	0.328	0.697	11.909	20.95% chord	30
1.952	0.353	0.388	0.666	7.979	20.95% chord	30
2.257	0.408	0.449	0.636	5.308	20.95% chord	30
2.343	0.424	0.466	0.627	4.715	20.95% chord	30
2.562	0.463	0.509	0.605	3.425	20.95% chord	30
2.867	0.518	0.570	0.574	2.083	20.95% chord	30
3.172	0.573	0.631	0.543	1.150	20.95% chord	30
3.185	0.576	0.633	0.542	1.115	20.95% chord	30
3.476	0.628	0.691	0.512	0.494	20.95% chord	30
3.781	0.683	0.752	0.482	-0.015	20.95% chord	30
4.023	0.727	0.800	0.457	-0.381	20.95% chord	30
4.086	0.739	0.812	0.451	-0.475	20.95% chord	30
4.391	0.794	0.873	0.420	-0.920	20.95% chord	30
4.696	0.849	0.934	0.389	-1.352	20.95% chord	30
4.780	0.864	0.950	0.381	-1.469	20.95% chord	30
5.000	0.904	0.994	0.358	-1.775	20.95% chord	30
5.305	0.959	1.055	0.328	-2.191	20.95% chord	30
5.532	1.000	1.100	0.305	-2.500	20.95% chord	30

Appendix B: QBlade Simulations

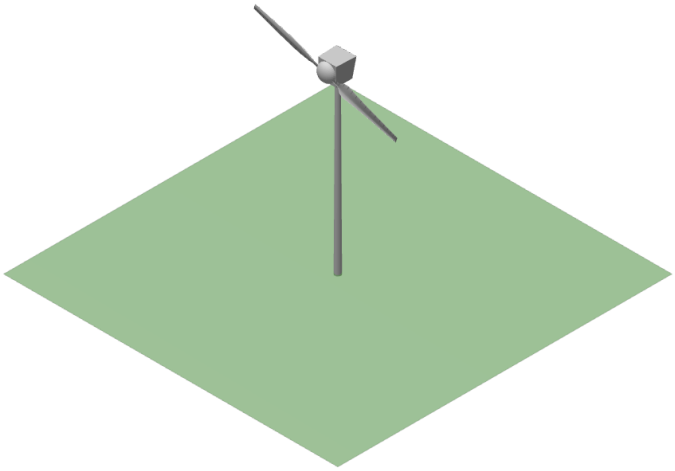

Wind Speed	TSR	Cp	Ct	Power (kW)	Torque (Nm)
5	7.58	0.41	0.70	2.5023	331.88
7	5.42	0.38	0.57	6.4182	851.24
10	3.79	0.24	0.36	11.718	1554.2
13	2.92	0.13	0.24	14.398	1909.6
15	2.53	0.09	0.20	15.422	2045.3

Appendix C : Riblet Dimensioning

$$\delta_v = 5\frac{v}{u^*}$$

Equation 5.4

$$s = \frac{s^+ v}{u^*}$$

Equation 5.5

$$l^+ = \frac{A_b{}^{\frac{1}{2}} u_\tau}{v}$$

Equation 5.6

s = riblet spacing (crest-to-crest)

s^*= riblet spacing in wall units (dimensionless)

h = riblet height

h^+= riblet height in wall units (dimensionless)

$l^+ =$ characteristic length scale in wall units

$A_b =$ cross-sectional area

δ_v = Viscous sublayer

$v =$ kinematic viscosity

$u^* =$ friction velocity

d = spacing between riblet grooves